TUDelft

Delft University of Technology

Halide solid electrolytes
From structure to properties

van der Maas, E.L.

DOI
Publication date
2023
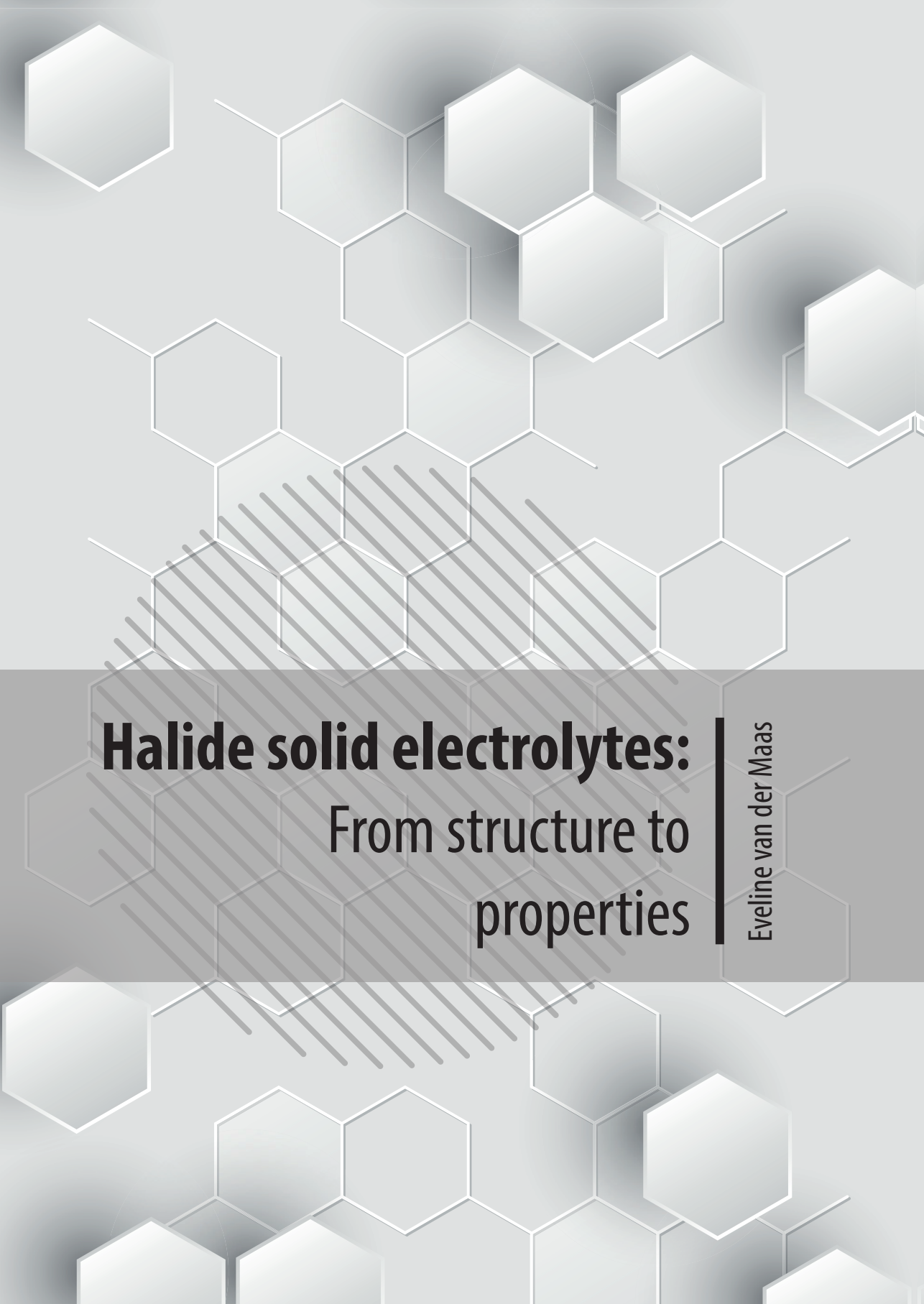**Document Version**
Final published version
Citation (APA)

Important note
To cite this publication, please use the final published version (if applicable).
Please check the document version above.

Halide solid electrolytes:
From structure to properties

Eveline van der Maas

Halide solid electrolytes.

From structure to properties

Halide solid electrolytes.

From structure to properties

Dissertation

for the purpose of obtaining the degree of doctor
at Delft University of Technology
by the authority of the Rector Magnificus, prof. dr. ir. T.H.J.J. van der Hagen
chair of the Board for Doctorates
to be defended publicly on
Tuesday 16 May 2023 at 12:30 o'clock

by

Eveline VAN DER MAAS

Master of Science in sustainable energy technology,
Delft university of technology, Nederland
born in Biel, Switzerland.

This dissertation has been approved by the promotors.

Composition of the doctoral committee:

Prof. ir. P.G. Luscuere	Chairman
Prof. dr. ir. M. Wagemaker,	Delft University of Technology, promotor
Dr. S. Ganapathy,	Delft University of Technology, copromotor

Independent opponents:

Prof.dr. W. Zeier	U. Münster, Germany
Dr. E.R.H. van Eck	Radboud U. Nijmegen, NL
Prof.dr. C. Masquelier	U. Picardie Jules Verne, France
Prof.dr. E.H. Brück	Technische Universiteit Delft
Prof.dr. F.M. Mulder	Technische Universiteit Delft

Contents

Summary

Batteries are an important aspect of sustainable energy technologies, as they can be used either for the storage of electric energy for the grid or for the electrification of the transport fleet, making these sectors less reliant on fossil fuels (chapter 1).

The Li-ion battery has revolutionized the world in many ways, enabling portable electric devices as honored by the Nobel prize in 2019 to John B. Goodenough, M. Stanley Whittingham and Akira Yoshino. As the Li-ion battery is quite a mature technology by now, large gains in performance parameters (especially energy density) will need alternative battery concepts and new chemistries.

There are many possibilities, and one of them is a switch from liquid to solid electrolytes (chapter 2).

The work presented in this thesis investigates the structure-to-property relationship of halide solid-electrolytes $Li_3M(III)X_6$. For solid electrolytes to replace liquid electrolytes, the material needs a combination of properties.

An important property is the ionic conductivity, which should be high enough for room-temperature operation of the battery and determines, among other design parameters, the rate-capability (or power density) of the battery.

Another property that is important is the electrochemical stability window, which determines the electrochemical stability of the electrolyte in contact with the electrodes of the material. Both of these properties are strongly related to the crystal structure and chemistry of the solid electrolyte (chapter 2).

Therefore, both the structure and properties are investigated using a variety of techniques, mostly x-ray and neutron diffraction, AC-impedance and solid-state NMR relaxometry (chapter 3). The work is presented in four data containing chapters:

- Chapter 4: The materials investigated show very complex behavior relating to diffusion on short time scales, as investigated by NMR T_1-relaxometry. The first chapter therefore provides an in-depth introduction to solid-state NMR relaxometry and spectral density fitting. Using two examples, namely Li_6PS_5X, a sulfide solid-electrolyte class previously studied in the research group, and halide $Li_3YCl_3Br_3$, it is illustrated how multiple jump processes can present in the curve of the relaxation rates vs. inverse temperature.

- Chapter 5: In this chapter, aliovalent substitution in Li_3InCl_6 with $Zr(IV)$ is explored. The $Zr(IV)$ replaces the $In(III)$ and introduces an additional Li-vacancy. The substitution can also affect the crystal structure of the material, affecting ionic diffusion in other ways than changing the charge carrier concentration. Using combined x-ray and neutron diffraction, it is found that the ordering of the $In(III)$ and $Zr(IV)$ is affected by the substitution. This affects also the diffusion on short timescales, as can

be observed with NMR relaxometry as well as from the solid-state NMR lineshape. The combination of the structure solution and the puzzle pieces provided by solid-state NMR suggest, that the structural change induced by the substituent leads to more three-dimensional conduction.

- Chapter 6: While chlorides have higher electrochemical stability, bromide anions are more polarizable and may have lower association energy with Li, which can lead to higher Li-ion conductivity. This chapter investigates the trade-off between ionic conductivity and electrochemical stability in materials $Li_3YClBr_xCl_{6-x}$. It is found that 75% Br is most beneficial for ionic conductivity rendering a very conductive material (~5 mS/cm at room temperature), higher concentration of bromine indeed lower the electrochemical stability window. The introduction of 25% Br, however, also leads to an increase in ionic conductivity while preserving the electrochemical stability. This suggests that Br-substitution can be a viable method to increase the ionic conductivity of Li-ion conducting chlorides while preserving the electrochemical stability.

- Chapter 7: The $Li_3M(III)Cl_6$ (M(III)= Ho, Y, Dy, Tm) usually are reported to crystallize in a trigonal crystal structure. This paper shows that synthesizing these materials by co-melting with some LiCl deficiency stabilizes an orthorhombic phase of the material. Both of these structures are based on quasi hexagonally close-packed Cl atoms, with the M(III) and Lithium on octahedral sites. The different crystal symmetry is caused by a change in the arrangement of the cations.

  The orthorhombic phase has ~8 times higher ionic conductivity compared to the trigonal phase. Ab initio molecular dynamic simulations revealed that this is due to a fast conduction pathway along the c-direction of the crystal structure. This path corresponds to jumps between face-sharing octahedra. Therefore, it is likely that the cation arrangement in the orthorhombic structure is favorable for that diffusion path, leading to an increase in ionic conductivity.

It is interesting to compare the effect of the different material design strategies aliovalent substitution (Chapter 5), halogen alloying (chapter 6) and tuning of the crystal structure (Chapter 7) on the properties of interest for $Li_3M(III)X_6$ solid electrolytes.

The electrochemical stability window is indeed higher for chlorides than for bromides, but it is found that 25% Br substitution preserves the stability of the chloride in Li_3YCl_6.

For ionic conductivity, the largest increase is observed for halogen alloying (factor ~40 increase in ionic conductivity when substituting 25% of the chlorine with bromine atoms), followed by the trigonal to orthorhombic phase transition (factor ~8 improvements) and, lastly, aliovalent substitution (factor ~1.6 improvement).

Regarding the measurement methods, two notable findings were found.

Firstly, this thesis showed that x-ray diffraction data is important in this system to reach reliable occupancies in the crystal structure solution (chapter 5), as neutrons scattered on lithium and most of the M(III) have a 180°phase shift and therefore cancel their signal when occupying the same site.

Lastly, it is shown that the complex shapes of the NMR T_1 relaxation rates can be explained using a superposition of individual, BPP-type jump processes. Fitting such a model is complex, and data measured at multiple larmor frequencies should be used to increase the reliability of the fit. To perform such a fit, a programm was developed in the scope of this thesis to simultaneously fit such measurements and analyze the error associated with the parameter by sampling the posterior probability distribution of the parameter using a Markov chain Monte Carlo sampler.

Samenvatting

Batterijen maken een belangrijk deel uit van duurzame energie-technologieën, aangezien ze gebruikt kunnen worden voor de opslag van energie voor het elektriciteitsnetwerk of als energiebron in elektrische auto's, zodat deze sectoren minder afhankelijk worden van fossiele brandstoffen (hoofdstuk 1). De Li-ion-batterij heeft de wereld op veel manieren veranderd, bijvoorbeeld in het mogelijk maken van draagbare elektrische apparaten zoals laptops en mobiele telefoons. Door de grote invloed die de uitvinding van de Li-ion batterij op de maatschappij had, kregen de uitvinders John B. Goodenough, M. Stanley Whittingham en Akira Yoshino in 2019 de Nobelprijs in scheikunde.

De Li-ion-batterij gebaseerd op kobalt oxide en grafiet is tegenwoordig een behoorlijk volwassen technologie. Om echter verbeteringen van de technologie te bereiken, is het daaroom nodig om alternatieve batterijconcepten te onderzoeken. Één van deze concepten is gebaseerd op het vervangen van de vloeibare elektrolyt in de batterij door een vaste stof (hoofdstuk 2).

Dit proefschrift onderzocht de "structure to property relationship" van vaste stof elektrolyten met chemische formule $Li_3M(III)X_6$ (waarin M(III)= Y, Sc, In of en andere lanthanide en X = Cl, Br of I). Om de vloeibare elektrolyt door en vaste stof te vervangen, moet de vaste stof bepaalde eigenschappen hebben.

Een belangrijke eigenschap is de ionische geleidbaarheid, die afdoende moet zijn voor het gebruik van de batterij bij kamertemperatuur aangezien dit de vermogensdichtheid van de batterij bepaalt. Een andere belangrijke eigenschap is de electrochemische stabiliteit, die het potentiaalvenster bepaald waaronder de batterij kan werken. Beide eigenschappen zijn sterk gerelateerd aan de kristalstructuur en chemie van de vaste stof elektrolyt (hoofdstuk 2).

Om deze reden worden zowel de structuur als ook de eigenschappen van de vaste stof elektrolyt onderzocht met behulp van analysetechnieken, zoals röntgen- en neutronendiffractie voor de analyse van de kristalstructuur, AC-impedantie en vaste stof NMR voor metingen van de geleiding van de Li-ionen (hoofdstuk 3). Het proefschrift is onderdeel in vier hoofdstukken:

- Hoofdstuk 4: De onderzochte materialen laten een zeer complex gedrag zien in verband met diffusie op korte tijdschalen, zoals onderzocht met NMR. Het eerste hoofdstuk is daarom een diepgaande introductie in solid-state NMR en het zo genaamde spectral density fitting. Aan de hand van twee voorbeelden, namelijk Li_6PS_5Cl, een zwavelhoudende vaste-stof elektrolyt eerder bestudeerd in de onderzoeksgroep, en halide $Li_3YCl_3Br_3$, wordt gedemonstreerd en uitgelegd hoe informatie over de diffusie kan worden verkregen uit dit soort metingen.

- Hoofdstuk 5: In dit hoofdstuk wordt de aliovalente substitutie van In(III) in Li_3InCl_6 met Zr(IV) onderzocht. De Zr(IV) vervangt het In(III) en introduceert een extra

lege vakature voor Li. De substitutie kan ook de kristalstructuur van het materiaal beïnvloeden, wat de ionische diffusie op andere manieren kan beïnvloeden dan het veranderen van de ladingdrager-concentratie. Met behulp van gecombineerde röntgen- en neutronendiffractie werd gevonden dat de ordening van de In(III) en Zr(IV) wordt beïnvloed door de substitutie. Dit beïnvloedt ook de diffusie op korte tijdschalen, zoals waarneembaar is met NMR. De combinatie van de structuuropheldering en de puzzelstukken aan informatie die worden verkregen uit vaste stof NMR en impedantie metingen suggereren dat de structuurverandering leidt tot meer driedimensionale geleiding.

- Hoofdstuk 6: Hoewel chloriden een hogere elektrochemische stabiliteit hebben, zijn bromide-anionen polariseerbaarder en kunnen daarom leiden tot een hogere Li-ion geleidbaarheid. Daarom onderzoekt dit hoofdstuk de afweging tussen ionische geleidbaarheid en electrochemische stabiliteit in stoffen met formule $Li_3YClBr_xCl_{6-x}$ (x = [0, 6] in stappen van 1.5). 75% Br is het meest gunstig is voor de ionische geleidbaarheid, wat een zeer geleidend materiaal oplevert (~5 mS/cm bij kamertemperatuur), helaas verlagen deze hoge Br-concentraties inderdaad het electrochemische stabiliteitsvenster. De introductie van 25% Br leidde echter wel tot een toename van de ionische geleidbaarheid zonder dat de electrochemische stabiliteit werd aangetast. Dit suggereert dat Br-substitutie tot en bepaalde concentratie een methode kan zijn om de ionische geleidbaarheid van chloriden te verhogen zonder de electrochemische stabiliteit aan te tasten.

- Hoofdstuk 7: $Li_3M(III)Cl_6$ (M(III)= Ho, Y, Dy, Tm) kristalliseert vaak in een trigonale kristalstructuur. Dit onderzoek laat zien dat het synthetiseren van deze materialen door co-smelten met een tekort aan LiCl een orthorhombische fase van het kristal stabiliseert. Beide structuren zijn gebaseerd op quasi hexagonaal dichtst gestapelde Cl-atomen, met de M(III) en lithium op oktaeder posities. De gevonden kristalsymmetrie wordt veroorzaakt door een verandering in derangschikking van de kationen.

De orthorhombische fase heeft ~8 keer hogere ionische geleidbaarheid in vergelijking met de trigonale fase. Ab initio moleculaire dynamische simulaties hebben aangetoond dat dit komt door een snel geleidingspad langs de c-richting van de kristalstructuur. Dit pad correspondeert met sprongen tussen aanliggende oktaeders, die en driehoekige vlakte samen delen, in plaats van het pad gevormd door een tetraeder die ingeklemd is tussen twee oktaeders. Daarom is het waarschijnlijk dat de kationrangschikking in de orthorhombische structuur gunstig is voor dat diffusiepad, wat leidt tot de toename van de ionische geleidbaarheid.

Het is interessant om de effecten van de verschillende materialenontwerpstrategieën, zoals aliovalente substitutie (Hoofdstuk 5), halogenverbinding (hoofdstuk 6) en afstemming van de kristalstructuur (Hoofdstuk 7) op de eigenschappen van belang voor $Li_3M(III)X_6$ vaste stof elektrolyten te vergelijken.

Het elektrochemische stabiliteitsvenster is inderdaad hoger voor chloriden dan voor bromiden, maar er werd gevonden dat 25% Br-substitutie de stabiliteit van de stof gebaseerd op chloride in Li_3YCl_6 behoudt.

Voor de ionische geleidbaarheid wordt de grootste toename waargenomen door Br-substitutie van Cl (factor ~40 toename in ionische geleidbaarheid bij het vervangen van 25% van de Cl door Br), gevolgd door de overgang van de trigonale naar de orthorhombische fase (factor ~8 verbetering) en ten slotte aliovalente substitutie van het M(III) met en M(IV) (factor ~1,6 verbetering).

Met betrekking tot de analysetechnieken zijn er ook twee opmerkelijke bevindingen gedaan.

Ten eerste heeft dit proefschrift aangetoond dat röntgendiffractie-data belangrijk zijn in dit systeem om betrouwbare atoombezettingsgraden te realiseren om zo een volledige opheldering te verkrijgen van de kristalstuctuur (hoofdstuk 5). Dit is omdat neutronen bij de diffractie aan lithium een 180°faseverschuiving hebben, wat tot destructieve interferentie kan leiden met In op dezelfde positie.

Ten slotte is aangetoond dat de complexe vormen van de NMR T_1 spin lattice relaxatietijden kunnen worden verklaard door middel van een superpositie van individuele, BPP-type sprongprocessen. Het fitten van zo'n model is complex en data gemeten bij meerdere larmor frequenties moeten worden gebruikt om de betrouwbaarheid van het resultaat te verhogen. In dit proefschrift is een programma gebaseerd op python ontwikkeld om dit soort metingen gelijktijdig te fitten en de fout geassocieerd met de parameter te analyseren door het sampling van de posterior probability distributie van de parameter met een Markov Chain Monte Carlo sampler.

Acknowledgments

My Ph.D. thesis was completed with the help of many individuals, to whom I express my sincere gratitude.

Swapna Ganapathy, my main supervisor and copromoter, deserves my first and foremost thanks for her invaluable guidance and support throughout both my master's thesis and my entire Ph.D. program. Her encouragement, advice, and unwavering dedication to my research were instrumental in helping me navigate this journey.

My gratefulness also goes to Marnix Wagemaker, my promoter, for giving me the opportunity to pursue a Ph.D. program and for his valuable feedback and support during my research.

Further, I would like to express my gratitude for my colleague Theodosios Famprikis, who taught me a lot about structural chemistry and diffraction, as well as analyzing structure-to-property relationships. The numerous engaging discussions were always fun and helped me to broaden my understanding of the subject. His dedication to science and high scientific standards often inspired me to do the best work I can do.

My gratitude also goes to Ernst van Eck for his assistance in getting me started with relaxometry measurements in the NMR laboratory in Nijmegen, teaching me how to conduct and analyze the measurements, and helping me to develop the data analysis method presented in this thesis.

Special thanks go to Steven Parnell for his help in obtaining neutron diffraction measurements, which were critical to the success of my research.

I would like to acknowledge Wenxuan Zhao, my former Master's student, whose great dedication and hard work built the groundwork for the publication in chapter 6. It was my honor to supervise him during the project.

Finally, I express my gratitude to all the other people in the lab and the institute who have helped me in one way or another during my research. Your contributions have been immensely valuable, and I am grateful for your assistance. I would also like to acknowledge the financial support provided by NWO, which made it possible for me to carry out this research.

Eveline
Zürich, April 2023

1

Climate, Sustainability, economy and batteries

1.1 Why we need sustainable energy technologies

Climate change is one of the main driver for investments and developments regarding renewable energy technologies. This includes the storage of energy generated by intermittent renewable energy sources, as well as the electrification of transport. Given the importance of climate change as a driver for storage technologies, this chapter sketches what climate change is and tries to make the importance of it clear to the reader. The (possible) role of batteries is then discussed in more detail.

1.1.1 What is climate change?

Despite being such a widely discussed topic, climate change as a term is often used vaguely. Therefore, the term climate change is defined first. Then, some risks of climate change are derived conceptually, based on the definition of the term.

The term climate is defined as the average state of the weather during 30 years. To understand the term climate we therefore first need to define the term weather. Weather is defined as the state of the atmosphere at a particular place and time regarding variables such as

- Temperature/heat

- cloudiness

- dryness/moisture

- sunshine

- wind

- rain

1

- atmospheric pressure

According this definition, weather is a very complex superposition of many variables, that dependent of each through, among others, conservation laws of mass, energy and momentum and the first law of thermodynamics.

If climate is the average state of the weather during 30 years, then climate change describes the change of the average over thirty years of the variables defining the weather. Global warming, another commonly used term when talking about climate change, usually refers to the increase of the average surface temperature/heat on earth, and can be seen as one of the features of climate change.

If, as a thought exercise, we think about the variables defining the weather and make up scenarios of what could happen if these are changing on the long-term. Due to the increased average temperature, ice-masses in many regions of the world can shrink, leading to higher sea level. This in combination with changes in rainfall can affect water management systems. The combination of increased flooding and droughts can affect soil quality, which can be problematic for agricultural activities.

This paragraph shows that already from the definition of the word climate change, a handful of factors can be derived that may pose a risk to the most basic needs of living beings, namely water, food and shelter.

1.1.2 What is the current state of climate change and how does it affect human livelihood?

The state of climate change is assessed periodically by the Intergovernmental Panel on Climate Change (IPCC). The IPCC is a United Nations body that assesses the (peer-reviewed and published) science related to climate change. It was established in 1988 to provide policymakers with scientific information to aid in the development of climate-related policies. The IPCC meets regularly to review the latest research on climate change and to publish reports that summarize the state of the science. These reports are widely regarded as the most authoritative and comprehensive assessments of climate change and its impacts.

Following are three selected citations from the IPCC's recommendations for policy makers [1], to give the reader an idea on the current estimation of the effect of these risks:

- "Risks in physical water availability and water-related hazards will continue to increase by the mid- to long-term in all assessed regions, with greater risk at higher global warming levels (high confidence). (...) Changes to streamflow magnitude, timing and associated extremes are projected to adversely impact freshwater ecosystems in many watersheds by the mid- to long-term across all assessed scenarios (medium confidence). (...) Challenges for water management will be exacerbated in the near, mid and long term, depending on the magnitude, rate and regional details of future climate change and will be particularly challenging for regions with constrained resources for water management (high confidence)."[1]

- "Climate change will increasingly put pressure on food production and access, especially in vulnerable regions, undermining food security and nutrition (high confidence). Increases in frequency, intensity and severity of droughts, floods and heatwaves, and continued sea level rise will increase risks to food security (high

confidence) in vulnerable regions from moderate to high between 1.5℃ and 2℃ global warming level, with no or low levels of adaptation (medium confidence).(...) Global warming will progressively weaken soil health and ecosystem services such as pollination, increase pressure from pests and diseases, and reduce marine animal biomass, undermining food productivity in many regions on land and in the ocean (medium confidence)."[1]

- "Concurrent and repeated climate hazards occur in all regions, increasing impacts and risks to health, ecosystems, infrastructure, livelihoods and food (high confidence). Multiple risks interact, generating new sources of vulnerability to climate hazards, and compounding overall risk (high confidence). (...) These interacting impacts will increase food prices, reduce household incomes, and lead to health risks of malnutrition and climate-related mortality with no or low levels of adaptation, especially in tropical regions (high confidence)."[1]

These estimates show that climate change poses a risk to society, affecting basic human needs. A question often raised in such discussions is the effect of anthropogenic climate change (climate change caused by human activities such as, for example, burning of fossil fuels and deforestation) and natural climate change. In fact, "the earth's temperature has varied before. How is the current warming any different?" is one of the frequently asked questions for the working group I of the ICCP, which works on the physical science basis [2] which states the following:

- "Earth's climate has always changed naturally, but both the global extent and rate of recent warming are unusual. The recent warming has reversed a slow, long-term cooling trend, and research indicates that global surface temperature is higher now than it has been for millennia."[2]

The report also states that 4 major differences between current and past warming periods. Those are that it is warming 1) rapidly, 2) almost everywhere, that 3) It has been a long time since it's been this warm and 4) The recent warming reversed a long-term global cooling trend [2].

These differences between past and current warmings point at anthropogenic climate change as at least part of the cause, making it clear that our behaviour needs to be adapted to mitigate climate change. While there have been many developments in the past that should help mitigate climate change (such as the increased use of solar panels for electricity generation, windmills and the beginning of the electrification of transport), it is not enough, again clearly stated in the IPCC report for policy makers [1]:

- "It is unequivocal that climate change has already disrupted human and natural systems. Past and current development trends (past emissions, development and climate change) have not advanced global climate resilient development (very high confidence). Societal choices and actions implemented in the next decade determine the extent to which mediumand long-term pathways will deliver higher or lower climate resilient development (high confidence). Importantly climate resilient development prospects are increasingly limited if current greenhouse gas emissions do not rapidly decline, especially if 1.5℃ global warming is exceeded in the near-term

1

(high confidence). These prospects are constrained by past development, emissions and climate change, and enabled by inclusive governance, adequate and appropriate human and technological resources, information, capacities and finance (high confidence)".[1]

1.1.3 What can batteries contribute

Batteries can play an important role in mitigating climate change by enabling electrical energy storage to store energy from renewable sources as well as electric cars, aiding the decarbonization of transport and reducing reliance on fossil fuels.

Renewable energy sources such as wind and solar energy are of intermittent nature. Batteries can help balancing the grid by storing excess renewable energy when production is high and demand is low, and providing additional energy when production is lower than demand. Additionally, batteries are rather good at stabilizing the grid thanks to relatively fast response times. Batteries designed for such grid-scale storage are very sensitive to price due to the amount of energy that needs to be stored, but less sensitive to energy density / weight (compared to portable applications).

Batteries can also be used to power electric vehicles (EVs), which can reduce greenhouse gas emissions from transportation. EVs produce zero tailpipe emissions and, when charged with electricity from renewable energy sources, can significantly reduce the carbon footprint of transportation given that the CO_2 footprint of the battery production is not too high. This is a very complex question, as it depends a lot on whether materials are mined or recycled and the source of electricity and heat in the processing of the components [3]. As the battery has to move in unison with the car, there are clear requirements regarding weight and volume of the battery that need to be considered in the design.

Overall, batteries can have multiple functions in a society centered around renewable energy technology and can therefore help reduce the dependency on fossil fuels.

Just as climate change is not the same as global warming, reducing emissions is not the same as sustainable. Sustainability was first defined by the United Nations Brundtland Commission [4]:

> "Sustainable development is development that meets the needs of the present without compromising the ability of future generations to meet their own needs."

Given this definition, it is clear that for batteries to be considered a sustainable technology, not only the emission balance needs to be considered, but also the raw-materials needed to make them. Unless the battery industry manages to become circular (by recycling batteries and using the recycled materials to make new batteries), it is clear that only abundant raw materials that are relatively accessible (can be extracted economically) should be used, which is currently not the case. The interested reader in what elements this entails is referred to the publication by P. Vesborg and T. Jaramillo [5]

References

[1] IPCC. *Summary for Policymakers*, pages 3–32. Cambridge University Press, Cambridge, United Kingdom and New York, NY, USA, 2021.

[2] P.W. Thorne J. Ahn F.J. Dentener C.M. Domingues S. Gerland D. Gong D.S. Kaufman H.C. Nnamchi J. Quaas J.A. Rivera S. Sathyendranath S.L. Smith B. Trewin K. von Schuckmann Gulev, S.K. and R.S. Vose. Urban systems and other settlements Supplementary Material. In *Climate Change 2021: The Physical Science Basis. Contribution of Working Group I to the Sixth Assessment Report of the Intergovernmental Panel on Climate Change*, chapter Changing State of the Climate System., pages 287–422. Cambridge University Press, Cambridge, UK and New York, NY, USA, 2022.

[3] Quanwei Chen, Xin Lai, Huanghui Gu, Xiaopeng Tang, Furong Gao, Xuebing Han, and Yuejiu Zheng. Investigating carbon footprint and carbon reduction potential using a cradle-to-cradle lca approach on lithium-ion batteries for electric vehicles in china. *Journal of Cleaner Production*, 369:133342, 2022.

[4] UNWCED: United Nations World Commission on Environment and Development. Our common future (brundtland report). Technical report, 1987.

[5] Peter C. K. Vesborg and Thomas F. Jaramillo. Addressing the terawatt challenge: scalability in the supply of chemical elements for renewable energy. *RSC Advances*, 2(21):7933, 2012.

1

2

Introduction to batteries

2.1 The Li-ion battery

Batteries are electrochemical energy storage devices that store energy in chemical form which can be released in electrical form. Batteries are often distinguished between primary batteries (non-rechargeable) and secondary batteries (rechargeable). Since the Li-ion battery was first commercialized in 1991 by Sony, batteries have been getting increasingly prominent in modern society. The high energy density storage in Li-ion batteries enabled portable electronic applications such as cell phones and laptops and more recently, electric transportation. The large societal impact of the technology was honoured with the Noble prize for chemistry in 2019, awarded to John B. Goodenough, M. Stanley Whittingham, and Akira Yoshino.

In the Li-ion battery developed by John B. Goodenough, M. Stanley Whittingham, and Akira Yoshino, graphite is used as the anode and Li_2CoO_2 (LCO) as the cathode. The battery is often referred to as the "rocking chair" battery, due to the two intercalation materials as electrodes. Intercalation materials are materials that consist of a host-structure, which has space to accommodate ions that intercalate, without large structural changes to the host material. Both graphite as well as LCO are layered materials, where the lithium can diffuse between the layers. Upon charge and discharge cycles, the lithium moves back and forth, like the motion of a rocking chair.

The lowest energy state of the battery (fully discharged) is when all the lithium is in the cathode, which is also how the battery is manufactured. When the battery is charged, the cathode potential is raised by the application of a voltage. In that state, it is energetically favourable for the lithium to leave the cathode as Li+ into the electrolyte, while simultaneously a Li+ enters the graphite and is reduced. The electron travels through the outer circuit, charging the cell. During discharge, no voltage has to be applied and the battery can discharge spontaneously to it's lowest energy state.

Since these pioneering cells, batteries have improved and cost has dropped. Between 1992 and 2016, the price of Li-ions batteries declined about 97% and the annual market

size increased by six orders of magnitude [1]. As the price dropped, the energy density increased from ~200Wh/liter in 1992 to ~700 Wh/l [1].

The biggest contributors to the decrease in cost are the economics of scale and the increase in energy density, while the battery concept has essentially stayed the same. The main changes were substitution of Co in the cathode with elements like Ni, Mn and Al as well as adding additives to the electrolyte to improve certain performance aspects.

2.1.1 Key measures for Li-ion batteries and battery materials

In this section, some key concepts are introduced that are used to compare battery materials and batteries.

Capacity

The capacity of a material depends on how much lithium/charge can be stored in the host:

$$C = \frac{nF}{M} \tag{2.1}$$

where n is the amount of Li stored per mol of material, F is the faradey constant and M the molar mass of the material.

Energy density

The theoretical energy density of a chemistry can be a useful estimate to compare different chemistries and is defined as the amount of energy stored per mass (gravimetric) or volume (volumetric) energy density of material.

The gravimetric is defined as follows:

$$E_{density,g} = \frac{nF\Delta E}{M} = C_t * V \tag{2.2}$$

where n is the number of moles of lithium ions involved in the reaction, F is the Faraday constant, ΔE is the potential difference between the potential of the cathode and the anode and M is the mass of the active materials per mole. The theoretical energy density can also be calculated by multiplying the theoretical capacity C_t with the average voltage V.

The volumetric energy density is the energy stored per volume:

$$E_{density,V} = \frac{Energy\,stored\,[Wh]}{Volume\,[l]} \tag{2.3}$$

Where the energy stored can be calculated from the output of a real battery (obtainable capacity times average voltage) and the Volume of the battery.

Power density

The power density of a battery determines how much power (Energy per unit time) the battery can deliver per surface area A

$$P/A = \frac{dE}{dT} = V\frac{dC}{dt} = \frac{V * I}{M} \tag{2.4}$$

and is proportional to the current drawn through the battery. The amount of current that can be drawn at a certain voltage depends on the electronic and ionic transport properties in the electrodes as well as the electrolyte (and current collectors).

Cycle life

The cycle life of a battery refers to the usable lifetime of the battery. Usually, a battery is considered at the end of its life when it reaches 80% of its initial capacity

2.2 Alternative battery concepts

The theoretical capacity and energy density are the upper limits achievable for a specific battery chemistry. If the chemistry stays the same, then all the improvements in energy density will arise from reducing the mass of inactive components, so current collector, separator, electrolyte and binder as well as denser packing. If, at some point, the potential of such improvements are exhausted, the only way to keep improving batteries is by alternating the chemistry. There are many alternative battery concepts out there, to name a few specifically aiming at high energy density:

- **Li-metal anode [2]**: The Lithium metal anode is often considered as the "holy grail" of anodes. Lithium has low redox potential (-3.04 V vs the standard hydrogen electrode) and can therefore increase the total output voltage of the battery. This, combined with the fact that Lithium is the lightest of all metals, and that no host-structure is needed (like graphite), makes Li-metal a very high capacity anode (~3860 mAh/g). The Li-metal anode has been commercialized by Moli energy in the 1980ies [3]. However, the cells had to be withdrawn due to fire incidents caused by the growth of the lithium in the shape of dendrites, which eventually lead to a short-circuit in the cell. This issue is not solved until this day.

- **Silicon anode [4]**: Silicon can be used as an anode at low voltage (0.06 vs Li/Li$^+$) and a theoretical capacity of 4200 mAh/g (compared to 372 mAh/g for graphite). The high capacity arises from the kind of reaction. The reaction between lithium and silicon is an alloying reaction, which usually have a higher capacity than intercalation materials Silicon is also a very abundant element and light weight. Alloying reactions usually have much larger structural and volume changes of the electrode particles, which can be problematic for the cycle life of the battery.

- **Li-sulfur battery [5]**: Sulfur is a potential candidate for the cathode material. The reaction between sulfur and lithium is a combination reaction, where two lithium and one sulfur combine to form Li_2S. The theoretical capacity of this cathode is 1672 mAh/g at 2.8 V vs Li/Li$^+$. Sulfur is also a light and very abundant element, making it a attractive choice of electrode. Drawbacks are that the electrical conductivity of sulfur is low, making it difficult to get good electronic percolation and that during charging the sulfur can dissolve in the electrolyte, leading to capacity fading and hence short cycle life.

- **Li-air battery [6]**: The lithium-air battery usually refers to a battery with lithium metal anode and a porous host on the cathode, where lithium reacts with gaseous oxygen to form Li_2O_2. The theoretical capacity of this reaction is 11'140 mAh/g (only including the weight of the lithium and the oxygen) at a voltage of ~3V. The lithium air battery often has poor reversibility, is usually cycled at low rates and can suffer from low cycle life especially when exposed to reactive gases other than oxygen.

- **All solid-state battery [7]**: For the solid-state battery, the liquid, organic electrolyte is replaced with a solid (either a polymer or an inorganic solid). This leads to advantages in safety against fires, as the electrolyte is generally not flammable. Solid-electrolytes are single ion conductors and therefore may enable higher power density. Further, the solid electrolyte may enable different shapes of cell design like bipolar stacking, which could lead to higher energy density. Finally, it is possible that solid-electrolytes can avoid certain problems that liquid electrolytes can not, such as for example sulphur dissolution or li-dendrite formation and hence enabling higher capacity electrodes, which can also improve the energy density. Drawbacks of solid electrolyte are for example that it is difficult to make electrodes and ensure electrical contact between cathode and the solid-electrolyte during cycling, lower rate capability and shorter cycle life (as of now).

While many of these concepts are very promising, solid-state electrolytes have been a big research topic since 2011 when the seminal paper of Kamaya et al. showed that solid electrolytes with conductivities similar to liquid electrolytes can be found [8].

2.3 Solid-state electrolytes

Solid-state electrolytes replace the separator and the liquid electrolytes in the Li-ion battery. Therefore, it has to replace the functions of these components, which are:

- The separator separates the Anode from the Cathode mechanically, to prevent short circuit of the battery due to contact between the electrodes.

- The liquid electrolyte transports the ions during charge and discharge.

- Both the separator and the liquid electrolyte are insulating for electrons, to prevent self discharge or a short circuit in the extreme case.

- The liquid electrolyte or the salt/additives it contains, can decompose at the electrodes to form passivation layer and stabilize the electrode/electrolyte interface.

- The liquid electrolyte can penetrate the porous electrode and adapt to it's shape, to ensure good contact between the electrolyte and the cathode.

- Can be processed economically on large scale.

The solid electrolyte therefore needs a specific set of properties to replace all these functions. These are among others:

- The solid electrolyte needs favourable mechanical properties to be able to both replace the separator, as well as mold to the electrodes and ensure electrical contact.

- It needs high ionic conductivity to transport the ions and ensure similar charge- and discharge rates. At the same time, it needs to be insulating for electrons to prevent self-discharge and short circuit.

- It needs to be chemically and electrochemically stable with the electrodes or be able to form a favourable interphase to passivate the reaction.

- It needs to be processable on large scale and economically competitive with the current Li-ion cells.

This thesis mostly focuses on two properties, the ionic conductivity and to a lesser degree, on the electrochemical stability. These are properties that are, to a first order, determined by the chemistry and crystal structure of the materials.

2.3.1 Structure of materials

The structure and chemistry of materials is what largely determines their properties. Solid materials can be distinguished between crystalline and amorphous materials. In crystalline materials, there is a unit that repeats periodically to fill space. This is not the case in an amorphous material, where no clear periodicity is present.

The materials investigated in this thesis are all crystalline materials.

Crystal structures

Crystal structures are comprised of periodically repeating units. A crystal structure is described in different parts:

- The smallest element in the crystal structure that is needed to describe it is the irreducible unit cell. It contains the atoms of the crystal and their arrangement, not related to each other by a symmetry operation.

- The space group of the crystal structure contains the symmetry operations acting on each atom, to create the unit cell. The unit cell is the basic building block of the crystal, which repeats periodically to fill space.

- The way these units can repeat periodically is described by the Bravais lattice.

Crystal structures can be studied using diffraction-based techniques (section 3.1.1) and the analysis of the crystal structure can give insight into the diffusion mechanism.

2.3.2 Fick's laws of Diffusion

In general, diffusion describes a particle flux/current driven by a chemical potential gradient. The total flux is described by Fick's first law of diffusion [9].

$$j = -D\nabla C \tag{2.5}$$

with j as the current density, D the diffusion coefficient and ∇C the concentration gradient. Depending on the direction of the chemical potential gradient, the flux goes in the same direction as the concentration gradient, or against it. Fick's first law combined with the continuity equation $-\nabla J = \frac{\delta C}{\delta t}$ leads to Fick's second law [9]

$$\frac{\delta C}{\delta t} = \nabla(D\nabla C) \tag{2.6}$$

The self diffusion coefficient of a single ion can generally be written as [10]

$$D^* = \lim_{t \to \infty} \frac{d}{dt}\left[\frac{1}{2dN}\left(\sum_i^N \left(\vec{R}\right)^2\right)\right] \tag{2.7}$$

Diffusion by hopping on a lattice

In a crystal, diffusion results from a hopping process of the diffusing atoms between different lattice sites. In the simplified case of diffusion between two planes with n charge carriers, with charge carrier concentration $c_{1,2} = n/a$ where a is the distance between planes $c_{1,2}$ and a hopping frequency Γ, the current density j between the sites can be written as [9]:

$$j = (c_1 - c_2)a\Gamma \tag{2.8}$$

Substituting c_1 with $c_1 = c_2 - a\frac{dc}{dx}$ leads to Fick's first law

$$j = -a^2\Gamma\frac{dc}{dx} \tag{2.9}$$

with the diffusion coefficient [9]

$$D = a^2\Gamma \tag{2.10}$$

depending on the amount of nearest Neighbors N, $\Gamma_{tot} = \sum_{i=i}^{N}\Gamma_i$ the diffusion coefficient is [9]

$$D = 1/Na^2\Gamma_{tot} \tag{2.11}$$

If, according to this formula, all jumps are counted for the jump frequency, then self-correlation effects are not considered (a markovian jump sequence is assumed). The uncorrelated diffusion coefficient can be related to the self diffusion coefficient D^* via the correlation factor f

$$f = \frac{D*}{D} \tag{2.12}$$

Another way to approach diffusion is related to the mean square displacement. The tracer diffusion coefficient D_{MSD} is derived in [9], a summary is provided below.

Assuming $C(x, t + \tau)$ is the concentration of the particles in plane x, which were at $C(x - X, t)$ at one timestep earlier, then

$$C(x, t + \tau) = \sum_X C(x - X, t)W(X, \tau) \tag{2.13}$$

where $W(X, \tau)$ is the normalized distribution function, which can be interpreted as the probability that the particle moved in the x-direction during the time period τ. Assuming the sole dependence on direction and $\tau = t - t_0$ implies the independence of position and starting time. Taking the Taylor expansion of the concentrations around $X, \tau = 0$ leads to:

$$C(x, t + t) + \tau\frac{\delta C}{\delta t} + ... =$$
$$\sum_X \left[C(x, t) - X*\frac{\delta C}{\delta x} + \frac{X^2}{2}s\frac{\delta^2 C}{\delta x^2} + ... \right]W(X, \tau) \tag{2.14}$$

If Δ is chosen sufficiently small, higher order terms of the Taylor expansion are negligible. For diffusion processes, $W(X, \tau)$ is localized around $X=0$ and the equation can be reduced to:

$$\frac{\delta C}{\delta t} = -\frac{\langle X \rangle}{\tau}\frac{\delta C}{\delta x} + \frac{\langle X^2 \rangle}{2\tau}\frac{\delta^2 C}{\delta^2 x} \tag{2.15}$$

In absence of a driving force, $\langle X \rangle$ equals 0 and the equation reduces to Fick's second law with diffusion coefficient

$$D_x = \frac{\langle X^2 \rangle}{2\tau} \tag{2.16}$$

which relates the diffusion coefficient to the mean squared displacement.

In three dimensions, with d the dimensionality of the diffusion process, the formula for the diffusion coefficient can be written as [11]:

$$D^* = \lim_{t \to \infty} \frac{1}{2d\tau} \langle |r(t) - r(0)|^2 \rangle \tag{2.17}$$

where r(t)-r(0) is the difference vector between the position of the atom at time t and at time 0. When the mean square displacement is sampled across enough atoms and time, then the diffusion coefficient measured is the self-diffusion coefficient.

Ionic conductivity
The ionic conductivity describes the flow of ions per surface area when a current is drawn through a material [10]:

$$\sigma_{ion} = \lim_{t \to \infty} \frac{d}{dt} \left[\frac{(ze)^2}{V k_B T 2d} \left(\sum_{i}^{N} \Delta \vec{R}(t) \right)^2 \right] \tag{2.18}$$

The ionic conductivity is related to the diffusivity by the Nernst-Einstein relation:

$$\sigma = \frac{ne^2 z^2 D_{sigma}}{k_B T} \tag{2.19}$$

where n is the particle density, e the electronic charge and z the ionic charge. The difference between the self diffusion coefficient D^* and the diffusivity calculated from the ionic conductivity is known as the Haven Ratio HR

$$HR = \frac{D^*}{D_\sigma} \tag{2.20}$$

Comparison of experimentally measured Diffusion coefficients
When comparing diffusion coefficients measured using experimental techniques, it needs to be considered what exactly is measured and how the diffusion coefficients relate to each other. For example, using AC-impedance measurements the conductivity of a pellet or tape is measured, and D_σ of the pellet or tape can be calculated. Using NMR T_1

relaxometry, the uncorrelated diffusion coefficient D is measured, usually within a crystallite (depends on size of the crystal, it's conductivity and the frequency of the measurement). Often, it is neglected that AC-impedance measures a pellet/tape with a certain microstructure whereas NMR is sensitive to motion within a grain. To compare the diffusivity obtained from NMR and AC-impedance measurements neglecting the above, the self-diffusion coefficients have to be the same. Therefore

$$D^* = f * D_{NMR} = HR * D_\sigma \tag{2.21}$$

or

$$D_{NMR} = \frac{HR}{f} D_\sigma \tag{2.22}$$

Both the correlation factor as well as the HR depend on the material measured and the respective diffusion mechanisms. The most important mechanism are listed below [9]:

1. **Vacancy** induced diffusion occurs when an atom exchanges it's place with a neighboring vacancy. After a jump, the atom is the neighbor of a vacancy. When the number of vacancies is small compared to the number of atoms, the probability for the atom to jump back to where it comes from is larger than for the ion to continue jumping elsewhere, resulting in correlation of consecutive jumps.

2. **Interstitial** diffusion is a diffusion mechanism where an ion jumps from a lattice site to a metastable interstitial site, and back to a lattice site. Usually, the interstitial site has a higher energy compared to the lattice site and is therefore not occupied on average.

3. **Collective** diffusion consists of a direct exchange of neighbouring atoms or a ring mechanism. The activation energy is usually high and the movements of the ions participating in the collective diffusion coefficient are correlated.

The two mechanisms of vacancy and interstitial diffusion are not always easily differentiated. In fast conductors it can be difficult to distinguish a lattice or an interstitial site. In this thesis, this assignment is done in a practical way:

1. If a position is occupied as seen by either neutron or x-ray diffraction - it is a lattice site (section 3.1.1).

2. If this is not the case, and the site lies on a diffusion pathway - it is an interstitial site

The temperature dependence of the self diffusion coefficient follows an Arrhenius relation [9]:

$$D = gf\upsilon^0 a^2 * \exp\left(-\frac{\Delta H}{k_B T}\right) * \exp\left(\frac{\Delta S}{k_B}\right) \tag{2.23}$$

where g is a geometrical factor, f the correlation factor, υ^0 the attempt frequency, and a the jump distance, which depends on the lattice. The activation enthalpy can be estimated from the diffusion coefficients of the same material at different temperatures.
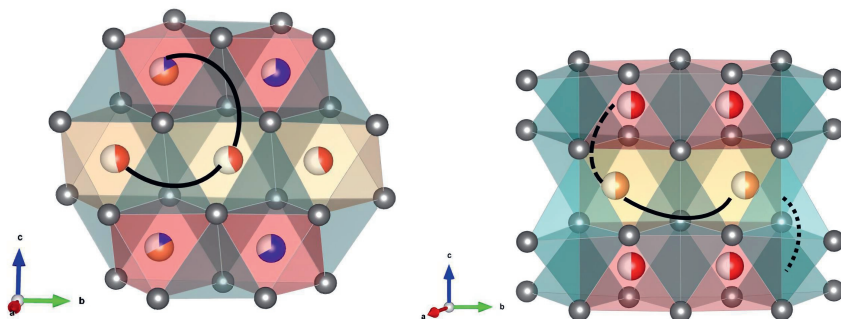
Figure 2.1: Possible jump paths of an ion in a framework of quasi cubic close packed ions (left) and quasi hexagonal close packed ions (right). The stacking is illustrated along the c-direction, the tetrahedral sites are marked in turquoise and the octahedral sites in yellow and red.

Diffusion in a crystal structure

Diffusion in a crystal structure follows above formalism, but with certain constraints given by the crystal structure. The diffusing ion will follow the lowest energy pathways in the potential energy landscape given by the host lattice, and will be able to diffuse along all the paths where the energy barrier is within $k_B T$.

An example is shown in Figure 2.1. In the Figure, two anionic frameworks are illustrated, one with quasi-cubic close-packing (q-ccp)(left) and quasi-hexagonal close-packing (q-hcp)(right). The framework show different possible jumps: The q-ccp only shows one possible jump trajectory, which is an oct-tet-oct jump (solid line). In this case, if all these three sites, have non-negligible occupancy on average, it is vacancy diffusion. If, for example, only the octahedra are occupied on average and the tetrahedral site is empty, it is interstitial diffusion. For the q-hcp framwork this concept stays the same, only that there are three different jump types: oct-tet-oct (solid line), oct-oct (striped line) and tet-tet (dotted line).

All of these different jumps can happen simultaneously and may have a different activation energy.

There are many criteria that have been identified that can indicate whether a material would be a good ion conductor. Some of the most important are:

- Empty space: As mentioned before, for a successful jump it is important that there are free lattice- or interstitial sites the ion can move to, this is only possible when there is empty space.

- The bottleneck of diffusion: The bottleneck usually refers to the part in the jump path, where the diffusing ion is closest to the surrounding atoms of the host lattice. It is usually quantified by the area span by the neighbouring atoms. The idea is that if the area is very small, there is not enough space for the ion to move through and therefore, the bottleneck is too small. Increasing the size of the bottleneck, for example by substitution of (part of) the atoms in the host-lattice by larger ones, could then increase diffusivity.

- Flat potential energy landscape: If the potential energy is flat, the activation energies for jumps is low and therefore diffusion is fast. There are many different ways how the activation energies could be lowered, such as for example by substitution of elements or crystallization in a (more) favourable crystal structure.

If these three factors are given, there is enough empty space, the bottlenecks are not too small and the potential energy landscape is flat, the diffusion will likely be fast. There are other factors used to explain whether or not a material would be a fast ion conductor, such as the effect of lattice polarizeability/dynamics or the configurational entropy.

2.3.3 Stability of solid electrolytes

Next to high ionic conductivity, the solid electrolyte needs to be stable and not disintegrate under the processing and operating conditions. Therefore, the solid electrolyte needs to be stable in different ways[12]:

- The **chemical stability** usually refers to the lack of chemical reactions under processing or storage conditions.

- The **electrochemical stability** describes the stability against electrochemical reactions at the interface between the solid electrolyte and the electrodes.

- The **mechanical stability** refers to the ability to sustain and function with mechanical stress, either from external or internal sources.

- The **thermal stability** implies resistance to decomposition or reactions at increased temperature.

Electrochemical stability of solid electrolyes

In this thesis, specifically the electrochemical stability of solid electrolytes was of interest. The main reason therefore is the idea that the halide solid electrolytes, especially the chlorides, will be less prone to oxidize compared to the more conductive sulphides. If that is indeed the case, it could enable the use of cathodes without protective coating and may lead to better cycle life.

There are two ways how electrochemical stabilities are calculated [13]:

- The **thermodynamic stability**, which is based on the difference between the formation energies of the compounds and the formation energies of more stable compounds in the chemical space. This does not take kinetic barriers of decomposition reactions into account.

- The **oxidative and reductive stability**, which refers to the stability of the solid electrolyte against reduction and oxidation.

The oxidative and reductive stability seems to better predict the electrochemical stability of solid-electrolytes and, in most cases, is wider compared to the thermodynamic stability [13, 14]. Further, the calculations agreed rather well with the measured reduction and oxidation potential for different chemistries.

2.4 Introduction to halide solid electrolytes

Halide solid electrolytes have been studied already for almost half a century. Lithium chloride spinels, firstly reported in 1975, $Li_2M(II)X_4$ (M(II) = Mn, Cd, Mg, Fe; X = Cl, Br, space group Fd-3m, number 227)) were the fastest known Li-ion conductors in the temperature range between 200 and 400 ℃ at that time [15].
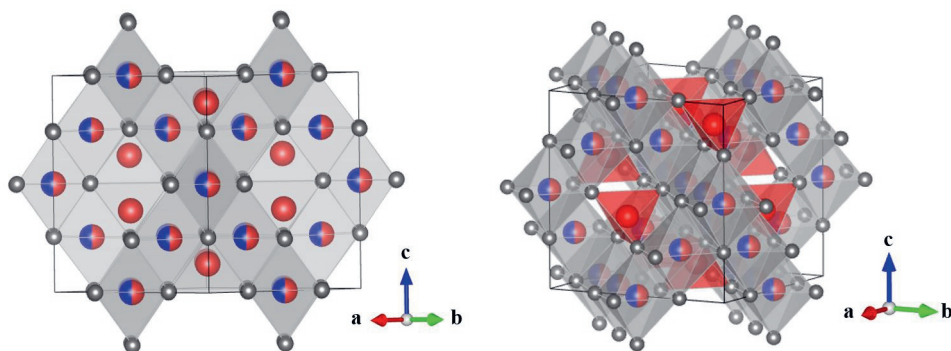

Figure 2.2: Illustration of the crystal structure of spinel $Li_2M(II)X_4$. The X atoms (grey) form a q-ccp framework, the M(II) (blue) and Li (red) co-occupy an octahedral site, the rest of the Li occupies a tetrahedral site that shares corners with the Li-M(II) site.

The lithium chloride spinels consist of q-ccp Cl atoms. The cations occupy octahedral sites (Li and M(II)) as well as tetrahedral sites (Li only). The octahedral sites show co-occupancy of Li and M(II), and the occupied tetrahedral sites all share corners (Figure 2.2) [16]. The materials are reported to have multiple order disorder phase transitions, which were observed indirectly through changes in the activation energy for diffusion in different temperature regimes [15].

Aliovalent substitutions of the $Li_2M(II)X_4$ (M(II)=Mg, Mn, Cd) showed increased ionic conductivity when the M(II) was aliovalently substituted with Fe^{3+}, In^{3+} and Y^{3+} [17].

This finding inspired the first synthesis of $M(I)_3M(III)Cl_6$ (M(I) = Li, Na, Ag; M(III) = In, Y), especially Li_3InCl_6 stood out as a very fast conductor for which 20 S/cm was reported at around 300 ℃ [17].

The crystal structures of $Li_3M(III)X_6$ (X = Cl, Br, I) materials were later studied extensively by the research group around Professor Gerd Meyer. The research activities were focused on determining the crystal structures from single crystal x-ray diffraction techniques [18–21] and characterizing the ionic conductivities. This is where the three main crystal structures were identified, the two q-hcp based phases (triogonal $P\bar{3}m1$ and orthorhombic Pnma, as descirbed in depth in section 7.3.1) and the q-ccp based phase (monoclinic C2/m, as described in section 5.3).

These research activities lasted roughly until the beginning of this century ~2000. Then, a group around Y. Tomita picked up the materials looking at the effect of M(II) substitution and halogen alloying on the crystal structure and ionic conductivity [22–26].
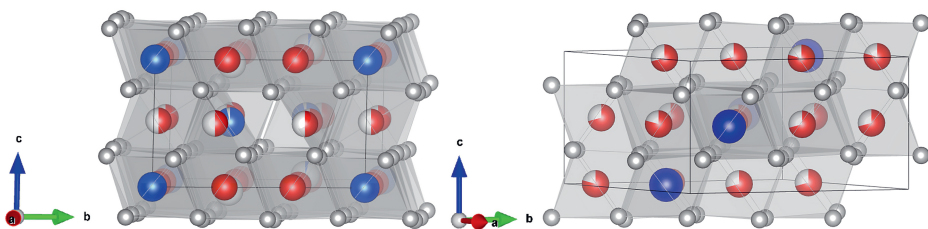
Figure 2.3: Illustration of the two q-hcp based crystal structures found for halide Li$_3$M(III)X$_6$. Left is the trigonal ($P\bar{3}m1$ and right the orthorhombic $Pnma$. The grey atoms are the halogen X that form the packing, illustrated along the c-direction. Lithium(red) and the M(III) (blue) occupy octahedral sites.

Figure 2.4: Illustration of the q-ccp based monoclinic ($C2/m$)crystal structure found for halide Li$_3$M(III)X$_6$. The grey atoms are the halogen X that form the packing, illustrated along the c-direction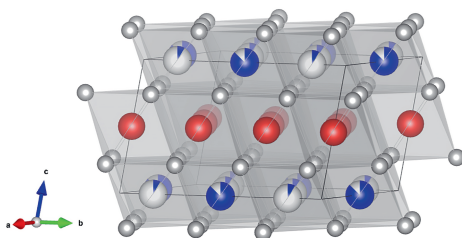. Lithium(red) and the M(III) (blue) occupy octahedral sites in a layered fashion. This is the solution as originally published by Bohnsack et al. [18]. More recent solutions based on neutron diffraction show co-occupancy of the partially occupied M(III) sites with Li, hence a partially occupied Li-layer as well as occupancy of some tetrahedra.

After the studies by Tomita et al., there is a period without publication about these materials (to the best of the authors knowledge). However, considering the surge in research activities in the field of solid electrolytes after the discovery of LGPS in 2011 [8] it was only a matter of time until halide solid electrolytes would come back into the focus of the scientific community. This happened in 2018, when Asano et al. published that Li$_3$YCl$_6$ and Li$_3$YBr$_6$ can reach conductivities on the order of mS/cm at room temperature and showcased working batteries without coated cathodes, showing a clear advantage regarding the electrochemical stability of the halide chemistry compared to the more popular sulphur chemistries.

After the publication by Asano et al., many research activities about halide solid electrolytes were started, this PhD-thesis is one of them. Many of those will be discussed in the four data-containing chapters in this thesis.

The first data-containing chapter discusses the complexity of spectral density fitting of nuclear magnetic resonance (NMR) relaxometry fitting in these materials, specifically in Li$_3$YCl$_3$Br$_3$. The second chapter studies the effect of Zr(IV) substitution in Li$_3$InCl$_6$ on the ionic conductivity of the materials. The third chapter investigates the trade-off between the ionic conductivity and the electrochemical stability of halogen alloyed materials Li$_3$YCl$_{6-x}$Br$_x$. Finally, the last chapter showcases that the two q-hcp phases can both be syn-

thesized for a variety of different M(III) (=Y, Ho, Yb, Dy) and investigates the differences between the two phases.

References

[1] Micah S. Ziegler and Jessika E. Trancik. Re-examining rates of lithium-ion battery technology improvement and cost decline. *Energy & Environmental Science*, 14(4):1635–1651, 2021.

[2] Ying Zhang, Tong-Tong Zuo, Jelena Popovic, Kyungmi Lim, Ya-Xia Yin, Joachim Maier, and Yu-Guo Guo. Towards better li metal anodes: challenges and strategies. *Materials Today*, 33:56–74, 2020.

[3] Shuang-Jie Tan, Wen-Peng Wang, Yi-Fan Tian, Sen Xin, and Yu-Guo Guo. Advanced electrolytes enabling safe and stable rechargeable li-metal batteries: Progress and prospects. *Advanced Functional Materials*, 31(45):2105253, 2021.

[4] Xiuxia Zuo, Jin Zhu, Peter Müller-Buschbaum, and Ya-Jun Cheng. Silicon based lithium-ion battery anodes: A chronicle perspective review. *Nano Energy*, 31:113–143, 2017.

[5] M Wild, L O'neill, T Zhang, R Purkayastha, G Minton, M Marinescu, and GJ Offer. Lithium sulfur batteries, a mechanistic review. *Energy & Environmental Science*, 8(12):3477–3494, 2015.

[6] Doron Aurbach, Bryan D McCloskey, Linda F Nazar, and Peter G Bruce. Advances in understanding mechanisms underpinning lithium–air batteries. *Nature Energy*, 1(9):1–11, 2016.

[7] Theodosios Famprikis, Pieremanuele Canepa, James A. Dawson, M. Saiful Islam, and Christian Masquelier. Fundamentals of inorganic solid-state electrolytes for batteries. *Nature Materials*, 18(12):1278–1291, December 2019.

[8] Noriaki Kamaya, Kenji Homma, Yuichiro Yamakawa, Masaaki Hirayama, Ryoji Kanno, Masao Yonemura, Takashi Kamiyama, Yuki Kato, Shigenori Hama, Koji Kawamoto, and Akio Mitsui. A lithium superionic conductor. *Nature Materials*, 10(9):682–686, September 2011.

[9] Helmut Mehrer. *Diffusion in solids: fundamentals, methods, materials, diffusion-controlled processes*, volume 155. Springer Berlin, Heidelberg, 2007.

[10] Nella M Vargas-Barbosa and Bernhard Roling. Dynamic ion correlations in solid and liquid electrolytes: how do they affect charge and mass transport? *ChemElectroChem*, 7(2):367–385, 2020.

[11] Jianjun Yang and S Tse John. First-principles molecular simulations of li diffusion in solid electrolytes li3ps4. *Computational Materials Science*, 107:134–138, 2015.

[12] Rusong Chen, Qinghao Li, Xiqian Yu, Liquan Chen, and Hong Li. Approaching practically accessible solid-state batteries: stability issues related to solid electrolytes and interfaces. *Chemical reviews*, 120(14):6820–6877, 2019.

[13] Tammo K. Schwietert, Violetta A. Arszelewska, Chao Wang, Chuang Yu, Alexandros Vasileiadis, Niek J. J. de Klerk, Jart Hageman, Thomas Hupfer, Ingo Kerkamm, Yaolin Xu, Eveline van der Maas, Erik M. Kelder, Swapna Ganapathy, and Marnix Wagemaker. Clarifying the relationship between redox activity and electrochemical stability in solid electrolytes. *Nature Materials*, January 2020.

[14] Tammo K. Schwietert, Alexandros Vasileiadis, and Marnix Wagemaker. First-Principles Prediction of the Electrochemical Stability and Reaction Mechanisms of Solid-State Electrolytes. *JACS Au*, 1(9):1488–1496, September 2021.

[15] W. Schmidt and H. D. Lutz. Fast Ionic Conductivity and Dielectric Properties of the Lithium Halide Spinels Li2MnCl4, Li2CdCl4, Li2MnBr4, and Li2CdBr4. *Berichte der Bunsengesellschaft für physikalische Chemie*, 88(8):720–723, August 1984.

[16] Li2cdcl4 crystal structure: Datasheet from "pauling file multinaries edition – 2012" in springermaterials (https://materials.springer.com/isp/crystallographic/docs/sd_1938427). Copyright 2016 Springer-Verlag Berlin Heidelberg & Material Phases Data System (MPDS), Switzerland & National Institute for Materials Science (NIMS), Japan.

[17] H.-J. Steiner and H. D. Lutz. Neue schnelle Ionenleiter vom Typ MI3MIIICl6 (MI = Li, Na, Ag; MIII = In, Y). *Zeitschrift für anorganische und allgemeine Chemie*, 613(7):26–30, July 1992.

[18] Andreas Bohnsack, Frauke Stenzel, Armin Zajonc, Gert Balzer, Mathias S. Wickleder, and Gerd Meyer. Ternäre halogenide vom typ a3mx6 vi. ternäre chloride der selten-erd-elemente mit lithium lithium, li3mcl6 (m=tb-lu, y, sc): Synthese, krisallstrukturen und ionenbewegung. *Zeitschrift für anorganische und allgemeine Chemie*, 623(7):1067–1073, July 1997.

[19] Andreas Bohnsack, Gert Balzer, Hans-U. Gödel, Mathias S. Wickleder, and Gerd Meyer. Ternäre halogenide vom typ a3mx6. vii. die bromide li3mbr6 (m=sm-lu, y): Synthese, kristallstruktur, ionenbeweglichkeit. *Zeitschrift für anorganische und allgemeine Chemie*, 623(9):1352–1356, September 1997.

[20] Michael O. Schmidt, Mathias S. Wickleder, and Gerd Meyer. Zur Kristallstruktur von Li3InCl6. *Zeitschrift für anorganische und allgemeine Chemie*, 625(4):539–540, April 1999.

[21] Michael Schmidt. *Neue Untersuchungen an ternären Halogeniden vom Typ A3MX6: Li3MI6 (M = Gd - Lu, Y) sowie A3InCl6 (A = Li - Cs)*. PhD thesis, Universität Köln, 1999.

[22] Yasumasa Tomita, Hiroshi Yonekura, Yasuo Yamauchi, Koji Yamada, and Kenkichiro Kobayashi. Substitution Effect in the Ion Conductor Li3InBr6, Studied by Nuclear Magnetic Resonance. *Zeitschrift für Naturforschung A*, 57(6-7):447–450, July 2002.

[23] Y Tomita, H Matsushita, H Yonekura, Y Yamauchi, K Yamada, and K Kobayashi. Li ion conductivity of solid electrolyte, LiMInBr (M=Mg, Ca, Sr, Ba). *Solid State Ionics*, 174(1-4):35–39, October 2004.

[24] K Yamada, K Kumano, and T Okuda. Lithium superionic conductors Li3InBr6 and LiInBr4 studied by 7Li, 115In NMR. *Solid State Ionics*, 177(19-25):1691–1695, October 2006.

[25] Y. Tomita, H. Matsushita, K. Kobayashi, Y. Maeda, and K. Yamada. Substitution effect of ionic conductivity in lithium ion conductor li3inbr6-xclx. *Solid State Ionics*, 179(21-26):867–870, September 2008.

[26] Yasumasa Tomita, Hiroo Nishiyama, Kenkichiro Kobayashi, Yoshiumi Kohno, Yasuhisa Maeda, and Koji Yamada. Substitution effect for br on the lithium ion conductivity of lithium indium bromide. *ECS Transactions*, 16(29):137–141, August 2009.

3

Experimental methods

In this chapter, the measurements and techniques used the most in this thesis are outlined.

3.1 Crystal structure determination

Crystal stuctures are most commonly studied using diffraction-based techniques, which are outlined in this chapter. In this chapter, when talking about diffraction, it is implied that it is the diffraction pattern arising from an elastic and coherent scattering event.

3.1.1 Basics of diffraction

In a diffraction experiment, the interference pattern of waves diffracted from an object is measured. If the object has a periodically repeating structural element in a direction in space, as for example in a crystal structure, then some waves of the incoming beam will reflect at the first element, part at the second, etc.

If we assume that the incoming beam is in monochrome, the interference pattern will depend on the distance between the repeating elements: The wave that diffracts at the second element will have travelled a longer path compared to the first wave. This is illus-

$$AB + BC = 2AB = 2d\sin(\theta)$$
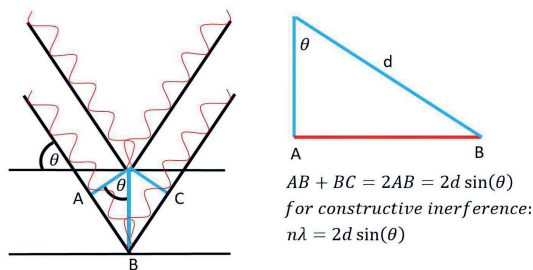$$for\ constructive\ inerference:$$
$$n\lambda = 2d\sin(\theta)$$

Figure 3.1: Derivation of bragg's law: monochromatic waves diffract from a set of planes with separated by a distance d, leading to a difference in the path length travelled by the wave (2dsin(θ)). The waves travelled from the different planes interfere constructively when the this distance is a multiple of the wavelength.

trated in the distance from point A to B in Figure 3.1. The same happens after the wave is diffracted, it will travel a path longer by the distance between B and C. Due to symmetry, AB = BC. From trigonometry, we can calculate the distance AB from the angle of the triangle and the distance between the repeating unit d. For constructive interference, this distance needs to be a multiple of the wavelength. This derivation leads to Bragg's law [1]

$$n\lambda = 2d_{hkl}\sin(\theta)) \tag{3.1}$$

When considering diffraction on a crystal, the distance d refers to the spacing between lattice planes (lattice parameter). It can be determined as accurately as the angle and the wavelength can be determined. In this thesis, only powder diffraction patterns are measured, which are an average across all orientations of the crystal. While Bragg's law predicts the angles 2θ where Bragg peaks are expected, the mathematics are more complicated when considering the intensity measured at the detector of an x-ray diffractometer.

The intensity measured for a scattering measurement on an object of interest A(x) is related to the Fourier transform [2]

$$I_q = \left| \phi_0 \int_{-\infty}^{\infty} A(x)\exp\left(iqx\right)dx \right|^2 \tag{3.2}$$

where I_q is the intensity (ignoring all other possible scatterign sources, absorption and broadening effects), A(x) the object of interest and q is the scattering vector, which is the difference vector of the incoming and outgoing wave. As the square of the fourier transform is measured, the phase information is lost and the object of interest can not be reconstructed directly from the Intensities. This is usually referred to as the phase problem. When a satisfactory model for the object A(x) is available, the phases can be estimated from the model and the object can be reconstructed.

When considering crystal structures, the object of interest is described by the location of atomic sites and the amount of the respective atoms that occupy them. Mathematically, this is called the structure factor and is defined as follows:

$$F(hkl) = \sum_j f_j * \exp\left(-2\pi i(hx_j - ky_j + lz_j)\right) \tag{3.3}$$

where hkl are the Miller indices and $f_{j,k}$ is the scattering factor of the jth atom.

The scattering factor depends on the element, but also on the nature of the scattered wave. Diffraction can be done with x-rays, neutrons (for neutrons, the scattering factor f is replaced by the scattering length b) as well as electrons. In this thesis, only the first two are used:

- X-rays interact with electrons in the sample, therefore the scattering intensity increases with the atomic number Z of the element. Considering that lithium has atomic number Z=3, x-rays are therefore not suitable to determine the location of lithium in the crystal structure in most cases. Also, distinguishing between elements with similar atomic number, such as for example Cl and S, is difficult using x-rays. Considering that the electrons are spread out in space and the measurement measures the Fourier transform of the electron density, the form factor of x-rays is a function that falls off at higher diffraction angle.

- Neutrons scatter from the nucleus of the atom. The scattering power of different elements is called the scattering length, which can be looked up in the neutron booklet [5]. The scattering length varies randomly with Z, and therefore neutrons are often useful where x-rays are not. Lithium is a special case, as averaged across the two isotopes it has a negative scattering cross section, the negative sign corresponding to a 180 °phase shift of the scattered wave.

Due to thermal vibrations, the atoms are not frozen but oscillate around an equilibrium position. Due to this motion, the atoms can move out of the Bragg condition, which leads to loss of intensity of the signal. This is modelled using the Debye-Waller factor DWF

$$\mathrm{DWF} = \left\langle \exp\left(iqu\right)\right\rangle \tag{3.4}$$

The signal intensity is also reduced by the form factor (which is almost constant for neutrons, due to the localization of the atomic core, and falls off for x-rays, due to the larger spatial extent of the electron clouds).

Diffraction peaks can be broadened by both the nature of the sample (particle size and strain) as well as the instrument resolution.

Finally, not only the scattering of the sample needs to be considered, but also scattering from all the other atoms in the path of the bean (air, argon, parts from the sample holder, etc), Such factors are usually considered as background intensity and are fit with a suitable function and substracted form the intensity measured.

Rietveld refinement

During a Rietveld refinement, a model of the crystal structure is either made or fine-tuned by minimizing the differences between the measured diffraction pattern (equation **??**) and the simulated diffraction pattern of a model of the crystal structure, usually using a least-square fit. It is the most commonly used method to obtain crystal structures of the material.

If the crystallographic phase is known (as was the case in this thesis), a Rietveld refinement is usually started from a known crystallographic information file, and parameters such as the lattice parameter, atomic positions, occupancies and thermal parameters are refined until a satisfactory model is found.

3.2 Characterisation of the dynamics

Li-ion dynamics can be probed in many different ways. Most of these probes, however, are accurate at a certain time/length scale. The most common measurement to measure ionic conductivity in solid electrolytes is AC-impedance measurements, which is sensitive to long-range diffusion of the atoms.

Less common but very useful is solid-state NMR, which can be used to characterize dynamics of atoms on a variety of timescales depending on the specific measurement.

3.2.1 AC-impedance

AC-impedance experiments are performed in order to measure the ionic conductivity of a solid electrolyte pellet or film. Pellets or films can be prepared in different ways:

- Cold-pressing: The powder is filled into a die set and pressed uniaxially or isostatically. This is the most common way for electrolytes with favourable mechanical properties (as most sulphides, halides).

- Cold-pressing and sintering: The pellet is consecutively sintered, this has to be done for materials that are hard and have significant contributions of grain boundary resistance (most oxides, phosphates).

- Hot pressing or Spark plasma sintering: the pellet is pressed and heated at the same time, during hot-pressing the pellet is heated conventionally whereas during spark plasma sintering the material is heated by applying high currents through the material.

- Tape-casting of solid electrolytes: a thin solid-electrolyte film is prepared by preparing a slurry of some solvent, the solid-electrolyte and possibly additives which is cast into a film.

The as-prepared pellet is then contacted electrically either by a cell that is made to encase the electrolyte, or by sputtering a thin metal layer on top of the solid electrolyte.

Once the electrical contact is established, a sinusoidal excitation signal is applied to the pellet

$$E(t) = |E|\sin(\omega t) \tag{3.5}$$

where E is the amplitude of the voltage signal and ω the angular frequency. Usually the voltage is controlled, but in principle current control is also possible. In any case, the electrical response is measured

$$I(t) = |I|\sin(\omega t + \theta) \tag{3.6}$$

The phase shift θ can arise due to a reactance (capacitance or inductance) of the system. The impedance is defined as

$$Z = \frac{E(t)}{I(t)} \tag{3.7}$$

The frequency of the sinusoidal signal is varied, usually between ~10^{-7} and ~10^{-3} Hz, resulting in information on the impedance of the pellet in the frequency range measured.

To extract information about the electrical behaviour, often a process referred to as equivalent circuit fitting is performed. Therefore, an electrical circuit is created and the value of the electrical components (such as capacitance, Resistance or inductance) are fit using a least square procedure. Often, can not be modeled using such idealized circuit elements, and many modified expression for circuit elements exist.

The most common equivalent circuit to fit the response of a solid-electrolyte pellet consists of a constant phase element (CPE) and a resistance (R) in parallel to model the
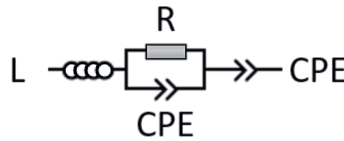
Figure 3.2: Common equivalent circuit used to fit the result of impedance measurements of solid-electrolyte. The inductance L is optional and can be used if the measurement system shows significant inductance due to cables. The resistance R in parallel with the constant phase element CPE represents the electrical resistance and capacitance of the pellet. The last CPE element models the electronically blocking behaviour of the electrodes at lower frequencies.

solid-electrolyte, and a CPE in series to model the ionically blocking current collectors. An inductance L may be added in series to represent the inductance of the measurement cables (Figure 3.2). Once the measurements are fit, the Resistance R can be used to calculate the ionic conductivity

$$\sigma = \frac{d}{RA} \tag{3.8}$$

where d is the pellet thickness and A is the surface area of the pellet.

Even though these measurements are standard measurements for anyone working on solid electrolytes, and the obtained conductivity is regarded as one of the most important measures for the performance of a material, research has shown that there can be large variations between the values obtained from measurements in different labs (range of up to 4.5 mS/cm and 128 meV for activation barriers)[6].

It is not as customary as it should be to report errors for the ionic conductivity. The total error associated with the conductivity arises from the uncertainty of the pellet geometry as well as the obtained resistance, and is best calculated using gaussian error propagation [7]:

$$RSD_\sigma = \frac{\delta\sigma}{\sigma} = \sqrt{\left(\frac{\delta l}{l}\right)^2 + \left(\frac{\delta A}{A}\right)^2 + \left(\frac{\delta R}{R}\right)^2} \tag{3.9}$$

3.2.2 NMR T_1 relaxomtery

NMR is a useful probe for all isotopes that have a non-zero nuclear spin. The spin has a magnetic moment and under normal circumstances, it's energy levels are degenerate. Placing the spin into a magnetic field B_0 lifts this degeneracy, resulting in discrete energy levels (see Figure 3.3 for the example of a Spin=1/2).

The populations of the spins across the different energy levels can be described by the Boltzmann distribution

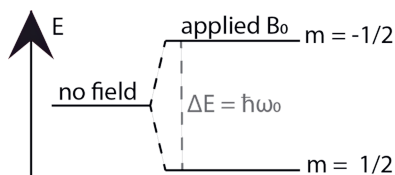$$\frac{N_+}{N_-} = \exp\left(-\frac{\Delta E}{k_B T}\right) \tag{3.10}$$

Figure 3.3: Change in energy of a spin 1/2 placed in a magnet of field B_0

where ΔE is the energy separation between the states, N_- is the number of spins at the lower energy level and N_+ the number of spins at the higher energy level.

Applying radio frequency pulses at the same frequency as the larmor frequency ω_0,

$$\Delta E = \hbar\omega_0 = \gamma\hbar B_0 \tag{3.11}$$

where $\hbar$ is the reduced Planck's constant, ω_0 the larmor frequency, γ the gyromagnetic ratio of the nuclei and B_0 the magnetic field strength, leads to spin transitions from the low energy to the high energy state, distorting the Boltzmann equilibrium (equation 3.10). Once the radio frequency field is removed, the spin populations will relax back to the equilibrium state given by the Boltzmann distribution.

The sum of the magnetic moment of all Spins is the net magnetization of the sample, which precesses around the B_0 field. The application of the radiofrequency pulse leads to phase coherence of the magnetic moment between the levels, which can bring the net magnetization out of the equilibrium along the z-direction, precessing in the xy-plane. Upon removal of the pulse, also the net magnetic moment relaxes back to it's equilibrium position, described by a characteristic time.

The precession of the net magnetization and the relaxation without driving force is described by the Bloch equations:

$$\frac{dM_x}{dt} = \gamma(M(t) * B(t))_x - \frac{M_x}{T_2} \tag{3.12}$$

$$\frac{dM_y}{dt} = \gamma(M(t) * B(t))_y - \frac{M_x}{T_2} \tag{3.13}$$

$$\frac{dM_z}{dt} = \gamma(M(t) * B(t))_z - \frac{M_z - M_{z0}}{T_1} \tag{3.14}$$

Where M_x, M_y, M_z are the components of the net magnetization vector in the respective directions (where the z-direction is along the B_0 field), T_1 is the spin-lattice relaxation time and T_2 the spin-spin relaxation time.

Spin-lattice relaxation time T_1

Considering the Bloch equation in the z-direction 3.14, we can see that T_1 describes the time constant for the magnetization to go from the xy plane back to the equilibrium position along the z-direction. Common methods to measure T_1 are using the following two pulse sequences (see Figure 3.4 for a visualization):
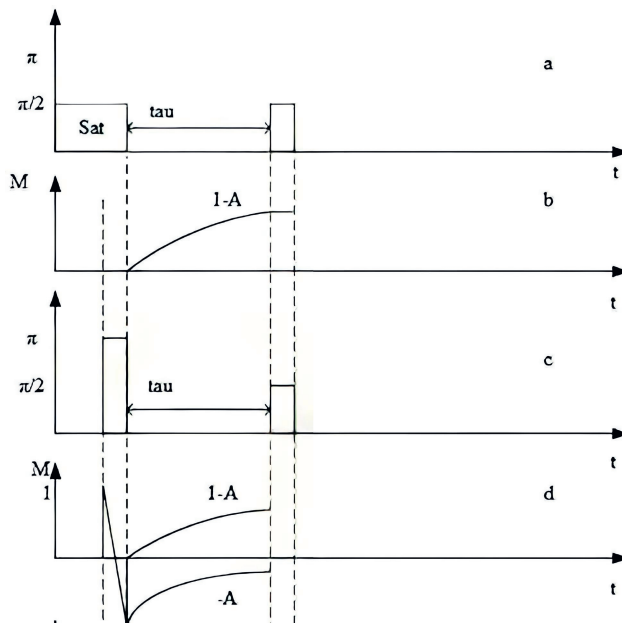
Figure 3.4: Visualization of the pulse program and the magnetization recovery pathways for the saturation recovery pulse sequence (a, b) and inversion recovery (c, d). A = exp($-\tau$/T1). Figure adapted from [8].

- In the **saturation recovery** experiment, the spin transitions are first saturated using a series of saturation pulses. Then, the system is left to wait for a period τ, after which a 90 degree pulse is applied and the response recorded. At very short times τ, the transitions are still saturated from the series of pulses and no signal is acquired. As the τ is increased, the system has time to recover and the signal recorded with the 90 degree pulse is increasing. The signal is largest once τ is long enough for the system to go back to equilibrium after the 90 degree pulse, indicating the magnetization is fully recovered.

- During an **inversion recovery**, the signal is first inverted with a 180°pulse, flipping the net magnetization from the z-direction to the minus z direction. Then the spins are left to evolve during a time τ, after which a 90 degree pulse is used to measure the state of the magnetization.

Both pulse sequences result in varying signal intensities as a function of the time τ. The measured free induction decays (FID) are Fourier transformed and phased. When the signal to noise is poor, filtering and line-broadening can help to get a less noisy spectra and in some cases, corrections for the shape of the baseline are useful. The resulting peak is then integrated. The build-up of the signal (see Figure 3.4 b and d) is then fit to extract the T_1.

Temperature dependence of the spin lattice relaxation time

T_1 depends on microscopic details of the nuclear system, the reservoir around it and the magnetic field strength. Conservation of energy demands that a transition from one energy level to the other is coupled with another reservoir of energy [9].

The diffusing ion is the source of an electric or magnetic moment. The electric moment relates to the quadrupole moment and hence is present for isotopes with $I > 1/2$. The magnetic moment relates to the dipole moment of the nuclei and is present for all isotopes with non-zero spin. If, like in a solid electrolyte, the ions are jumping around, the electric/magnetic moment arising from the nuclei are oscillating due to the motion, which can impact spin-lattice relaxation.

As the temperature of the sample is changed, the jump frequency of the Li-ions changes, often according to the Arrhenius expression. When the jump frequency is approximately equal to the Larmor frequency, the relaxation is fastest (section 3.2.2). The relaxation rates decrease as the difference between the jump-frequency and the Larmor frequency increases.

Quantitatively, the relaxation rates as a function of temperature are described by Redfield theory. For an introduction to Redfield theory and how it affects spin relaxation for different interactions, the reader is referred to Dong's chapter titled "NMR relaxation rates" in the Encyclopedia of spectroscopy and spectrometry [10] or to the section 3.2.2 in this thesis.

Spin interactions

The four main spin interactions that can lead to spin-lattice relaxation are [10]:

- The **quadrupolar interaction** is the only interaction of electric nature, and describes the interaction of asymmetric charge distribution around the nuclei (for spin > 1/2) with surrounding electric field gradients. For materials with considerable quadrupole moment, the magnitude of the quadrupole interaction is usually on the order of 10^6 Hz.

- The **dipolar interaction** describes the interaction between the magnetic moments of the spins and scales proportional to $1/r^3$, where r is the distance between spins. The dipolar interaction is typically on the order of 10^3 Hz.

- **Chemical shift anisotropy** is a measure for the differences in shielding of the spin in space by surrounding electron clouds of other atoms. If chemical shift anisotropy occurs, it is typically on the order of 10^3 Hz.

- **J-coupling** or scalar coupling occurs when the magnetic moments of two or more nuclei interact through their bonding electrons and leads to a splitting of the NMR-resonance peaks. It can in principle lead to spin-lattice relaxation, but is less relevant for ion conductors as the materials have mostly bonds of more ionic nature.

Lithium NMR

Lithium has two NMR active isotopes, ^{6}Li and ^{7}Li. These isotopes have quite different properties as can be seen in Table 3.1. Both isotopes have a spin larger than 1/2, but have a relatively large gyromagnetic ratio and a small quadrupole moment. Therefore,

despite that the quadrupole interaction is usually stronger than the dipole interaction, spin relaxation of lithium usually effectively occurs via the dipolar interaction.

Table 3.1: NMR properties of ^{6}Li and ^{7}Li. *The larmor frequency is given for a 500MHz spectrometer.

	^{6}Li	^{7}Li
Spin	1	3/2
Abundance [%]	7.6%	92.4%
Gyromagnetic ratio γ [10^7 rad s^{-1} T^{-1}, calc.]	3.937	10.398
Quadrupole moment Q [fm^2]	−0.0808	−4.01
Larmor frequency* [MHz]	73.6	194.37

3

References

[1] William Henry Bragg and William Lawrence Bragg. The reflection of x-rays by crystals. *Proceedings of the Royal Society of London. Series A, Containing Papers of a Mathematical and Physical Character*, 88(605):428–438, 1913.

[2] Deviderjit Singh Sivia. *Elementary scattering theory: for X-ray and neutron users*. Oxford University Press, 2011.

[3] Brian H. Toby and Robert B. Von Dreele. *GSAS-II* : the genesis of a modern open-source all purpose crystallography software package. *Journal of Applied Crystallography*, 46(2):544–549, April 2013.

[4] Brian H. Toby and Robert B. Von Dreele. What's new in GSAS-II. *Powder Diffraction*, 29(S2):S2–S6, December 2014.

[5] A. J. Dianoux, G. H. Lander, and Institut Laue-Langevin, editors. *Neutron data booklet*. Old City, Philadelphia, PA, 2nd ed edition, 2003.

[6] Saneyuki Ohno, Tim Bernges, Johannes Buchheim, Marc Duchardt, Anna-Katharina Hatz, Marvin A Kraft, Hiram Kwak, Aggunda L Santhosha, Zhantao Liu, Nicolo Minafra, et al. How certain are the reported ionic conductivities of thiophosphate-based solid electrolytes? an interlaboratory study. *ACS Energy Letters*, 5(3):910–915, 2020.

[7] Irina V. Krasnikova, Mariam A. Pogosova, Alexey O. Sanin, and Keith J. Stevenson. Toward Standardization of Electrochemical Impedance Spectroscopy Studies of Li-Ion Conductive Ceramics. *Chemistry of Materials*, 32(6):2232–2241, March 2020.

[8] Hongzhi Wang, Ming Zhao, Jerome L. Ackerman, and Yiqiao Song. Saturation-inversion-recovery: A method for T1 measurement. *Journal of Magnetic Resonance*, 274:137–143, January 2017.

[9] Charles P. Slichter. *Principles of Magnetic Resonance*. Springer Series in Solid-State Sciences. Springer International Publishing, 1996.

[10] J.C. Lindon, G.E. Tranter, and D. Koppenaal. *Encyclopedia of Spectroscopy and Spectrometry*. Elsevier Science, 2016.

4

NMR relaxometry in lithium compounds: Spectral density fitting

In this chapter, an introduction to spectral density fitting of temperature-dependent NMR spin-lattice relaxation rates is given from the perspective of a user of the technique interested in the motional processes in solid ion conductors. During the work of this thesis, many halide solid electrolytes were investigated using solid-state NMR relaxometry. Most of them showed complex shapes of the relaxation rates that were not straightforward to interpret. Hence, much time was spent on trying to understand and analyse these measurements and the learning curve was steep. Hopefully, this chapter can help flattening the learning curve for other scientists new to the method. A publication of this chapter is in preparation, which will be published including scripts for data fitting and error analysis.

4.1 Introduction
4.1.1 Redfield equation
The spin-lattice relaxation rates can best be described by Redfield's equations. When the dominant relaxation mechanism is dipolar relaxation, the expression reads

$$\frac{1}{T_1} = K_D[J_1(\omega_0) + 4J_2(2(\omega_0))] \tag{4.1}$$

Where T_1 is the spin-lattice relaxation time, ω_0 is the Larmor frequency of the observed nucleus in the static B_0 field and the function J is the spectral density of motion. Under the approximation that only two spins are considered, K_D is related to the dipolar interaction,

$$K_D = \frac{3}{2}\left(\frac{\mu_0\gamma^2\hbar}{4\pi r^3}\right)^2 \tag{4.2}$$

where μ_0 is the vacuum magnetic permeability. For a static systems of spins, this expression can be replaced by the van Vleck second moment/ the powder average of the van Vleck second moment [1]. The radius r represents the distance between the two spins and is assumed to be independent of time [2].

4.1.2 Spectral density function J

The spectral density $J(\omega_0, x_i)$ is the Fourier transform of the auto-correlation function $G(t,x)$, whose time-dependence defines the motion of the diffusing nuclei [2]

$$J(\omega, x_i) = \int_{-\infty}^{\infty} G(t, x_i) \exp(i\omega t)\, dt \qquad (4.3)$$

As the spectral density is specific for a auto-correlation function which defines the motion, it is not necessarily known which spectral density suits a material/measurement series, this needs to be determined. Many different spectral densities have been developed, see for example the review by Beckman [2].

A commonly used spectral density is the BPP spectral density, named after its inventors Bloembergen, Purcell and Pound [3], which is designed for random, three dimensional motion. The underlying correlation function is an exponential function

$$G(t) = \exp\left(-\frac{|t|}{\tau_c}\right) \qquad (4.4)$$

with the correlation time τ_c, which can be thought of as the mean residence time of a diffusing ion on it's lattice site (as long as the jump frequency is not much faster compared to the Larmor frequency). The inverse is therefore related to the jump-frequency of the moving ion between lattice sites [4]. When normalized accordingly, the BPP spectral density becomes [2]

$$J_{BPP} = \frac{2\tau_c}{1 + \omega_0^2 \tau_c^2} \qquad (4.5)$$

The correlation time τ_c is thermally activated (Arrhenius condition)

$$\tau_c = \tau_0 \exp\left(\frac{E_a}{k_B T}\right) \qquad (4.6)$$

with an activation energy E_a and pre-exponential factor τ_0. The pre-exponential factor τ_0 is usually of the order of magnitude of phonon frequencies in the material [4]. Considering that the relaxation rate peak has a maximum approximately at the condition $\tau_c \omega_0 \approx 1$ (see section 4.1.4), NMR spin lattice relaxation is sensitive to motions on the timescale of $2\pi/\omega_0 = 10^{-8} - 10^{-10}\,s$.

Substituting these parts into equation 4.1, we get the following expression

$$\frac{1}{T_1} = K_D \left[\frac{2\tau_c}{1 + \omega_0^2 \tau_c^2} + 4 \frac{2\tau_c}{1 + 4\omega_0^2 \tau_c^2} \right]. \qquad (4.7)$$

which, by substituting the correlation time τ_c (equation 4.6), reads as

$$\frac{1}{T_1} = \frac{3}{2}\left(\frac{\mu_0 \gamma^2 \hbar}{4\pi r^3}\right)^2 \left[\frac{2\tau_0 \exp\left(\frac{E_a}{k_B T}\right)}{1 + \omega_0^2 \left(\tau_0 \exp\left(\frac{E_a}{k_B T}\right)\right)^2} + 4 \frac{2\tau_0 \exp\left(\frac{E_a}{k_B T}\right)}{1 + 4\omega_0^2 \left(\tau_0 \exp\left(\frac{E_a}{k_B T}\right)\right)^2} \right] \qquad (4.8)$$

When studying Li-ion conductors using NMR spin lattice relaxation times, two things are measured, namely the temperature and the T_1. The Larmor frequency ω_0 is given based on the magnetic field strength of the magnet used. The unknown parameters are the K_D, the activation energy E_a, and the pre-exponential factor τ_0, which we need to treat as fitting parameters. For one measurement series, we have N measurements of T_1 at temperature T_N, and one would fit three variables, the τ_0, the E_a and the K_D.

4.1.3 From correlation time to diffusivity

Once a reliable fit of these variables is achieved, the obtained correlation times can be used to calculate the jump rates or the diffusivity, if information on the length a of the jump is available, for example from a crystal structure solution[5]:

$$D_{NMR} = \frac{a^2}{2d\tau_c} \tag{4.9}$$

Where d is the dimensionality of the diffusion process. This equation if of similar form as equation 2.11 (if the amount of nearest neighbours is 6) and is a solution to Fick's first law. The diffusion coefficient can be compared to measurements of ionic conductivity converted to a value for the diffusivity using the Nernst-Einstein relationship (equation 2.19).

4.1.4 Understanding the BPP model

Using above formulas, we can simulate how a series of measurements would look like to get a basic understanding for what we expect to see. To do so, we need to make some choices of values for

- Temperature range: experimentally this is set by the probe that is measured on. The temperature range in the simulations is larger than the usual temperature ranges of the probe, this is for better illustration.

- Larmor frequency (depending on the NMR nuclei measured and the B_0 field of the magnet)

- K_D (also depending on the NMR nuclei measured, and the distances between nuclei)

- E_a (Material and jump process dependent)

- τ_0 (Material dependent, typically in the range of phonon frequencies)

In figure 4.1, such a simulation is shown for ^{6}Li and ^{7}Li, as a function of three different magnetic field strengths and a temperature range from 200-600K.

On the y-axis, the natural logarithm of the relaxation rate ($1/T_1$) is shown as a function of (inverse) temperature.

Figure 4.1: Simulated BPP model for a material with E_a = 0.2 eV, τ_0=$1*10^{-12}$ s, for ^{6}Li (purple, K_D = $1*10^7$ [$\left(\left(\frac{rad}{s}\right)^2\right]$ and ^{7}Li (blue, K_D = $1*10^9$ [$\left(\left(\frac{rad}{s}\right)^2\right]$) at magnetic fields B_0 of 7.04, 11.75 and 19.97 Tesla.
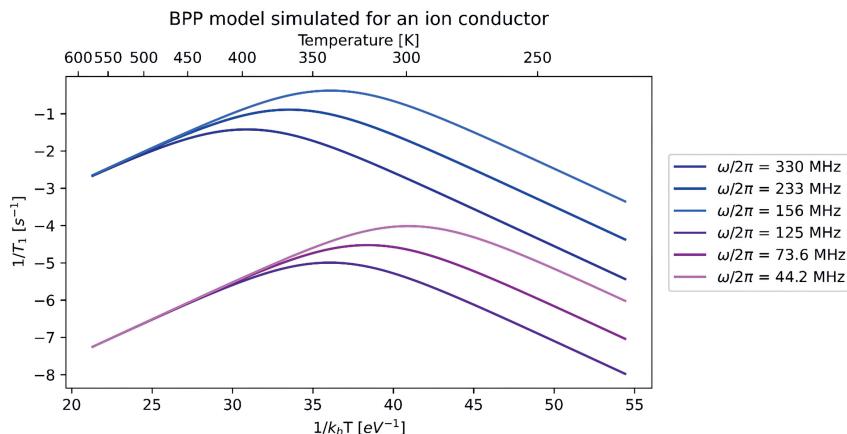
Relaxation rates ^{6}Li vs ^{7}Li

The first thing that can be noticed, is that the relaxation rates for ^{7}Li are higher compared to the ones for ^{6}Li. This is due to the different K_D-values, which were chosen as $1*10^9$ for ^{7}Li and $1*10^7$ for ^{6}Li. These numbers are close to experimental values obtained in this thesis. We can understand this difference if we look at equation 4.2; the K_D is dependent on the gyromagnetic ratio of the isotope measured. The gyromagnetic ratio of ^{7}Li is almost 2.5 times larger compared to that of ^{6}Li (see table 3.1), and hence relaxation is faster (for exact calculation of the difference in T_1 between the two nuclei, not only the homonuclear dipolar coupling of two spins need to be considered, but the powder average of the van Vleck second moment, therefore the difference is not exactly 2.5^4).

Position of the maxima

Next to the relaxation rates being higher for ^{7}Li, the maxima of the curves for ^{7}Li are shifted to higher temperature. To a smaller degree, also the maxima of ^{7}Li measured at different field are shifted, the higher the field the higher the temperature of the maximum (see the temperatures of the maxima extracted from the plot in the appendix table 8.1).

This is due to the difference in Larmor frequency of the two isotopes. The relaxation rate is at its highest as the product of $\tau_c^* \omega_0$ = 1 (see appendix table 8.1 for the $\tau_c^* \omega_0$ calculated at the maxima for the simulations in Figure 4.1).

The Larmor frequency depends on the gyromagnetic ratio and the magnetic field (see equation 3.11). Therefore, the higher the field and the gyromagnetic ratio, the larger the Larmor frequency and hence the higher the temperature of the maximum.

Other than from simulations, the position of the maxima can be investigated analytically by taking the derivative of equation 4.7, setting it to zero

$$\frac{d}{d\tau_c} K_D \left[\frac{2\tau_c}{1 + \omega_0^2 \tau_c^2} + 4 \frac{2\tau_c}{1 + 4\omega_0^2 \tau_c^2} \right] = K_D \left[\frac{2(1 - (\tau_c\omega_0)^2)}{(1 + (\tau_c\omega_0)^2)^2} + \frac{8(1 - 4(\tau_c\omega_0)^2)}{(1 + 4(\tau_c\omega_0)^2)^2} \right] = 0 \qquad (4.10)$$

and trying to solve the equation for $\omega_0\tau_c$. This equation can be solved but it is rather complicated, therefore it makes sense to make a simplifying approximation. Again considering equation 4.7, the biggest contribution to the relaxation rate comes from the first term in the sum (this can be simulated by simulating the contributions separately using values typical for fast ion conductors). Taking the derivative of the first term and equating it to zero reads as follows:

$$\frac{d}{d\tau_c} \left[\frac{2\tau_c}{1 + (\omega_0\tau_c)^2} \right] = K_D \frac{2((\tau_c\omega_0)^2 - 1)}{((\tau_c\omega_0)^2 + 1)^2} = 0 \qquad (4.11)$$

Here it is clear, that as K_D is not zero, $(\tau\omega_0)^2$-1 has to be zero and hence at the maximum, $\tau\omega_0 = 1$. Now that we know that at the maxima, the condition $\omega_0 \tau \approx 1$ is true, we can investigate what that means for the relaxation rate at the maxima. Putting $\omega_0 \tau = 1$ into equation 4.7, we find

$$\frac{1}{T_1}(T = T_{max}) = K_D \left[\frac{2\tau_c}{1 + 1} + \frac{4 * 2 * \tau_c}{1 + 2^2} \right] = K_D \left[\frac{13}{5} \tau_c \right] \qquad (4.12)$$

Far away from the maxima
At temperatures far away from the maxima, the natural logarithm of the relaxation rate curve becomes a straight line (see Figure 4.1). At temperatures above the maxima, the simulations at different Larmor frequencies show the same line, whereas at temperature below the maxima, they are parallel to each other but with an offset. To understand this, different limits of equation 4.7 can be investigated:

As previously established, at the position of the maximum we have the condition

$$\omega_0\tau_c \approx 1. \qquad (4.13)$$

At temperatures far below the maximum, the correlation time is much longer than at the maximum. Therefore we must have the condition

$$\omega_0\tau_c \gg 1 \qquad (4.14)$$

Equivalently, at temperatures far above the maximum, the correlation time is much shorter than at the maximum and therefore we have the condition

$$\omega_0\tau_c \ll 1 \qquad (4.15)$$

Low temperature limit

Let's investigate what our relaxation rates in equation 4.7 look like in these limits. Considering the low temperature limit in equation 4.14, we can make the approximation:

$$\frac{1}{T_1} = K_D \left[\frac{2\tau_c}{1+\omega_0^2\tau_c^2} + 4\frac{2\tau_c}{1+4\omega_0^2\tau_c^2} \right] \approx K_D \left[\frac{2\tau_c}{\omega_0^2\tau_c^2} + 4\frac{2\tau_c}{4\omega_0^2\tau_c^2} \right] = K_D \left[\frac{4}{\omega_0^2\tau_c} \right] \tag{4.16}$$

Using equation 4.6 and taking the natural logarithm on both sides, as done in figure 4.1, we get:

$$\ln\left(\frac{1}{T_1}\right) = \ln\left(K_D \left[\frac{4}{\omega_0^2\tau_c} \right]\right) = \ln\left(\frac{K_D * 4}{\omega_0^2\tau_0\exp\left(\frac{E_a}{k_B T}\right)} \right) = \ln\left(\frac{K_D * 4}{\tau_0}\right) + \ln\left(\frac{1}{\omega_0^2}\right) - \frac{E_a}{k_B T} \tag{4.17}$$

From this we can see that at the low temperature limit, our relaxation rates are linear in temperature and can therefore be represented with

$$y = mx + q \tag{4.18}$$

where, if we set x = 1/k_BT like in figure 4.1:

$$m = -E_a \tag{4.19}$$

and

$$q = \ln\left(\frac{K_D * 4}{\tau_0}\right) + \ln\left(\frac{1}{\omega_0^2}\right) \tag{4.20}$$

The slope of the curve is therefore the activation energy, whereas the offset depends on the K_D, τ_0 as well as ω_0. The Larmor frequency ω_0 is field dependent (equation 3.11). At larger B_0, the ω_0 is larger, and therefore $\ln(1/\omega_0^2)$ is smaller, and the curve in Figure 4.1 is shifted down.

High-temperature limit

Similarly, we can look at the high-temperature slope using the condition in equation 4.15

$$\frac{1}{T_1} = K_D \left[\frac{2\tau_c}{1+\omega_0^2\tau_c^2} + 4\frac{2\tau_c}{1+4\omega_0^2\tau_c^2} \right] \approx K_D \left[\frac{2\tau_c}{1} + 4\frac{2\tau_c}{1} \right] = K_D \left[10\tau_c \right] \tag{4.21}$$

Again, using equation 4.6 and taking the natural logarithm on both sides, as done in figure 4.1, we get:

$$\ln\left(\frac{1}{T_1}\right) = \ln(K_D\left[10\tau_c\right]) = \ln\left(K_D * 10 * \tau_0 exp\left(\frac{E_a}{k_B T}\right)\right) = \ln(K_D * 10 * \tau_c) + \frac{E_a}{k_B T} \tag{4.22}$$

as already predicted, here we also get a linear equation (if x = 1/k_B T), this time with

$$m = +E_a \tag{4.23}$$

and

$$q = \ln(K_D * 10 * \tau_0)$$ (4.24)

The slope of the curve is therefore also the activation energy in the high-temperature limit. The q, however, is not dependent on ω_0 and is therefore field-independent, which is why the slopes coincide.

4.1.5 A modified BPP-model

Many measurements in literature show deviations to the BPP model, for example in the form of asymmetric slopes ($m \neq \pm E_A$). For those cases, a modified BPP-model exists. It contains a parameter β describing the asymmetry of the slopes

$$\beta = \frac{E_{A,LT}}{E_{A,HT}} + 1$$ (4.25)

This parameter is linked to the spectral density as folllows [5, 6]:

$$J(\omega_0) \propto \frac{\tau_c}{1 + (\omega_0 \tau_c)^\beta}$$ (4.26)

When β equals 2, the spectral density is the same as the BPP-spectral density.
The full expression that is fit to the relaxation rates reads as follows

$$\frac{1}{T_1} = K_D \left[\frac{2\tau_c}{1 + (\omega_0 \tau_c)^\beta} + \frac{4\tau_c}{1 + (2\omega_0 \tau_c)^\beta} \right]$$ (4.27)

Common reasons named for the asymmetry of the spectral density or reasons for this deviation from the BPP model are [5]:

- Correlation effects because of both disorder and strong Coulomb interactions of the moving ions. This leads to a difference in activation energy for short-range versus long-range processes.

- A distribution of motional correlation times.

Maxima of the modified BPP-model
Similar to the BPP-model, we can investigate the position of the maxima of the curve by taking the derivative of the first term in the sum of equation 4.27 and setting it to zero:

$$\frac{d}{d\tau_c} K_D \frac{2\tau_c}{1 + (\omega_0 \tau_c)^\beta} = -2K_D \frac{\beta(\tau_c \omega_0)^\beta - (\tau_c \omega_0)^\beta - 1}{(1 + (\omega_0 \tau_c)^\beta)^2}$$ (4.28)

As K_D is not zero, the condition $\beta (\tau_c \omega_0)\beta - (\tau_c \omega_0)\beta - 1 = 0$ has to be fulfilled at the maxima. The condition $\omega_0 \tau_c = 1$ found for the BPP-model ($\beta = 2$), but is not true for $\beta < 2$. Still, information about the correlation time from the maxima can be obtained by estimating β from the slopes of the high and low-temperature limits (equation 4.25), and solving the maximum condition for the correlation time.

Low temperature limit of the modified BPP model
In the low temperature limit $\omega_0 \tau_c \gg 1$, we find the following:

$$K_D \left[\frac{\tau_c}{1 + (\omega_0 \tau_c)^\beta} + \frac{4\tau_c}{1 + (2\omega_0 \tau_c)^\beta} \right] \approx K_D \left[\frac{\tau_c}{(\omega_0 \tau_c)^\beta} + \frac{4\tau_c}{(2\omega_0 \tau_c)^\beta} \right] = K_D \omega_0^{-\beta} \tau_c^{-\beta+1} \left[1 + 4 * 2^{\beta-1} \right]$$
(4.29)

Looking at the natural logarithm of the expression

$$\ln\left(\frac{1}{T_1}\right) = -\beta * \ln(K_D \omega_0) + (\beta - 1)\left(\ln(\tau_0) + \frac{E_a}{k_B T}\right) + \ln\left(1 + 4 * 2^{\beta-1}\right)$$
(4.30)

shows a similar dependence on the Larmor frequency ω_0 as for the regular BPP-model. With $x = 1/k_B T$, the slope of the curve is equal to $(\beta - 1) E_a$. Therefore, the condition

$$E_{LT} = (\beta - 1)E_{HT}$$
(4.31)

is fulfilled and consistent with the definition in equation 4.25.

High temperature limit of the modified BPP model
In the high-temperature limit $\omega_0 \tau_c \ll 1$, the beta term falls away as $1 + (\omega_0 \tau_c)\beta \approx 1$, and the solution is the same as for the BPP model. (section 4.1.4).

4.1.6 Other spectral densities
Considering that the BPP model describes uncorrelated, 3D diffusion and the modified BPP-model mostly accounts for correlation effects, it is clear that not all diffusive atoms in solid-state conductors will follow these models. Therefore, many spectral densities were developed in literature (see the review of Beckmann [2]).

For example, layered conductors often show two-dimensional diffusion. Considering the layering of Li-layers and mixed Li/M(III) layers in the monoclinic phase, two more spectral densities are used in this thesis (chapter 5).

Those are a semi-empirical model by Richards for two dimensional diffusion [7]:

$$J(\omega_0 \tau_c) = C * \ln\left(1 + \frac{1}{\omega_0^2 \tau_c^2}\right)$$
(4.32)

as well as a modified version with a similar parameter β to account for correlations due to Coulomb interactions of the moving ion [8]:

$$J(\omega_0 \tau_c) = C * \ln\left(1 + \frac{1}{\omega_0^2 \tau_c^\beta}\right)$$
(4.33)

4.1.7 Multiple BPP-type jump processes
In many solid ion conductors, multiple possible jump processes can be found depending on the crystal symmetry.

For example, in the halide solid electrolytes based on quasi-hexagonal close packing, we can find oct-oct, oct-tet-oct, and tet-tet jumps (as illustrated in Figure 2.1).

In principle, these jump processes can all occur simultaneously at different rates if they differ in activation energy or the pre-exponential factor. This has been shown for example for argyrodite Li_6PS_5I, where multiple maxima were resolved by using measurements at different larmor frequencies or by adding $T_1\rho/T_2$ measurements [9].

From theory we know that if there are multiple relaxation processes that do not interact, then the relaxation rates are additive [10]

$$\frac{1}{T_{1\,tot}} = \frac{1}{T_{1,a}} + \frac{1}{T_{1,b}} + ... + \frac{1}{T_{1,N}} \tag{4.34}$$

Hence, it should be possible to fit the data obtained with a superposition of individual spectral densities for each jump process in such a case.

The T_1 extracted from a saturation recovery or inversion recovery is not necessarily a sum of the different T_1 (unless the different T_1 are of different enough magnitude that they are resolved in the shape of the recovered magnetization during the pulse sequence). However, if the T_1 do not resolve in the measurement, the least-square fit of the T_1 value to the measured intensities will be some weighed average of the two, depending on which one dominates the response. In such cases, however, the T_1 are of similar value and the extracted T_1 can be used as an estimate for $T_{1\,tot}$.

To explore what kind of shapes the function of the relaxation rates would take on, three jump processes that differ in their activation energy were simulated in Figure 4.2. If this material existed and was measured for the temperature range shown, the solid line would be obtained, which is the natural logarithm of the sum of the rates (equation 4.34).

Imagining that this is indeed the case and we measured the solid line, the reverse problem of fitting the measurements with a model is a much more complicated problem, as the measured data shows few characteristic features. It is not obvious where the maxima are located, and without knowing it would not be possible to tell that it represents three jump processes.

Without characteristic features (slopes, position of the maxima) finding the correct activation energies is likely impossible as no educated guesses on the initial parameters can be made. If some features are resolved, educated initial guesses can be made and a solution may be found.

To get more information on such characteristic features, it is useful to have measurements at multiple Larmor frequencies due to the dependence on $\omega_0 \tau_c$. It is further necessary to investigate the errors estimated from the fit very closely, as the motional parameters are also strongly correlated (see for example table 4.2).

4.1.8 Experimental considerations

When considering ionic conductors, the most interesting property to get out of the simulation is the correlation time, as the inverse of τ_c gives us access to the jump frequency of the ion. The most direct access to the correlation time in such measurements are at the maximum, due to the condition of $\tau_c \omega_0 \approx 1$.

At temperatures below and above the maximum, the only access to τ_c is via spectral density fitting. To fit the measurements with a spectral density, it is useful to first visually inspect the curve. For example, if the curve is symmetric with slopes $m = \pm E_a$ (or other relations derived in section 4.1.4), the BPP model is a good candidate. If the slopes are

Figure 4.2: Relaxation rates (striped line) as well as their sum (full line, this would be measured in an experiment) simulated for three different activation energies (0.15, 0.2 and 0.25 eV). Blue is simulated ^{7}Li, purple is ^{6}Li, both on a magnet with B_0 = 11.75 Tesla. All other parameters are kept the same as in Figure 4.1.

4
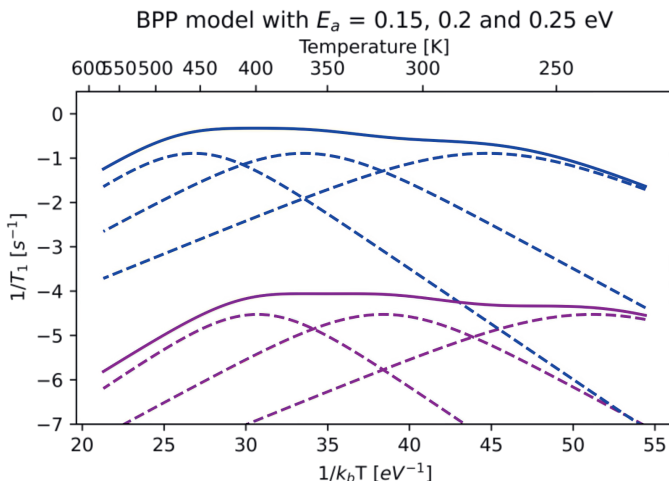
not symmetric but otherwise the data looks as expected for the BPP model, the modified BPP-model might be a good candidate. In any way, knowledge about the various different spectral densities and matching it with characteristics of the curve can help identify a suitable spectral density.

To be able to distinguish between different spectral densities, the maximum as well as enough points on the high- and low temperature slope need to be experimentally accessible. Whether this is possible depends on the Larmor frequency of the measurement (NMR-active isotope and B_0), and on the correlation times of the diffusing atom in the temperature range accessible (depends on the diffusivity).

As the correlation time depends on the jump activation energies and pre-exponential factors, which are the properties we want to find, the experimental parameters to be determined are the isotope to be measured, the magnetic field B_0, and the probe which determines the temperature range.

Temperature and frequency range

To illustrate the effect of those parameters on the measurement, some relaxation rate curves as a function of inverse temperature were simulated (Figure 4.3). Except for the activation energy, all the parameters are kept the same. The larmor frequencies simulated correspond to ^{6}Li (purple) and ^{7}Li (blue) on different B_0. For an activation energy of 0.2 eV, the curves show the maximum as well as the high and low temperature slopes, this is not the case for materials with higher and lower activation energies.

For the material with higher E_a=0.3 eV (Figure 4.3), the measurements using ^{6}Li clearly show the maxima. The measurements using ^{7}Li would just reach the maximum, but not reveal the high-temperature slope. The material with lower activation energy (0.1 eV) would only show the high-temperature slope but not the maximum or low temperature slope.

Figure 4.3: Relaxation rates simulated for three different activation energies (0.1, 0.2 and 0.3 eV). All other parameters are kept the same (as in Figure 4.1).
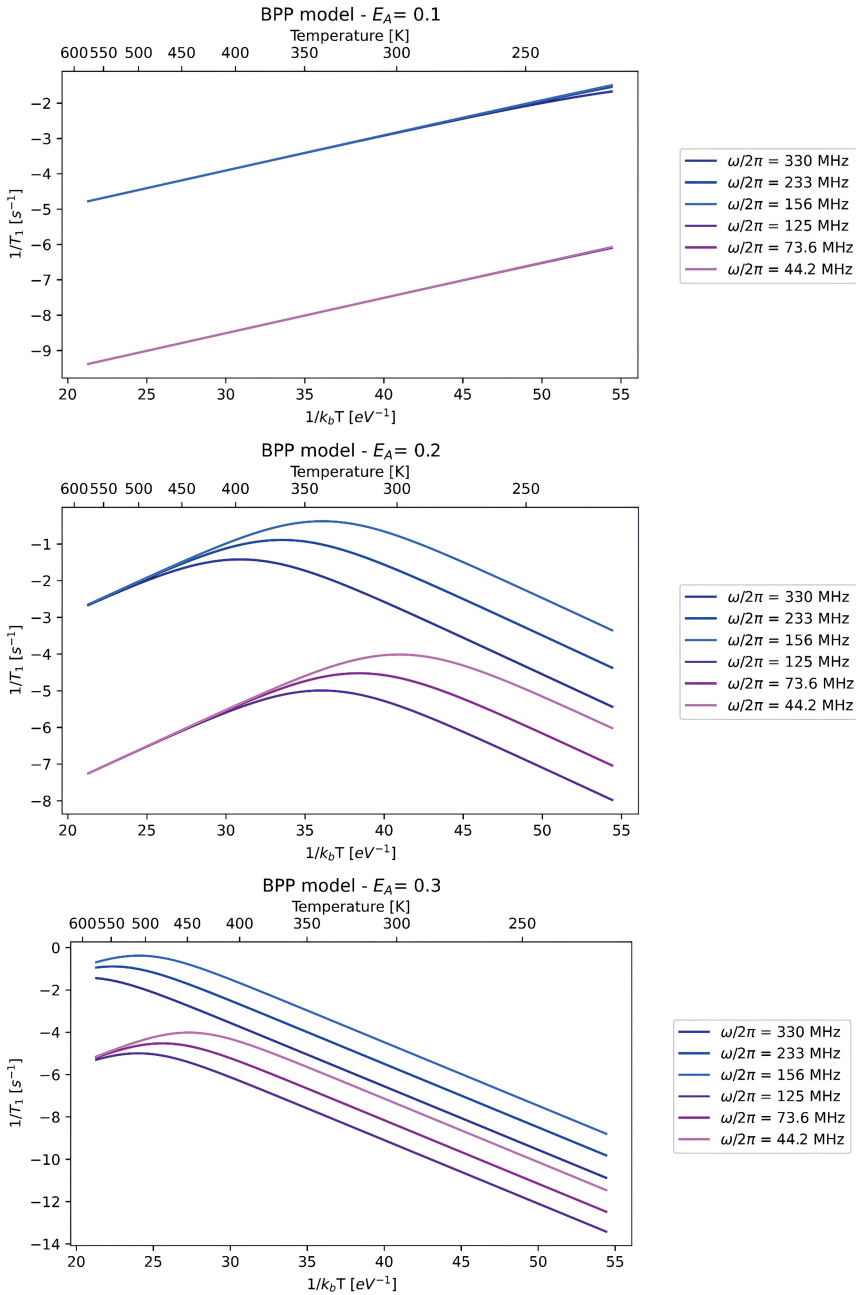
If the maximum and both slopes are not accessible experimentally at the available ω_0, then T_1 relaxation measurements may not be suitable probe for the material at hand. In that case, for a material with longer correlation times it is possible to do:

- T_2 (spin-spin) relaxation measurements or line-width analysis as a function of temperature if the lineshape is broadened by the dipolar interaction

- spin-lattice relxation measurements in the rotating frame T_1, ρ

- Measure at higher temperature

If the correlation time is too fast, the only option is measuring at higher ω_0 and lower temperature. Finally, the material measured needs to be thermally stable in the temperature considered, as phase transitions can lead to either different interaction strengths (of the quadrupole or dipole interaction) or affect the diffusion (different spectral density or correlation time). Often, a phase transition will lead to a discontinuity in the curve of the T_1 (see chapter 7 for an example).

Error estimation

For the fitting as well as the error analysis, the lmfit package implemented in python is used [11]. Therefore, the error estimation is discussed closely in line with the documentation of lmfit.

The scale of the standard error estimated for the parameters (by default) (Figure 4.3)is closely tied to the goodness of fit statistics χ^2 and reduced χ^2. Usually, a fit with a reduced χ^2 around 1 is considered a good fit. However, this requires that the data uncertainties as well as the sampling of the datapoints is correct [11].

For example, in a diffraction experiment we count the amount of waves that are scattered by the sample at a certain angle. The data uncertainty of this adheres to counting statistics, and therefore the data uncertainty is the square-root of the amount of counts.

In the case of the fitting procedure here, the data uncertainty is not known. There are multiple uncertainties that could contribute to this:

- **Error associated with temperature**: In the temperature-dependent experiments, the temperature is set by the probe with a heater or connected to a variable temperature gas flow. Often, a thermocouple is placed close to the sample measuring the surrounding temperature. As in any measurement series as a function of temperature, it is possible that the temperature measured at the thermocouple deviates from the sample temperature. While this deviation can be minimized by calibration of the probe and waiting a suitable amount of time for temperature equilibration, there can still be an offset. This can for example arise from a heat gradient between the thermocouple and the sample, which can depend on the pressure of the heating gas.

- **Error from the measurement**: While errors in from the measurement itself should be small for correctly setup pulse sequences for commercial magnets, the error is never zero. Errors in setting up the pulse sequence add to that error, for example if not enough saturation pulses are used in a saturation recovery experiment, there

can be some residual magnetization at the beginning which may affect the value of T_1 fit to the data.

- **Error associated with data processing**: Once the pulse sequence is measured, the free induction decay (FID) acquired has to be Fourier transformed, phased and integrated. The phasing can be difficult if the spectra does not have a flat baseline (if the dead time before the signal is acquired is large) or the signal to noise is poor (for example if the NMR nuclei measured has low abundance). While such effects can be corrected for by correcting the baseline post- measurement or filtering the signal to minimize noise, these subtleties can still introduce an error in the integrated signal and hence the estimated T_1. The data points sampled should further be spaced out exponentially and across a suitable amount of time.

- **Error associated with fitting of** T_1: The T_1 is a parameter that is fit to data from the measurement itself, and therefore there is an error associated with the fit.

It is therefore clear, that the uncertainty of the T_1 is not known in the case of these NMR experiments.

According to the documentation of the lmfit package, this is a common problem and therefore the uncertainties reported are the ones that increase χ^2 by reduced χ^2, which is equivalent to rescaling the uncertainty in the data such that χ^2 would be one [11]. Considering the high correlations of the pre-exponential factor and τ_0 and E_a, it can be difficult to trust the errors calculated in this way.

If that is the case, it makes sense to explore the parameter space around the solution found. In lmfit, this can be done using a Markov Chain Monte Carlo (MCMC) method [11]. MCMC a method for sampling the posterior distribution of a model, from which the uncertainty in the model's parameters given the observed data can be obtained.

The posterior probability distributions of the parameters can be visualized in a corner plot (see Figure 4.4 for an example) [12].

For the algorithm to run, four parameters have to be chosen:

- **N-walker** The number of Markov chains to be followed simultaneously

- **N-steps** The number of steps of each walker. The number of steps should be much larger than the autocorrelation time of the parameter.

- **N-burn** Number of points at the beginning of the Markov chain to discard

- Boundaries for **ln_sigma**: As the data uncertainty is not known, the data uncertainty is treated as a nuisance parameter in lmfit to be marginalized out [11]. The uncertainty s_n is a strictly positive quantity $s_n = \exp(\text{lnsimga})$.

There are two ways to test whether the algorithm worked, either by making sure that the correlation time of the chains is much shorter than the number of steps, or by checking the acceptance fraction of the number of steps by each walker. Generally, an acceptance fraction between 0.3-0.5 is expected [11].

Figure 4.4: Visualization of the a corner plot for a BPP-type fit for the Li_6PS_5Cl used in section 4.2. Both axes (x and y) list the parameter of the fit. The contour plots belonging to two different parameter visualize the relationship between them. The histogram shows the posterior probability distribution of the parameter on the x-axis. The histogram is useful for the decision which parameter estimate is the most appropriate (median, maximum likelihood etc.) and serves to calculate the standard error estimated as half the difference between the 15.8% and 84.2% percentiles. The uncertainty of the data $s_n = \exp(\text{lnsimga})$.
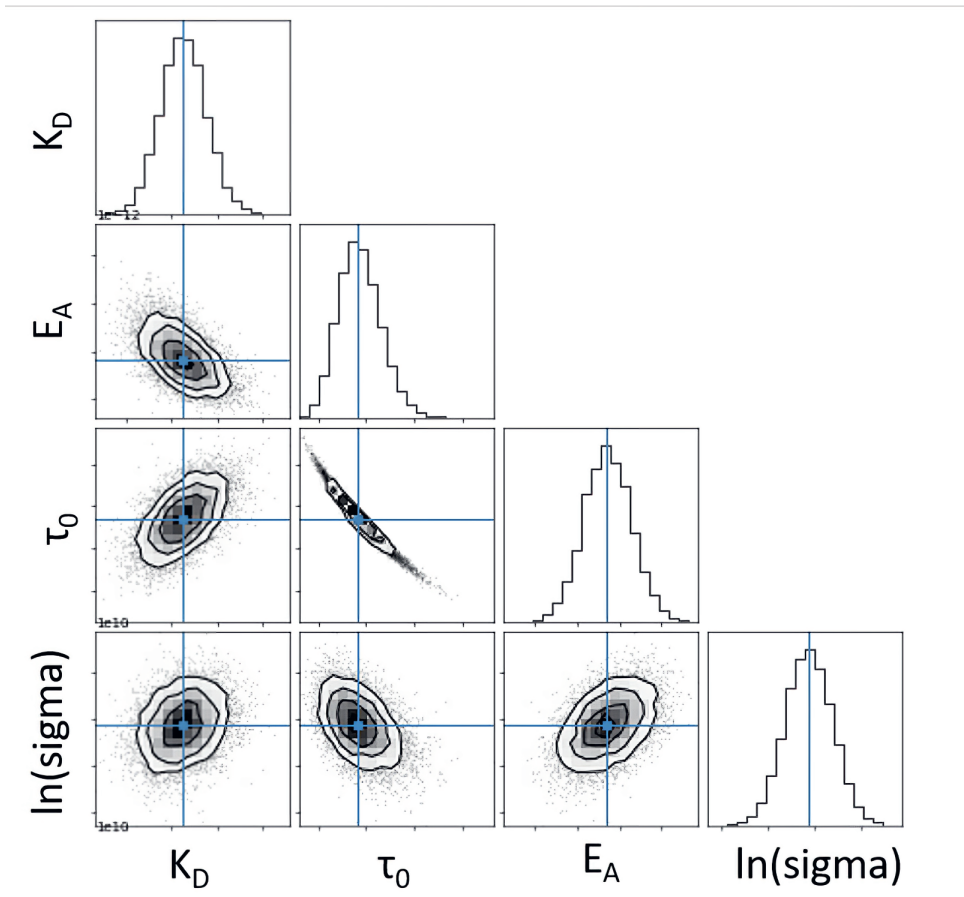

4.2 NMR relaxometry in Li-ion conducting argyrodites Li_6PS_5X

Li_6PS_5X (X=Cl, Br, I) are fast and rather well studied ion conductors and therefore useful as a first example to demonstrate the theory discussed above. Li_6PS_5X crystallize in cubic $F\bar{4}3m$ (see Figure 4.5) [13]. The argyrodites consist of quasi-ccp of the Phosporous, Sulfur and halogen atoms. There are two sulphur sites, the 16e site forms a PS_4^{3-} unit with the phosporous and the 4c site, which is a free sulphur site. There are one X (4a) and P (4b)

site. It has been shown that, depending on the halogen, there are different degrees of site mixing between the Sulfur 4c and halogen 4a sites, which is beneficial for ion conduction. The disorder is larger for Cl than for Br; for I no disorder has been observed.

The lithium is positioned in a tetrahedral sites coordinated by three S and one X atom (if fully ordered). The diffusion mechanism in this material is rather complex, three different jump types are reported as observed from MD simulations [14]. Two jump-processes are in so-called cages, one between face sharing tetrahedra and one between edge-sharing polyhedra. The third jump-process is between the cages and is also between edge-sharing tetrahedra [14]. This jump has a higher activation energy compared to the other [14], likely due to the larger distance as can be seen in Figure 4.5.

Figure 4.5: Visualization of the crystal structure of Li$_6$PS$_5$X as published by Deiseroth et al [13]. On the left, the structure is shown without the lithium sites, to illustrate the close packed nature. Cl is shown in green, S in yellow and the pink tetrahedra belong to the PS$_4^{3-}$ units. On the right, the same angle is shown including the lithium sites and polyhedra (turquoise). There are three cages shown in the structure, one at the top and two at the bottom, as can be imagined by the three turquoise hexagon. The hexagon share edge.
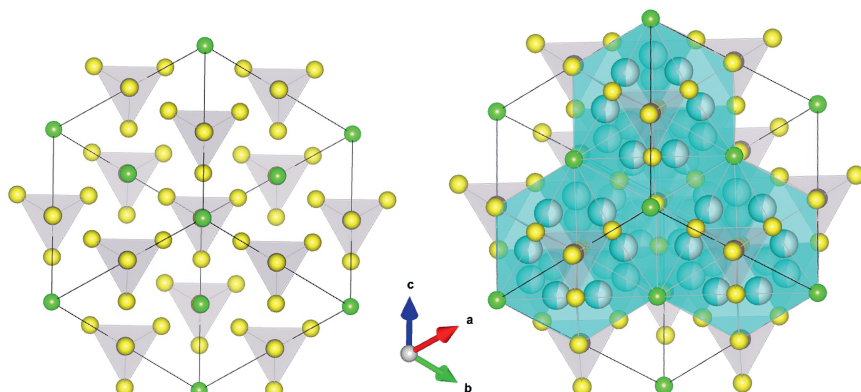

4.2.1 NMR relaxometry of Li$_6$PS$_5$Cl

The data presented in this chapter is published in Ganapathy et al. [15] and the reader is referred to that paper for experimental details about the measurements and to [16] for the synthesis of the materials.

4.2.2 BPP-spectral density fit

Individual Fits

^{7}Li spin lattice relaxation rates of the material Li$_6$PS$_5$Cl were measured at three different Larmor frequencies (ω_0 = 156 MHz on the 400 MHz spectrometer, ω_0 = 233 MHz on the 600 MHz spectrometer and ω_0 = 330 MHz on the 850 MHz spectrometer). The T$_1$ extracted from the measurements are shown in Figure 4.6.

Figure 4.6: $1/T_1$ relaxation rates of the argyrodite Li_6PS_5Cl measured at three different ω_0.
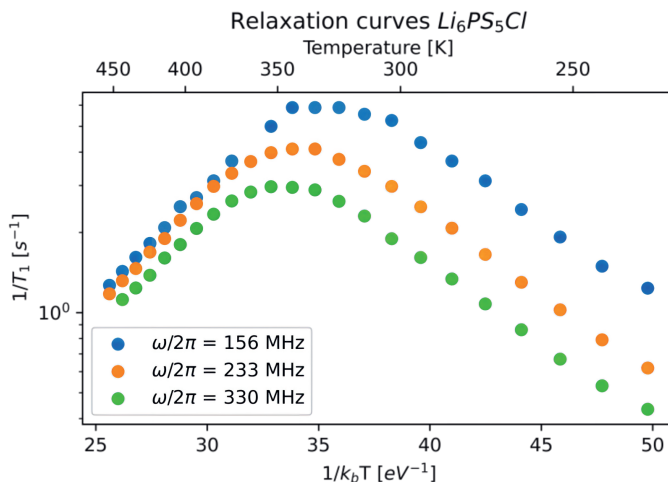

The measurements displays the full maxima as well as the high and low-temperature slopes. The high-temperature slopes fall almost on top of each other (it is possible that the temperature calibration for $\omega_0/2\pi = 330$ MHz is slightly shifted compared to the other measurements), while the low-temperature slopes show a constant offset. The maximum are shifted in temperature, with the measurement at the lowest frequency corresponding to the maxima at the lowest temperature and vice versa. All these aspects indicate that the BPP-model might be the right spectral density to fit this data with.

Table 4.1: Activation energies extracted from fitting a linear equation to the high and low-temperature slopes of the measurements ($\ln(1/T_1)$ vs $1/k_BT$) of Li_6PS_5Cl measured on the 400, 600 and 850 MHz spectrometer. The β is calculated from these activation energies according to equation 4.25.

$\omega_0/2\pi$ [MHz]	Variable	Li_6PS_5Cl
	$E_{A,HT}$ [eV]	0.19
156	$E_{A,LT}$ [eV]	0.12
	β	1.63
	$E_{A,HT}$ [eV]	0.20
233	$E_{A,LT}$	0.14
	β	1.70
	$E_{A,HT}$ [eV]	0.18
330	$E_{A,LT}$ [eV]	0.13
	β	1.72

In Figure 4.7, the curves were individually fit with the BPP model. While the fit of the high-temperature slope is rather good, the low-temperature slope is not adequately fit. In table 4.1, the values calculated for the slopes are shown together with a index for the

Figure 4.7: T_1 measurements of the argyrodite Li_6PS_5Cl, individually fit with the BPP-model. Due to the asymmetry of the slopes, the fit is a bad representation of the data.
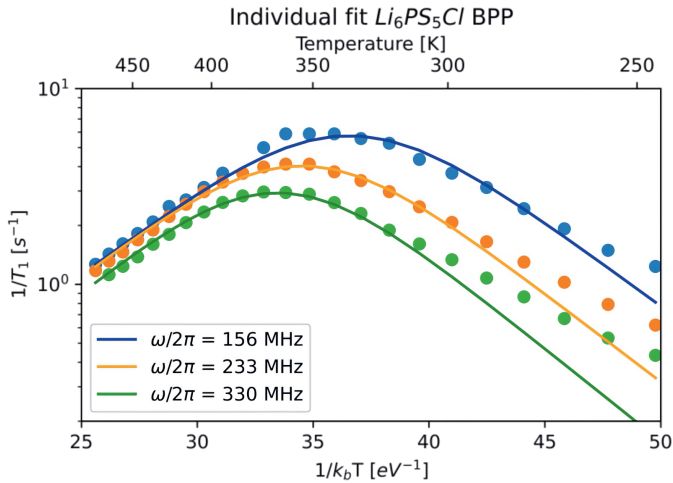
asymmetry of the slopes β measured from the data. Considering the BPP model predicts m = ± E_a, the value of β should be 2. The β for the data here is 1.7, hence the slopes are not indicative for the BPP spectral density, as can also be seen from the fit.

The fits of the modified BPP spectral density are shown in Figure 4.8. As to be expected, the model fits the data much better compared to the BPP-model. The fitting parameters are shown in table 4.2.

Considering that the material is the same, the correlation time(s) of the diffusion process should be the same at the same temperature. Hence, it should be possible to fit all three datasets using the same parameters for τ_0, E_a and β (given that there is no mismatch in the temperature calibration of the probes the measurements were made with). If the spectral density is not correct, it will show more clearly when the fit is performed on data measured at multiple frequencies compared to data measured at one frequency only.

Figure 4.9 shows that the model fits the measured data well also in a combined fit. Compared to the individual fits, the activation energy is smaller and the β and τ_0 are larger. Considering the large correlation between the parameters, the combined fit likely increases the reliability of the fitting procedure due to the larger content of information in the data (Table 4.2).

The activation energy found is 0.269 eV with a pre-exponential factor of $1.0*10^{-13}$ s and a β of 1.57. Hanghofer et al. found E_a = 0.32 eV, τ_0 = $1.3*10^{-14}$ and β = 1.53 for a Li_6PS_5Cl material with slightly lower ionic conductivity as seen from AC-impedance measurements [5]. Also the high-temperature slope of the NMR-relaxation data is slightly steeper [5], therefore the results of the fitting procedure are considered in line with literature.

Figure 4.8: Individual fits of the relaxation rates $1/T_1$ of Li_6PS_5Cl measured on the 400, 600 and 850 spectrometer of the argyrodite Li_6PS_5Cl with the modified BPP-model.
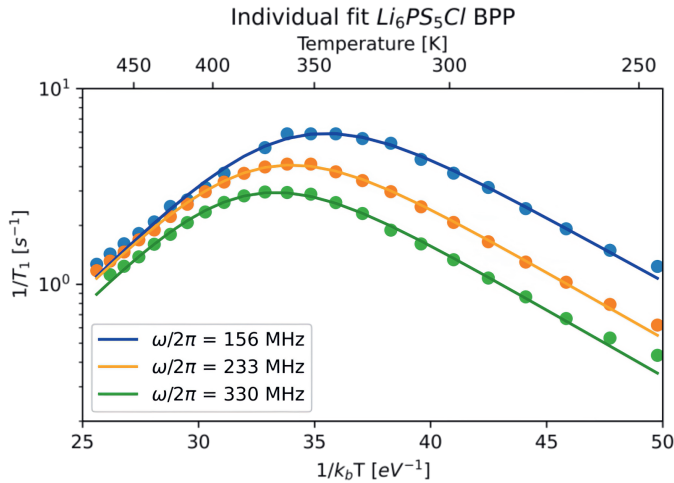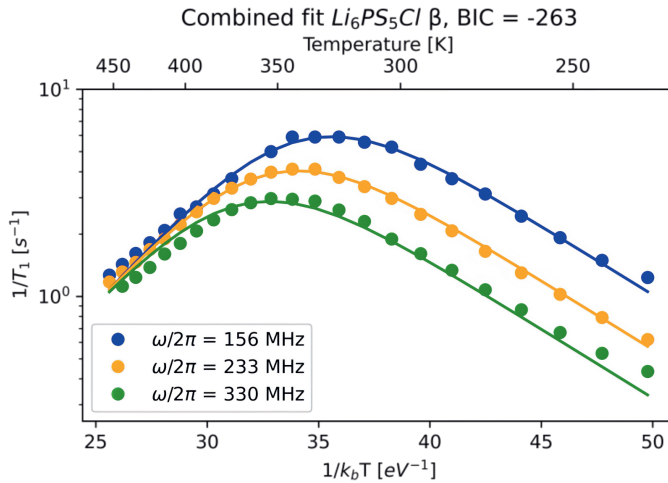

Figure 4.9: Simultaneous fit of the relaxation rates $1/T_1$ measured on the 400, 600 and 850 spectrometer of the argyrodite Li_6PS_5Cl with the modified BPP-model.

Comparison with results from molecular dynamics simulations leave some open questions [14]. Jump-path analysis for Li-ion diffusion in Li_6PS_5Cl showed three jump processes with different rates, referred to as the intercage, intracage and doublet jumps. De Klerk et al. [14] have determined the rates and activation energies of said jumps, and the energy of 0.269 eV found here is closest to the energy calculated for the intercage jump (~0.26 eV, Table 4.3). The intracage and doublet jumps are predicted to be at lower energy

Table 4.2: Parameter values, errors and selected values from the correlation matrix for both individual and combined fits of the relaxation rates (measured on a 400, 600 and 850MHz spectrometer) of Li$_6$PS$_5$Cl with the modified BPP-model. The errors are calculated from raising χ^2 by reduced χ^2.

$\omega_0/2\pi$ [MHz]	Parameter	Value	Error [%]	C(a,b)	C(a, β)
156	K_D	$1.07 \cdot 10^{10}$	2.10%		
	τ_0	$6.30 \cdot 10^{-14}$	29.60%		
	E_a	0.29	3.52%	-0.902	0.871
	β	1.47	7.23%		
233	K_D	$1.15 \cdot 10^{10}$	0.99%		
	τ_0	$8.57 \cdot 10^{-14}$	14.39%		
	E_a	0.28	1.95%	-0.993	0.893
	β	1.56	3.98%		
330	K_D	$1.17 \cdot 10^{10}$	1.32%		
	τ_0	$5.07 \cdot 10^{-14}$	21.05%		
	E_a	0.29	2.58%	-0.994	0.9
	β	1.56	5.65%		
all	K_D	-	-		
	τ_0	$1.00 \cdot 10^{-13}$	19.88%		
	E_a	0.27	2.64%	-0.995	0.883
	β	1.57	4.89%		

(~0.13-0.17 eV, Table 4.3). The contribution of those motions to the NMR-relaxation rates should therefore be at lower temperature (when measuring at the same Larmor-frequency), or may show when measured at a higher B$_0$ field.

Table 4.3: Table of jump energies for the different jump types in Li$_6$PS$_5$Cl calculated in de Klerk et al. [14]. The material simulated has 50% Cl on the 4c position, which is closest to the crystal structure solution used for the relaxometry measurements with 55% Cl on the 4c [16]). The values obtained for 300K (in italic) are much lower compared to the values at 450 and 600K. The values at 450 and 600K are considered to be more trustworthy due to their good agreement and because higher temperatures (higher jump-frequency) implies better statistics within the same simulation time.

T [K]	Intercage [eV]	Error	Intracage [eV]	Error	Doublet [eV]	Error
300 K	*0.18*	0.02	*0.1*	0.01	*0.1*	0.01
450 K	0.27	0.02	0.13	0.01	0.14	0.01
600 K	0.25	0.01	0.15	0.01	0.17	0.01

Measuring both ^{31}P NMR ($\omega_0/2\pi$ = 121 MHz) and ^{7}Li (ω_0 = 116 MHz), the ion dynamics were further investigated by Hanghofer et al. for Li$_6$PS$_5$X (X = Cl, Br, I) [17]. While the ionic conductivites as measured by AC-impedance measurements follow the trend σ_{Cl} > σ_{Br} > σ_I, the trend is reversed when considerng the activation energies obtained from ^{7}Li NMR (E$_a$ measured from the high-temperature slope are 0.32 eV for X=Cl, 0.21 eV for

X=Br, and 0.2 eV for X = I [17]).

Interestingly, the energies from the low-temperature slope show a different trend with high energies for X = I, Cl (E_a is 0.18 eV for X=I and 0.17 eV for X=Cl) and low activation energy for X = Br (E_a = 0.1 eV). These energies result in a β of ~1.5 for X=Cl, Br and ~1.9 for I (almost BPP-type behaviour).

The ^{31}P measurement make the picture even more interesting. The T_1 measurements show one BPP-type peak for X=Cl, and two rate-peaks for X=Br, I. The faster of those processes was ascribed to rotational dynamics of the PS_4 units and the slower process to translational lithium motion relative to the phosphorous.

This indirect sensing of lithium motion through phosphorous NMR makes sense when considering that the dipolar interaction strength strongly depends on the radius between the spins. As the lithium moves, the distances between the lithium and phosphorous atoms will change and the electromagnetic field created by the heteronuclear dipole interaction is modulated, which can also enhance spin-lattice relaxation.

The energies of the different jumps were further investigated by Hogrefe et al. for Li_6PS_5I [9] by adding measurements in the rotating frame (lower frequency). The ^{31}P T_1,ρ and ^{7}Li T_1,ρ showed one additional jump process each. These measurements also showed higher values for β (1.92 and 1.7) compared to ~1.57 obtained for the chloride in this thesis (see table 4.2).

Considering these different rates resolve in Li_6PS_5I, it is interesting to investigate whether they appear as well in Li_6PS_5Cl but as a superposition, as the rates are expected to differ less in frequency.

4.2.3 Multiple jump processes in Li_6PS_5Cl

A fit using a sum of two BPP-type spectral densities is shown in Figure 4.10. The fit looks similar to the fit of the modified BPP model (see Figure 4.10, bottom figure, for comparison of the different models for the measurements at $\omega_0/2\pi$ =330 MHz). The two jump processes clearly show different activation energies as seen from the difference in the slopes (Figure 4.10, bottom figure, blue striped lines).

Table 4.4: Comparison of the values of the fitting parameters obtained from fitting the modified BPP model and the two BPP-type jump model for Li_6PS_5Cl

	Variable	Li_6PS_5Cl	Error [%]
MBPP	β	1.570	4.89%
	$\tau_{0\beta}$ [s]	$1.00 \cdot 10^{-13}$	20%
	EA, β [eV]	0.269	2.64%
Fit 2 BPP	τ_{01}	$1.55 \cdot 10^{-12}$	99.4%
	EA, $_1$ [eV]	0.157	12.7%
	τ_{02} [s]	$1.01 \cdot 10^{-13}$	28.1%
	EA, $_2$ [eV]	0.25	3.57%

The activation energy of the modified BPP-model matches the higher energy obtained from the two jump-process model (see table 4.4 for the fitting parameter values). The

Figure 4.10: Simultaneous fit of the relaxation rates $1/T_1$ measured on the 400, 600 and 850 spectrometer of the argyrodite Li_6PS_5Cl with the model consisting of two BPP-type jump processes (top). Comparison of the different models using the data measured on the 850MHz spectrometer (bottom).
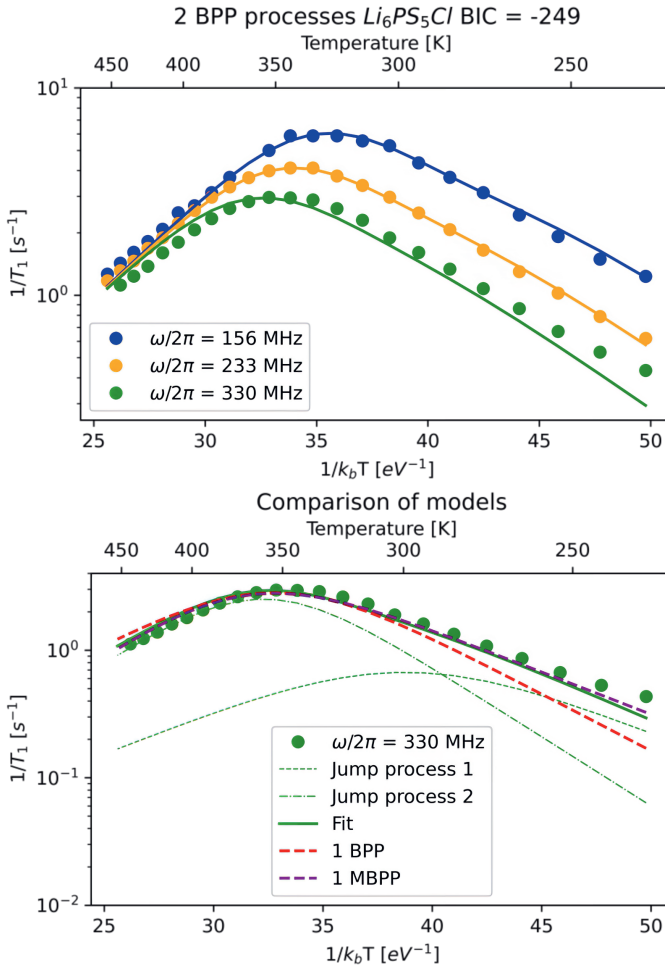
lower jump energy shows a good match with the values for the intercage and doublet jumps calculated from MD simulations in de Klerk et al. (0.157 eV ± 12.7% for the NMR spectral density fits compared to 0.13 eV and 0.15 eV for the MD simulations at 450K and 600K) [14] (see table 4.3).

To check the viability of this solution, MCMC-based error analysis was performed to investigate the solution space around the parameters found. The corner plot (Appendix, Figure 8.1) shows, that there is one clear maximum likelihood solution for all parameter. The comparison of the maximum likelihood estimate and the median estimate is shown in table 8.2. Especially for τ_0 there is quite a large difference (up to a factor 2), which is also

the parameter with the largest error (24% to 87%) and the most skewed distribution as can be seen from the histograms in the Appendix, Figure 8.1.

4.2.4 Multiple jump processes in Li_6PS_5Br

Considering the agreement between the activation energies from solid-state NMR and MD simulations, it is interesting to investigate whether similar results can be achieved Li_6PS_5Br, or whether it is coincidence.

The relaxation rates of Li_6PS_5Br can also be fit using the modified BPP model (Appendix Figure 8.2). Again, also for this material a two BPP-type jump process model can be fit to the data, see Appendix Figure 8.3. The errors calculated using the MCMC-algorithm are small (1-16%, appendix table 8.3).

The E_a show a similar picture as obtained for Li_6PS_5Cl; the activation energy of the modified BPP model is similar to the large one of the two BPP models. The values from the two BPP-jump process model further seems to be in line with the values obtained from MD simulations (table 4.6 for MD simulations, table 4.5 for fitting parameter values): The intercage jump has values between 0.18 and 0.26 eV, compared to 0.2 eV from the NMR and the intracage/doublet jumps between 0.1 and 0.17, compared to 0.144 from the NMR. Unfortunately, the values in literature for the MD simulations show a rather large spread to be able to concisely compare with the values as obtained from solid-state NMR.

Table 4.5: Comparison of the values of the fitting parameters obtained from fitting the modified BPP model and the two BPP-type jump model for Li_6PS_5Br

	Variable	Li_6PS_5Br	Error
MBPP	β	1.42	2.45%
	$\tau_{0\beta}$ [s]	$5.84 \cdot 10^{-13}$	6.37 %
	EA, β [eV]	0.202	1.14%
Fit 2 BPP	τ_{01} [s]	$1.37 \cdot 10^{-12}$	16%
	EA, $_1$ [eV]	0.144	2%
	τ_{02} [s]	$5.73 \cdot 10^{-13}$	12%
	EA, $_2$ [eV]	0.200	1%

Table 4.6: Table of jump energies for the different jump types in Li_6PS_5Br calculated in de Klerk et al. [14].

T [K]	Intercage [eV]	Error	Intracage [eV]	Error	Doublet [eV]	Error
300 K	0.18	0.02	0.11	0.01	0.1	0.01
450 K	0.22	0.02	0.14	0.01	0.13	0.01
600 K	0.26	0.02	0.17	0.01	0.17	0.01

4.2.5 Conductivities

The conductivities of Li$_6$PS$_5$Cl and Li$_6$PS$_5$Br as obtained from AC-impedance, as well as a conductivity calculated from the diffusion coefficient obtained from the correlation time at the same temperature (both the modified-BPP and the 2BPP-jump model) are summarized in table 4.7.

To compare the values of the conductivities (or diffusion coefficients, as σ ∝ D (equation 2.19) obtained by each technique, the self-diffusion coefficients need to be compared, which are related to the measured diffusion coefficients by the correlation factor f and the HR (equation 2.22).

Other than these correlation factors, AC-impedance measures ion-conduction on longer timescales which can include contributions of ion conduction across grain boundaries, compared to the values from obtained from NMR where the measurement is sensitive to timescales of $\omega_0/2\pi$, which will only contain bulk contributions in the self diffusion coefficient.

For simplicity, the values of $\frac{D_\sigma}{D_{NMR}} = \frac{f}{HR}$ are shown in table 4.7. The correlation factor was calculated from MD simulations and is is reported to be very small for both materials, f < 0.2 [14]. Considering the common understanding of ion conduction in these materials, with the intracage and doublet-jump in the cage and the intercage jump connecting the cages, this makes sense: If the intercage jump is rate-limiting for macroscopic diffusion (aka presents a bottleneck), naturally the faster diffusion within the cage will be self-correlated. Therefore, a hypothetical HR is also reported assuming the correlation factor is 0.1 (table 4.7).

Table 4.7: Comparison of conductivities of Li$_6$PS$_5$Cl and Li$_6$PS$_5$Br obtained from AC-impedance measurements, NMR relaxometry using the modified BPP model as well as the 2BPP-type jump process model.

Conductivity [mS/cm] at 300K	Li$_6$PS$_5$Cl	Li$_6$PS$_5$Br
AC-impedance	4.73[16]	2.2[5]
MBPP	1.18	2.69
2BPP, $E_{A,2BPP,1}$	1.63	2.77
2BPP, $E_{A,2BPP,2}$	8.16	10.55
2BPP sum	9.79	16.15
f/HR		
MBPP	4.01	0.82
2BPP sum	0.48	0.13
HR if f = 0.1		
MBPP	0.025	0.12
2BPP sum	0.207	0.734

4.2.6 Conclusion

To summarize, the diffusion in the argyrodite Li$_6$PS$_5$X (X=Cl, Br) is not BPP-type, instead it can be fit by both the modified BPP model as well as a model consisting of two BPP-

type jump processes. The fits with the modified BPP-model are consistent with what is published in literature, but can not support the results from MD simulations.

The two BPP-type jump process model fits the data equally well as the modified BPP-models, though with more fitting parameters. An argument can be made for the additional fitting parameter, as the result agrees very well with the results from MD simulations for both Li_6PS_5Cl and Li_6PS_5Br and the posterior probability distributions of the parameter show only one viable solution with small errors in said area.

Notably, the errors obtained for the two-jump process model for Li_6PS_5Br are smaller than the ones obtained for Li_6PS_5Cl. This could have to do with the smaller energy difference between the two jumps of Li_6PS_5Br (0.2 and 0.144 eV) compared to Li_6PS_5Cl (0.25 and 0.157 eV), as the maxima are closer and somewhat more accessible in the temperature range measured.

The good agreement from the energies obtained from MD simulations and the two BPP-jump process model indicate that the model can provide additional, physically viable information about the diffusion in Li_6PS_5Cl compared to the modified BPP model. For future research, it would be interesting to repeat such measurements at higher ω_0 and/or lower temperatures, to see whether it is possible to resolve the maxima for the fast processes.

4.3 NMR relaxometry of $Li_3YCl_3Br_3$

The data of the argyrodite Li_6PS_5Cl does show a good fit using the modified BPP-model and may be fit using a two jump-process model. This is not the case for some halide solid electrolytes, which in some cases can not be fit using the modified BPP model when including data measured at multiple fields. For example, Li_3InCl_6 clearly showed two maxima in the measurements for ^7Li measured on the 300MHz spectrometer (see chapter 5). The halogen alloyed material $Li_3YCl_3Br_3$ shows an even more complex behaviour with at least three distinct jump processes. The process of fitting such a complex curve and evaluating the validity are the focus of this chapter.

4.3.1 Structure of $Li_3YCl_3Br_3$

The crystal structure of $Li_3YCl_3Br_3$ is monoclinic with space-group *C2/m* (12). The anionic framework is built by quasi ccp of the halogens, which distribute statistically. The diffraction pattern and structural solution of this material can be found in chapter 6. In such a framework, there is only one possible jump path along an oct-tet-oct path (see Figure 2.1), unless there is a significantly different activation energy along the unique crystallographic axis, as is found for Li_3InCl_6 (chapter 5).

Considering that the halogens are distributed statistically, there is a large variety of differently coordinated octahedral sites, tetrahedral sites and their combinations. These jumps may have different activation energies and pre-exponential factors. If this is the case, this should be observable using solid-state NMR.

4.3.2 Methods

The material was synthesized and characterized as described in chapter 6.

The relaxation rates at various temperatures were measured on a Bruker Avance 500 MHz spectrometer using a saturation recovery pulse sequence with 21 saturation trains and recycle delays covering three orders of magnitude in time, spaced logarithmically. The T$_1$ were extracted using ssnake [18]. Both the isotopes ^{6}Li and ^{7}Li were measured, at Larmor frequencies of 73.6 and 194.37 MHz respectively.

The T$_1$ as a function of temperature were fit using a custom-made program written in Python (packages matplotlib, lmfit, numpy). The solutions assumes that all jump processes in the material are BPP-type processes.

4.3.3 Results

The relaxation curves measured are displayed in figure 4.11. The ^{7}Li curve shows a clear maximum at ~350 K. Additionally, there are two points where it looks like the slope changes, at around ~470 K and at low-temperatures around ~260K. These changes in slope indicates the presence of other jump processes, the slope is positioned where the maxima would be. The curve measured for ^{6}Li looks quite different, there are two clear maxima at around 270K and 370K, where the maxima at 370 K looks somewhat noisy. As we clearly see three points in the measurement for ^{7}Li, we know that there is also a third one, just not clearly resolved in the data.

To fit these curves, first reasonable estimates need to be made for the parameters. Therefore, it makes sense to try and fit the outer most jump processes in parts, if they do not represent an overlay of different processes. This is done and visualized in red in Figure 4.11 (top). The middle jump process (bottom) quite obviously is an overlay and the values do not make sense, as the E$_a$ is lower compared to the process with the minima at lower temperature, with a similar τ_0. As we can not get an educated guess for the third process, it needs to be guessed. Once a initial parameter set is made, the guess can be plotted and visually inspected and changed if necessary. Then, the minimization needs to be set up using the following conditions:

- The K$_D$ need to be able to vary (here, even different starting values are suggested, due to the different interaction of ^{6}Li and ^{7}Li)

- The E$_a$ and τ_0 need to be the same for the different datasets

- The Larmor frequency needs to be different for the different datasets but fixed

Once this is setup, the minimization can be attempted. In the case here, the starting values had to be adjusted multiple times, until the minimizer managed to converge. The obtained result is shown in Figure 4.12 (top) and the fits are plotted individually for each ω_0 in the appendix Figure 8.4.

Though the fit in Figure 4.12 (top), the individual fits (Fig 8.4) show that the data measured at 194 MHz is clearly better fit compared to the data measured at 73.6 MHz. The reason for this behaviour is that the relaxation rates of ^{7}Li are higher compared to the relaxation rates of $_6$Li, and given the same relative error the residuals will affect the result less strongly.

Therefore, another minimization was performed by multiplying the residuals of the data measured at 73.6 MHz with a factor N=4 to equalize the difference (different values

Figure 4.11: Measurements of the relaxation rates of ^{6}Li (blue) and ^{7}Li (orange) for the ion conductor Li$_3$YCl$_3$Br$_3$. Parts of the curves (shown in red) were fit with the BPP-model to find guesses that can be used for the full minimization. This is only possible for the highest and lowest activation energy process (top), as the middle maxima has overlayed slopes on both the high and low-temperature side, rendering an unfeasible value (0.132 eV which is smaller than 0.152 eV for the process showing the maxima at lower temperature).

4
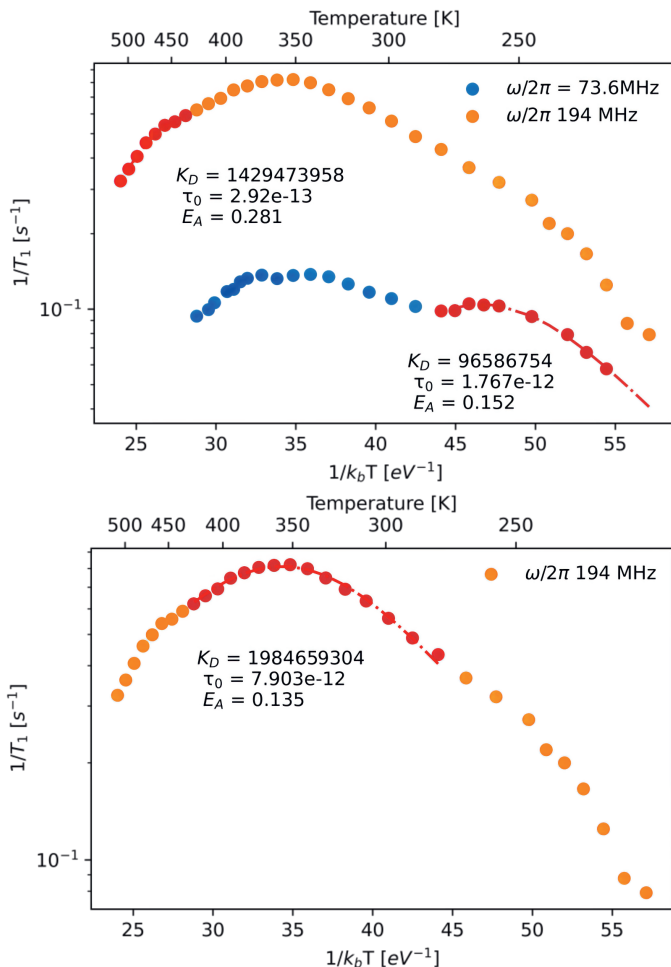
between 2 and 6 were tested and had no influence on the obtained fit). The resulting activation energies are very different (see Figure 4.12 (bottom)), indicating that there are two possible solutions to fit the data. This will from now be referred to as the solution from the weighed and unweighed solution.

Error Analysis

Due to the two possible solutions, the complexity of the model and the high number of parameter, the posterior probability distribution of the parameter were investigated for both solutions as described in section 4.1.8. The results are visualized as a corner plot in

the appendix figure 8.6 -8.7.

For both solutions, the posterior probability distributions show one histogram for each parameter, indicating that the solutions are both in a local minima. The unweighed solution has a lower Bayesian information criteria (BIC) (see Figure 4.12) and somewhat smaller errors (see Appendix table 8.4- 8.5), but the shape qualitatively does not fit as well for the measurements of ^{6}Li. From this data, it is difficult to proof that one solution should be better than the other one.

Figure 4.12: Relaxation rates $1/T_1$ of ^{6}Li and ^{7}Li of Li₃YCl₃Br₃ fit using a model containing of three independent BPP-type jump processes, once without weighing the residuals (top) and once by weighing the data measured at 73.6MHz by a factor N=4 (bottom). The E_a [eV] of the individual processes are indicated in the plot. BIC stands for Bayesian information criterion, models with lower BIC are usually preferred.
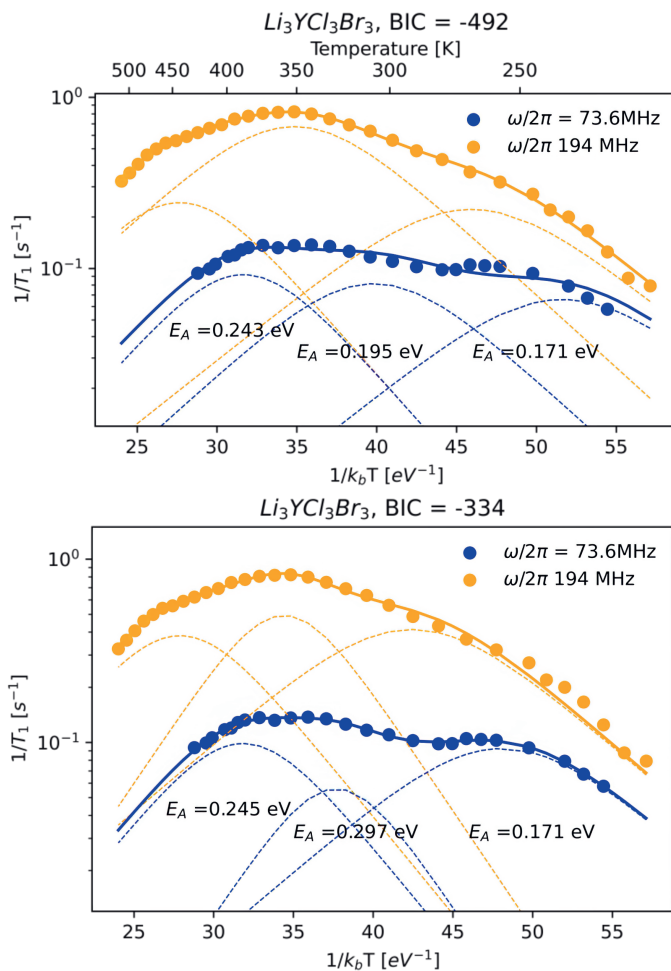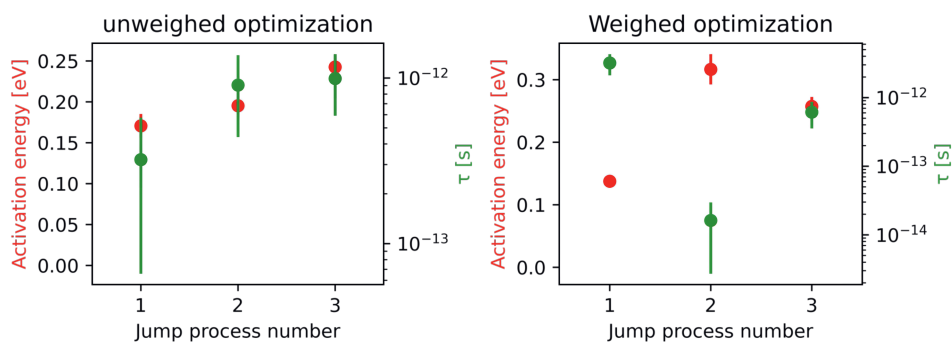
Figure 4.13: E_a and τ_0 as obtained from the two jump models of the weighed and unweighed optimization

4

As to be expected from the results of the BPP-model, the scatter plots (appendix figure 8.6 -8.7) show that τ_0 and E_a are correlated. This is also reflected in the posterior probability distributions. While the posterior probability distribution of E_a occupies a rather narrow region and is symmetric, τ_0 shows the broadest distributions (and hence has the largest standard error, between 24.1% and 67.9 %). The distribution of τ_0 is also slightly skewed (also showing in the somewhat larger difference between the Median and MLE (Appendix table 8.4) compared to the other parameters, which have a more symmetric distribution). This is due to the exponential relationship describing the correlation time, where τ_0 is proportional to the natural logarithm of E_a.

Errors for the activation energies are ~4-8% and errors for K_D are between 4.2% and 26.2%.

To reduce the error and better be able to differentiate between the two solutions, it could be useful to measure the relaxation rates at more Larmor frequencies (either at different magnetic field or using spin-lattice relaxation measurements in the rotating frame), or to increase the temperature range (if possible with the available probe). If that is not possible, additional information would need to be gained as for example from MD simulations.

Diffusivity

The values obtained for τ_0 for both the weighed and unweighed solutions are visualized in Figure 4.13. Using these values, we can calculate τ_c (Equation 4.6), and the results for τ_c can be used to calculate the diffusivity (equation 4.9) and conductivity (equation 2.19).

To calculate the diffusivity, a jump-distance needs to be chosen. Given the quasi-ccp arrangement of the halogens, only oct-tet-oct paths are possible and the jump-distance is therefore assumed to be an oct-tet distance of 2.443 Å(calculated from the structure solution of chapter 6). The same structure solution was also used to estimate a charge carrier concentration (the number of lithium atoms per unit cell divided by the unit cell volume).

The ionic conductivities (with upper and lower limits calculated assuming that τ_0 and E_a are within one standard error) calculated from the values of the fit at 300K are reported

in the annex, table 8.6.

The unweighed solution results in ionic conductivities of 31.4 (9.98 - 269) mS/cm, 4.3 (1.62 - 15.5) mS/cm and 0.628 (0.244-1.92) mS/cm for the three jumps.

The weighed solution results in ionic conductivities of 17.3 (9.41 - 37.1) mS/cm, 2.56 (0.71 - 18.96) mS/cm and 0.647 (0.279-1.77) mS/cm for the three jumps.

The ionic conductivity as measured from AC-impedance measurements at 30 degrees is $\approx$ 3.5 mS/cm (see results chapter 6). Measuring at more larmor frequencies should help to distinguish between the models, improve the reliability of the fit in general and should reduce the errors (at least if the temperatures of the probes are all equally calibrated).

4.4 Summary and conclusions

In the first section of this chapter, it is described how Redfield theory relates the relaxation rates to the spectral density. Using the BPP-spectral density as an example, it is explained how spectral density fitting of the measured relaxation rates can give access to the correlation times τ_c. These can be used to calculate diffusivity using the Einstein-Smoluchowski relation. Finally, the conductivity can be calculated from the diffusivity using the Nernst-Einstein relation.

Then, the equations of the BPP-spectral density and the modified BPP-spectral density are studied in detail, to learn how measurements are expected to look like if they behave according to these spectral densities and what information can be extracted from different temperature regions of the measurements. The superposition principle is applied for multiple uncorrelated (BPP-type) motional processes and the relaxation rates expected for such a system are simulated. The reverse problem of fitting such measurements with this spectral density is discussed.

Finally, experimental considerations are discussed such as the accessible temperature and frequency range and the measurement errors are addressed. The method used for error estimation in pythons lmfit package (used for the analysis in this thesis) is discussed.

Spectral density fitting is complex and much care needs to be taken during the measurements as well as the analysis of the measurements. Visual analysis of the obtained curve is necessary to chose a suitable spectral density. Therefore, it helps to understand the different spectral densities and how they behave in different temperature limit and when measured at multiple frequencies.

In the second section, the theory laid out in the first section is applied to the ion-conductor Li_6PS_5Cl, which is commonly fit using the modified BPP-model. The results from these, however, is not in accordance with the results from MD simulations, which show other jump processes at lower frequency. The relaxation rates can also be fit with a spectral density consisting of two superimposed BPP-type jump processes, which agree well with the results from MD simulations. This is also shown for isostructural Li_6PS_5Br. The fact that Li_6PS_5I in literature [9] can resolve more motional processes with modified BPP models with values for β close to 2 (BPP-type), is another indicator that multiple BPP-processes could be appropriate. Also the conductivities and HR calculated from the model are more realistic compared to the modified BPP-model. Doing more measurements, for example at higher magnetic field B_0 and lower temperatures, could give access to this in-

formation making the second jump process observable.

In the third section, a three BPP-type jump model is used to fit the relaxation rates measured for $Li_3YCl_3Br_3$. Two possible solutions are found with different parameters for the jumps, showcasing the difficulty of spectral density fitting with such complex models. MCMC error analysis was performed for both solutions, but did not give a clear indication which solution is better. The conductivities calculated using the estimates of the correlation times are around what is found from AC-impedance for both models, hence both are physically plausible.

References

[1] J. H. Van Vleck. The Dipolar Broadening of Magnetic Resonance Lines in Crystals. *Physical Review*, 74(9):1168–1183, November 1948.

[2] Peter A Beckmann. Spectral densities and nuclear spin relaxation in solids. *Physics Reports*, 171(3):85–128, December 1988.

[3] N. Bloembergen, E. M. Purcell, and R. V. Pound. Relaxation Effects in Nuclear Magnetic Resonance Absorption. *Physical Review*, 73(7):679–712, April 1948.

[4] A. Kuhn, M. Kunze, P. Sreeraj, H.-D. Wiemhöfer, V. Thangadurai, M. Wilkening, and P. Heitjans. NMR relaxometry as a versatile tool to study Li ion dynamics in potential battery materials. *Solid State Nuclear Magnetic Resonance*, 42:2–8, April 2012.

[5] I. Hanghofer, M. Brinek, S. L. Eisbacher, B. Bitschnau, M. Volck, V. Hennige, I. Hanzu, D. Rettenwander, and H. M. R. Wilkening. Substitutional disorder: structure and ion dynamics of the argyrodites Li_6PS_5Cl, Li_6PS_5Br and Li_6PS_5I. *Physical Chemistry Chemical Physics*, 21(16):8489–8507, 2019.

[6] P Heitjans and J Kärger. *Diffusion in condensed Matter*. Springer, 2005.

[7] Peter M Richards. Effect of low dimensionality on prefactor anomalies in superionic conductors. *Solid State Communications*, 25(12):1019–1021, 1978.

[8] W Küchler, P Heitjans, A Payer, and R Schöllhorn. 7li nmr relaxation by diffusion in hexagonal and cubic lixtis2. *Solid State Ionics*, 70:434–438, 1994.

[9] Katharina Hogrefe, Isabel Hanghofer, and H. Martin R. Wilkening. With a Little Help from [31] P NMR: The Complete Picture on Localized and Long-Range Li^+ Diffusion in Li_6PS_5I. *The Journal of Physical Chemistry C*, 125(41):22457–22463, October 2021.

[10] J.C. Lindon, G.E. Tranter, and D. Koppenaal. *Encyclopedia of Spectroscopy and Spectrometry*. Elsevier Science, 2016.

[11] Matthew Newville, Till Stensitzki, Daniel B. Allen, and Antonino Ingargiola. LMFIT: Non-Linear Least-Square Minimization and Curve-Fitting for Python. September 2014.

[12] Daniel Foreman-Mackey. corner.py: Scatterplot matrices in python. *The Journal of Open Source Software*, 1(2):24, jun 2016.

[13] Hans-Jörg Deiseroth, Shiao-Tong Kong, Hellmut Eckert, Julia Vannahme, Christof Reiner, Torsten Zaiß, and Marc Schlosser. Li6ps5x: a class of crystalline li-rich solids with an unusually high li+ mobility. *Angewandte Chemie International Edition*, 47(4):755–758, 2008.

[14] Niek J. J. de Klerk, Irek Rosłoń, and Marnix Wagemaker. Diffusion Mechanism of Li Argyrodite Solid Electrolytes for Li-Ion Batteries and Prediction of Optimized Halogen Doping: The Effect of Li Vacancies, Halogens, and Halogen Disorder. *Chemistry of Materials*, 28(21):7955–7963, November 2016.

[15] Swapna Ganapathy, Chuang Yu, Ernst R. H. van Eck, and Marnix Wagemaker. Peeking across Grain Boundaries in a Solid-State Ionic Conductor. *ACS Energy Letters*, 4(5):1092–1097, May 2019.

[16] Chuang Yu, Swapna Ganapathy, Jart Hageman, Lambert van Eijck, Ernst R. H. van Eck, Long Zhang, Tammo Schwietert, Shibabrata Basak, Erik M. Kelder, and Marnix Wagemaker. Facile Synthesis toward the Optimal Structure-Conductivity Characteristics of the Argyrodite Li $_6$ PS $_5$ Cl Solid-State Electrolyte. *ACS Applied Materials & Interfaces*, 10(39):33296–33306, October 2018.

[17] Isabel Hanghofer, Bernhard Gadermaier, and H Martin R Wilkening. Fast rotational dynamics in argyrodite-type li6ps5x (x: Cl, br, i) as seen by 31p nuclear magnetic relaxation—on cation–anion coupled transport in thiophosphates. *Chemistry of Materials*, 31(12):4591–4597, 2019.

[18] S.G.J. van Meerten, W.M.J. Franssen, and A.P.M. Kentgens. ssNake: A cross-platform open-source NMR data processing and fitting application. *Journal of Magnetic Resonance*, 301:56–66, April 2019.

4

5

Re-investigating the structure-property relationship of the solid electrolyte $Li_{3-x}In_{1-x}Zr_xCl_6$ and the impact of In-Zr(IV) substitution

Adapted version of the paper published in **RSC Journal of Mat. Chem. A**

Authors: *Eveline van der Maas* Theodosios Famprikis, Saskia Pieters, Jonas P. Dijkstra, Zhaolong Li, Steven R. Parnell, Ron Smith, Ernst R.H. van Eck*, Swapna Ganapathy*, Marnix Wagemaker*.

*Corresponding authors
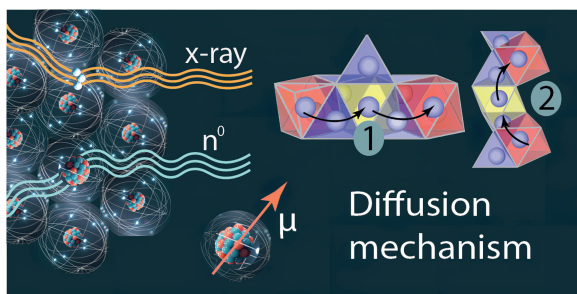
5.1 Abstract

Chloride based solid electrolytes are considered interesting candidates for catholytes in all solid state batteries due to their high electrochemical stability, which allows the use of high voltage cathodes without protective coatings. Aliovalent Zr(IV) substitution is a widely applicable strategy to increase the ionic conductivity of Li$_3$M(III)Cl$_6$ solid electrolytes. In this study, we investigate how Zr(IV) substitution affects the structure and ion conduction in Li$_{3-x}$In$_{1-x}$Zr$_x$Cl$_6$ (0 ≤ x ≤ 0.5).

Rietveld refinement using both X-ray and neutron diffraction is used to make a structural model based on two sets of scattering contrasts. AC-impedance measurements and solid-state NMR relaxometry measurements at multiple Larmor frequencies are used to study the Li-ion dynamics. In this manner the diffusion mechanism and its correlation with the structure are explored and compared to previous studies, advancing the understanding of these complex and difficult to characterize materials.

It is found that the diffusion in Li$_3$InCl$_6$ is most likely anisotropic considering the crystal structure and two distinct jump processes found by solid-state NMR. Zr-substitution improves ionic conductivity by tuning the charge carrier concentration, accompanied by small changes in the crystal structure which affect ion-transport even on short timescales, likely reducing the anisotropy.

5.2 Introduction

Replacing the flammable, liquid electrolyte with ion-conducting solids can lead to advances in the safety of high energy density batteries[1]. Many solid electrolyte materials with room temperature ionic conductivity of mS/cm have been developed in recent years. These include the families of the oxides (e.g. garnets [2]), phosphates (e.g. NaSICON [3]), sulfides (e.g. argyrodites Li$_6$PS$_5$X (X=Cl, Br, I) [4], Li$_{10}$GeP$_2$S$_{12}$-type [5]) or hydrides (e.g. borohydrides/closoboranes [6]).

For solid-electrolytes to become a safer and feasible alternative, all-solid-state batteries need to be able to compete with liquid electrolyte based batteries both in terms of energy density and charging rates. Therefore, the amount of solid electrolyte has to be minimized both in the separator as well as in the cathode composite, without compromising on the internal resistance and electrode loading. This necessitates a solid electrolyte with a high ionic conductivity. The Li-ion conducting solid electrolytes with the highest conductivity so far are sulfide based, that can reach 10^{-2} S/cm [4, 5].

Halide solid electrolytes with composition Li$_3$M(III)X$_6$ (M(III) = Lanthanides, Sc, In, X = Cl, Br, I) have been receiving renewed interest from the scientific community since 2018, after Asano et al. published that Li$_3$YCl$_6$ and Li$_3$YBr$_6$ could reach the 10^{-3} S/cm ionic conductivity and showcased good performance in batteries using standard electrodes [7].

Improved fundamental understanding of the conduction mechanism in Li$_3$M(III)Cl$_6$ halide solid electrolytes may help formulate design guidelines to attain comparable ionic conductivities.

n interesting factor to understand, especially for solid-electrolytes used in cathode composites, is anisotropy of the diffusion or in its extreme case reduced dimensionality, which may arise for certain crystal structures. While one-dimensional diffusion is typically not favourable for long-range ion conduction, two-dimensional conductors need

favourable microstructure for good percolation [8].

Examples for anisotropy/reduced dimensionality in layered (Li-)ion conducting materials are manifold, as for example graphite [9], LiCoO2 [10], LiFePO4 [11], TiO2-β [12], Li in hexagonal TiS2 [13], hectorite-type silicate [14] and β-alumina [15].

Considering that crystallites of solid electrolytes like the monoclinic Li_3InCl_6, which has a layered atomic arrangement, may grow into platelets and may have anisotropic properties, this could very well impact the efficacy of ionic transport in composites, especially in combination with layered oxide cathodes.

Compared to most other relevant solid electrolyte families, chlorides have a higher oxidative stability and are compatible with 4V cathodes [16–18].

This is an important property, as otherwise electronically insulating coatings have to be utilized to protect the electrolyte from the high potential of the cathode. In this context, it was recently demonstrated that a spinel $Li_2In_xSc2/3_{-x}Cl_4$ (0≤x≤0.666) solid electrolyte, in combination with an uncoated $LiNi_{0.85}Co_{0.1}Mn_{0.05}O_2$, cathode achieved more than 3000 cycles with 80% capacity retention (cycled between 2.8–4.3V vs Li/Li+)17, which represents a milestone in the development of all-solid state batteries. The compatibility of In-, Sc-, Zr- and Y-containing chloride solid electrolytes with high-voltage cathodes and the corresponding evolution of the all solid-state battery impedance have been thoroughly investigated by Kochetkov et al [19].

A commonly employed strategy to increase the ionic conductivity of a material is through aliovalent substitution. In aliovalent substitution an atom is replaced with another of different charge, which is compensated by a change in charge carrier concentration. In most Li-ion conducting materials, an optimum Li+/VLi¬ charge carrier concentration exists: At higher Li+ concentrations, more Li+ is available in the electrolyte to transport the charge. At too high Li+ concentrations, the probability of a Li+ to have access to a neighbouring vacancy is reduced, which can become the rate-limiting factor and reduce ionic conductivity. For the chloride $Li_3M(III)Cl_6$, this was successfully achieved by Zr(IV) substitution for M(III) = Y (ref. [20]), Er (ref.[20, 21]), Yb (ref. [22–24]), In (ref. [25–27]) and Sc (ref. [27]). The Zr(IV) replaces the M(III), and the excess charge is compensated by a lithium vacancy. In all structures, the ionic conductivity measured by impedance spectroscopy has been shown to increase up to a certain substituent concentration [20–27].

When the $Li_3M(III)Cl_6$ materials were first investigated, a trend between the M(III) Shannon radius and the crystal structure was found. Larger M(III) would crystallize in trigonal $P\bar{3}m1$ (M(III) = Y, Tb-Tm) [28], intermediate size in orthorhombic $Pnma$ (Yb, Lu)[28] and even smaller (M(III) = In, Sc) in monoclinic $C2/m$ [29]. This still holds under the same synthetic conditions, but different synthesis has shown to be able to disturb this trend [30–32].

For the materials with M(III) = Y (ref.[20]), Er (ref[20]), Yb (ref.[22]), a trigonal $P\bar{3}m1$ to orthorhombic $Pnma$ phase transition has been observed upon Zr-substitution. This is rationalized by the reduction of the average transition metal radius [20] by introducing the smaller Zr(IV)-ion (the Shannon radius of Zr is 0.72 Å in 6-fold coordination, compared to Y(0.90 Å), Er (0.89 Å) and Yb (0.87 Å))[33]. The $Pnma$ phase can also be synthesized without Zr-substitution, by synthesizing the material by co-melting of the reagents with small LiCl deficiency [30].

For $Li_3M(III)Cl_6$ with smaller M(III), such as In (0.80 Å) investigated in this report and Sc

(0.75 Å), the structure crystallizes in monoclinic $C2/m$ [25, 27]. The end member Li$_2$ZrCl$_6$ can also crystallize in monoclinic $C2/m$ [34] (isostructural to Li$_3$InCl$_6$) when synthesized with conventional ampoule synthesis (full solid solution range exists), as well as in trigonal $P\bar{3}m1$ when synthesized mechanochemically [32].

Figure 5.1: Simplified crystal structure of Li$_3$InCl$_6$. The structure can be considered as a double LiCl unit cell with a small monoclinic distortion and Li replaced by In(III) and vacancies (the cubic cell is illustrated by the black cube). Most cations are on octahedrally coordinated sites within the Cl cubic close packing arranged in a layered fashion in alternating Li- and In/Li layers.
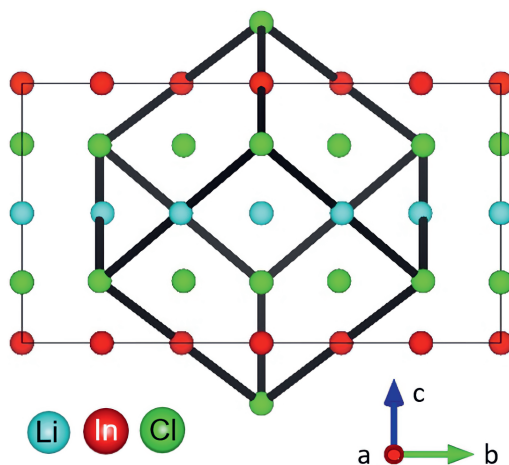
In both cases, substitution with M(III)= In (ref [27, 31], trigonal structure can exist below 40% In) and Fe (trigonal structure only, ref [34], solubility up to 25%) were shown to improve ionic conductivity, though to a lesser extent than the In-rich compositions. Mixtures between the larger and smaller M(III) can be synthesized, and the resulting crystal structure also seems to depend on the average M(III) radius, as also observed for Zr-doping and demonstrated by the Li-Y-In-Cl solid electrolytes investigated by Li et al [35].

The monoclinic structure of the Li$_3$InCl$_6$ consists of a doubled LiCl unit cell with a small monoclinic distortion and part of the Li+ replaced by In3+ in a layered arrangement (see Figure 5.1). In this structure, Zr(IV) substitution does not lead to a phase transition [25]. While the monoclinic structure type is less common in chlorides, similar structures are found for bromide and iodide analogues [36–38].

Upon Zr- substitution, the changes in lattice parameter are small [25] and the anionic framework remains quasi cubic close packed. It is therefore unlikely that the increase in ionic conductivity arises from a change in the size of the bottleneck or interaction of the Li-ions with the anionic lattice. This raises the question: To what extent is the increase in ionic conductivity on Zr(IV) substitution due to the change in charge carrier concentrations, changes in the crystal structure and/or changes in the diffusion pathway(s)?

In a recent study [25], this question was investigated using a structural model obtained from Rietveld refinement based on neutron diffraction data alone, bond valence calculations, AC-impedance measurements as well as solid-state NMR measurements. It was

concluded that the occupancy of the secondary In-site, which breaks the layered arrangement of the Li-atoms in the ab-plane, promotes ion conduction also along the c-direction. While the bond valence calculations show similar activation energies for all possible jump pathways, the solid-state NMR measurements for Li_3InCl_6 indicate two motional modes, rendering the picture unclear.

In ref. [27], a similar study was performed for the same substitution series. In this case, bond valence calculations, also based on structural models obtained from neutron diffraction alone, show some difference in the activation energies for both diffusion pathways (0.483 eV and 0.456 eV for paths along the ab-plane, and 0.509 eV along the c-direction). Therefore, it was suggested that though 3D diffusion is possible, the diffusion is likely faster in the ab-plane and therefore anisotropic, however no experimental data on short-range ion transport was presented.

Finally, in ref. [39], the $Li_{3-x}In_{1-x}Zr_xCl_6$ substitution series is investigated by ab initio molecular dynamics simulations. An increase in conductivity from 1.2 to 22 mS/cm has been found for a Zr concentration of 25%. These simulations reproduce published experimental trends25 as well as the trends found in the present work, albeit with a larger magnitude and high error bar for the tracer diffusion coefficient, probably because of the challenge of simulating such disordered materials (i.e. featuring partially occupied and/or shared atomic positions) with the number of atoms that are usually simulated by ab initio methods.

In this contribution, we re-investigate the structure-property relationship of the Li_3InCl_6 solid electrolyte and the impact on it of Zr(IV) substitution, exclusively using experimental techniques. To do so, the series $Li_{3-x}In_{1-x}Zr_xCl_6$ (x=[0, 0.5], steps of 0.1) was synthesized. Combined Rietveld refinement of x-ray and neutron powder diffraction data was employed for the structural characterization. The long range ionic conductivity was measured using AC-impedance spectroscopy. Information about the ionic conductivity at short timescales were obtained from solid-state NMR spin lattice relaxometry measurements. The measurements were performed at multiple Larmor frequencies, to be able to better distinguish model suitability and to resolve different motional modes. Finally, the static NMR-lineshape at high temperature was analysed, providing information on the ionic motion at longer timescales [40].

Owing to the combined x-ray and neutron diffraction data refinement, we can report accurate atomic occupancies which reveals clear trends upon Zr substitution. The solid-state NMR measurements at multiple fields allow us to resolve and fit the two motional modes in Li_3InCl_6 mentioned by ref. [25] which we demonstrate to be distinct in their activation energy. The second mode is not apparent for the doped materials, and the two modes may have approached each other as indicated in ref. [25], which correlates with the reduction of the In-occupancy in the c-direction. For the doped materials $Li_{3-x}In_{1-x}Zr_xCl_6$ with x=0.3 and x=0.5, we show that unambiguous fitting of spectral densities is a very complex problem, emphasizing that results need to be interpreted with care. We find residual chemical shift anisotropy, represented by asymmetric satellites, in the static line shapes at high temperatures. This means that the motion does not fully average out the chemical shift across all sites, indicating that there are differences in the jump-rates across different sites also in the timescale of T2, ¬which considering the crystal structure we interpret as anisotropic ion conduction.

5.3 Results

Crystal structure

Figure 5.2: Simultaneous Rietveld fit to the (a) x-ray diffraction data and (b) neutron diffraction data of $Li_{2.7}In_{0.7}Zr_{0.3}Cl_6$ in the C2/m space group. (c) The structure of Li_3InCl_6 (top) and $Li_{2.7}In_{0.7}Zr_{0.3}Cl_6$ (bottom). The anionic lattice is formed by cubic close packing of the chlorine atoms in Cl1 (8j) and Cl2 (4i). Li4 (4g) co-occupies the In2 (4g) site. The tetrahedral Li3 (8j) site could not be observed for dopant concentrations larger than x =0.3 in $Li_{3-x}In_{1-x}Zr_xCl_6$. Upon substitution, Zr preferentially occupies the In1(2b) site and the In2(4g) occupancy is reduced. (d) Effective scattering length density map of the neutron diffraction data of Li_3InCl_6 . Negative scattering length density is plotted in turquoise, positive scattering length density in yellow. The tetrahedral Li3 (8j) site is circled in black. For refinements of the other datasets, see Appendix Figures 8.9-8.13.
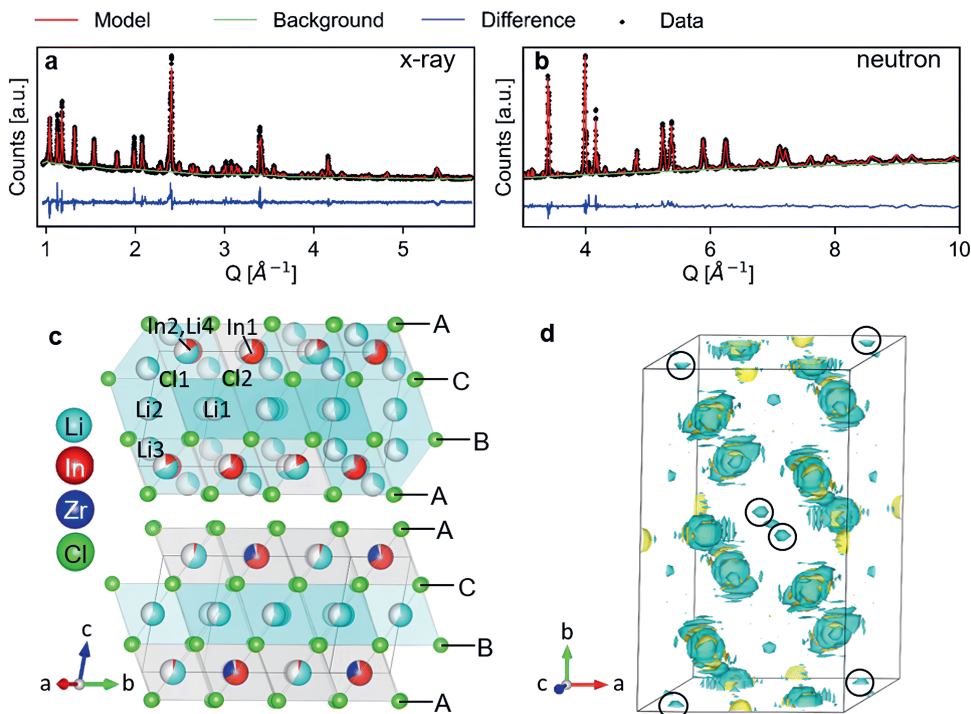
The long-range structure of the samples was characterized by simultaneous Rietveld refinement of x-ray (Figure 5.2a) and neutron (Figure 5.2b) powder diffraction data (also see Appendix Figures 8.9-8.13)). The materials crystallized in the monoclinic space group $C2/m$ (12), consistent with previous work [25, 28].

The structure is based on cubic close packing of Cl anions. The cations occupy mostly octahedral sites and are arranged in layers (Figure 5.2c). One layer is occupied by Li (between B and C), followed by a mixed cation Li/In/Zr layer (between layers A and C, A and B). The lattice parameter a showed a small increase (6.404-6.416 Å) with increasing Zr-dopant concentration, while c decreased (6.380-6.357 Å), which is consistent with literature25 (Appendix Figure 8.8)). The increase of the a-parameter could be related to the lower Li-content in the layer, leading to larger Coulombic repulsion between the Cl atoms.

The decrease in the c-parameter can be rationalized by the smaller size and higher charge of Zr compared to In, leading to a decrease in the interlayer distance. The angle beta showed only a slight increase (109.776 – 109.961°) while the lattice volume showed a maximum at x=0.2, but with small absolute changes (within 1.5 Å3) (Appendix Figure 8.8). For compositions with x=0 and 0.2 we find the occupation of a tetrahedral site in the mixed cation layer (Li3 in Figure 5.2c top image, in the M- layer). The occupancy of this site can be visualized from the effective neutron scattering-length-density map shown in Figure 5.2d. An effective scattering length density map is the Fourier transform of the diffracted signal, combining the intensity information from the measurement and the phase information from the model. This is the neutron-equivalent of the electron density maps from x-ray diffraction data. Our measurements further show that the tetrahedral site disappears at higher dopant concentrations ($x \leq 0.3$).

Figure 5.3: (a) Trends of the site occupancies as a function of the composition. (b) Effective scattering length density maps calculated from the neutron diffraction data (top; negative density in blue and positive density in yellow) and electron density maps calculated from the x-ray diffraction data (bottom; positive density in yellow). The unit cell was cut in half along the mirror plane, as visible in the atomic arrangement in the middle. The black circles are around the In2 / Li4 (4g) site, illustrating that the opposite scattering length of the Li and the In cancel out the neutron signal for Li_3InCl_6 on that site.
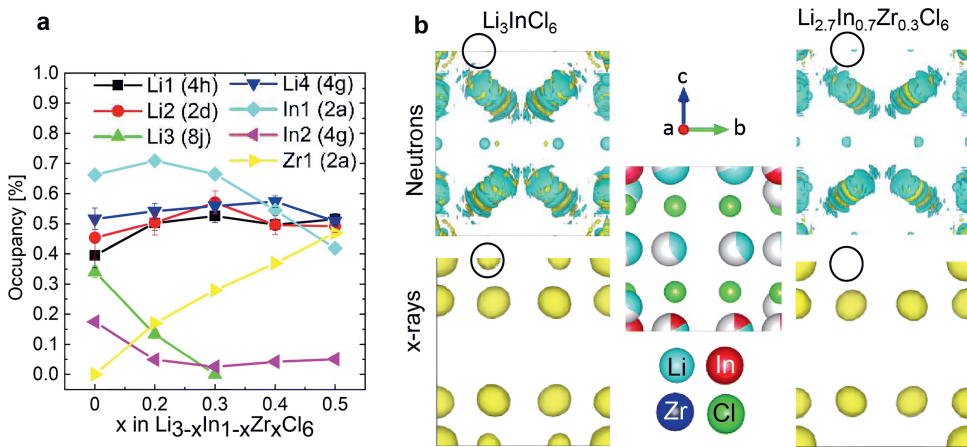
The Rietveld refinement based on the neutron diffraction data alone was not stable, despite the good contrast between the elements. This difficulty is partly due to the opposite sign of the coherent scattering length of Li and In, as can be seen from the effective scattering length density maps (Figure 5.3b). Li has a negative scattering length (bL_i = -1.9 fm) about half the magnitude of that of In (bI_n = 4.065 fm) [41].

A negative scattering length means that the scattered neutrons are 180°out of phase, and hence the waves scattered from Li and In on the same site will interfere destructively, resulting in an effective scattering length of the site, which is weighed by the site occupancy. If the ratio of the occupancies of Li:In is $-bIn;bLi$ (approximately 2:1), the effective scattering length approaches zero and thus the site will result in no scattered intensity. The site also does not have to be fully occupied, leaving the refinement under-defined.

It is therefore crucial to use an additional contrast (x-ray diffraction data) to accurately determine the crystal structure. X-ray diffraction is sensitive to the occupancy of In and Zr (due to the number of electrons), which can also be distinguished using neutrons due to the larger scattering length of Zr compared to In (7.16 compared to 4.065 fm), and the neutron diffraction data also adds information about the lithium occupancies thanks to the negative scattering length. This synergy is illustrated in the effective scattering length density map of Figure 5.3b. Looking at the (electron) density calculated from the x-ray diffraction data, we can clearly see density on the In2(4g) site for Li_3InCl_6. For the doped material $Li_{2.7}In_{0.7}Zr_{0.3}Cl_6$, no electron density is observed on the same site (at the same isosurface level). In the effective neutron scattering length density map from the corresponding materials, there is no effective density in Li_3InCl_6 and some negative effective scattering length density is observed for $Li_{2.7}In_{0.7}Zr_{0.3}Cl_6$. Using both contrasts in a simultaneous refinement, the occupancies of the sites converge, the results of which are shown in Figure 5.3a. The site occupancies show three clear trends:

1. The Zr only occupies the In1 (2b) site, and hence the Zr-occupancy of the site increases linearly as the total In-occupancy drops.

2. Already at small dopant concentrations, the In occupancy on the In2 (4g) site decreases and then stays low around 5%. The non-zero occupancy is clearly visible from the x-ray diffraction data of Li_3InCl_6, and was also observed previously from single crystal x-ray diffraction[41].

3. For the lithium sites, we observe an approximately linear decrease of the tetrahedral Li3 (8j) site occupancy, as x increases. This indicates that the tetrahedral site is a higher energy site as it is abandoned upon lowering the overall Li concentration, which is consistent with the fact that many related halide structures that occur in nature only feature Li with octahedral coordination, as for example all LiX (X = Cl, Br, I) binary halide salts.

The structure solution found here differs from other solutions published in literature.

- In line with previous studies [25, 27] the present work indicates Li occupancy of a tetrahedral site, based on neutron diffraction data, however at different location

- In previous studies [25, 27], the Zr is reported to occupy both In sites, whereas in the present study it is only found on the In1 site.

- The In-occupancy of the In2-Li4 site in the present work is higher for Li_3InCl_6 and reduces upon the introduction of Zr, a trend that is not reported in previous studies [25, 27].

- The present results indicate that the occupancy of the tetrahedral Li-site disappears at 30% Zr content already, which only occurs at a Zr-content of 80% in [27] and is not reported in ref. [25].

The discrepancies with models in literature can in principle arise from differences in synthesis and therewith actual differences in structural details (as for example reported in ref [42] for trigonal Li_3YCl_6). In refs. [25, 27] the materials are synthesized by ball-milling

and a low-temperature annealing step at 260℃. In this contribution, the materials were synthesized by an ampoule synthesis, with a short ball-milling step to get a fine powder, and another, shorter thermal step to obtain a more crystalline material for diffraction (after the ball milling, the ionic conductivity of the powder was much lower and the Bragg-peaks broader). The use of both neutron as well as x-ray diffraction data can be another reason for the differences in atomic occupancies, considering the correlations when refining with neutron diffraction data, especially for the In2-Li4 occupancies.

Figure 5.4: Ionic conductivities and activation energies extracted from the Arrhenius relationship obtained from AC-impedance spectroscopy measurements. For individual AC-impedance spectra fits, parameters and errors, see the report in the supplementary files. For the validity of the equivalent circuit models used, see the Kramers-Kronig relationship in Appendix Figure 8.14. For the full Arrhenius diagrams, see Appendix Figure 8.15. Errors of the ionic conductivity are estimated from Gaussian error propagation as suggested by Krasnikova et al. [43] given in the Appendix Table 8.7. Errors in the activation energy errors are determined from the linear fit and given in the Appendix Table 8.8.
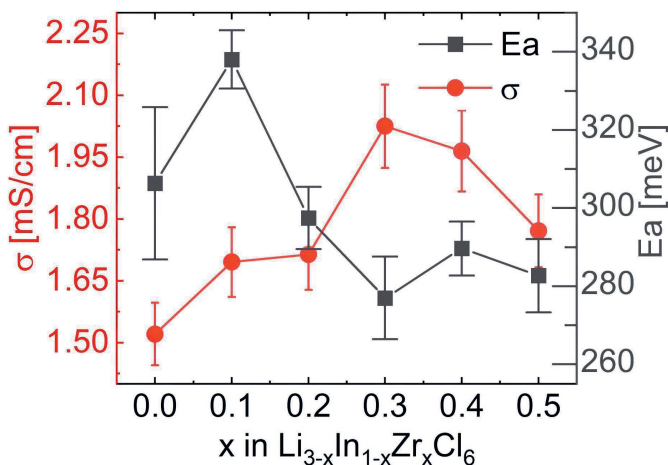
To measure the ionic conductivity with AC-impedance spectroscopy, the as-synthesized powders were cold-pressed into pellets. The ionic conductivity showed a maximum at x = 0.3 at 2.02 mS/cm, an increase by a factor ~1.6 compared to Li_3InCl_6 (1.52 mS/cm) (Figure 5.4; See Appendix Figure 8.14 for the confirmation of validity of the equivalent circuits using the Kramers-Kronig relationship; See Appendix Table 8.7 for error calculations).

The maximum in ionic conductivity also corresponds with the lowest activation energy of 280 meV, though the differences in activation energy between the different compositions is small and not significant in most cases. These values correspond remarkably well with values reported in ref. [27], who found 1.5 mS/cm for undoped Li_3InCl_6 and a maximum value of 2.1 mS/cm also at 30% Zr content. The conductivities found in ref. [25] are lower, with a maximum of 1.2 mS/cm found at 40% Zr content.

To obtain information about the dynamics at shorter timescales, we have conducted a series of solid-state NMR measurements. Spin lattice relaxation measurements as a function of temperature can give information on timescales of the inverse of the Larmor fre-

Figure 5.5: Relaxation rates of Li in Li_3InCl_6 measured at three different Larmor frequencies. 116MHz corresponds to 7Li measured on a 300MHz, 155MHz to 7Li on a 400MHz and 44MHz to 6Li on a 300 MHz spectrometer. The fit of the relaxation rate (solid line) represents a model with two BPP-type jump processes, the Bayesian information criteria of this fit is -476.3 (compared to -300 for other spectral densities, see Appendix Figure 8.17). The contribution of the individual jump processes to the relaxation rate are shown in red and black (same processes in all plots, the sum of the two individual rates is the full rate) and illustrate which process the individual datasets are sensitive to. For the figure with logarithmic axis, see Appendix Figure 8.16.
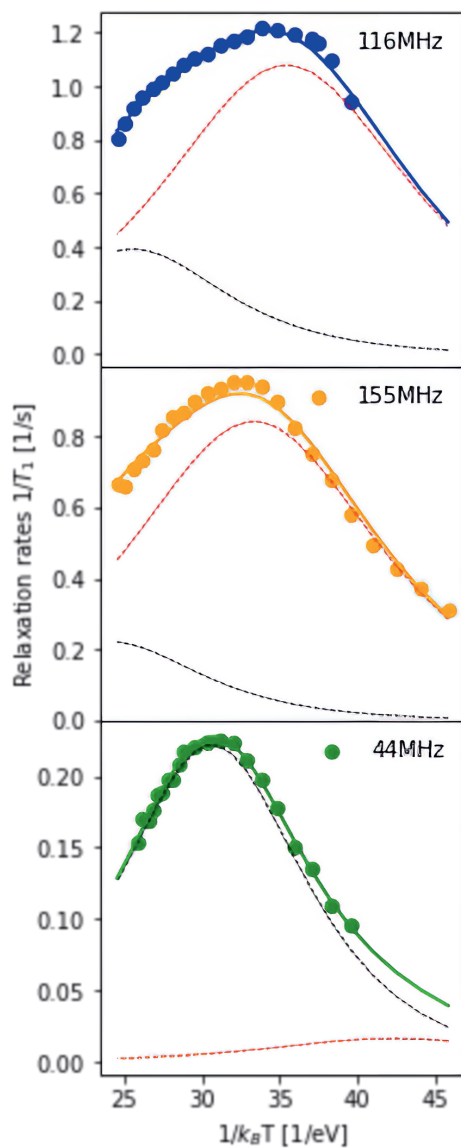
quency (τ_0), which is in the order of 10^{-8} seconds for the presently applied fields. Such frequencies allow to probe diffusion on the scale of less than one jump event to multiple jumps, hence including local back and forth hopping. This allows the separation of jump processes that differ significantly in frequency, the extraction of activation energies of jump processes (compared to activation energies of diffusion across a fabricated pellet, as in impedance), as well as providing insights into correlated diffusion. This is due to the fact that the temperature dependence of NMR relaxation rates depends on the Fourier transform of the correlation function of the diffusing atom usually referred to as the spectral density (see chpater 4).

A variety of spectral density functions can be found in literature[44], developed to represent different diffusion mechanisms. In this work, four spectral densities were considered and compared:

1. For uncorrelated three dimensional motion, the Bloembergen, Purcell and Pound (BPP) spectral density function (BPP model) was developed [45] in 1948. For BPP-type behaviour, the relaxation rates as a function of inverse temperature should show a symmetric curve with a maximum at the temperature where the hopping frequency is of the order of the Larmor frequency. Deviations from the BPP model lead to loss of symmetry between the high- and low temperature limits

2. A semi empirical model for 2D conduction has been derived by Richards[46] by looking at the low and high temperature limits of the relaxation curve. Lower dimensional conduction affects the slope on temperatures above the maximum where $\tau_0\,\omega_c \ll 1$.

3. An empirical model was further developed for ion conduction in the layered sodiumion conductor beta alumina [47, 48]. This model is based on the BPP model, but introduces a fitting parameter β, to account for the deviation from the BPP model (see section 4.1.6)). The parameter has no physical basis.

4. A similar parameter as in model (3) has been introduced to the semi empirical model by Richards[46], to account for correlations between Coulomb interactions of the moving ion (see section 4.1.6).

All of these spectral densities were tested for simultaneous fitting of the data measured at multiple Larmor frequencies in this work.

The temperature dependence of the ^{6,7}Li spin-lattice relaxation times in Li_3InCl_6 was measured at three different Larmor frequencies as shown in Figure 5.5. The dataset collected at the lowest Larmor frequency (τ_0= 44 MHz, ^{6}Li on a 300 MHz spectrometer) shows a single maximum in the relaxation rate at a higher temperature than the measurements for ^{7}Li, even though the Larmor frequency of ^{6}Li is lower compared to ^{7}Li. There is only one explanation for this i.e. the jump processes are not the same, suggesting multiple processes, as already suggested in ref. [25].

If the jump processes are (to some approximation) independent of each other, the relaxation rates ($R = 1/T_1$) of the two processes are additive [49]. Following this assumption, a model containing two BPP-type jump processes was constructed and fit to the three datasets simultaneously (Figure 5.5), revealing activation energies of 0.189 eV for the faster

5 Re-investigating the structure-property relationship of the solid electrolyte $Li_{3-x}In_{1-x}Zr_xCl_6$ and the impact of In-Zr(IV) substitution

74

Figure 5.6: NMR relaxometry of $Li_{3-x}In_{1-x}Zr_xCl_6$ x=0.3 (a) and x=0.5 (b) fit with spectral density (3), the empirically modified BPP model. For a comparison of how the different models fit the datasets, see Appendix Figure 8.18-8.19. For the fitting parameters, see Appendix Table 8.9.
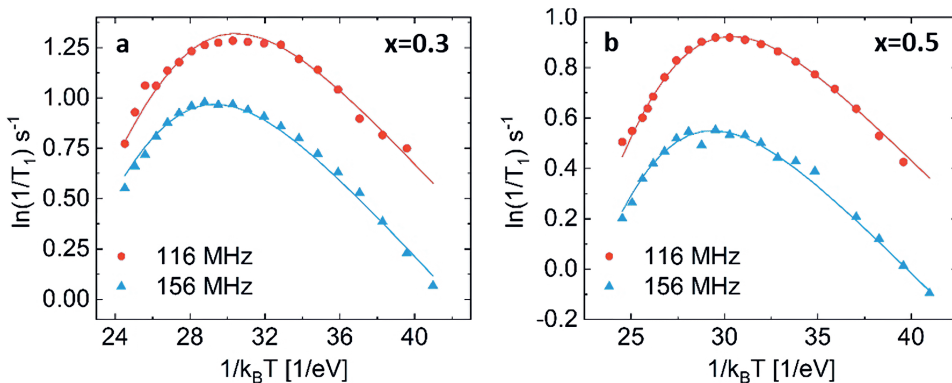
5

jump process (Figure 5.5, black dotted line) and 0.131 eV (Figure 5.5, red dotted line) for the slower jump process. Comparison between fits using the standard spectral densities (1-4) are shown in the 8.17.

To investigate to what extent the two processes contribute to the total diffusivity, the diffusion constant was calculated for the distinct hopping process, assuming an octahedral-tetrahedral-octahedral (oct-tet-oct) diffusion path (see discussion below) with an average jump distance of 2.1 Å(similar to the procedure in ref. [50]). The faster process (red line, Ea = 0.131 eV) (Appendix Table 8.9) leads to a diffusion coefficient of $\approx 10^{-12}$ m²s⁻¹ Appendix Table 8.11, which is the same order of magnitude as the diffusivity calculated from impedance measurements using the Nernst-Einstein relationship (Appendix Table 8.11). The slower process (black line, Ea=0.189 eV) leads to a diffusivity of the order $\approx 10^{-13}$ m²s⁻¹. Therefore, we can assume that the first jump process is the main contributor to macroscopic diffusion in Li_3InCl_6.

Both substituted materials with composition x=0.3 and x=0.5 were best fit with the two empirical models ((3), (4) in the list above), which both fit the data almost equally well (Bayesian information criteria of -318 and -333, see Figure S11, S12). Spectral density (3) is the same spectral density as used in Helm et al. (see Table S4 for comparison of the obtained values) [25]. They reported a clear trend in the activation energies from the solid-state NMR spectral-density fitting, similar in shape to the trend observed from AC-impedance spectroscopy. Considering the high correlation among fitting parameter reproduced from their data (>|0.9|, see Appendix Table 8.10) and relatively few points on the high-temperature slope (Figure S13), the data does not contain the information needed to unambiguously fit activation energies (see the large difference in the values in Appendix Table 8.10).

In fact, even the regular BPP model (with one fitting parameter less), results in a very large absolute correlation between the pre-exponential factor and the activation energy (0.99) for the measurements in this work, indicating that the measurements should be

performed for a large temperature range and at multiple Larmor frequencies for accurate determination of the correct spectral densities and activation energies. The development of a better method to estimate errors in these highly correlated systems in subject of future research.

For $Li_{3-x}In_{1-x}Zr_xCl_6$, x=0.3 the individual fits results in activation energies of 256 and 257 meV and β values of 0.365 and 0.427 respectively, whereas the combined fit yield an activation energy of 0.30± 0.02 eV and β of 0.29±0.04. Despite the higher ionic conductivity measured from AC-impedance spectroscopy, the activation energy found at present is much higher (0.3eV for x=0.3) than the values found for the activation energies of unsubstituted Li_3InCl_6 (Ea = 0.131 for the fast process, 0.189 eV for the slow process).

The empirically modified spectral density that fits the observed relaxation rate well most likely leads to different activation energies than the BPP model due to the empirical parameter β, which needs to be further investigated, as it is not clear whether the values obtained from these models can be compared. Measuring at a larger Larmor frequency or temperature range may be beneficial, which is a subject of further study. From the data presented here, it can be concluded that the Zr-substituent also affects the high frequency Li-ion motion, as indicated by the different shape of the relaxation curves.

The static NMR lineshape is already motionally narrowed at room temperature (Appendix Figure 8.21). At higher temperatures sharp features appear in the satellites which can be fit by residual quadrupolar coupling (6 kHz) combined with chemical shift anisotropy (Appendix Figure 8.21, span 3 ppm, skew ± of -0.76). Less pronounced but similar features are observed for the Zr-substituted samples (Appendix Figure 8.22). This can be interpreted in two ways: Either, the motion averages out the chemical shift anisotropy more effectively in the doped samples (but not fully), or this is an effect of the more disordered local environment due to the Zr-dopant.

It is interesting to relate these findings to the possible diffusion pathways in the crystal structure and structural changes as a function of the degree of substitution. In Figure 5.7, two possible diffusion pathways have been illustrated. Both of them occur via a chain of face-sharing tetrahedral and octahedral sites, as is known to happen for cubic-close-packed lattices [51]. One is along the c-direction, and involves the Li2 (2c) octahedra, the tetrahedral Li-site Li3(8j) observable from diffraction and the shared In2/Li4 (4g) octahedral site (Figure 5.7a). The other path is along the Li-layer in the ab-plane (Figure 5.7b), involving both octahedral Li-sites in the layer and vacant tetrahedrons.

Considering these two diffusion paths and comparing them to the structural changes found and the findings from AC-impedance (Figure 5.8) and solid-state NMR spectroscopy, the following observations and considerations can be made.

1. Pristine Li_3InCl_6 has the lowest ionic conductivity of the series, while it has the highest In2 (4g) site occupancy, the highest tetrahedral (8j) Li site occupancy and shows two jump processes as probed by solid-state NMR.

2. The conduction in the ab-plane of the material (Figure 5.7) occurs along oct-tet-oct paths, possible in both the Li- as well as the mixed cation layer. The large number of octahedra occupied by the In(III) or Zr(IV) cations blocks conduction in the mixed cation layer, making long-range diffusion less probable. In addition, along the c-direction, there is a possible oct-tet-oct path, which connects the octahedra in the

76

5 Re-investigating the structure-property relationship of the solid electrolyte $Li_{3-x}In_{1-x}Zr_xCl_6$ and the impact of In-Zr(IV) substitution

Figure 5.7: Illustration of the possible diffusion pathways in the crystal structure. (a) Diffusion along the c-direction involving the tetrahedral Li3(8j) site the octahedral Li2 (2c) site and the octahedral In2/Li4 (4g) site (b) Diffusion along the ab plane, illustrating the two different jump processes i.e. 1: jump through the empty tetrahedral site sharing faces with the lithium octahedral sites (Li1 (4i), Li2 (2c)); 2: jump between the Li2 (2c) octahedral site, the occupied tetrahedral Li3 (8j) site and can continue along the In2/Li4 site, as in (a). Diffusion in the M-layer in the ab-plane has similar possible diffusion paths, but with the In1 (2a) site blocking due to the high In/Zr occupancy, strongly reduces the number of free pathways.
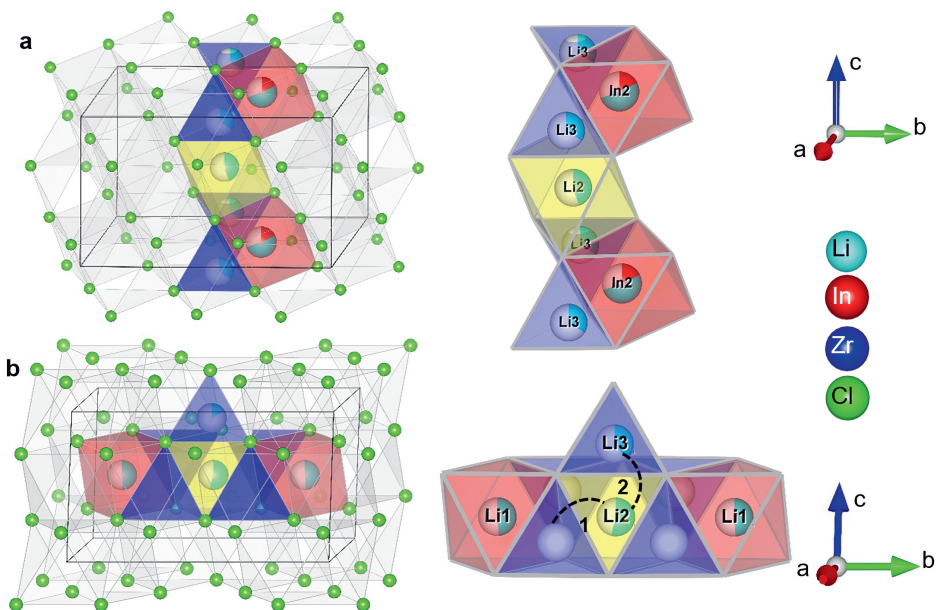
Li2(2c) octahedra with the tetrahedral Li3(8j) site and the In2/Li4 (4g) site. Due to the high cumulative occupancy of the In2/Li4 site (0.7), this path is also less probable compared to the oct-tet-oct in the Li-layer, (occupancies 0.4-0.45), because of the lower probability of having a vacant site to jump to. Specifically, all sites occupied by In can be considered as permanently blocking the conduction along the c-direction. From the activation energies of the spectral density fits (ppendix Table 8.9) the contribution to the diffusivity of both jump processes can be calculated (Appendix Table 8.11) and is found to be 1:10. Due to the lower probability of conduction in the c-direction, we infer that the faster diffusion process occurs in the ab-plane, and the slower process along the c-direction. Anisotropy of the diffusion is further supported by measurements of the static lineshapes (Appendix Figures ??-??).

3. Upon increasing amount of x in $Li_{3-x}In_{1-x}Zr_xCl_6$, the In2(4g) site occupancy drops to 5%, after which it remains constant (Figure 5.3a, Figure 5.7). The Li that is removed for charge compensation is first removed from the tetrahedral site. These two trends, in principle, open up the path along the c-direction.

Figure 5.8: Comparison of the ionic conductivity σ as measured from impedance with the occupancies of the Li3 (8j) and In2 (4g) sites for $Li_{3-x}In_{1-x}Zr_xCl_6$. The conductivity reaches its maximum as the tetrahedral Li3 (8j) site disappears. The occupancy of the In2 (4g) site drops to its minimum value already before the maximum in ionic conductivity is reached.
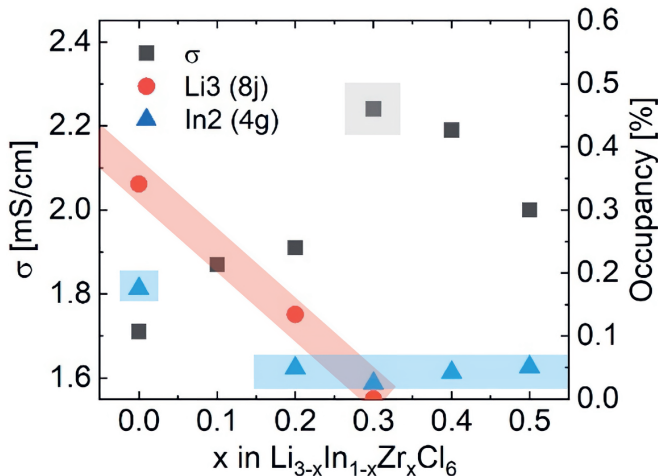
4. From the NMR spectral density fits, the faster jump process (0.131eV, red dotted line) observed in the pristine ¬Li₃InCl₆ is not detected anymore for 7Li measured on the 300MHZ spectrometer (ωL = 116MHz). This can have two limiting cases: • The frequency of the faster jump process is reduced below what can be observed considering the Larmor frequencies and the temperature range measured. • The frequencies of both jump processes cannot be distinguished in the temperature and frequency range measured. This is possible if the frequencies approach each other. This is as also suggested by the data in ref. [25], where also intermediate substituent concentrations were measured.

5. Due to the empirical parameter β, it is not straightforward to interpret the results from the spectral density fitting of the $Li_{3-x}In_{1-x}Zr_xCl_6$ x=0.3 and x=0.5 materials. All that can be concluded is that the jump process is not BPP type, and that only one process appears in the temperature range and at the frequencies measured. The line shapes show a decrease in chemical shift anisotropy from the pristine material to the substituted ones, which can be due to improved averaging of the environments by the motional process or the larger distribution of local environments due to the Zr-dopant.

Summarizing all these factors, from the NMR spin lattice relaxometry it is clear that the introduction of Zr affects the Li-ion motion on fast timescales. Considering the two jump processes for Li₃InCl₆, which have diffusivities in the ratio of 1:10, there is clearly one dominant jump process for the diffusion. Considering the possible diffusion paths in the crystal structure, these are likely in the ab-plane and along the z-direction. Anisotropic

conduction seems to apply at longer timescales, as seen from the residual chemical shift anisotropy in the static line shapes (time scale of T2 relaxometry41) at high temperatures. This is present for both Li_3InCl_6 as well as, at a lesser degree, the Zr-substituted samples. The chemical shift anisotropy could be lower either due to the larger distribution in local environments due to the introduction of Zr, or because of more effective averaging in three dimensions. The monoclinic symmetry with the layered arrangement of the In and Zr already suggests a different motional process along the ab-plane and the c-direction. Introducing the Zr dopant, the In2-occupancy drops, in principle opening up the path along the c-direction allowing for a decrease in the anisotropy. The optimum in ionic conductivity is therefore likely a combination of optimized charge charrier concentration as well as improved conduction pathways along the c-direction due to the different unit cell.

5.4 Conclusion

The substitution series $Li_{3-x}In_{1-x}Zr_xCl_6$ (x=[0 - 0.5], steps of 0.1) was synthesised, resulting in a maximal ionic conductivity at x=0.3 of 2.02 mS/cm at room temperature. Correlations between the structural models, derived from combined refinement of the x-ray and neutron diffraction, and the hopping processes, probed by solid-state NMR, reveal a complex diffusion mechanism. The authors would like to highlight the importance of measuring both neutron and x-ray diffraction, for accurate determination of atomic occupancies in this system from powders, as well as measuring NMR-relaxometry data at multiple Larmor frequencies, due to the complex shape of the curve of temperature dependent relaxation rates and the complexity of models, resulting in highly correlated fitting parameter sets.

For Li_3InCl_6, we find two distinct motional processes where one of the processes appears to dominate the long range diffusion and transport. From the layered structure, the diffusion path analysis and consideration of the most likely jump events, we assign the fast diffusion jump process to jumps within the Li layer in the ab-plane, and the slower jump process to jumps along the c-direction. Upon Zr substitution, the path along the c-direction seems to open up, due to a reduction in the In occupancy on the mixed In2/Li4 site. The second jump process probed for the pristine sample disappears for the substituted versions, and they most likely approach the timescale of the first, indicating reduced anisotropy. Nevertheless, the NMR spectral density fitting did not lead to an unambiguous choice of a spectral density. The residual chemical shift anisotropy in the static lineshapes of the substituted materials is less than that observed for the pristine material, though it is not completely averaged out. While the reduction could be due to a larger distribution in local environments due to the introduction of Zr, the fact that there is residual chemical shift anisotropy indicates that also for the substituted materials, the motion does not include all sites equally, even on longer timescales, and is hence anisotropic.

This paper shows that aliovalent doping does not only affect the charge carrier concentration, but can also lead to changes in the unit cell parameters affecting diffusivity on different timescales. For future studies, it would be interesting to combine this strategy with other successful strategies such as for example halogen alloying, which can affect ionic conductivity due to a change in lattice parameter (bottleneck size), lattice polarizability as well as potentially the configurational entropy.

5.5 Materials and Methods

Synthesis - The materials were synthesized from the precursors LiCl, InCl3 and ZrCl4. All precursors were bought anhydrous from Sigma Aldrich and used as received. The materials were handled in an Ar-filled glovebox. Stoichiometric mixtures of the precursors were weighed and mixed in an agate mortar, then sealed under 200mbar argon in quartz ampoules. The ampoules were annealed at 450 ℃ for 24 h, and then cooled down to room temperature over a 24 h duration. The resulting aggregates were then ball-milled for one hour (12 times 5 minutes with 2 minutes break) in a ZrO2 ball mill jar at 450 RPM, with 3 mm ZrO2 balls, a ball to sample weight ratio of 1:25 and a batch size of 4g. The ball-milled mixture was reannealed in evacuated quartz ampoules for 8 h at 450℃. The reason for this synthesis route is that the powder obtained from the first annealing step resulted in x-ray diffraction patterns with varying relative intensities, which were assumed to be due to preferential orientation. Therefore, the powder was ball-milled, to reduce the crystallite size. The ball-milled powder, however, had an order of magnitude lower ionic conductivity, and showed very broad peaks in the x-ray diffraction pattern. Therefore, the fine powder was annealed again, which gave the desired combination of high ionic conductivity, but an x-ray diffraction pattern of sufficient quality for Rietveld refinement. Recent research suggests that materials of the here investigated Li3MX6 structure families exhibit varying degrees of stacking faults [52, 53]. It can't be excluded that the reason for the varying intensities here are due to a different peak shape due to possible stacking faults, but in the final synthesis product stacking faults were not needed for the final Rietveld refinement.

X-ray diffraction – The x-ray diffraction patterns were collected on a Panalytical l X'Pert Pro X-ray diffractometer with a Cu K-alpha source in a 2θ range of 10 to 100 degrees in reflection geometry. Due to the moisture sensitivity of the samples, a custom made airtight sample holder was used. The sample holder consisted of a zero diffraction silicon wafer (SilTronix), closed off with a kapton half-cylinder. The instrument parameter file was created by measuring a LaB6 standard obtained from NIST.

Neutron Diffraction – Neutron diffraction measurements were performed on the time of flight (TOF), high-flux, medium resolution diffractometer Polaris at ISIS [54], Rutherford Appleton Laboratory, United Kingdom. 1g each of the $Li_{3-x}In_{1-x}Zr_xCl_6$ (x =0,0.2,0.3,0.4,0.5) samples were filled in cylindrical vanadium cans under argon atmosphere and sealed with indium wire. Normalized diffraction data collected in the highest resolution backscattering detector bank (bank 5, Q-range ~2.25 to 16 Å were used in Rietveld structure refinement. Note the sample with x = 0.1 was not measured due to limitations in beamtime.

Rietveld Refinement – Combined Rietveld refinement of the x-ray and neutron diffraction data was performed with the software GSAS-II [55]. The relative amounts of the elements In, Zr and Li was fixed to values obtained by ICP. The structure published by Bohnsack et al. [28] was used as the starting structure. Both Li and Zr were initially put on the two partially occupied In sites, but Li clearly preferred a specific site (In2), and Zr the other indium (In1) site, hence the reversed positions were removed. We highlight the importance of using two contrasts here, as the co-occupancy of the In2 site with Li

5 Re-investigating the structure-property relationship of the solid electrolyte $Li_{3-x}In_{1-x}Zr_xCl_6$ and the
impact of In-Zr(IV) substitution

80

makes the refinement of the occupancies difficult from neutron diffraction data alone, due to the opposite sign scattering length density. Observed scattering-density maps of both the neutron and x-ray data were also calculated using GSAS-II [55, 56]. From the density maps calculated of the neutron diffraction data, an additional tetrahedral site was added for the materials Li_3InCl_6 and $Li_{2.8}In_{0.8}Zr_{0.2}Cl_6$ (Li3). Vesta[57] was used for visualizations of the crystal structure and density maps.

AC-impedance – The ionic conductivity of the materials was evaluated on dense cylindrical pellets. To make the pellets, 0.2 g of solid electrolyte powder was loaded in a home made cell consisting of stainless steel plungers in an insulating Al_2O_3 ring of 1 cm diameter. The powder was compressed with uniaxial load of 1.6 tons, screwed tight and sealed with blu tack. The resulting pellet were 0.1cm ± 5% thick. The impedance measurements were conducted on an Autolab FRA32M with the ECI10M high frequency module in a frequency range from 1 Hz to 10 MHz using an excitation amplitude of 0.1V. The individual AC-impedance spectra were fit using RelaxIS. The validity of the equivalent circuit model was confirmed using the Kramers Krönig analysis also implemented in RelaxIS (Appendix Fifure 8.14). The fitted values for the pellet resistance was used to calculate the ionic conductivity and Arrhenius relationship. For the ionic conductivity, the errors were calculated using Gaussian error propagation [43], for the activation energies from the fit to the Arrhenius behaviour (Appendix Table 8.8).

AC-impedance measurements are the common standard to evaluate the ionic conductivity of solid electrolytes, as the time and length scales correspond the most with the relevant scales for battery operation. Unfortunately, research has shown that values of the ionic conductivity and activation energy can vary strongly for the same materials in different labs [58]. Solid-state NMR can be used as a complementary probe for the motion the Li-ions on a much shorter timescale.

Solid-state NMR – Solid-state NMR measurements were performed on an Agilent 400 MHz spectrometer (B_0=9.4 T, 155.5 MHz for ^7Li) and an Agilent 300 MHz spectrometer (B_0=7.1 T, 116.6 MHz for ^7Li and 44 MHz for ^6Li). Chemical shifts were referenced with respect to a 0.1 M LiCl solution. Variable temperature measurements were performed using a 5 mm static goniometer probe. T_1 relaxation times were determined at various temperatures using a saturation recovery experiment. The T_1s as well as the static line-shapes were fit using the ssNAKE program [59]. For a detailed explanation of the theory behind the spectral density fitting as well as the CSA, see SI Text 1.

References

[1] Theodosios Famprikis, Pieremanuele Canepa, James A. Dawson, M. Saiful Islam, and Christian Masquelier. Fundamentals of inorganic solid-state electrolytes for batteries. *Nature Materials*, 18(12):1278–1291, December 2019.

[2] Chengwei Wang, Kun Fu, Sanoop Palakkathodi Kammampata, Dennis W. McOwen, Alfred Junio Samson, Lei Zhang, Gregory T. Hitz, Adelaide M. Nolan, Eric D. Wachsman, Yifei Mo, Venkataraman Thangadurai, and Liangbing Hu. Garnet-Type Solid-State Electrolytes: Materials, Interfaces, and Batteries. *Chemical Reviews*, 120(10):4257–4300, May 2020.

[3] Rachel DeWees and Hui Wang. Synthesis and properties of nasicon-type latp and lagp solid electrolytes. *ChemSusChem*, 12(16):3713–3725, 2019.

[4] Laidong Zhou, Nicolò Minafra, Wolfgang G. Zeier, and Linda F. Nazar. Innovative Approaches to Li-Argyrodite Solid Electrolytes for All-Solid-State Lithium Batteries. *Accounts of Chemical Research*, 54(12):2717–2728, June 2021.

[5] Noriaki Kamaya, Kenji Homma, Yuichiro Yamakawa, Masaaki Hirayama, Ryoji Kanno, Masao Yonemura, Takashi Kamiyama, Yuki Kato, Shigenori Hama, Koji Kawamoto, and Akio Mitsui. A lithium superionic conductor. *Nature Materials*, 10(9):682–686, September 2011.

[6] Jakob B. Grinderslev, Mads B. Amdisen, Lasse N. Skov, Kasper T. Møller, Lasse G. Kristensen, Marek Polanski, Michael Heere, and Torben R. Jensen. New perspectives of functional metal borohydrides. *Journal of Alloys and Compounds*, 896:163014, March 2022.

[7] Tetsuya Asano, Akihiro Sakai, Satoru Ouchi, Masashi Sakaida, Akinobu Miyazaki, and Shinya Hasegawa. Solid Halide Electrolytes with High Lithium-Ion Conductivity for Application in 4 V Class Bulk-Type All-Solid-State Batteries. *Advanced Materials*, 30(44):1803075, November 2018.

[8] Bettina V. Lotsch and Joachim Maier. Relevance of solid electrolytes for lithium-based batteries: A realistic view. *Journal of Electroceramics*, 38(2-4):128–141, June 2017.

[9] Jakob Asenbauer, Tobias Eisenmann, Matthias Kuenzel, Arefeh Kazzazi, Zhen Chen, and Dominic Bresser. The success story of graphite as a lithium-ion anode material – fundamentals, remaining challenges, and recent developments including silicon (oxide) composites. *Sustainable Energy & Fuels*, 4(11):5387–5416, 2020.

[10] R. Fallahzadeh and N. Farhadian. Molecular dynamics simulation of lithium ion diffusion in LiCoO2 cathode material. *Solid State Ionics*, 280:10–17, November 2015.

[11] J Li, W Yao, S Martin, and D Vaknin. Lithium ion conductivity in single crystal LiFePO4. *Solid State Ionics*, 179(35-36):2016–2019, October 2008.

[12] Martin Wilkening, Christopher Lyness, A. Robert Armstrong, and Peter G. Bruce. Diffusion in confined dimensions: Li $^+$ Transport in Mixed Conducting tio $_2$-β nanowires. *The Journal of Physical Chemistry C*, 113(12):4741–4744, March 2009.

[13] M. Wilkening and P. Heitjans. Li jump process in h - Li 0.7 Ti S 2 studied by two-time Li 7 spin-alignment echo NMR and comparison with results on two-dimensional diffusion from nuclear magnetic relaxation. *Physical Review B*, 77(2):024311, January 2008.

[14] Caroline Hiebl, Patrick Loch, Marina Brinek, Maria Gombotz, Bernhard Gadermaier, Paul Heitjans, Josef Breu, and H. Martin. R. Wilkening. Rapid Low-Dimensional Li $^+$ Ion Hopping Processes in Synthetic Hectorite-Type Li $_{0.5}$ [Mg $_{2.5}$ Li $_{0.5}$]Si $_4$ O $_{10}$ F $_2$. *Chemistry of Materials*, 32(17):7445–7457, September 2020.

[15] Mohammed Tareque Chowdhury, Reiji Takekawa, Yoshiki Iwai, Naoaki Kuwata, and Junichi Kawamura. Lithium ion diffusion in Li β-alumina single crystals measured by pulsed field gradient NMR spectroscopy. *The Journal of Chemical Physics*, 140(12):124509, March 2014.

[16] Shuo Wang, Qiang Bai, Adelaide M. Nolan, Yunsheng Liu, Sheng Gong, Qiang Sun, and Yifei Mo. Lithium Chlorides and Bromides as Promising Solid-State Chemistries for Fast Ion Conductors with Good Electrochemical Stability. *Angewandte Chemie International Edition*, 58(24):8039–8043, June 2019.

[17] Laidong Zhou, Tong-Tong Zuo, Chun Yuen Kwok, Se Young Kim, Abdeljalil Assoud, Qiang Zhang, Jürgen Janek, and Linda F. Nazar. High areal capacity, long cycle life 4 V ceramic all-solid-state Li-ion batteries enabled by chloride solid electrolytes. *Nature Energy*, January 2022.

[18] Yoonjae Han, Sung Hoo Jung, Hiram Kwak, Seunggoo Jun, Hunho H. Kwak, Jong Hoon Lee, Seung-Tae Hong, and Yoon Seok Jung. Single- or Poly-Crystalline Ni-Rich Layered Cathode, Sulfide or Halide Solid Electrolyte: Which Will be the Winners for All-Solid-State Batteries? *Advanced Energy Materials*, 11(21):2100126, June 2021.

5

[19] Ivan Kochetkov, Tong-Tong Zuo, Raffael Ruess, Baltej Singh, Laidong Zhou, Kavish Kaup, Jürgen Janek, and Linda Nazar. Different interfacial reactivity of lithium metal chloride electrolytes with high voltage cathodes determines solid-state battery performance. *Energy & Environmental Science*, page 10.1039.D2EE00803C, 2022.

[20] Kern-Ho Park, Kavish Kaup, Abdeljalil Assoud, Qiang Zhang, Xiaohan Wu, and Linda F Nazar. High-voltage superionic halide solid electrolytes for all-solid-state li-ion batteries. *ACS Energy Letters*, 5(2):533–539, 2020.

[21] Qinong Shao, Chenhui Yan, Mingxi Gao, Wubin Du, Jian Chen, Yaxiong Yang, Jiantuo Gan, Zhijun Wu, Wenping Sun, Yinzhu Jiang, Yongfeng Liu, Mingxia Gao, and Hongge Pan. New Insights into the Effects of Zr Substitution and Carbon Additive on Li $_{3-x}$ Er $_{1-x}$ Zr $_x$ Cl $_6$ Halide Solid Electrolytes. *ACS Applied Materials & Interfaces*, 14(6):8095–8105, February 2022.

[22] Se Young Kim, Kavish Kaup, Kern-Ho Park, Abdeljalil Assoud, Laidong Zhou, Jue Liu, Xiaohan Wu, and Linda F Nazar. Lithium ytterbium-based halide solid electrolytes for high voltage all-solid-state batteries. *ACS Materials Letters*, 3(7):930–938, 2021.

[23] Guofeng Xu, Liang Luo, Jianwen Liang, Shangqian Zhao, Rong Yang, Changhong Wang, Tianwei Yu, Limin Wang, Wei Xiao, Jiantao Wang, Jinqiu Yu, and Xueliang Sun. Origin of high electrochemical stability of multi-metal chloride solid electrolytes for high energy all-solid-state lithium-ion batteries. *Nano Energy*, 92:106674, February 2022.

[24] Juhyoun Park, Daseul Han, Hiram Kwak, Yoonjae Han, Yong Jeong Choi, Kyung-Wan Nam, and Yoon Seok Jung. Heat treatment protocol for modulating ionic conductivity via structural evolution of li3-xyb1-xmxcl6 (m= hf4+, zr4+) new halide superionic conductors for all-solid-state batteries. *Chemical Engineering Journal*, 425:130630, 2021.

[25] Bianca Helm, Roman Schlem, Björn Wankmiller, Ananya Banik, Ajay Gautam, Justine Ruhl, Cheng Li, Michael Ryan Hansen, and Wolfgang G. Zeier. Exploring aliovalent substitutions in the lithium halide superionic conductor li3-xin1-xzrxcl6 (0≤ x ≤ 5. *Chemistry of Materials*, 33(12):4773–4782, June 2021.

[26] Xuming Luo, Xianzhang Wu, Jiayuan Xiang, Dan Cai, Min Li, Xiuli Wang, Xinhui Xia, Changdong Gu, and Jiangping Tu. Heterovalent Cation Substitution to Enhance the Ionic Conductivity of Halide Electrolytes. *ACS Applied Materials & Interfaces*, 13(40):47610–47618, October 2021.

[27] Hiram Kwak, Daseul Han, Jun Pyo Son, Jong Seok Kim, Juhyoun Park, Kyung-Wan Nam, Hyungsub Kim, and Yoon Seok Jung. Li+ conduction in aliovalent-substituted monoclinic Li2ZrCl6 for all-solid-state batteries: Li2+xZr1-xMxCl6 (M = In, Sc). *Chemical Engineering Journal*, 437:135413, June 2022.

[28] Andreas Bohnsack, Frauke Stenzel, Armin Zajonc, Gert Balzer, Mathias S. Wickleder, and Gerd Meyer. Ternäre halogenide vom typ a3mx6 vi. ternäre chloride der selten-erd-elemente mit lithium lithium, li3mcl6 (m=tb-lu, y, sc): Synthese, krisallstrukturen und ionenbewegung. *Zeitschrift für anorganische und allgemeine Chemie*, 623(7):1067–1073, July 1997.

[29] Michael O. Schmidt, Mathias S. Wickleder, and Gerd Meyer. Zur Kristallstruktur von Li3InCl6. *Zeitschrift für anorganische und allgemeine Chemie*, 625(4):539–540, April 1999.

[30] Jianwen Liang, Eveline van der Maas, Luo, Jing, Xiaona Li, Ning chen, Keegan R. Adair, Weihan Li, Junjie Li, Yongfeng Hu, Jue Liu, Li Zhang, Shangqian Zhao, Shigang Lu, Jiantao Wang, huan huang, Wenxuan Zhao, Steven Parnell, Ronald I. smith, Swapna Ganapathy, Marnix Wagemaker, and Xueliang Sun. A Series of Ternary Metal Chloride Superionic Conductors for High-Performance All-Solid-State Lithium Batteries. *A Series of Ternary Metal Chloride Superionic Conductors for High-Performance All-Solid-State Lithium Batteries*, 2022.

[31] Shuai Chen, Chuang Yu, Shaoqing Chen, Linfeng Peng, Cong Liao, Chaochao Wei, Zhongkai Wu, Shijie Cheng, and Jia Xie. Enabling ultrafast lithium-ion conductivity of Li2ZrCl6 by indium doping. *Chinese Chemical Letters*, 33(10):4635–4639, October 2022.

[32] Kai Wang, Qingyong Ren, Zhenqi Gu, Chaomin Duan, Jinzhu Wang, Feng Zhu, Yuanyuan Fu, Jipeng Hao, Jinfeng Zhu, Lunhua He, Chin-Wei Wang, Yingying Lu, Jie Ma, and Cheng Ma. A cost-effective and humidity-tolerant chloride solid electrolyte for lithium batteries. *Nature Communications*, 12(1):4410, July 2021.

[33] R. D. Shannon and C. T. Prewitt. Effective ionic radii in oxides and fluorides. *Acta Crystallographica Section B Structural Crystallography and Crystal Chemistry*, 25(5):925–946, May 1969.

[34] Hiram Kwak, Daseul Han, Jeyne Lyoo, Juhyoun Park, Sung Hoo Jung, Yoonjae Han, Gihan Kwon, Hansu Kim, Seung-Tae Hong, Kyung-Wan Nam, et al. New cost-effective halide solid electrolytes for all-solid-state batteries: Mechanochemically prepared fe3+-substituted li2zrcl6. *Advanced Energy Materials*, 11(12):2003190, 2021.

[35] Xiaona Li, Jianwen Liang, Keegan R Adair, Junjie Li, Weihan Li, Feipeng Zhao, Yongfeng Hu, Tsun-Kong Sham, Li Zhang, Shangqian Zhao, et al. Origin of superionic li3y1−x in x cl6 halide solid electrolytes with high humidity tolerance. *Nano Letters*, 20(6):4384–4392, 2020.

[36] Andreas Bohnsack, Gert Balzer, Hans-U. Gödel, Mathias S. Wickleder, and Gerd Meyer. Ternäre halogenide vom typ a3mx6. vii. die bromide li3mbr6 (m=sm-lu, y): Synthese, kristallstruktur, ionenbeweglichkeit. *Zeitschrift für anorganische und allgemeine Chemie*, 623(9):1352–1356, September 1997.

[37] Roman Schlem, Tim Bernges, Cheng Li, Marvin A. Kraft, Nicolo Minafra, and Wolfgang G. Zeier. Lattice Dynamical Approach for Finding the Lithium Superionic Conductor Li$_3$ErI$_6$. *ACS Applied Energy Materials*, 3(4):3684–3691, April 2020.

[38] Michael Schmidt. *Neue Untersuchungen an ternären Halogeniden vom Typ A3MX6: Li3MI6 (M = Gd - Lu, Y) sowie A3InCl6 (A = Li - Cs)*. PhD thesis, Universität Köln, 1999.

[39] Yunsheng Liu, Shuo Wang, Adelaide M. Nolan, Chen Ling, and Yifei Mo. Tailoring the Cation Lattice for Chloride Lithium-Ion Conductors. *Advanced Energy Materials*, 10(40):2002356, 2020.

[40] Martin Wilkening and Paul Heitjans. From micro to macro: Access to long-range li+ diffusion parameters in solids via microscopic 6, 7li spin-alignment echo nmr spectroscopy. *ChemPhysChem*, 13(1):53–65, 2012.

[41] A. J. Dianoux, G. H. Lander, and Institut Laue-Langevin, editors. *Neutron data booklet*. Old City, Philadelphia, PA, 2nd ed edition, 2003.

[42] Roman Schlem, Ananya Banik, Saneyuki Ohno, Emmanuelle Suard, and Wolfgang G. Zeier. Insights into the Lithium Sub-structure of Superionic Conductors Li$_3$YCl$_6$ and Li$_3$YBr$_6$. *Chemistry of Materials*, 33(1):327–337, January 2021.

[43] Irina V. Krasnikova, Mariam A. Pogosova, Alexey O. Sanin, and Keith J. Stevenson. Toward Standardization of Electrochemical Impedance Spectroscopy Studies of Li-Ion Conductive Ceramics. *Chemistry of Materials*, 32(6):2232–2241, March 2020.

[44] Peter A Beckmann. Spectral densities and nuclear spin relaxation in solids. *Physics Reports*, 171(3):85–128, December 1988.

[45] N. Bloembergen, E. M. Purcell, and R. V. Pound. Relaxation Effects in Nuclear Magnetic Resonance Absorption. *Physical Review*, 73(7):679–712, April 1948.

[46] Peter M Richards. Effect of low dimensionality on prefactor anomalies in superionic conductors. *Solid State Communications*, 25(12):1019–1021, 1978.

[47] John L. Bjorkstam and Marco Villa. Second-order quadrupolar and low-dimensionality effects upon NMR resonance spectra. *Physical Review B*, 22(11):5025–5032, December 1980.

[48] R. Böhmer, K.R. Jeffrey, and M. Vogel. Solid-state Li NMR with applications to the translational dynamics in ion conductors. *Progress in Nuclear Magnetic Resonance Spectroscopy*, 50(2-3):87–174, March 2007.

5

84

5 Re-investigating the structure-property relationship of the solid electrolyte $Li_{3-x}In_{1-x}Zr_xCl_6$ and the impact of In-Zr(IV) substitution

[49] Roland Y. Dong. *NMR Relaxation Rates*, pages 1855–1862. Academic Press, 2017.

[50] Maria Gombotz and H. Martin R. Wilkening. Fast li-ion dynamics in the mechanosynthesized nanostructured form of the solid electrolyte Li3YBr6. *ACS SUSTAINABLE CHEMISTRY & ENGINEERING*, 9(2):743–755, January 2021.

[51] Yan Wang, William Davidson Richards, Shyue Ping Ong, Lincoln J. Miara, Jae Chul Kim, Yifei Mo, and Gerbrand Ceder. Design principles for solid-state lithium superionic conductors. *Nature Materials*, 14(10):1026–1031, October 2015.

[52] Maximilian A. Plass, Sebastian Bette, Robert E. Dinnebier, and Bettina V. Lotsch. Enhancement of Superionic Conductivity by Halide Substitution in Strongly Stacking Faulted $Li_3HoBr_{6-x}I_x$ Phases. *Chemistry of Materials*, page acs.chemmater.2c00024, March 2022.

[53] Elias Sebti, Hayden A. Evans, Hengning Chen, Peter M. Richardson, Kelly M. White, Raynald Giovine, Krishna Prasad Koirala, Yaobin Xu, Eliovardo Gonzalez-Correa, Chongmin Wang, Craig M. Brown, Anthony K. Cheetham, Pieremanuele Canepa, and Raphaële J. Clément. Stacking Faults Assist Lithium-Ion Conduction in a Halide-Based Superionic Conductor. *Journal of the American Chemical Society*, page jacs.1c11335, March 2022.

[54] RI Smith, S Hull, MG Tucker, HY Playford, DJ McPhail, SP Waller, and ST Norberg. The upgraded polaris powder diffractometer at the isis neutron source. *Review of scientific instruments*, 90(11):115101, 2019.

[55] Brian H. Toby and Robert B. Von Dreele. What's new in GSAS-II. *Powder Diffraction*, 29(S2):S2–S6, December 2014.

[56] Brian H. Toby and Robert B. Von Dreele. *GSAS-II* : the genesis of a modern open-source all purpose crystallography software package. *Journal of Applied Crystallography*, 46(2):544–549, April 2013.

[57] Koichi Momma and Fujio Izumi. *VESTA* : a three-dimensional visualization system for electronic and structural analysis. *Journal of Applied Crystallography*, 41(3):653–658, June 2008.

[58] Saneyuki Ohno, Tim Bernges, Johannes Buchheim, Marc Duchardt, Anna-Katharina Hatz, Marvin A Kraft, Hiram Kwak, Aggunda L Santhosha, Zhantao Liu, Nicolo Minafra, et al. How certain are the reported ionic conductivities of thiophosphate-based solid electrolytes? an interlaboratory study. *ACS Energy Letters*, 5(3):910–915, 2020.

[59] S.G.J. van Meerten, W.M.J. Franssen, and A.P.M. Kentgens. ssNake: A cross-platform open-source NMR data processing and fitting application. *Journal of Magnetic Resonance*, 301:56–66, April 2019.

6

Investigation of Structure, Ionic Conductivity and Electrochemical Stability of Halogen-Substitution in Solid-State Ion Conductor Li$_3$YBr$_x$Cl$_{6-x}$

As Published in ACS J. Phys. chem. C

Authors: *Eveline van der Maas*†, Wenxuan Zhao †, Zhu Cheng, Theodosios Famprikis, Michel Thijs, Steven R. Parnell, Swapna Ganapathy*, Marnix Wagemaker*.

* Corresponding authors
†These authors contributed equally to the manuscript
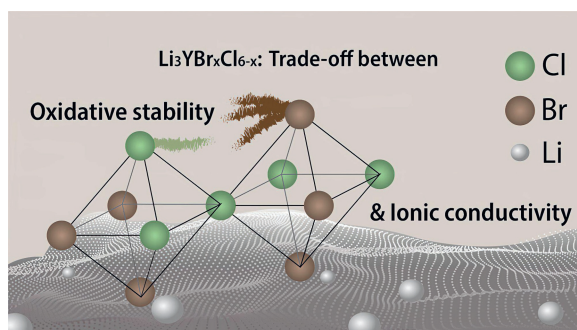
6.1 Abstract

Li_3YX_6 (X = Cl, Br) materials are Li-ion conductors that can be used as solid electrolytes in all solid-state batteries. Solid electrolytes ideally have high ionic conductivity and (electro)chemical compatibility with the electrodes. It was proven that introducing Br to Li_3YCl_6 increases ionic conductivity but, according to thermodynamic calculations, should also reduce oxidative stability. In this paper, the trade-off between ionic conductivity and electrochemical stability in $Li_3YBr_xCl_{6-x}$ halogen-substituted compounds is investigated. The compositions of $Li_3YBr_{1.5}Cl_{4.5}$ and $Li_3YBr_{4.5}Cl_{1.5}$ are reported for the first time, along with a consistent analysis of the whole $Li_3YBr_xCl_{6-x}$ (x = 0–6) tie-line.

The results show that, while Br-rich materials are more conductive (5.36×10^{-3} S/cm at 30 ℃ for x = 4.5), the oxidative stability is lower ($\approx$ 3 V compared to $\approx$ 3.5 V). Small Br content (x = 1.5) does not affect oxidative stability but substantially increases ionic conductivity compared to pristine Li_3YCl_6 (2.1 compared to 0.049×10^{-3} S/cm at 30 ℃). This work highlights that optimization of substitutions in the anion framework provide prolific and rational avenues for tailoring the properties of solid electrolytes.

6.2 Introduction

Solid-state electrolytes for all-solid-state batteries (ASSBs) have been intensively researched in recent years, due to the improved safety they offer compared to liquid electrolytes and because they may enable alternative electrodes [1]. In 2018, Asano et al. reported that the ternary halides Li_3YCl_6 and Li_3YBr_6 have ionic conductivities of $\approx 1 \times 10^{-3}$ S/cm and showcased ASSBs with Coulombic efficiencies of 94% using (uncoated) LiCoO2 as the active material in the cathode composite [2]. Since then, the material family $Li_3M(III)X_6$ (M(III) = Y, In, Sc, lanthanides; X = Cl, Br, I)) and other halide solid electrolytes have gained renewed interest in the scientific community due to their favorable combination of ionic conductivity ($\approx$mS/cm) and high-voltage cathode compatibility [3–5].

More recently, Zhou et al. [6] reached a milestone in the development of ASSBs using a Li2InxSc0.66−xCl4 electrolyte. The ASSB with this electrolyte possessing a 2 × 10^{-3} S/cm ionic conductivity and a 4.7 × 10−10 S/cm electronic conductivity, reached 3000 cycles at 80% capacity retention when cycled between 2.8–4.3 V vs Li/Li+ using LiNi0.85Co0.1Mn0.05O2 as the cathode (6.21 mg/cm2) at 3C [6]. Considering these promising results, further improvements and fundamental understanding of such electrolytes may accelerate the development of practical ASSBs. A strategy that has been successfully employed to tune the ionic conductivity of $Li_3M(III)X_6$ materials is halogen substitution [7–12].

Specifically for the compositional tie-line between Li_3YCl_6 and Li_3YBr_6, the Li3YBr3Cl3 composition was shown to have a 7.2 × 10^{-3} S/cm ionic conductivity at room temperature (compared to the $\approx$1 × 10^{-3} S/cm of the end members Li_3YCl_6/Li_3YBr_6 [2]). Based on thermodynamic phase equilibrium calculations, it has been predicted that Li_3YCl_6 should be stable between 0.62 and 4.21 V vs Li/Li+ and Li_3YBr_6 between 0.59 and 3.15 V vs Li/Li+ (ref [13]).

According to these calculations, the materials would decompose into the YX3 precursor and the halogen gas X2 at high potentials (oxidation) and to metallic Y and LiX (X = Cl, Br) at low potentials (reduction). These calculations suggest that introducing Br may

reduce the high-voltage stability, leading to a trade-off between cathode compatibility and ionic conductivity. However, it has been shown that such calculations do not always reflect the practically relevant stability window of solid electrolytes, as the (possible) formation of intermediate phases are not considered [14].

More generally, it has been proposed that the reduction and oxidation potential of the solid electrolyte upon lithiation/delithiation is a more accurate measure of the practical electrochemical stability window because the energetics of the reaction intermediates and non-equilibrium states are captured. [14] The stability window based on the oxidation and reduction potentials was found to be larger compared to thermodynamic calculations and matched the experimentally measured oxidation and reduction voltages for argyrodite-type Li6PS5Cl, garnet-type Li7La3Zr2O12, and NASICON-type Li1.5Al0.5Ge1.5(PO4)3 (ref [14]). For Li_3YBr_6, this method proposes a stability window between 0 and 3.43 V vs Li/Li+ (ref [15]) (compared to the previously predicted window of 0.59–3.15 V vs Li/Li+). For Li_3YCl_6, no data simulated data using this method isavailable. Specifically for $Li_3M(III)Cl_6$ (M(III) = Bi, Dy, Er, Ho, In, Lu, Sc, Sm, Tb, Tl, Tm, Y), the influence of the M(III) in different chlorides on the high-voltage stability was calculated to be between 4.26 and 4.38 V, with the majority at 4.26 V vs Li/Li+ [16].

Recent experimental results showed that the difference in the high-voltage stability between solid-electrolytes with different M(III)/M(IV) is larger than expected in some cases, and that not only the electrochemical stability is relevant in such systems, but also the stability against oxygen release especially in combination with high capacity $LiNi_{0.85}Co_{0.1}Mn_{0.05}O_2$ [17]. In this study, we report an experimental study of the substitution series $Li_3YBr_xCl_{6-x}$ (x = [0, 6] steps of 1.5) and investigate the influence of the halogen composition on the crystal structure, ionic conductivity, and the electrochemical stability window. It is found that the composition $Li_3YBr_xCl_{6-x}$ (x = 1.5) is a good compromise, with increased ionic conductivity compared to Li_3YCl_6 while maintaining the higher oxidative stability of Li_3YCl_6 compared to the bromide end-member.

6.3 Methods

Synthesis of Halide SSEs

For the ampule synthesis of $Li_3YBr_xCl_{6-x}$, stoichiometric mixtures of the precursors (x ≤ 3: LiCl (>99%, Sigma-Aldrich), LiBr (>99.99%, Sigma-Aldrich), YCl3(99.99%, Sigma-Aldrich); x > 3: LiCl, LiBr, YBr3(99.9% REO)) were filled in quartz ampules in an argon-filled glovebox. Then the ampules were evacuated and refilled to 200 mbar argon, flame-sealed, and placed in a muffle furnace. The powder mixtures were heated to 650 ℃ (above their melting point) in 4 h, held at that temperature for 24 h, and then cooled down to room temperature over 24 h. The resulting products were pulverized using pestle and mortar until a fine powder was obtained.

The mechanochemical synthesis of $Li_3YBr_xCl_{6-x}$ with x = 3 was carried out by ball milling of precursors (YCl3 and LiBr in a molar ratio of 1:3). Each 45 mL ZrO2 ball mill jar (Fritsch) was filled with a total amount of 3 g of material with 20 g of Φ3 mm and 60 g of Φ10 mm ZrO2 balls as milling media and tightly closed in the glovebox. The milling was conducted for 288 cycles of 5 min (each followed by 5 min rest) with a rotation speed of 500 rpm. After every 2 h, the mixtures were homogenized in the argon-filled box by scraping off the material pressed to the wall. A small part of the resulting material was

taken out every 4 h for analysis. The as-milled products were subsequently put in the furnace for a sequential crystallization. The annealing was performed in quartz ampules in the same way as described above, at a temperature of 200–600 ℃ for 5 h with a heating rate of 2 ℃ per minute. The ampules were naturally cooled down to room temperature after annealing.

X-ray Diffraction

The samples were analyzed using a X'Pert-Pro diffractometer (PANalytical) equipped with a Cu Kα radiation (λ = 1.5406 Å) source operating at 45 kV and 40 mA. The samples were prepared by filling the powder into an airtight holder, which consisted of a silicon zero-diffraction wafer separated from the environment with a Kapton film arch. The data were collected at room temperature and atmospheric pressure by scanning over the 2θ range of 10 to 90°. The measured X-ray diffraction patterns were analyzed by Le Bail refinement using GSAS-II [18, 19].

Neutron Diffraction

Neutron diffraction was performed on the PEARL [20] diffractometer of the Reactor Institute Delft at a wavelength of 1.667 Å. The sample was filled in 7 mm diameter vanadium cans, which were filled in an argon-filled glovebox and sealed using rubber O-rings.

Rietveld Refinement

Rietveld refinement of the neutron diffraction data was performed using GSAS-II [18, 19]. For the monoclinic phase, Y and Li were found to occupy the same crystallographic site. Due to the opposite sign coherent scattering length of these atoms (bLi = -1.90 fm, bY = 7.75 fm), this led to a diminution of the signal intensity. As the full occupancy of the site is also not known, it was not possible to automatically refine this ratio due to divergence of the fit. Therefore, the refinement was done manually trying out (almost) all possible configurations, and deciding on the best fit based on visual inspection and the goodness of fit. Due to this difficulty, no conclusions have been drawn in this report on the differences between the occupancy parameters extracted. Crystal structures were visualized in VESTA [21]

AC Impedance

AC impedance spectroscopy was used to determine the ionic conductivity of the synthesized powders. A homemade cell was used consisting of an insulating alumina hollow cylinder with two stainless steel plungers that are used both to initially compress the powder into a pellet and act as current collectors. The cell was assembled in an Ar-filled glovebox by filling 100 mg of powder into the alumina cylinder (inner diameter of Φ10 mm) and cold-pressing the powder into a pellet (392 MPa) using the steel plungers. The assembly was screwed tight under pressure using three (electronically insulated) screws. The measurements were performed on an Autolab electrochemical workstation (AUT86298) in a frequency range between 1 MHz and 100 Hz. The obtained data were fit using the commercial software RelaxIS (rhd instruments). The datasets were fit using a L-R-CPE circuit, which was validated by the Kramers–Kronig relations. The values of the parameter fits were used to calculate the ionic conductivities and the Arrhenius relationship. The error

of individual conductivity measurements was calculated from Gaussian error propagation as proposed by Krasnikova et al. [22]:

$$RSD_\sigma = \frac{\delta\sigma}{\sigma} = \sqrt{\left(\frac{\delta l}{l}\right)^2 + \left(\frac{\delta A}{A}\right)^2 + \left(\frac{\delta R}{R}\right)^2} \qquad (6.1)$$

considering the influence of pellet thickness l and the error of the fit of the resistance R. Due to the nature of the setup, the error in the area, A, is considered negligible by the authors. A 5% error was estimated for the pellet thickness (from the standard deviation of the thickness measured by the micrometer at different positions across the pellet), due to deviations in the thickness across the pellet. The error of the activation energy was calculated based on the fit of the Arrhenius relationship.

Electrochemical Measurements

The redox activity of the solid electrolytes was measured in the same assembly as the ionic conductivity, consisting of an alumina cylinder and stainless steel plungers. The solid electrolyte−carbon composites were made by ball milling of the solid electrolytes with Super C45 and carbon nanofibers in the weight ratio of 0.85:0.10:0.05 for 2 h at 300 rpm. This mixture was tested for both oxidation and reduction stability. Depending on the reaction, either a lithium source or drain is needed as the counter electrode with a known constant potential.

Lithium titanate ($Li_4Ti_5O_{12}$, from altair nano) was used as a lithium drain. As the material does not have a constant potential at the beginning of the lithiation, the material was prelithiated chemically using n-butyllithium (1.6 M from Merck Sigma). The amount of n-butyllithium needed to half lithiate the $Li_4Ti_5O_{12}$ to Li5.5Ti5O12 (prelithiated LTO) was calculated, and the reaction was carried out in hexane while stirring continuously inside an Ar-filled glovebox. After the reaction, the hexane was evaporated. For the measurements, the prelithiated LTO, the $Li_3YBr_xCl_{6−x}$ solid electrolyte, Super C45, and carbon nanofibers were ball milled with the ratio of 0.45:0.40:0.10:0.05 for 2 h at 300 rpm. Twenty-five milligrams of that mixture was used as the electrode.

As a lithium source, Li−In alloy was used. A Φ7 mm indium foil (≈58 mg) was prelithated with Φ3 mm Li foil (≈1 mg) by pressing the foils on top of each other. Li in indium is at 0.62 V vs Li/Li+, and therefore, the in foil will lithiate spontaneously. The fabrication of ASSBs starts with a cold pressing of 150 mg of the $Li_3YBr_xCl_{6−x}$ solid electrolytes under the pressure of 392 MPa. Sequentially, 16 mg of the halide−carbon mixture was placed and pressed under the pressure of 490 MPa on the one side, and the reference electrodes were then pressed on the other side (prelithiated LTO and In−Li alloy under the pressure of 490 and 50 MPa, respectively).

The oxidation and reduction voltages were measured by drawing a constant current of 6.5 µA/cm2 to 0 V vs Li/Li+ (reduction of the solid electrolyte), i.e., galvanostatically charging to 3.5 V versus prelithiated LTO or discharging to -0.62 V versus the In−Li alloy with a current density of 6.5 µA/cm2. For the determination of the electrochemical stability window, the differential capacity was calculated based on the charge and discharge profiles.

Battery Assembly

ASSBs were assembled using single crystal NCM 811 (MSE supplies) as a cathode and Li–In as an anode. To ensure reversibility on the anode side, argyrodite Li6PS5Cl (acquired from NEI corporation) was used as an interlayer between the halide SE and the Li–In alloy. During assembly, the first 50 mg of the halide solid electrolyte was pressed at 20 MPa for 2 min. Then 50 mg of argyrodite was added on the other side and the pressing repeated. Around 10 mg of NCM 811 (composite 70% NCM 811 and 30% halide solid electrolyte, mixed using pestle and mortar) was added on the halide SE side. Prelithiated In foil (52 mg of indium foil, 8 mm diameter, and 2 mg of Li-metal foil pressed on) was then added on the argyrodite Li6PS5Cl side. The whole cell was pressed at 5 MPa for 1 min. The cells were cycled at C/10 between 2.75 and 4.3 V vs Li/Li+.

6.4 Results

A series of $Li_3YBr_xCl_{6-x}$ (x = [0, 6] steps of 1.5) solid electrolytes were synthesized by direct co-melting of the precursors in evacuated silica ampules at 650 ℃. The powders obtained were phase-pure for all compositions. The X-ray diffraction patterns shown in Figure 6.1a clearly show that the materials crystallize in two different phases, depending on the ratio between Cl and Br.

The Li_3YCl_6 sample crystallized in the trigonal $P\bar{3}m1$ (#164) [23] space group, as does $Li_3YBr_xCl_{6-x}$ with x = 1.5. The materials with x > 1.5, as well as the full bromide Li_3YBr_6, crystallize in monoclinic $C2/m$ (#12) [24] space group. Due to the larger anion radius of Br, the lattice parameters increase as Br is added to the system (Figure 6.1b).

Between the compositions $Li_3YBr_xCl_{6-x}$, x = 1.5 and x = 3, where the phase transition occurs, the volume of the unit cell decreases due to the smaller unit cell size of the monoclinic phase. The volume per chemical formula unit increases linearly with bromine content (Figure 8.23)). With conventional Rietveld refinement, it was not possible to refine the X-ray data due to mismatch in peak intensities, especially the peaks between 2ϑ= 18−25°for the $C2/m$ phase.

To investigate this effect, different synthesis methods were applied (mechanochemical synthesis, mechanochemical synthesis + annealing step, co-melting) comparing the resulting morphology and diffraction patterns (Figures 8.24 - 8.25 and section 8.3).

While mechanochemical synthesis leads to a fine powder with no distinct features in the microstructure, heat treatment above 500 ℃ leads to the formation of platelets (Figure 8.26), which corresponds to the disappearance of the Bragg peaks between 2θ = 18−25°(Figure 8.24). This suggests that the anisotropic, platelet-like morphology, which can show as preferred orientation due to nonrandom orientation of the powder when the X-ray diffraction data is measured in Bragg–Brentano geometry, could be at least a source of the discrepancy.

However, recent literature has reported the occurrence of stacking faults in Li_3YCl_6 [25] and $Li_3HoBr_xI_{6-x}$ [7] presenting an alternative origin for the discrepancy (SI section 8.3). As described in ref [25], neutron diffraction data are less sensitive to stacking faults compared to X-ray diffraction in Li_3YCl_6, due to the different contrast. Further, due to the larger amount of sample and the transmission geometry, the neutron diffraction data are also less sensitive to preferred orientation, compared to X-ray diffraction data measured in Bragg–Brentano geometry. Therefore, neutron diffraction was performed to confirm the monoclinic average symmetry and to learn more about the structural effect of anion

Figure 6.1: (a) X-ray diffraction patterns of the series of $Li_3YBr_xCl_{6-x}$ (x = 0–6) solid electrolytes. Magnified images of a group of characteristic peaks from the diffraction patterns of the $Li_3YBr_xCl_{6-x}$ samples are shown. (b) Evolution of the lattice parameters of $Li_3YBr_xCl_{6-x}$ as a function of x as obtained from the Le Bail refinement of the X-ray diffraction data. For comparison, the lattice parameters of each halide achieved from previous reports are shown (Li_3YBr_6/Cl6 from ref [2], Li3YBr3Cl3 from ref [9]).
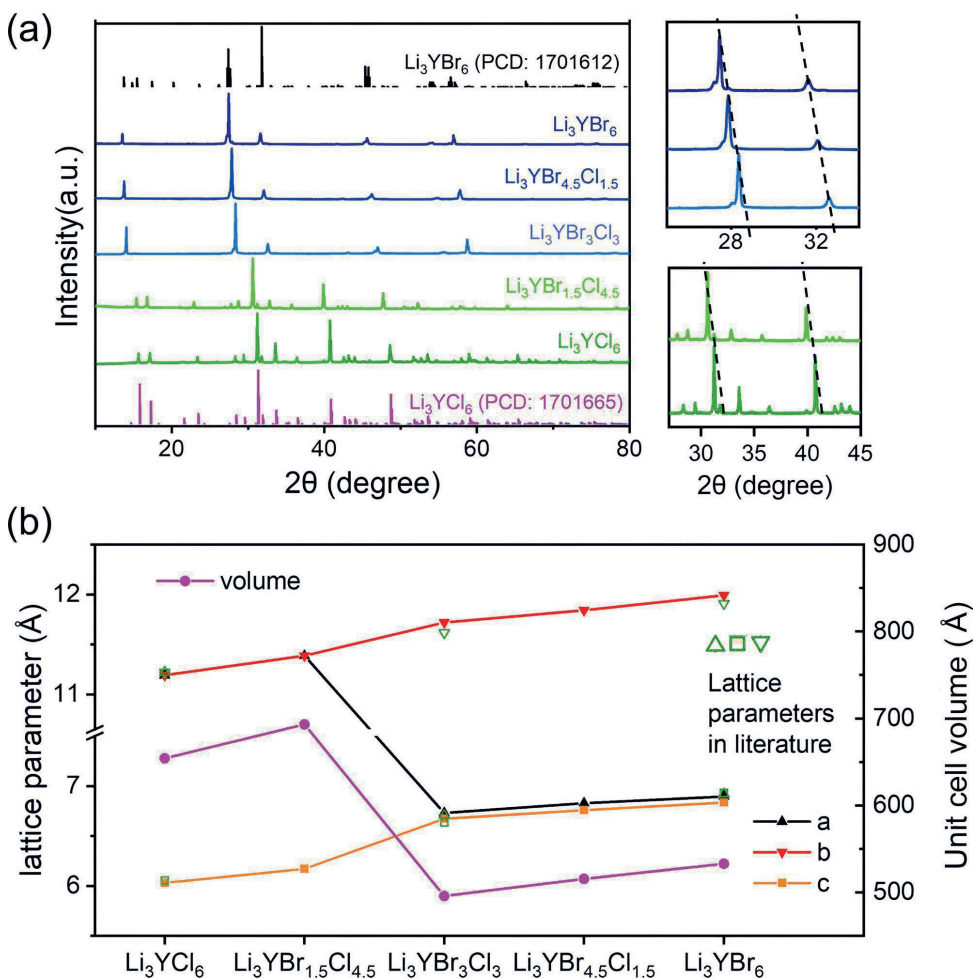
substitution in $Li_3YBr_xCl_{6-x}$ by means of Rietveld refinement (Figure 6.2a,b, Figures 8.27 - 8.31).

The crystal structures of the trigonal and monoclinic phases have distinct structural characteristics (Figure 6.2). The trigonal structure with the compositions $Li_3YBr_xCl_{6-x}$ at x = 0 and 1.5 is built by hexagonal close-packing (hcp)-like arrangement of the halogen atoms, with the Y and Li in octahedral positions. The Rietveld refinement shows that the Cl and Br atoms distribute statistically across the halogen sites (as consistent with literature; see refs [7, 8]) and small differences in the Y and Li occupancies (SI Tables S4 and S5). The monoclinic phase with the compositions $Li_3YBr_xCl_{6-x}$ at x = 3, 4.5, and 6 on the other hand,

Figure 6.2: Rietveld refinement of the neutron diffraction data (top) and crystal structure (bottom) for the monoclinic (a) and trigonal (b) phase of Li$_3$YBr$_x$Cl$_{6-x}$. (a) Structure solution of Li$_3$YBr$_x$Cl$_{6-x}$ for x = 3 The cubic close packing-like framework is highlighted along the c-direction, as illustrated by the alternating layers A, B, and C. The Y atoms mostly occupy the Y1 (2a) site, with some on the Y2(4h) site. The 4h site is shared with Li. The lithium is distributed across the 4h site and the other empty octahedra. (b) Structure solution for Li$_3$YBr$_x$Cl$_{6-x}$ for x = 1.5. The hexagonal close packing like framework is along the c-direction, as indicated by the alternating A and B layers. There is one fully occupied Y site, i.e., Y3(1a). The Y2(2d) site is almost fully occupied, while the Y1(2d) site is only 7% occupied.
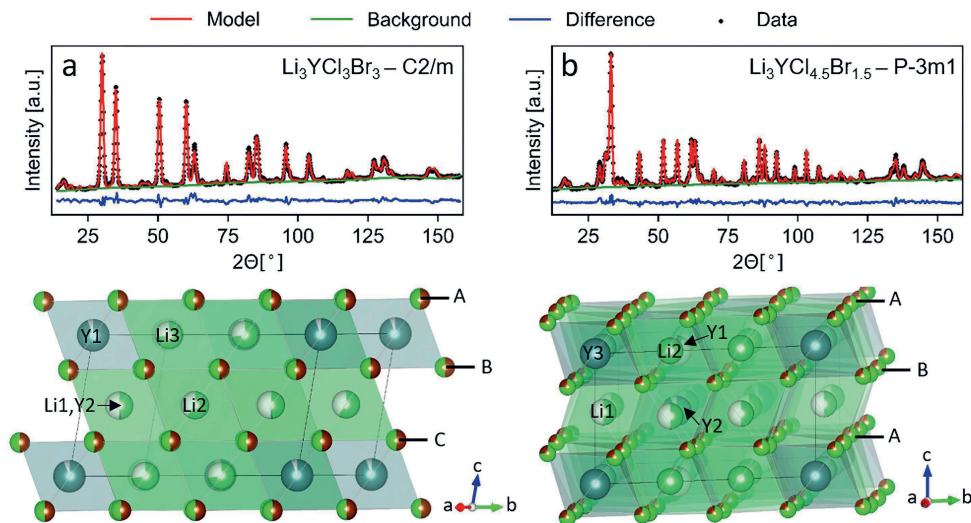
shows cubic close packing (ccp) of the halogen atoms. Similar to the trigonal phase, the Cl and Br distribute statistically across the halogen sites and the Y and Li reside on octahedral sites. Also here, there appear to be small redistributions of the Li and Y, but there is no clear trend as a function of x (SI Tables S1–S3). No tetrahedral sites were necessary for a physically consistent refinement as reported in isostructural chlorides [26, 27]. Despite that the tetrahedral voids are not occupied on average, they are still available as interstitial sites for the diffusion pathways.

The ionic conductivities of the various Li$_3$YBr$_x$Cl$_{6-x}$ solid electrolytes as a function of temperature are determined by broadband AC impedance spectroscopy (Figure 6.3). The ionic conductivity at 30 ℃ is lowest for Li$_3$YCl$_6$ at 0.05 × 10^{-3} S/cm. Already the small amount of Br in Li$_3$YBr$_{1.5}$Cl$_{4.5}$ leads to a large increase in ionic conductivity to 2.1 × 10^{-3} S/cm, where the material is still in the trigonal phase. The ionic conductivity increases further as x is increased and reaches a maximum of 5.36 × 10^{-3} S/cm for Li$_3$YBr$_{4.5}$Cl$_{1.5}$ in the monoclinic phase. The activation energy reflects a similar trend: it has the highest value for the chloride end-member Li$_3$YCl$_6$ (0.685 eV), reduces to 0.413 eV for Li$_3$YBr$_{1.5}$Cl$_{4.5}$, and reaches its minimum of 0.276 eV for Li$_3$YBr$_{4.5}$Cl$_{1.5}$ (Figure 6.3; see Figure 8.32 for the complete conductivity datasets and Arrhenius relationship fits). There are many reasons that could cause differences in ionic conductivities in this substitution series:

- The association energy of Li with Br is smaller than that with Cl, due to the smaller electronegativity/larger lattice polarizability. [28–30]

Figure 6.3: Ionic conductivity σ[S/cm] at 30 ℃ and activation energies extracted from the Arrhenius relationship (see Figures 8.32) of $Li_3YBr_xCl_{6-x}$.
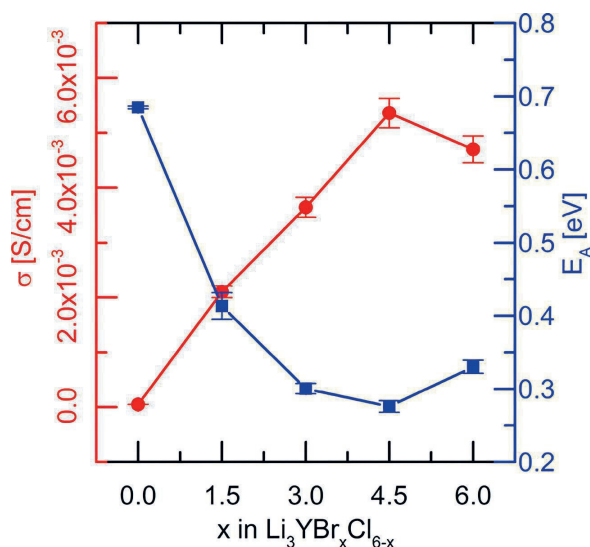
- As the crystal structure transitions from the trigonal to the monoclinic phase, the anionic framework transforms from hexagonal close packing (hcp) to cubic close packing (ccp). In the hexagonal close packing, lithium can jump through face-sharing octahedral–octahedral (oct–oct), octahedral–tetrahedral–octahedral (oct–tet–oct), and tetrahedral–tetrahedral (tet–tet) pathways. In the cubic close packed framework, only oct–tet–oct paths exist [31]. Calculations have shown that hcp chlorides have slightly lower activation energies (0.25 eV oct–oct and 0.29 oct–tet–oct) compared to ccp bromides (0.28 oct–tet–oct). [13]

- With the introduction of more (larger) Br, the lattice expands, rendering larger polyhedral faces ("bottlenecks") for the Li to jump through [32, 33].

- (Small) changes in the Y and/or Li site occupancies may affect the ionic conductivity [34, 35]. Finally, there are reports that the increase in configurational entropy in mixed (poly)anion substituted samples may alter the ionic conductivity [36, 37].

While it is not possible to deconvolute these factors based on the data presented here, some general observations can be made. First of all, if the increase in ionic conductivity due to the larger lattice polarizability was the only/main factor at play, the activation energy should decrease monotonically with x, which is not the case. A similar argument can be made for the configurational entropy, if it was the only/main factor at play the maximum in ionic conductivity should be found at x = 3 in $Li_3YBr_xCl_{6-x}$. The trigonal phase has much higher activation energies (0.685 eV for x = 0, 0.413 eV for x = 1.5) compared to the monoclinic phase (0.300 eV for x = 3, 0.276 eV for x = 4.5, 0.330 eV for x = 6), it is therefore rather likely that the ccp-like packing is more favorable, as also postulated

theoretically in literature for sulfides (where, however, Li preferentially resides in tetrahedral coordination). (32) Considering the large change in ionic conductivity from Li$_3$YCl$_6$ to Li$_3$YBr$_{1.5}$Cl$_{4.5}$, it is likely that the increase of the lattice parameters aids the conductivity in the $P\bar{3}m1$ phase.

To investigate the effect of site occupancies, more compositions should be considered and X-ray diffraction data should be refined simultaneously with the neutron diffraction data for more accurate site occupancies. The deconvolution of these different effects and determination of detailed site occupancies are subject of future research.

Experimentally measuring the solid electrolyte stability window is challenging. Previous reports have often determined the electrochemical stability window using cyclic voltammetry (CV), which shows a pair of peaks to reflect the reduction and oxidation reactions [9, 38, 39]. However, the short exposure time of a CV scan makes it challenging to probe the electrochemical stability window of solid electrolytes, in which the kinetics of decomposition are sluggish due to the limited contact area, poor electronic conductivity, and charge transfer [14]. To circumvent these problems, the electrochemical stability was measured as reported in Schwietert et al. [14]. Electrochemical cells were assembled using a simultaneous reference and counter electrode (in this case a Li intercalation (Li$_4$Ti$_5$O$_{12}$ (LTO-C)) and alloying compound (Li–In) with constant potential for the Li concentrations measured) and a composite of the solid electrolyte mixed with carbon black as a working electrode (see schematic Figure 6.4a). The composite was then oxidized and reduced using galvanostatic measurements at 6.5 μA/cm2, so that the oxidation and reduction potential could be measured with minimal overpotential. The voltage curve of these cells is shown in Figure 6.4b. The curves show clear plateaus with large specific capacities (100–240 mAh/g of solid electrolyte), indicating that there is significant oxidation and reduction of the solid electrolytes.

The onset of the voltage plateaus corresponds to the onset voltages of the peaks in the differential capacity curves (Figure 6.4c). This onset voltage is where decomposition is initiated, and is the limiting value used for the decomposition window that is plotted in Figure 6.4d. The plot shows that the oxidative stability of Li$_3$YBr$_x$Cl$_{6-x}$ can be split into two groups, one with an oxidation onset at 3.0 V for $3 < x \leq 6$ and 3.5 V for $x < 3$. This two groups can be distinguished in two ways, namely their crystal structure ($P\bar{3}m1$ vs $C2/m$), as well as the dominant anion (Cl-rich vs Br-rich). Oxidation of the halogen would, according to thermodynamic calculations, lead to the formation of halogen gas. Therefore, two Br atoms would need to be in close proximity to each other. Low enough Br concentrations could ensure that the Br are enough separate in space that the necessity for to Br atoms in close proximity is not given and oxidation cannot happen. On the other hand, it could also be due to the trigonal crystal structure (or the hcp-like arrangement of the anions) which could be less prone to oxidize compared to the monoclinic structure (or ccp-like arrangement of the anions). For Li$_3$YBr$_6$, the oxidation onset value from the dC/dV curve is at 3 V which is smaller than the calculated thermodynamic decomposition window (3.15 V) and the intrinsic (oxidation and reduction) window (3.43 V). For Li$_3$YCl$_6$, the oxidation onset at 3.5 V is also smaller compared to the calculated thermodynamic decomposition window (4.21 V). It is interesting to consider the position of the maxima of the dC/dV curves, as in principle it could be more representative of bulk values, should interface effects lower the onset potential. For Li$_3$YBr$_6$, the maximum of the dC/dV curve

Figure 6.4: Electrochemical stability assessment in ASSBs with $Li_3YBr_xCl_6-x$ (a) Schematic view of the cell configuration. Different configurations of pellets are pressed between the blocking electrodes. Carbon and $Li_3YBr_xCl_6-x$ composites are used as working electrodes, while $Li_4Ti_5O_{12}$ (LTO)-C and In−Li are used as counter electrodes, respectively. (b) Galvanostatic charge and discharge curves of $Li_3YBr_xCl_6-x$-C|$Li_3YBr_xCl_6-x$|LTO-C and $Li_3YBr_xCl_6-x$-C|$Li_3YBr_xCl_6-x$|In−Li ASSBs, respectively. (c) Differential capacity dC/dV curves of the redox activities of $Li_3YBr_xCl_6-x$ solid electrolytes. (d) Electrochemical stability window inferred from the experimental voltage profiles. The dashed lines indicate the redox potential barriers of Li_3YCl_6 and Li_3YBr_6, and the arrows indicate where the barriers shift within the $Li_3YBr_xCl_6-x$ solid electrolytes. The thermodynamic decomposition windows [13] and intrinsic windows predicted based on DFT calculation [15] are also plotted for comparison. The thermodynamic decomposition window is the voltage at which the material decomposes to the most stable known products, whereas the intrinsic window represents the voltage at which the solid electrolytes de/lithiate, allowing the formation of reaction intermediates.
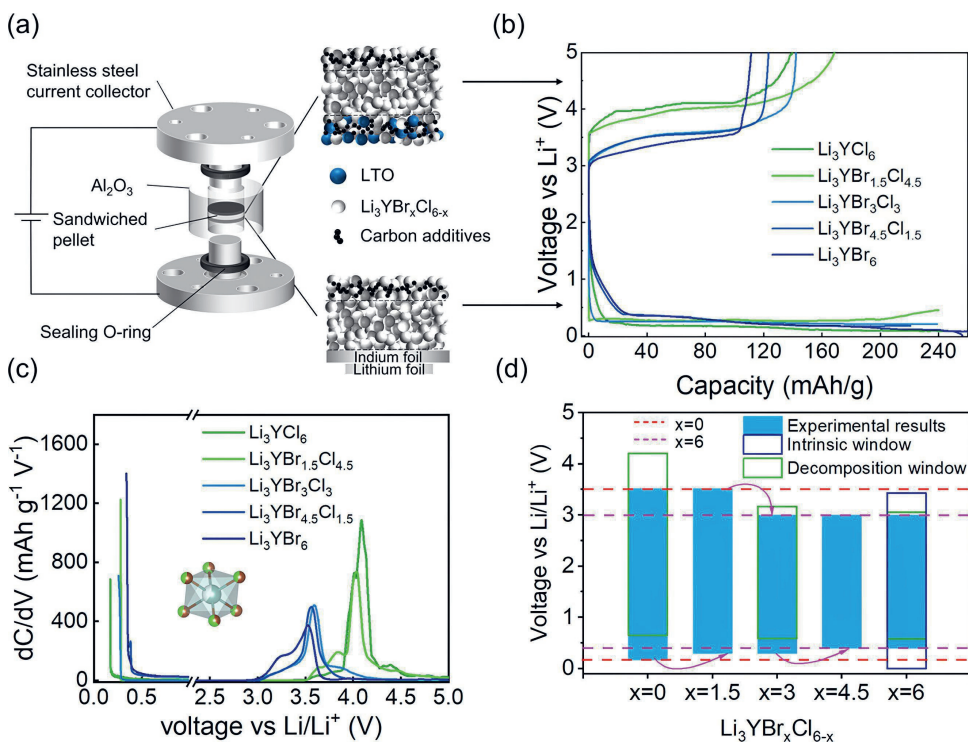
is at 3.4 V, which corresponds with the voltage predicted by the calculations of the intrinsic window. For Li_3YCl_6, the maximum of the dC/dV curve is at 4.2 V, the value predicted for the thermodynamic decomposition window. To conclude, the experimental data confirm the trend in oxidation potential predicted by theoretical calculations between Li_3YBr_6 and Li_3YCl_6, but neither calculation method accurately predicts the values observed here. Considering the mixed halide samples $Li_3YBr_xCl_6-x$ (x = 1.5, 3, 4.5), there is a clear trend. Low Br concentrations do not affect the oxidation potential, as trigonal $Li_3YBr_{1.5}Cl_{4.5}$ follows the behavior of the trigonal chloride end-member Li_3YCl_6. All other compositions, crystallizing in the monoclinic phase, $Li_3YBr_xCl_6-x$ (x = 3, 4.5) show similar behavior to monoclinic bromide end-member Li_3YBr_6 (see Figure 6.4d). The electrolytes $Li_3YBr_xCl_6-x$

(x = 1.5, 4.5) were tested in full cells using single crystal NCM811/halide SE composite as cathode, halide SE as electrolyte, a Li6PS5Cl interlayer, and Li–In as anode (see Figure 8.33). Li$_3$YBr$_x$Cl$_{6-x}$ with x = 1.5 showed a first cycle Coulombic efficiency of 79.95%, compared to 73.05% for x = 4.5 (in comparison, the same cathode tested in a liquid cell had 83.79% Coulombic efficiency). This is an indicator for less SE decomposition during the first cycle. Concluding, results of the ionic conductivity and electrochemical window measurements show that there is a trade-off in the Li$_3$YBr$_x$Cl$_{6-x}$ substitution range. While the ionic conductivity is highest at x = 4.5 in the monoclinic phase, the electrolyte starts to oxidize at 3 V, similar to Li$_3$YBr$_6$. Small Br concentrations, here represented by x = 1.5, increase the ionic conductivity significantly in the $P\bar{3}m$1 phase but maintain the high oxidation potential of Li$_3$YCl$_6$.

6.5 Conclusion

The substitution series Li$_3$YBr$_x$Cl$_{6-x}$ (x = 0, 1.5, 3, 4.5, 6) were synthesized by co-melting of the precursors. The proposed crystal structures (trigonal $P\bar{3}m$1/monoclinic $C2/m$) for Li$_3$YCl$_6$/Li$_3$YBr$_6$ are a good fit to neutron diffraction data as demonstrated by Rietveld refinement. The composition Li3YCl4.5Br1.5 crystallized in trigonal $P\bar{3}m$1 (like Li$_3$YCl$_6$), and the compositions Li$_3$YBr$_x$Cl$_{6-x}$ with x = 3, 4.5 in monoclinic $C2/m$ (like Li$_3$YBr$_6$).

Already a small Br content (x = 1.5) increases the ionic conductivity by 2 orders of magnitude compared to Li$_3$YCl$_6$ (2.02 compared to 0.047 × 10^{-3} S/cm at 30 ℃). The maximum ionic conductivity of 5.18 × 10^{-3} S/cm at 30 ℃ is reached for the monoclinic Li$_3$YBr$_x$Cl$_{6-x}$ with x = 4.5. The investigation of the oxidative stability confirm that the solid electrolytes with high Cl content have a higher oxidation potential compared to the ones with high Br content. A small amount of Br substitution (x = 1.5) does not affect the oxidation potential and the measurement shows similar behavior to stable Li$_3$YCl$_6$, whereas larger Br contents (x = 3, 4.5) show behavior similar to the less electrochemically stable Li$_3$YBr$_6$.

These results show a clear trade-off between ionic conductivity and electrochemical stability in this substitution series.

We highlight the lightly Br-substituted Li3YCl4.5Br1.5 as the best compromise, achieving the "best of both end-members", with a conductivity ≈200 higher than trigonal Li$_3$YCl$_6$ and an oxidative stability ≈0.5 V higher than monoclinic Li$_3$YBr$_6$. This work highlights that careful optimization of composition and substitutions in the anion framework provide prolific and rational avenues for designing the properties of future solid electrolytes.

References

[1] Theodosios Famprikis, Pieremanuele Canepa, James A. Dawson, M. Saiful Islam, and Christian Masquelier. Fundamentals of inorganic solid-state electrolytes for batteries. *Nature Materials*, 18(12):1278–1291, December 2019.

[2] Tetsuya Asano, Akihiro Sakai, Satoru Ouchi, Masashi Sakaida, Akinobu Miyazaki, and Shinya Hasegawa. Solid Halide Electrolytes with High Lithium-Ion Conductivity for Application in 4 V Class Bulk-Type All-Solid-State Batteries. *Advanced Materials*, 30(44):1803075, November 2018.

[3] Xiaona Li, Jianwen Liang, Xiaofei Yang, Keegan R. Adair, Changhong Wang, Feipeng Zhao, and Xueliang Sun. Progress and perspectives on halide lithium conductors for all-solid-state lithium batteries. *Energy & Environmental Science*, 13(5):1429–1461, 2020.

[4] Changhong Wang, Jianwen Liang, Jung Tae Kim, and Xueliang Sun. Prospects of halide-based all-solid-state batteries: From material design to practical application. *Science Advances*, 8(36):eadc9516, September 2022.

[5] Qian Zhang, Zhiqing Gao, Xiaomeng Shi, Chao Zhang, Kang Liu, Jun Zhang, Liang Zhou, Chunjie Ma, and Yaping Du. Recent advances on rare earths in solid lithium ion conductors. *Journal of Rare Earths*, 39(1):1–10, January 2021.

[6] Laidong Zhou, Tong-Tong Zuo, Chun Yuen Kwok, Se Young Kim, Abdeljalil Assoud, Qiang Zhang, Jürgen Janek, and Linda F. Nazar. High areal capacity, long cycle life 4 V ceramic all-solid-state Li-ion batteries enabled by chloride solid electrolytes. *Nature Energy*, January 2022.

[7] Maximilian A. Plass, Sebastian Bette, Robert E. Dinnebier, and Bettina V. Lotsch. Enhancement of Superionic Conductivity by Halide Substitution in Strongly Stacking Faulted $Li_3HoBr_{6-x}I_x$ Phases. *Chemistry of Materials*, page acs.chemmater.2c00024, March 2022.

[8] Andreas Bohnsack and Gerd Meyer. Ternäre Halogenide vom Typ A3MX6. V. Synthese, Kristallstrukturen und Natrium-Ionenleitfähigkeit der ternären Iodide Na3MI6 (M = Sm, Gd-Dy) sowie der Mischkristalle Na3GdBr6-xIx. *Zeitschrift für anorganische und allgemeine Chemie*, 623(1-6):837–843, 1997.

[9] Zhantao Liu, Shuan Ma, Jue Liu, Shan Xiong, Yifan Ma, and Hailong Chen. High Ionic Conductivity Achieved in $Li_3Y(Br_3Cl_3)$ Mixed Halide Solid Electrolyte via Promoted Diffusion Pathways and Enhanced Grain Boundary. *ACS Energy Letters*, 6(1):298–304, January 2021.

[10] Y. Tomita, H. Matsushita, K. Kobayashi, Y. Maeda, and K. Yamada. Substitution effect of ionic conductivity in lithium ion conductor li3inbr6-xclx. *Solid State Ionics*, 179(21-26):867–870, September 2008.

[11] Yasumasa Tomita, Hiroo Nishiyama, Kenkichiro Kobayashi, Yoshiumi Kohno, Yasuhisa Maeda, and Koji Yamada. Substitution effect for br on the lithium ion conductivity of lithium indium bromide. *ECS Transactions*, 16(29):137–141, August 2009.

[12] Alysia Zevgolis, Brandon C. Wood, Zerina Mehmedović, Alex T. Hall, Thomaz C. Alves, and Nicole Adelstein. Alloying effects on superionic conductivity in lithium indium halides for all-solid-state batteries. *APL Materials*, 6(4):047903, April 2018.

[13] Shuo Wang, Qiang Bai, Adelaide M. Nolan, Yunsheng Liu, Sheng Gong, Qiang Sun, and Yifei Mo. Lithium Chlorides and Bromides as Promising Solid-State Chemistries for Fast Ion Conductors with Good Electrochemical Stability. *Angewandte Chemie International Edition*, 58(24):8039–8043, June 2019.

[14] Tammo K. Schwietert, Violetta A. Arszelewska, Chao Wang, Chuang Yu, Alexandros Vasileiadis, Niek J. J. de Klerk, Jart Hageman, Thomas Hupfer, Ingo Kerkamm, Yaolin Xu, Eveline van der Maas, Erik M. Kelder, Swapna Ganapathy, and Marnix Wagemaker. Clarifying the relationship between redox activity and electrochemical stability in solid electrolytes. *Nature Materials*, January 2020.

[15] Tammo K. Schwietert, Alexandros Vasileiadis, and Marnix Wagemaker. First-Principles Prediction of the Electrochemical Stability and Reaction Mechanisms of Solid-State Electrolytes. *JACS Au*, 1(9):1488–1496, September 2021.

[16] Dongsu Park, Haesun Park, Yongheum Lee, Sang-Ok Kim, Hun-Gi Jung, Kyung Yoon Chung, Joon Hyung Shim, and Seungho Yu. Theoretical Design of Lithium Chloride Superionic Conductors for All-Solid-State High-Voltage Lithium-Ion Batteries. *ACS Applied Materials & Interfaces*, 12(31):34806–34814, August 2020.

[17] Ivan Kochetkov, Tong-Tong Zuo, Raffael Ruess, Baltej Singh, Laidong Zhou, Kavish Kaup, Jürgen Janek, and Linda Nazar. Different interfacial reactivity of lithium metal chloride electrolytes with high voltage cathodes determines solid-state battery performance. *Energy & Environmental Science*, page 10.1039.D2EE00803C, 2022.

[18] Brian H. Toby and Robert B. Von Dreele. *GSAS-II* : the genesis of a modern open-source all purpose crystallography software package. *Journal of Applied Crystallography*, 46(2):544–549, April 2013.

6

[19] Brian H. Toby and Robert B. Von Dreele. What's new in GSAS-II. *Powder Diffraction*, 29(S2):S2–S6, December 2014.

[20] L. van Eijck, L. D. Cussen, G. J. Sykora, E. M. Schooneveld, N. J. Rhodes, A. A. van Well, and C. Pappas. Design and performance of a novel neutron powder diffractometer: PEARL at TU Delft. *Journal of Applied Crystallography*, 49(5):1398–1401, October 2016.

[21] Koichi Momma and Fujio Izumi. *VESTA* : a three-dimensional visualization system for electronic and structural analysis. *Journal of Applied Crystallography*, 41(3):653–658, June 2008.

[22] Irina V. Krasnikova, Mariam A. Pogosova, Alexey O. Sanin, and Keith J. Stevenson. Toward Standardization of Electrochemical Impedance Spectroscopy Studies of Li-Ion Conductive Ceramics. *Chemistry of Materials*, 32(6):2232–2241, March 2020.

[23] Andreas Bohnsack, Frauke Stenzel, Armin Zajonc, Gert Balzer, Mathias S. Wickleder, and Gerd Meyer. Ternäre halogenide vom typ a3mx6 vi. ternäre chloride der selten-erd-elemente mit lithium lithium, li3mcl6 (m=tb-lu, y, sc): Synthese, krisallstrukturen und ionenbewegung. *Zeitschrift für anorganische und allgemeine Chemie*, 623(7):1067–1073, July 1997.

[24] Andreas Bohnsack, Gert Balzer, Hans-U. Gödel, Mathias S. Wickleder, and Gerd Meyer. Ternäre halogenide vom typ a3mx6. vii. die bromide li3mbr6 (m=sm-lu, y): Synthese, kristallstruktur, ionenbeweglichkeit. *Zeitschrift für anorganische und allgemeine Chemie*, 623(9):1352–1356, September 1997.

[25] Elias Sebti, Hayden A. Evans, Hengning Chen, Peter M. Richardson, Kelly M. White, Raynald Giovine, Krishna Prasad Koirala, Yaobin Xu, Eliovardo Gonzalez-Correa, Chongmin Wang, Craig M. Brown, Anthony K. Cheetham, Pieremanuele Canepa, and Raphaële J. Clément. Stacking Faults Assist Lithium-Ion Conduction in a Halide-Based Superionic Conductor. *Journal of the American Chemical Society*, page jacs.1c11335, March 2022.

[26] Bianca Helm, Roman Schlem, Björn Wankmiller, Ananya Banik, Ajay Gautam, Justine Ruhl, Cheng Li, Michael Ryan Hansen, and Wolfgang G. Zeier. Exploring aliovalent substitutions in the lithium halide superionic conductor li$_{3-x}$in$_{1-x}$zr$_x$cl$_6$ (0≤ x ≤ 5. *Chemistry of Materials*, 33(12):4773–4782, June 2021.

[27] Hiram Kwak, Daseul Han, Jun Pyo Son, Jong Seok Kim, Juhyoun Park, Kyung-Wan Nam, Hyungsub Kim, and Yoon Seok Jung. Li+ conduction in aliovalent-substituted monoclinic Li2ZrCl6 for all-solid-state batteries: Li2+xZr1-xMxCl6 (M = In, Sc). *Chemical Engineering Journal*, 437:135413, June 2022.

[28] Sokseiha Muy, Roman Schlem, Yang Shao-Horn, and Wolfgang G. Zeier. Phonon–Ion Interactions: Designing Ion Mobility Based on Lattice Dynamics. *Advanced Energy Materials*, 11(15):2002787, April 2021.

[29] Marvin A. Kraft, Sean P. Culver, Mario Calderon, Felix Böcher, Thorben Krauskopf, Anatoliy Senyshyn, Christian Dietrich, Alexandra Zevalkink, Jürgen Janek, and Wolfgang G. Zeier. Influence of Lattice Polarizability on the Ionic Conductivity in the Lithium Superionic Argyrodites Li $_6$ PS $_5$ X (X = Cl, Br, I). *Journal of the American Chemical Society*, 139(31):10909–10918, August 2017.

[30] Roman Schlem, Tim Bernges, Cheng Li, Marvin A. Kraft, Nicolo Minafra, and Wolfgang G. Zeier. Lattice Dynamical Approach for Finding the Lithium Superionic Conductor Li $_3$ ErI $_6$. *ACS Applied Energy Materials*, 3(4):3684–3691, April 2020.

[31] Yan Wang, William Davidson Richards, Shyue Ping Ong, Lincoln J. Miara, Jae Chul Kim, Yifei Mo, and Gerbrand Ceder. Design principles for solid-state lithium superionic conductors. *Nature Materials*, 14(10):1026–1031, October 2015.

[32] Saneyuki Ohno, Ananya Banik, Georg F. Dewald, Marvin A. Kraft, Thorben Krauskopf, Nicoló Minafra, Paul Till, Manuel Weiss, and Wolfgang G. Zeier. Materials design of ionic conductors for solid state batteries. *Progress in Energy*, 2(2):022001, 2020.

[33] Ana Martínez-Juárez, Carlos Pecharromán, Juan E. Iglesias, and José M. Rojo. Relationship between Activation Energy and Bottleneck Size for Li $^+$ Ion Conduction in NASICON Materials of Composition LiMM'(PO $_4$) $_3$; M, M' = Ge, Ti, Sn, Hf. *The Journal of Physical Chemistry B*, 102(2):372–375, January 1998.

6

[34] Roman Schlem, Sokseiha Muy, Nils Prinz, Ananya Banik, Yang Shao-Horn, Mirijam Zobel, and Wolfgang G. Zeier. Mechanochemical Synthesis: A Tool to Tune Cation Site Disorder and Ionic Transport Properties of Li3MCl6 (M = Y, Er) Superionic Conductors. *Advanced Energy Materials*, n/a(n/a):1903719, 2020.

[35] Roman Schlem, Ananya Banik, Saneyuki Ohno, Emmanuelle Suard, and Wolfgang G. Zeier. Insights into the Lithium Sub-structure of Superionic Conductors Li_3YCl_6 and Li_3YBr_6. *Chemistry of Materials*, 33(1):327–337, January 2021.

[36] Florian Strauss, Jing Lin, Marie Duffiet, Kai Wang, Tatiana Zinkevich, Anna-Lena Hansen, Sylvio Indris, and Torsten Brezesinski. High-Entropy Polyanionic Lithium Superionic Conductors. *ACS Materials Letters*, 4(2):418–423, February 2022.

[37] Yue Deng, Christopher Eames, Benoit Fleutot, Rénald David, Jean-Noël Chotard, Emmanuelle Suard, Christian Masquelier, and M. Saiful Islam. Enhancing the Lithium Ion Conductivity in Lithium Superionic Conductor (LISICON) Solid Electrolytes through a Mixed Polyanion Effect. *ACS Applied Materials & Interfaces*, 9(8):7050–7058, March 2017.

[38] Jianwen Liang, Eveline van der Maas, Luo, Jing, Xiaona Li, Ning chen, Keegan R. Adair, Weihan Li, Junjie Li, Yongfeng Hu, Jue Liu, Li Zhang, Shangqian Zhao, Shigang Lu, Jiantao Wang, huan huang, Wenxuan Zhao, Steven Parnell, Ronald I. smith, Swapna Ganapathy, Marnix Wagemaker, and Xueliang Sun. A Series of Ternary Metal Chloride Superionic Conductors for High-Performance All-Solid-State Lithium Batteries. *A Series of Ternary Metal Chloride Superionic Conductors for High-Performance All-Solid-State Lithium Batteries*, 2022.

[39] Jianwen Liang, Xiaona Li, Shuo Wang, Keegan R. Adair, Weihan Li, Yang Zhao, Changhong Wang, Yongfeng Hu, Li Zhang, Shangqian Zhao, Shigang Lu, Huan Huang, Ruying Li, Yifei Mo, and Xueliang Sun. Site-Occupation-Tuned Superionic Li_xScCl_{3+x} Halide Solid Electrolytes for All-Solid-State Batteries. *Journal of the American Chemical Society*, 142(15):7012–7022, April 2020.

6

7

A Series of Ternary Metal Chloride Superionic Conductors for High-Performance All-Solid-State Lithium Batteries

Authors: Jianwen Liang†, *Eveline van der Maas* †, Jing Luo†, Xiaona Li, Ning Chen, Keegan R. Adair, Weihan Li, Junjie Li, Yongfeng Hu, Jue Liu, Li Zhang, Shangqian Zhao, Shigang Lu, Jiantao Wang, Huan Huang, Wenxuan Zhao, Steven Parnell, Ronald I. Smith, Swapna Ganapathy, Marnix Wagemaker,* and Xueliang Sun*

* Corresponding authors
†These authors contributed equally to the manuscript

7.1 Abstract

Understanding the relationship between structure, ionic conductivity, and synthesis is the key to the development of superionic conductors. Here, a series of $Li_{3-3x}M_{1+x}Cl_6$ (- 0.14- x larger than 0.5, M = Tb, Dy, Ho, Y, Er, Tm) solid electrolytes with orthorhombic and trigonal structures are reported. The orthorhombic phase of Li-M-Cl shows an approximately one order of magnitude increase in ionic conductivities when compared to their trigonal phase. Using the Li-Ho-Cl components as an example, their structures, phase transition, ionic conductivity, and electrochemical stability are studied. Molecular dynamics simulations reveal the facile diffusion in the z-direction in the orthorhombic structure, rationalizing the improved ionic conductivities. The performance of all-solid-state batteries of $NMC811/Li_{2.73}Ho_{1.09}Cl_6/In$ demonstrate is showcased at both 25 and -10 degC.

7.2 Introduction

The development of high-performance all-solid-state batteries is contingent on the finding and synthesis of solid-state electrolytes (SSEs) with high ionic conductivity, good chemical stability, wide electrochemical windows, and desirable mechanical properties [1–4]. Recently, several families of SSEs have attracted significant interest, such as sulfides or oxides with polyanionic frameworks (PS_4^{3-}, PO_4^{3-}, etc.) and halides with close-packed anion sublattice structures [5–10].

Among these candidates, a promising family of metal chloride SSEs generally possess a wide electrochemical stability window (≈4 V), and good chemical stability toward ambient air and cathode materials (e.g., LiCoO2) [11–14]. Some of them can be even synthesized at large scales from aqueous solutions [6].

Although chloride-based SSEs have been known for a few decades [15–18], the research was of rather fundamental nature. In 2018, asano et al. [14] reported conductivities in the milli-Siemens range for Li_3YX_6 (X=Cl, Br) and showcased room-temperature operation of all solid-state batteries [14]. Since then, metal halide SSEs have received renewed attention [19–32].

Until now, only a few metal chloride SSEs have achieved high room-temperature (RT) ionic conductivity over 10^{-3} Scm^{-1}, including Li_3InCl_6 [33, 34] Zr-doped Li_3MCl_6 (M = Y, Er, Yb, In) [19, 22, 25, 31], $Li_3Y_{1-x}In_xCl_6$ [20], Li_xScCl_{3+x} [21], $Li_2Sc_{2/3}Cl_4$ [22], etc.

In the search for new metal chloride SSEs, a better understanding of the relationship between structure and ionic conductivity can give guidelines for materials design [33, 35–37]. Ternary chlorides with the composition of $Li_3M(III)Cl_6$, where M(III) represents a trivalent rare earth metal, can crystallize in three crystal structures, namely trigonal ($P\bar{3}m1$), orthorhombic ($Pnma$) and monoclinic (C2/m) [6, 18].

As the ionic radius of Cl^{-1} is larger than that of the rare earth M^{+3} ions, the Cl^{-1} anions form a quasi-close packed framework. Li^{+1} and M(III) typically occupy octahedral sites.

Whether the structure is monoclinic, orthorhombic or trigonal is determined (to first order) by the Shannon radius of the M(III).

For small radii (M(III)=In, Sc), the materials crystallize in the monoclinic structure. The monoclinic structure is formed by quasi ccp close packed Cl atoms, with the M(III) and Li mostly occupying octahedral sites, though the lithium can also occupy tetrahedral sites (chapter 5).

The orthorhombic $Pnma$ phase has been reported for intermediate M(III)= Yb, Lu, whereas even larger M(III) = Tb, Dy, Ho, Er, Tm crystallize in trigonal $P\bar{3}m1$ [6, 18]. Both phases have a quasi hexagonally close packed framework of Cl^{-1} anions with lithium and holmium on octahedral sites. The two phases mainly differ in the arrangement of the cations. Only Li_3YCl_6 has been reported in both space groups, while its $Pnma$ phase is metastable at RT. That was explained by an order-disorder phase transition connecting the two phases, with a phase transition temperature close to RT [18].

The cation and vacancy arrangements imposed by the different symmetry of the trigonal and orthorhombic structures may result in distinct Li^{+1} migration. In the competition between the hcp stacked trigonal and orthorhombic structures, the average metal radius has been suggested to play a decisive role [6], where the structures crystallize in the $Pnma$

space group with smaller M3+ ions (Yb, Lu) and $P\bar{3}m1$ the space group with larger M3+ ions (Tb, Dy, Ho, Er, Tm) at RT.

In this work, we investigate the interplay between composition, structure, and Li-ion conductivity through the preparation of a series of Li-M(III)-Cl SSEs. Using Li-Ho-Cl as an example, a series of orthorhombic $Li_{3-3x}Ho_{1+x}Cl_6$ (0.04 <x<= 0.2, where x is calculated based on the ratio between LiCl and $HoCl_3$ from the synthesis process) are reported for the first time. The trigonal-to-orthorhombic phase transition also occurs in all Li-M(III)-Cl (M = Y, Er, Dy, Tm) structures except for the Li-Tb-Cl system.

The orthorhombic Li-Ho-Cl materials show a cold-pressed ionic conductivity up to $1.3*10^{-3}$ S cm^{-1} at RT. That is over fourfold greater than that of the Li_3HoCl_6 (x=0) with trigonal structure ($P\bar{3}m1$). In general, the orthorhombic phase has about a factor 8 higher ionic conductivity, as shown for the materials with M(III) = Y, Er, Dy and Tm.

A structural investigation is combined with molecular dynamics simulations to reveal the relationship between structure and Li-ion conductivity. The increase in ionic conductivity from the trigonal to the orthorhombic phase is rationalized by the fact that the orthorhombic phase results in easier Li+ transport along the c-lattice direction, which is a critical step in the diffusion network and corresponds to jumps between face-sharing octahedra.

Finally, all-solid-state batteries with an In/Li-Ho-Cl/NMC811 configuration were assembled and demonstrate excellent electrochemical performance at RT and temperatures as low as −10 ℃.

Overall, this study demonstrates that the trigonal and orthorhombic phase can both be synthesized for a variety of M(III) (M = Ho, Y, Er, Dy, Tm). The orthorhombic *Pnma* phase is first reported for M = Ho, Er, Dy, Tm, and the synthesis protocol to synthesize this phase is included. Owing to the higher ionic conductivity, the orthorhombic phase is a more attractive structure for these materials compared to the trigonal counterpart.

7.3 Results

7.3.1 Influence of Synthesis on the Structure of Li-Ho-Cl Halide SSEs

The Li-Ho-Cl halide SSEs were synthesized from a stoichiometric mixture of LiCl and $HoCl_3$ precursors directly by comelting at 650 ℃ for 24 h.

As shown in the X-ray diffraction (XRD) patterns of $Li_{3-3x}Ho_{1+x}Cl_6$ materials (Figure 7.1a,b), when x is lower than 0 the products can be indexed to a trigonal structure of Li_3HoCl_6 with the space group of $P\bar{3}m1$ (ICSD No. 04-009-8880) [18], whereas materials with x larger 0 crystallized in the orthorhombic *Pnma* phase (x is calculated based on the nominal stoichiometry between LiCl and $HoCl_3$).

Neutron powder diffraction (NPD) and Rietveld refinement of the Li_3HoCl_6 (Figure 7.1c) further confirmed the trigonal structure. The unit cell of Li_3HoCl_6 sample contains eight crystallographic atom positions. There is a slight difference in the occupations of the Ho1 and Ho2 sites when compared to the reported trigonal phase of Li_3HoCl_6. When the value of x is in the range from 0.04 to 0.2, $Li_{3-3x}Ho_{1+x}Cl_6$ crystallized in a different structure (Figure 7.1b; Figure S1, Supporting Information).

The XRD patterns of $Li_{2.4}Ho_{1.2}Cl_6$ (x= 0.2), $Li_{2.73}Ho_{1.09}Cl_6$(x= 0.09), and $Li_{2.87}Ho_{1.043}Cl_6$ (x= 0.043) reveal that the new phase has a similar orthorhombic structure to Li_3YbCl_6 (ICSD

Figure 7.1: XRD and neutron diffraction patterns of the Li-Ho-Cl system. a) XRD patterns of Li_3HoCl_6 (x= 0) and $Li_{3.42}Ho_{0.86}Cl_6$ (x=-0.14) samples. Both patterns were indexed to the same space group of $P\bar{3}m1$. b) XRD patterns of $Li_{2.4}Ho_{1.2}Cl_6$ (x= 0.2) and $Li_{2.73}Ho_{1.09}Cl_6$ (x= 0.09) samples. The patterns were indexed to the same space group of $Pnma$. Fitted time-of-flight NPD patterns of c) the Li_3HoCl_6 sample, d) the $Li_{2.73}Ho_{1.09}Cl_6$ sample and the fit resulting from the Rietveld refinement.
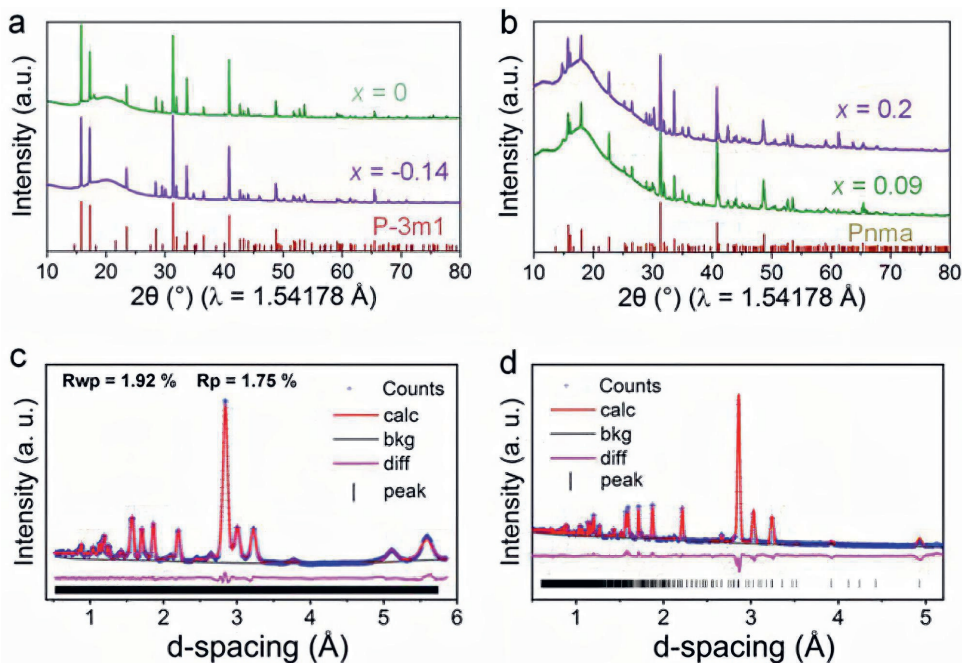
No. 04-009-8883) [18].

The structure of the $Pnma$ phase was confirmed by NPD Rietveld refinement (Figure 7.1d; Figures S2, and S3, Supporting Information) of the material $Li_{2.73}Ho_{1.09}Cl_6$ sample. Although the ratio of LiCl to $HoCl_3$ in the synthesis process is slightly lower than 3:1 (2.5 to 1), the refinement converged to the final stoichiometry of Li_3HoCl_6. The small amount of difference might be due to the trace amount of $HoCl_3$ impurity in the final product.

Both Li-Ho-Cl orthorhombic and trigonal structures are built up by hcp anion stacking, forming octahedral of six Cl^{-1} with central $Ho3+$, $Li+$, or empty sites. The two phases differ in their arrangement of the cations (Figure 7.2a-c).

In the orthorhombic $Pnma$ structure, the unit cell has three octahedral sites: 4c, 8d1, and 8d2 (Figure 7.2b). The 4c site is fully occupied by the $Ho3+$. Both Li1 and Li2 are partially occupied in the 8d sites with occupancy parameters of 0.848 and 0.652, respectively. Each $HoCl_6^{3-}$ octahedron is surrounded by three edge-sharing $LiCl_6^{5-}$ octahedra with a short Ho-Li distance (Figure 7.2d,e).

7.3.2 2.2. The Influence of Synthesis on the Ionic Transport

Ionic conductivities of the cold-pressed $Li_{3-3x}Ho_{1+x}Cl_6$ SSEs were measured by temperature-dependent alternating-current impedance. The conductivity plateau at 25 ℃ corresponds

Figure 7.2: The structure and anion/cation arrangements of orthorhombic and trigonal structures of Li_3HoCl_6. a-c) The different cation arrangements of Ho and vacancy sites in orthorhombic and trigonal structures. d,e) Orthorhombic structure of the Li_3HoCl_6 unit cell. f) The $HoCl_6^{-3}$ octahedron in the orthorhombic phase of Li_3HoCl_6. g,h) Trigonal structure of the Li_3HoCl_6 unit cell. i) The $HoCl_6^{-3}$ octahedron in the trigonal phase of Li_3HoCl_6. Green, Li; Blue, Ho; Red, Cl.
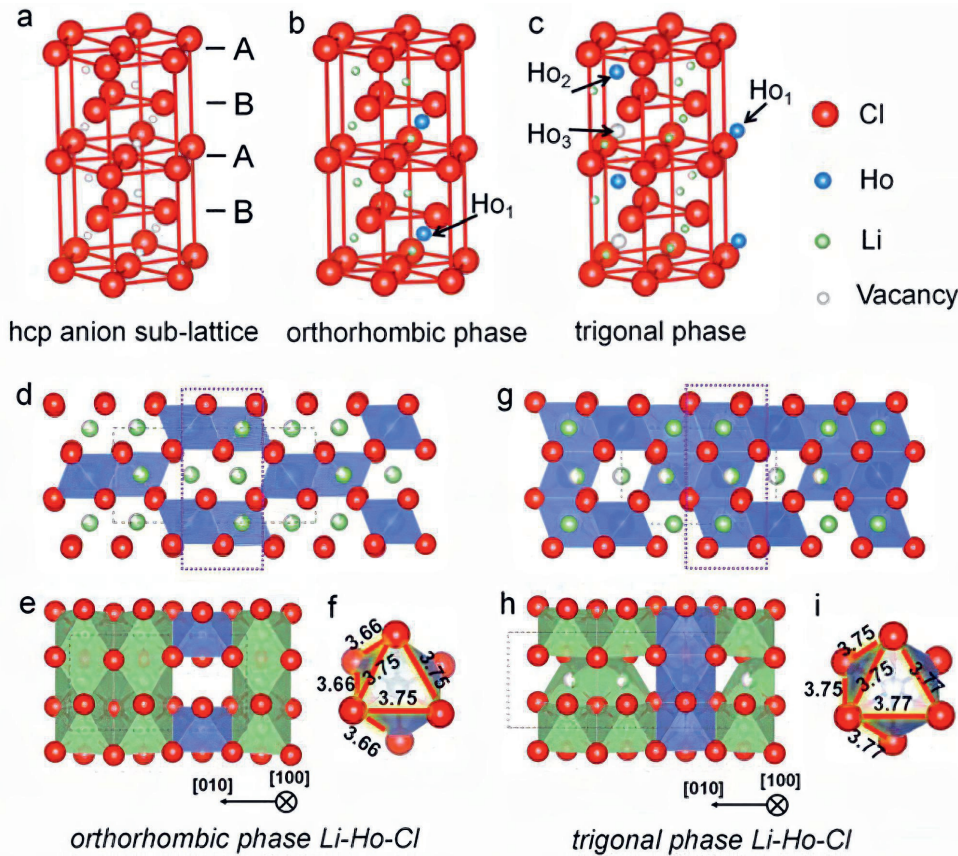
to $=1.3 * 10-3\ Scm^{-1}$ is associated with the long-range ion trans-port as shown in the conductivity isotherms in Figure 7.3a.

Figure 7.3b shows the comparison of representative Nyquist plots at 25 ℃ for the $Li_{2.73}Ho_{1.09}Cl_6$ ($Pnma$) and the Li_3HoCl_6($P\bar{3}m1$). The equivalent circuit (Figure 7.3b) consists of one parallel constant phase element (CPE)/resistor (R) in series with a CPE. The ideality factor α of the CPE in parallel with the resistance are 0.876 and 0.868 for the $Li_{2.73}Ho_{1.09}Cl_6$ and Li_3HoCl_6 with capcacitances of 49.58 pF cm^{-2} for $Li_{2.73}Ho_{1.09}Cl_6$ and 47.83 pF cm^{-2} for Li_3HoCl_6.

Arrhenius plots and the extracted activation energies (Ea) with RT ionic conductivities of all $Li_{3-3x}Ho_{1+x}Cl_6$ are presented in Figure 7.3c,d. For the $Pnma$ structures (0.04 < x <= 0.2), the RT ionic conductivities gradually increase with decreasing x, where the maximum ionic conductivity of $1.3 * 10^{-3}$ Scm^{-1} is obtained at x= 0.09. The trigonal $P\bar{3}m1$ phase (x

Figure 7.3: a) Conductivity isotherms σ (ν) of the as-prepared $Li_{2.73}Ho_{1.09}Cl_6$ SSE recorded at different tempera-
tures. b) Representative Nyquist-plots for the as-prepared $Pnma$ phase $Li_{2.73}Ho_{1.09}Cl_6$ and $P\bar{3}m1$ phase Li_3HoCl_6
SSEs at 25 °C. c) Arrhenius-plots of the $Li_{3-3x}Ho_{1+x}Cl_6$ SSEs (-0.14 $\leq$ x $\leq$ 0.5). d) The RT ionic conductivities and
corresponding activation energies of the $Li_{3-3x}Ho_{1+x}Cl_6$ SSEs (-0.14 $\leq$ x $\leq$ 0.5).
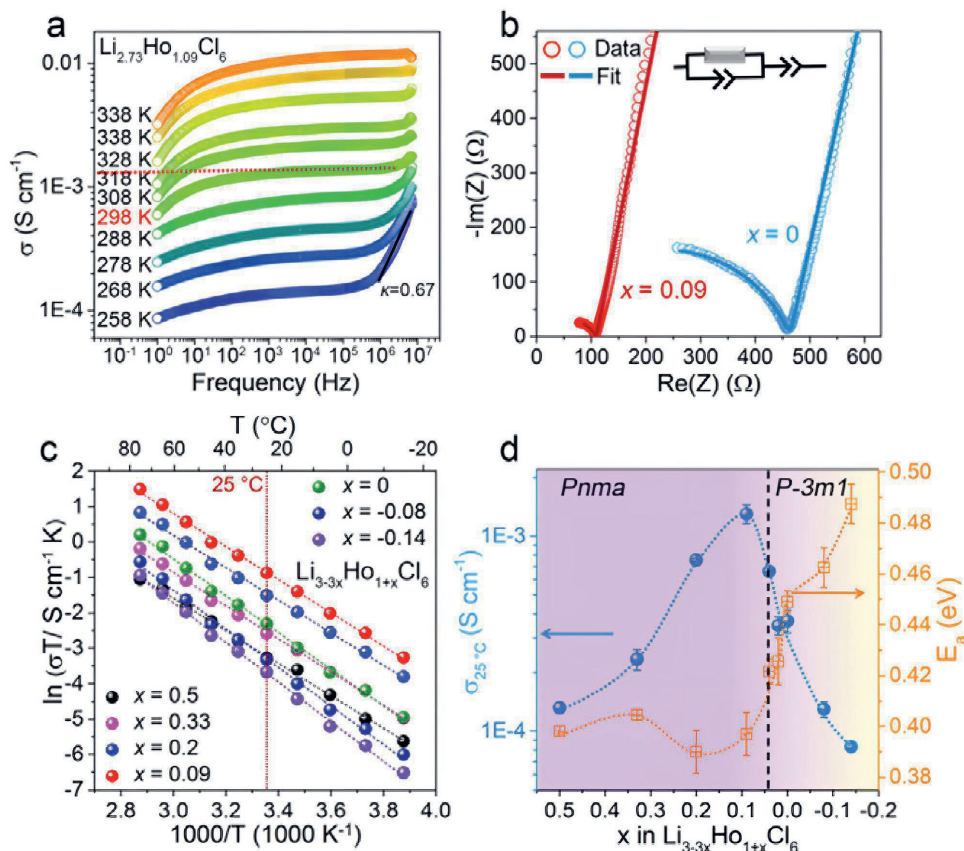
leq 0.02) exhibits a much lower RT Li+ conductivity of 2.9 * 10^{-4} Scm^{-1}.

   The higher conductivity of the orthorhombic Pnma phase shows slightly lower activa-
tion energies (0.4 vs 0.42 eV), though the difference is very small and likely within error
of measurement (Figure 7.3d). The difference in ionic conductiviy is therefore likely due
to a different prefactor D_0, as can be seen by the offset of the slope in (Figure 7.3c).

7.3.3 The Trigonal-to-Orthorhombic Phase Transition Process

The trigonal-to-orthorhombic phase transition under LiCl deficient synthesis occurs not
only for the material with Holmium, but also for other M(III) = Y, Er, Dy (Figure 7.4 a-b).
The synthesis was also attempted for Tb, but the orthothombic phase could not be obtained
(Figure 7.4 a-b).

   For all materials synthesized in both the trigonal $P\bar{3}m1$ and orthorhombic Pnma phase,
the orthorhombic phase showed higher ionic conductivity, on average by a factor 8 (Figure

7.4 c).

Figure 7.4: a) XRD patterns of the $Li_{2.73}Ho_{1.09}Cl_6$ (x= 0.09, M = Er, Y, Dy, *Pnma* phase). b) XRD patterns of the Li_3MCl_6 (x= 0, M = Er, Y, Dy, Tb, $P\bar{3}m1$phase). c) The RT ionic conductivities of the $Li_{3-3x}Ho_{1+x}Cl_6$ SSEs.
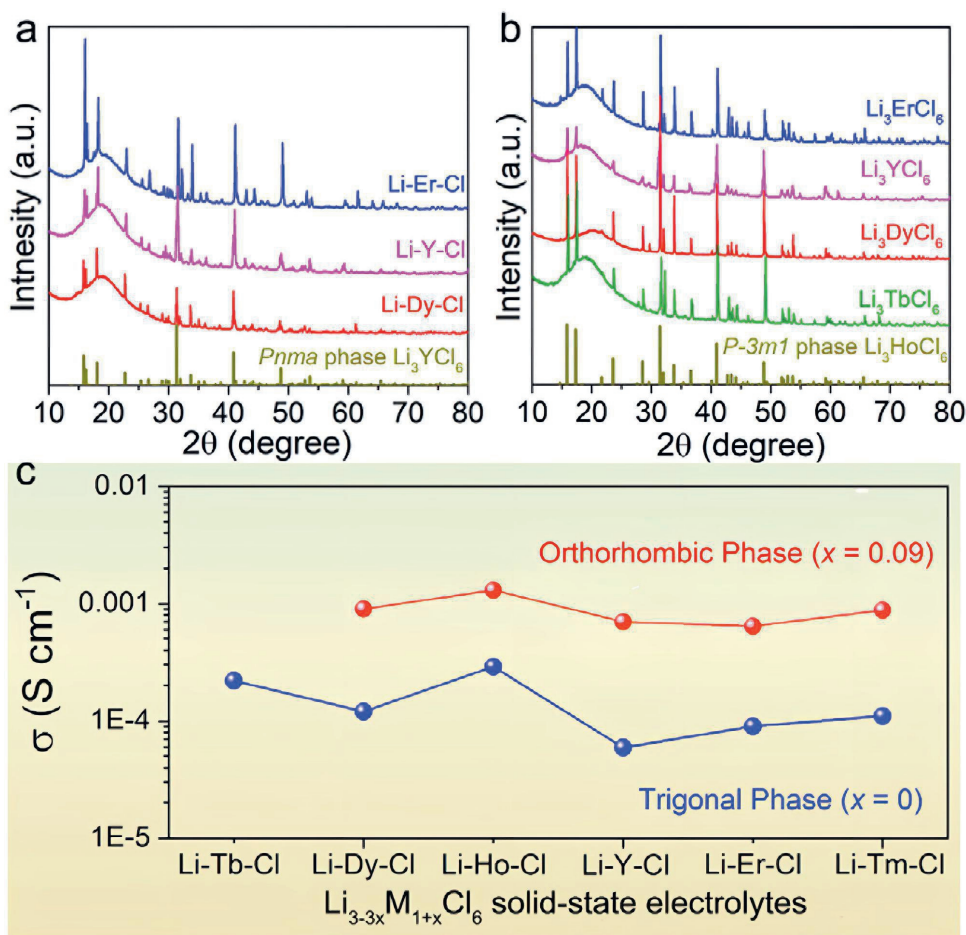
The $Li_{2.73}Dy_{1.09}Cl_6$, $Li_{2.73}Y_{1.09}Cl_6$, $Li_{2.73}Er_{1.09}Cl_6$, and $Li_{2.73}Tm_{1.09}Cl_66$ with orthorhombic phase possesses a RT ionic conductivity of $9.0*10^{-4}$, $7.0*10^{-4}$, $6.4*10^{-4}$, and $8.9*10^{-4}$ Scm^{-1}, respectively.

7.3.4 Computational Understanding of Ionic Conductivity

To understand the difference in ionic conductivities between the two structures, both phases were simulated by ab initio Molecular Dynamics for the composition of Li_3HoCl_6. The *Pnma* phase shows higher long-range diffusion, as illustrated in Figure 7.5a,b. The activation energies extracted from the slope of the Arrhenius plot are similar, but have a slight difference in the experimental observations (Figure 7.3). To further investigate the reason for the higher conductivity we consider the equation for the diffusion coefficient

$$D = gf\upsilon^0 a^2 * \exp\left(-\frac{\Delta H}{k_B T}\right) * \exp\left(\frac{\Delta S}{k_B}\right) = D_0 * \exp\left(-\frac{\Delta H}{k_B T}\right) \qquad (7.1)$$

Here, g is the geometrical factor, f is the correlation factor, v0 is the attempt frequency, and a is the jump distance, which can all be summarized into the preexponential factor D_0. The geometrical factor describes the effect of a porous network on diffusion. The correlation factor describes the percentage of back and forth movements of atoms between sites, and is defined as

$$f = \frac{D_{tracer}}{D_{hopp}} \qquad (7.2)$$

where DT_{racer} is the tracer diffusion coefficient and D_{jump} the jump-diffusion coefficient. Both the attempt frequencies and the amplitudes of the Li+ ions or Cl vibrations extracted by the Fourier transform of the diffusion paths [38] are similar in both phases (Figure S16, Supporting Information). The increase in ionic conductivity is therefore not due to an increase in attempt frequency. The influence of jump distance a (~3.1 Å) approximated by the distance between the different Wyckoff sites in both phases is also excluded. Hence, the difference observed in D0 has to arise either from the geometrical factor or the correlation factor. The jumps between different Li sites under different temperatures are illustrated in Figure 7.5c,d and Figures S17-S20 (Supporting Information).

The red lines represent jumps that occurred, with the thickness of the line indicating the frequency of the jump occurring. For the *Pnma* phase at 500 K (Figure 7.5c), there is a clear long-range diffusion path along the z-direction between the Wyckoff 8d1 and 8d2 sites. Even though jumps between the 8d1-8d1 and 8d2-8d2 sites in the xy-plane are also possible, the relative amount of these jumps is lower compared to the relative amount of jumps between the 8d1-8d2 site within the time simulated at all temperatures (between 4% and 31%, appendix table 8.12). Thus the jumps along the z-direction have a lower activation energy than cross-plane jumps, indicating that the high conductivity is mainly but not exclusively due to these 1D diffusion pathways. For the $P\bar{3}m1$ phase, the jumps along the z-direction are between the 6h and 6g sites and occur about equally often (39.3-51.6%) as jumps between the same Wyckoff sites (48.4-60.7%) (Figure 7.5d; appendix table 8.12). The jumps around the hexagon appear to happen frequently (thick red lines) whereas the jumps to connect the hexagons happen rarely (no lines or very thin red lines). A different initial arrangement of Ho on the sites would lead to different diffusion pathways [6, 39], but this was not investigated in the scope of this report and was extensively studied in Schlem et al.[39] The study shows that disorder between the M1(1a) and M2(2d), which can be introduced by mechanochemical synthesis, increases the ionic conductivity in the $P\bar{3}m1$ phase (in the simulations here, the M1(1a) and M2(2d) were large, therefore a conductive version of the $P\bar{3}m1$ phase was simulated).

The increase in ionic conductivity is rationalized by two simultaneous mechanisms. One is the different M(III) distribution leading to a redistribution of the Li atoms, which is more favorable. This is accompanied by an increase in the triangular area of face sharing octahedra/tetrahedra, which increases the size of the bottleneck.[39]. Considering that both the *Pnma* and $P\bar{3}m1$ phase consist of hexagonal close packing of the chlorine atoms, the difference between the two phases essentially is the different cation distribution, hence

Figure 7.5: a) Mean squared displacement (MSD) of the $P\bar{3}m1$ and $Pnma$ phase at 600 K as a function of the simulation time (the $P\bar{3}m1$ phase was run longer than shown here). For the total MSD per simulation, see Figure S15 of the Supporting Information. b) Logarithm of the Tracer diffusion coefficient versus 1/kbT for different temperatures. The ionic jumps between different Li sites in c) $Pnma$ phase and d) $P\bar{3}m1$ phase at 500 K. The Li-sites (blue), Ho-trajectories (green), and Li-ion jumps that occurred during the simulation (red). The size of the Li-sites and the thickness of the Lines represent the occupancy of the site during the simulation and the jump frequency, respectively.
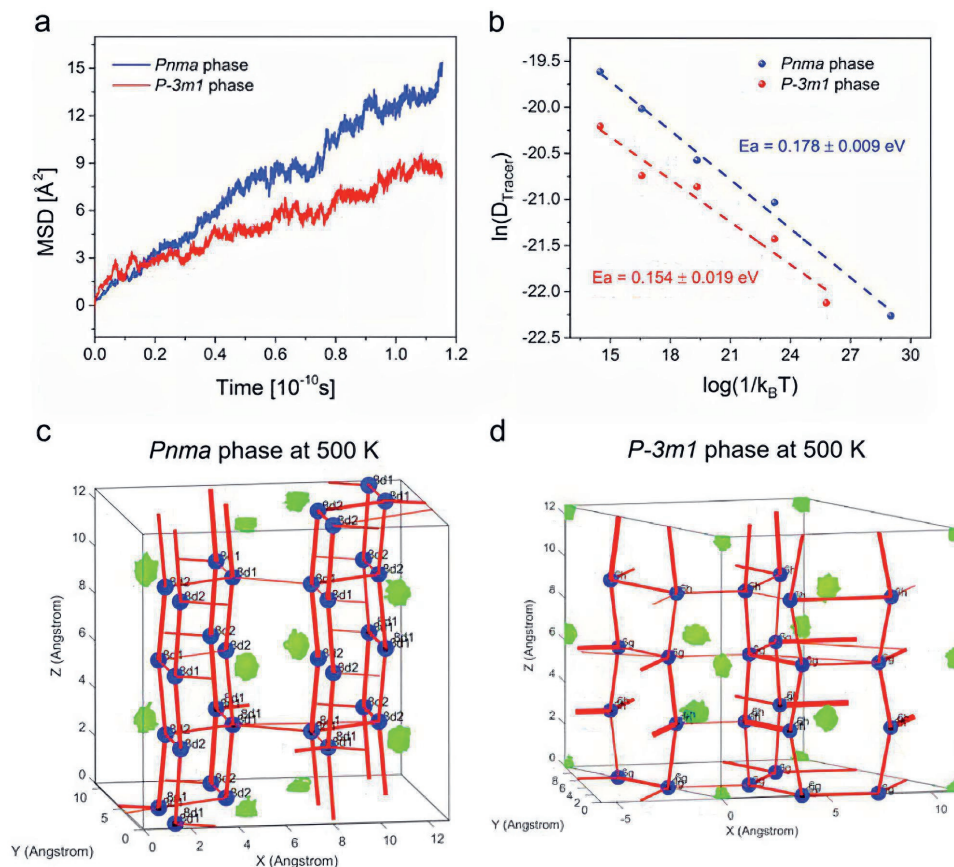
the rationale here is similar to their first mechanism. The diffusion in the z-direction, which is very fast according to the ab initio simulations here, corresponds to jumps between face sharing octahedra, while the diffusion in the xy-plane is diffusion between face sharing oct-tet-oct path. The results therefore indicate that the M(III) distribution in the $Pnma$ phase favors jumps between face-sharing octahedras, which, considering the higher tracer diffusivity, is a faster path than the oct-tet-oct path in the xy-plane.

7.4 Solid-state NMR relaxometry of Li$_3$YCl$_6$

To investigate the short-range diffusion in the *Pnma* and *P$\bar{3}$m1* phases experimentally, NMR relaxometry measurements were made for Li-Y-Cl materials in both phases. The behaviour of the ^{7}Li t$_1$ measurements are quite different for the two materials (see Figure 7.6).

The trigonal *P$\bar{3}$m1* is not stable in temperature, as indicated by the discontinuity of the trends in the relaxation rates. The chemical shift spectra around the discontinuities in of the relaxation rates further show distinct lineshapes (Annex Figure 8.34), another indicator for a phase transition and proof for the change in environment around the lihtium).

The Pnma phase, on the other hand, shows a continuous curve and the phase is therefore probably stable in the temperature range measured. This indicates that the Pnma phase could be a high temperature phase stabilized at room temperature.

The curve of the relaxation rates of the Pnma phase can be fit with the BPP-model with τ_0 = 2.3E-14 s and E$_a$ = 0.369 eV. Calculating the conductivity from this jump process as described in chapter 4, a conductivity of 0.23 mS/cm is obtained, which is very close to the 0.7 mS/cm measured for impedance.

To improve the accuracy of these results, it would be beneficial to measure at more ω_0 and a larger temperature range, especially towards the lower temperatures. As the conductivity calculated from NMR is lower compared to the AC-impedance measurements, it is possible that another, faster jump process is present, as the one seen along the c-direction from MD-simulations.

7

Figure 7.6: T$_1$ relaxation rates for the *Pnma* and *P$\bar{3}$m1* phases of Li$_3$YCl measured at ω_0 of 116 MHz. The rates of the Pnma phase can be fit using the BPP model (striped blue line). The *P$\bar{3}$m1* shows quite different relaxation rates with two abrupt changes in the rates (striped orange lines), which are indicative of a phase transition.
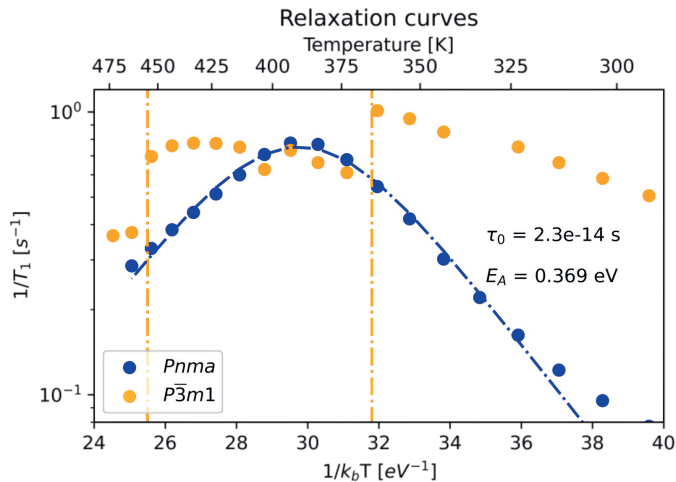
7.5 Electrochemical Studies

Figure 7.7a presents the charge/discharge profiles of the ASSLB operated at 25 ℃ and -10 ℃. At 25 ℃, the initial charge/discharge capacities are 209 and 172 mAh g-1 (0.1 C, 1 C = 200 mA g-1), corresponding to an initial Coulombic efficiency of 82.3%. At -10 ℃, the NMC811/$Li_{2.73}Ho_{1.09}Cl_6$/In ASSLB exhibits an initial Coulombic efficiency of 79.4% and a reversible capacity of 142 mAh g-1 at 0.025 C, which might be caused by the sluggish Li+ migration within the cathode layer at a lower temperature. The NMC811/$Li_{2.73}Ho_{1.09}Cl_6$/In ASSLBs show good cycling performance at both temperatures (Figure 7.7b; Figure S24, Supporting Information), with specific capacities of 125.5 and 90 mAh g-1 remaining after 180 cycles (25 ℃) and 100 cycles at -10 ℃. The typical delithiation/lithiation behavior of NMC811 is clearly visible in the differential capacity curves (Figure 7.7c).

The rate capabilities at different current densities ranging from 20 to 200 mA g-1 (0.1 C to 1 C) at 25 ℃ are displayed in Figure 7.7d. The capacity gradually decreases along with an increase of current density, with 98 mAh g-1 achieved at 1 C (58% capacity retention of that at 0.1 C). The capacity can be recovered upon returning to the initial 0.1 C rate. The in situ EIS spectra in Figure 7.7e show that the mid-frequency semicircle related to the NMC811/$Li_{2.73}Ho_{1.09}Cl_6$ interfacial resistance increased slightly during the charging process and decreased again during the discharging process, which might be caused by the mild volume shrinkage of NMC811 during delithiation and corresponding volume recovery once lithiated [40].

Synchrotron-based high energy X-ray photoelectron spectra (HEXPS) of NMC811/$Li_{2.73}Ho_{1.09}Cl_6$ composites at different states (Figure 7.7f,g) remain the same, indicating that there is a stable interface between NMC811 and $Li_{2.73}Ho_{1.09}Cl_6$ regardless of the static physical contact or during the charge/discharge cycling process. Such conclusion can be further supported by the Ho L3-edge XANES spectra (Figure 7.7h) and the corresponding first derivative spectra (Figure 7.7i) of the NMC811/$Li_{2.73}Ho_{1.09}Cl_6$ composite at different charge/discharge states.

7

Figure 7.7: Electrochemical performance of NMC811/Li$_{2.73}$Ho$_{1.09}$Cl$_6$/In ASSLBs. a) The charge/discharge curves and b) the cycling performance recorded at 25 ℃ (0.1 C). c) The dQ/dV curves for the first three cycles at 0.1 C at 25 ℃. d) Rate capability at 0.1, 0.2, 0.5, 0.8, and 1 C at 25 ℃. e) EIS spectra of NMC811/Li$_{2.73}$Ho$_{1.09}$Cl$_6$/In ASSLB carried out after 2 h of charge/discharge and 2 h of rest. f,g) HEXPS of Ho 4d and Cl 1s spectra of NMC811-Li$_{2.73}$Ho$_{1.09}$Cl$_6$ cathode at a photon energy of 3000 eV recorded at different charge/discharge states, i.e., (f1,g1) pristine, (f2,g2) after first charge, (f3,g3) after the first discharge, and (f4,g4) fully discharged after 50 cycles. Ex situ h) Ho L3-edge and i) the first derivatives of Ho L3-edge XANES spectra of NMC811-Li$_{2.73}$Ho$_{1.09}$Cl$_6$ cathode composites at different charge-discharge states.
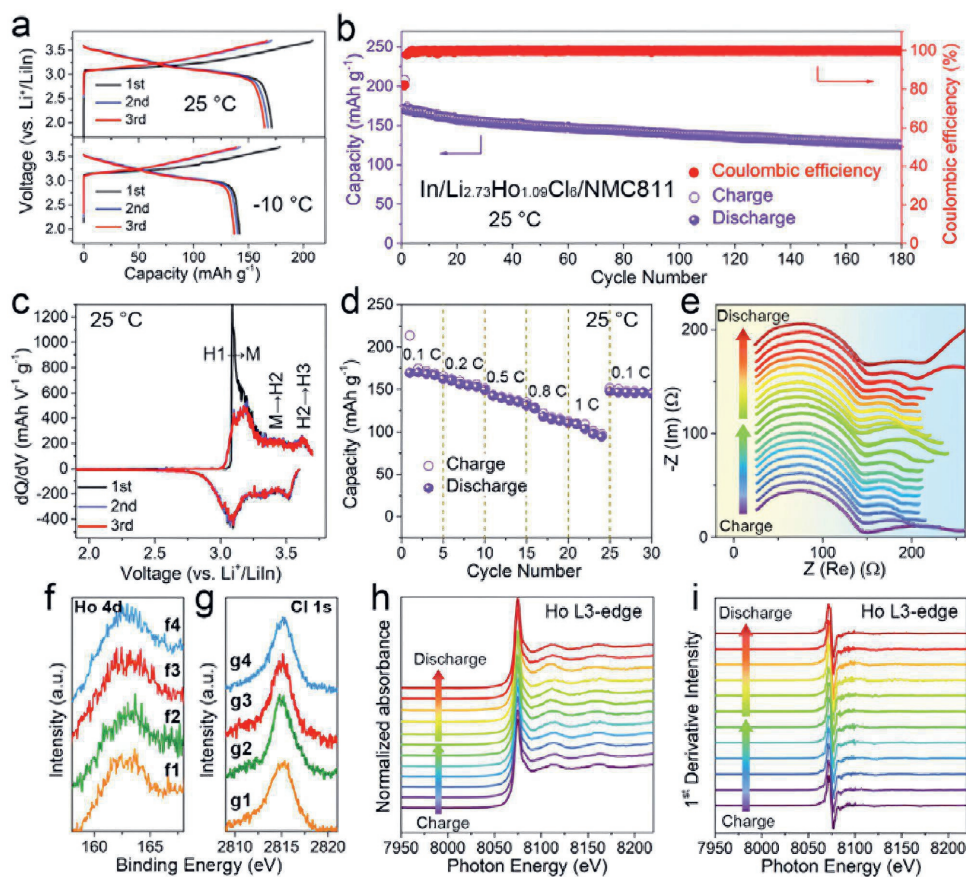
7.6 Conclusions

In summary, the ternary metal chloride solid electrolyte series of Li$_{3-3x}$M$_{1+x}$Cl$_6$ (-0.14 < x <= 0.2, M = Tb, Dy, Ho, Y, Er, Tm) reveal a phase transition from trigonal ($P\bar{3}m1$) to orthorhombic ($Pnma$) upon increasing x values. Both $P\bar{3}m1$ and $Pnma$ structures consist of the hcp framework of Cl^{-1} anions but differ in their cations (including Li+ and M3+) arrangement. Using Li$_{3-3x}$Ho$_{1+x}$Cl$_6$ (-0.14 < x <= 0.2) as an example, the relationship between structure and Li-ion conductivity is revealed by temperature-dependent EIS, X-ray and neutron diffractions, and ab initio molecular dynamics (MD) simulations.

The highest RT Li+ conductivity of 1.3 * 10^{-3} S cm-1 is achieved for the orthorhombic

$Li_{2.73}Ho_{1.09}Cl_6$ sample, which is over four times higher than that of the trigonal Li_3HoCl_6 ($0.3 \, {}^*10^{-3}$ S cm-1). About a factor 8 difference in ionic conductivities is observed in the isostructural Li-Dy-Cl, Li-Y-Cl, Li-Er-Cl, and Li-Tm-Cl composites. The phase transition to *Pnma* triggers a significant increase in Li+ diffusivity and reduces the activation energy barrier for Li+ diffusion in all different Li-M-Cl systems.

Ab initio MD simulations consistently derive a higher diffusivity and reduced activation energy of the *Pnma* phase due to the facile diffusion in the z-direction compared to the $P\bar{3}m1$ phase. The good ionic conductivity and stability of this material is showcased by the electrochemical performance of all-solid-state batteries with $MC811/Li_{2.73}Ho_{1.09}Cl_6/In$ at both RT and -10℃.

7.7 Experimental Section

Preparation of the $Li_{3-3x}M_{1+x}Cl_6$

All preparations and sample treatments were carried out under argon atmosphere (O2 < 1 ppm, H2O < 1 ppm). The $Li_{3-3x}M_{1+x}Cl_6$ (M = Tb, Dy, Ho, Y, Er, Tm) SSEs were synthesized using the following procedure: the starting materials of lithium chloride (LiCl, Alfa Aesar, 99.9%) and trivalent rare earth chloride (MCl3, Alfa Aesar, >99.9%) were weighted in the appropriate stoichiometric ratio and directly put into quartz tubes. The quartz tubes were sealed and heated to 650 ℃ (4 h heating), annealed for 24 h, and then cooled to room temperature.

Preparation of the LPO-Coating NMC811 Cathode

The NMC811 cathode was obtained from China Automotive Battery Research Institute Co. Ltd, China. The Li_3PO_4 thin layer was deposited on the surface of NMC811 using trimethyl phosphate (TMPO) and lithium tertbutoxide (LiOtBu) as precursors by atomic layer deposition (ALD, Cam-bridge Nanotech, USA). The deposition temperature for Li_3PO_4 thin layer was set at 250 ℃. TMPO and LiOtBu were alternatively introduced into the reaction chamber with a pulse time of 2 s, and the pulsing of each precursor was separated by a 15 s in 1 cycle. The thickness of the Li_3PO_4 thin layer was controlled around 10 nm (100 cycles).

Characterizations

Powder XRD measurements of $Li_{3-3x}M_{1+x}Cl_6$ (M = Tb, Dy, Ho, Y, Er, Tm) were carried out on a Bruker AXS D8 Advance with a Cu K α radiation (λ = 1.54178 Å). All samples were placed into a special holder to avoid possible air exposure during the test. Air stable performance was performed in a lithium battery dry room with a supply dew point around -50 ℃ and humidity around 1%. High-energy X-ray photoelectron spectroscopy of NMC811-$Li_{2.73}Ho_{1.09}Cl_6$ cathode at different charge/discharge states was carried on the soft X-ray microcharacterization beamline (SXRMB) in Canadian Light Source (CLS) under different energies. Holmium (Ho) XAFS data were measured at Hard X-ray MicroAnalysis (HXMA) beamline in CLS.

Neutron Diffraction

The time of flight powder neutron diffraction patterns were collected on the high-flux medium resolution diffractometer Polaris at ISIS [41], Rutherford Appleton Laboratory,

United Kingdom. 1.575 g of $Li_{2.73}Ho_{1.09}Cl_6$ powder was loaded into a 6 mm diameter thin-walled cylindrical vanadium can and sealed with an indium wire inside the glovebox. The sample was mounted in the diffractometer and data were collected at room temperature for a duration of 400 μAh integrated proton beam current to the ISIS neutron target (corresponding to =2 h total exposure). Data reduction and generation of files suitable for profile refinement used the Mantid open-source software [42].

The data were analyzed with the Rietveld refinement program GSAS-2 software [43]. As an initial guess, the structure file of the *Pnma* phase of Li3YCl6 was used, and Y was replaced by Ho. The lattice parameter and atomic positions were refined first, followed by sample broadening effects due to crystallite size. Instrument parameters were refined for small corrections in the time of flight due to sample placement and wavelength-dependent average penetration depth. The chlorine occupancies were fixed to 1, the holmium and the lithium occupancies were refined, where the lithium occupancy of the 8d1 site was fixed to 1, while the Li 8d2 and the Ho 4c site occupancies were refined but constrained to charge compensation.

Conductivity Measurements

Cold-pressed pellets (diameter of 10 mm, =380 MPa) were attached with carbon on both sides and then sealed in custom-built Model Cells for EIS tests. Ionic conductivity measurements were carried out in the temperature range from 258 to 338 K using a versatile multichannel potentiostat 3/Z (VMP3) impedance analyzer in the range of 7 MHz to 1 Hz with an amplitude of 10 mV. The activation energies of the $Li_{3-3x}M_{1+x}Cl_6$ samples were determined according to the Arrhenius equation of $\sigma T = \sigma 0\ exp(-Ea/kBT)$, where σ, T, $\sigma 0$, Ea, and kB are the ionic conductivity, the temperature in K, the pre-exponential factor, the activation energy, and the Boltzmann constant, respectively. The electronic conductivities of the samples were calculated by the Ohm's law of $\sigma e = Ie * L/(V * A)$, where σe, Ie, L, V, and A is the electronic conductivity, the equilibrium current, the thickness of the SSE, the applied voltage, and the area of the SSE pellet, respectively.

MD Simulations

Density functional theory calculations were performed in VASP [44–46] using the GGA approximation [47] and the PAW-PBE basis set [48, 49]. A 1 * 1 * 2 supercell was used, which results in a size of 80 atoms (12.89 * 11.21 * 12.45) for the *Pnma* phase and 60 atoms (11.33 * 9.76 * 12.45) for $P\bar{3}m1$. For both structures, cut-off energy of 450 eV and a k-point mesh of 2 * 2 * 2 was used for the relaxation as well as the molecular dynamics simulation. The values were chosen based on the convergence test of the total energy. The MDs were performed in the NVT ensemble, with a time step of 2 fs and an equilibration time of 2.5 ps for all simulations. The simulations were run for a different length depending on the phase and temperature, to reach a certain amount of jumps also at lower temperatures and for the less conducting phase. The output of the MD simulations was analyzed using the code published elsewhere [38].

Structure generation for the (MD) Simulations

For the $P\bar{3}m1$ phase, the cif file published in Bohnsack et al.[18] was used as a starting structure. The Ho partial occupancies were changed to 80% (from 97%) and 20% (from 3%), due to computational limitations concerning the size of the supercell and the refinement result of the $P\bar{3}m1$ phase Li_3HoCl_6 sample. The partial occupancies of both Li and Ho lead to very many possible configurations in the supercell. Therefore, the ten structures with the lowest Ewald-sum of the configurational space were selected as implemented in Pymatgen [50]. After minimization without symmetry restrictions, the lowest energy configuration of the ten structures was selected for the MD simulations. For the *Pnma* phase, the cif file for Li3YCl6[18] was used as a starting structure. The partial occupancy was accommodated by placing Li-atoms on their sites so that the Li-Li distances are maximized. Ten structures were then relaxed without symmetry restrictions and the lowest energy configuration was used as starting point for the MDs.

Electrochemical Characterizations

All-solid-state batteries preparation processes were conducted inside an Ar-filled glove box. There was no liquid electrolyte used during the battery assembly process. The configuration of the solid-state batteries was a homemade model cell, with solid electrolyte, cathode composite, and In foil anode pressed into the cell layer by layer using stainless-steel terminals and hydraulic press. The electrochemical stability was evaluated by cyclic voltammetry (CV) measurements using a versatile multichannel potentiostat 3/Z (VMP3) with a $Li/Li3PS4/Li_{3-3x}Ho_{1+x}Cl_6/Li_{3-3x}Ho_{1+x}Cl_6$-Au cell in a scanning range of -0.2 to 5 V (vs Li/Li+) at 0.1 mV s-1. The active $Li_{3-3x}Ho_{1+x}Cl_6$-Au layer was prepared by mixing Au and $Li_{3-3x}Ho_{1+x}Cl_6$ with a mass ratio of 1:1. Symmetrical all-solid-state $Li/Li_{3-3x}Ho_{1+x}Cl_6/Li$ cells were assembled with bare Li metal as the electrodes and cold-pressed $Li_{3-3x}Ho_{1+x}Cl_6$ pellet as the solid-state electrolyte layer. Commercial $LiNi0.8Mn0.1Co0.1O2$ (NMC811) with a 5 nm Li_3PO_4 coating by ALD without infusion was used as the cathode active material.[58] For the preparation of cathode composites, NMC811 and as-prepared $Li_{3-3x}Ho_{1+x}Cl_6$ SSEs with a mass ratio of 7:3 were ground together in an agate mortar for 10 min. 80 mg of the as-synthesized $Li_{3-3x}Ho_{1+x}Cl_6$ was compressed at 2 tons to form a solid-state electrolyte layer. Approximately 10 mg of cathode composite was then spread on one side of the $Li_{3-3x}Ho_{1+x}Cl_6$ pellet and further pressed at 3 tons (=380 MPa). The diameter of the pallet was 1 cm. Then a piece of In foil was put on the other side of the $Li_{3-3x}Ho_{1+x}Cl_6$ and pressed at 1 ton (=125 MPa). The cells were cycled in the voltage range of 1.9-3.7 V (vs Li+/Li-In) by using the homemade model cells and a Land cycler (Wuhan, China) at room temperature and -10 ℃.

Acknowledgements

References

[1] Theodosios Famprikis, Pieremanuele Canepa, James A. Dawson, M. Saiful Islam, and Christian Masquelier. Fundamentals of inorganic solid-state electrolytes for batteries. *Nature Reviews*, 18(12):1278–1291, December 2019.

[2] Zhizhen Zhang, Yuanjun Shao, Bettina Lotsch, Yong-Sheng Hu, Hong Li, Jürgen Janek, Linda F. Nazar, Ce-Wen Nan, Joachim Maier, Michel Armand, and Liquan Chen. New horizons for inorganic solid state ion conductors. *Energy & Environmental Science*, 11(8):1945–1976, 2018.

[3] Rusong Chen, Qinghao Li, Xiqian Yu, Liquan Chen, and Hong Li. Approaching practically accessible solid-state batteries: stability issues related to solid electrolytes and interfaces. *Chemical reviews*, 120(14):6820–6877, 2019.

[4] Manuel Weiss, Fabian J Simon, Martin R Busche, Takashi Nakamura, Daniel Schröder, Felix H Richter, and Jürgen Janek. From liquid-to solid-state batteries: ion transfer kinetics of heteroionic interfaces. *Electrochemical Energy Reviews*, 3(2):221–238, 2020.

[5] Qing Zhao, Sanjuna Stalin, Chen-Zi Zhao, and Lynden A. Archer. Designing solid-state electrolytes for safe, energy-dense batteries. *Nature Reviews Materials*, 5(3):229–252, February 2020.

[6] Xiaona Li, Jianwen Liang, Xiaofei Yang, Keegan R. Adair, Changhong Wang, Feipeng Zhao, and Xueliang Sun. Progress and perspectives on halide lithium conductors for all-solid-state lithium batteries. *Energy & Environmental Science*, 13(5):1429–1461, 2020.

[7] Roman Schlem, Tim Bernges, Cheng Li, Marvin A. Kraft, Nicolo Minafra, and Wolfgang G. Zeier. Lattice Dynamical Approach for Finding the Lithium Superionic Conductor Li$_3$ErI$_6$. *ACS Applied Energy Materials*, 3(4):3684–3691, April 2020.

[8] Qing Zhang, Daxian Cao, Yi Ma, Avi Natan, Peter Aurora, and Hongli Zhu. Sulfide-Based Solid-State Electrolytes: Synthesis, Stability, and Potential for All-Solid-State Batteries. *Advanced Materials*, 31(44):1901131, 2019.

[9] Saneyuki Ohno, Ananya Banik, Georg F. Dewald, Marvin A. Kraft, Thorben Krauskopf, Nicoló Minafra, Paul Till, Manuel Weiss, and Wolfgang G. Zeier. Materials design of ionic conductors for solid state batteries. *Progress in Energy*, 2(2):022001, 2020.

[10] Yunsheng Liu, Shuo Wang, Adelaide M. Nolan, Chen Ling, and Yifei Mo. Tailoring the Cation Lattice for Chloride Lithium-Ion Conductors. *Advanced Energy Materials*, 10(40):2002356, 2020.

[11] Shuo Wang, Qiang Bai, Adelaide M. Nolan, Yunsheng Liu, Sheng Gong, Qiang Sun, and Yifei Mo. Lithium Chlorides and Bromides as Promising Solid-State Chemistries for Fast Ion Conductors with Good Electrochemical Stability. *Angewandte Chemie International Edition*, 58(24):8039–8043, June 2019.

[12] Yizhou Zhu and Yifei Mo. Materials design principles for air-stable lithium/sodium solid electrolytes. *Angewandte Chemie*, 132(40):17625–17629, 2020.

[13] Dongsu Park, Haesun Park, Yongheum Lee, Sang-Ok Kim, Hun-Gi Jung, Kyung Yoon Chung, Joon Hyung Shim, and Seungho Yu. Theoretical Design of Lithium Chloride Superionic Conductors for All-Solid-State High-Voltage Lithium-Ion Batteries. *ACS Applied Materials & Interfaces*, 12(31):34806–34814, August 2020.

[14] Tetsuya Asano, Akihiro Sakai, Satoru Ouchi, Masashi Sakaida, Akinobu Miyazaki, and Shinya Hasegawa. Solid Halide Electrolytes with High Lithium-Ion Conductivity for Application in 4 V Class Bulk-Type All-Solid-State Batteries. *Advanced Materials*, 30(44):1803075, November 2018.

[15] H.-J. Steiner and H. D. Lutz. Neue schnelle Ionenleiter vom Typ MI3MIIICl6 (MI = Li, Na, Ag; MIII = In, Y). *Zeitschrift für anorganische und allgemeine Chemie*, 613(7):26–30, July 1992.

[16] EJ Plichta, WK Behl, D Vujic, WHS Chang, and DM Schleich. The rechargeable li x tis2/lialcl4/li1- x coo2 solid-state cell. *Journal of The Electrochemical Society*, 139(6):1509, 1992.

[17] R Kanno, Y Takeda, and O Yamamoto. Ionic conductivity of solid lithium ion conductors with the spinel structure: Li2mcl4 (m= mg, mn, fe, cd). *Materials Research Bulletin*, 16(8):999–1005, 1981.

[18] Andreas Bohnsack, Frauke Stenzel, Armin Zajonc, Gert Balzer, Mathias S. Wickleder, and Gerd Meyer. Ternäre halogenide vom typ a3mx6 vi. ternäre chloride der selten-erd-elemente mit lithium lithium, li3mcl6 (m=tb-lu, y, sc): Synthese, krisallstrukturen und ionenbewegung. *Zeitschrift für anorganische und allgemeine Chemie*, 623(7):1067–1073, July 1997.

[19] Kern-Ho Park, Kavish Kaup, Abdeljalil Assoud, Qiang Zhang, Xiaohan Wu, and Linda F Nazar. High-voltage superionic halide solid electrolytes for all-solid-state li-ion batteries. *ACS Energy Letters*, 5(2):533–539, 2020.

[20] Xiaona Li, Jianwen Liang, Keegan R Adair, Junjie Li, Weihan Li, Feipeng Zhao, Yongfeng Hu, Tsun-Kong Sham, Li Zhang, Shangqian Zhao, et al. Origin of superionic li3y1−x in x cl6 halide solid electrolytes with high humidity tolerance. *Nano Letters*, 20(6):4384–4392, 2020.

[21] Jianwen Liang, Xiaona Li, Shuo Wang, Keegan R. Adair, Weihan Li, Yang Zhao, Changhong Wang, Yongfeng Hu, Li Zhang, Shangqian Zhao, Shigang Lu, Huan Huang, Ruying Li, Yifei Mo, and Xueliang Sun. Site-Occupation-Tuned Superionic Li $_x$ ScCl $_{3+x}$ Halide Solid Electrolytes for All-Solid-State Batteries. *Journal of the American Chemical Society*, 142(15):7012–7022, April 2020.

[22] Laidong Zhou, Chun Yuen Kwok, Abhinandan Shyamsunder, Qiang Zhang, Xiaohan Wu, and Linda F Nazar. A new halospinel superionic conductor for high-voltage all solid state lithium batteries. *Energy & Environmental Science*, 13(7):2056–2063, 2020.

[23] Hiram Kwak, Daseul Han, Jeyne Lyoo, Juhyoun Park, Sung Hoo Jung, Yoonjae Han, Gihan Kwon, Hansu Kim, Seung-Tae Hong, Kyung-Wan Nam, et al. New cost-effective halide solid electrolytes for all-solid-state batteries: Mechanochemically prepared fe3+-substituted li2zrcl6. *Advanced Energy Materials*, 11(12):2003190, 2021.

[24] Se Young Kim, Kavish Kaup, Kern-Ho Park, Abdeljalil Assoud, Laidong Zhou, Jue Liu, Xiaohan Wu, and Linda F Nazar. Lithium ytterbium-based halide solid electrolytes for high voltage all-solid-state batteries. *ACS Materials Letters*, 3(7):930–938, 2021.

[25] Juhyoun Park, Daseul Han, Hiram Kwak, Yoonjae Han, Yong Jeong Choi, Kyung-Wan Nam, and Yoon Seok Jung. Heat treatment protocol for modulating ionic conductivity via structural evolution of li3-xyb1-xmxcl6 (m= hf4+, zr4+) new halide superionic conductors for all-solid-state batteries. *Chemical Engineering Journal*, 425:130630, 2021.

[26] Roman Schlem, Ananya Banik, Saneyuki Ohno, Emmanuelle Suard, and Wolfgang G. Zeier. Insights into the Lithium Sub-structure of Superionic Conductors Li $_3$ YCl $_6$ and Li $_3$ YBr $_6$. *Chemistry of Materials*, 33(1):327–337, January 2021.

[27] Maria Gombotz and H. Martin R. Wilkening. Fast Li Ion Dynamics in the Mechanosynthesized Nanostructured Form of the Solid Electrolyte Li3YBr6. *ACS SUSTAINABLE CHEMISTRY & ENGINEERING*, 9(2):743–755, January 2021.

[28] Luise M Riegger, Roman Schlem, Joachim Sann, Wolfgang G Zeier, and Jürgen Janek. Lithium-metal anode instability of the superionic halide solid electrolytes and the implications for solid-state batteries. *Angewandte Chemie International Edition*, 60(12):6718–6723, 2021.

7

[29] Zhantao Liu, Shuan Ma, Jue Liu, Shan Xiong, Yifan Ma, and Hailong Chen. High Ionic Conductivity Achieved in Li $_3$ Y(Br $_3$ Cl $_3$) Mixed Halide Solid Electrolyte via Promoted Diffusion Pathways and Enhanced Grain Boundary. *ACS Energy Letters*, 6(1):298–304, January 2021.

[30] Yuanyuan Fu and Cheng Ma. Interplay between li3yx6 (x= cl or br) solid electrolytes and the li metal anode. *Science China Materials*, 64(6):1378–1385, 2021.

[31] Bianca Helm, Roman Schlem, Björn Wankmiller, Ananya Banik, Ajay Gautam, Justine Ruhl, Cheng Li, Michael Ryan Hansen, and Wolfgang G. Zeier. Exploring aliovalent substitutions in the lithium halide superionic conductor li$_{3-x}$in$_{1-x}$zr$_x$cl$_6$ (0≤ x ≤ 5. *Chemistry of Materials*, 33(12):4773–4782, June 2021.

[32] Beniamin Zahiri, Arghya Patra, Chadd Kiggins, Adrian Xiao Bin Yong, Elif Ertekin, John B Cook, and Paul V Braun. Revealing the role of the cathode–electrolyte interface on solid-state batteries. *Nature Materials*, 20(10):1392–1400, 2021.

[33] Xiaona Li, Jianwen Liang, Jing Luo, Mohammad Norouzi Banis, Changhong Wang, Weihan Li, Sixu Deng, Chuang Yu, Feipeng Zhao, Yongfeng Hu, et al. Air-stable li 3 incl 6 electrolyte with high voltage compatibility for all-solid-state batteries. *Energy & Environmental Science*, 12(9):2665–2671, 2019.

[34] Xiaona Li, Jianwen Liang, Ning Chen, Jing Luo, Keegan R Adair, Changhong Wang, Mohammad Norouzi Banis, Tsun-Kong Sham, Li Zhang, Shangqian Zhao, et al. Water-mediated synthesis of a superionic halide solid electrolyte. *Angewandte Chemie*, 131(46):16579–16584, 2019.

[35] Jianwen Liang, Xiaona Li, Keegan R. Adair, and Xueliang Sun. Metal Halide Superionic Conductors for All-Solid-State Batteries. *ACCOUNTS OF CHEMICAL RESEARCH*, 54(4):1023–1033, February 2021.

[36] Yihan Xiao, Yan Wang, Shou-Hang Bo, Jae Chul Kim, Lincoln J Miara, and Gerbrand Ceder. Understanding interface stability in solid-state batteries. *Nature Reviews Materials*, 5(2):105–126, 2020.

[37] Sokseiha Muy, Johannes Voss, Roman Schlem, Raimund Koerver, Stefan J Sedlmaier, Filippo Maglia, Peter Lamp, Wolfgang G Zeier, and Yang Shao-Horn. High-throughput screening of solid-state li-ion conductors using lattice-dynamics descriptors. *Iscience*, 16:270–282, 2019.

[38] Niek J.J. de Klerk, Eveline van der Maas, and Marnix Wagemaker. Analysis of Diffusion in Solid-State Electrolytes through MD Simulations, Improvement of the Li-Ion Conductivity in β-Li3PS4 as an Example. *ACS Applied Energy Materials*, 1(7):3230–3242, July 2018.

[39] Roman Schlem, Sokseiha Muy, Nils Prinz, Ananya Banik, Yang Shao-Horn, Mirijam Zobel, and Wolfgang G. Zeier. Mechanochemical Synthesis: A Tool to Tune Cation Site Disorder and Ionic Transport Properties of Li3MCl6 (M = Y, Er) Superionic Conductors. *Advanced Energy Materials*, n/a(n/a):1903719, 2020.

[40] Raimund Koerver, Wenbo Zhang, Lea de Biasi, Simon Schweidler, Aleksandr O Kondrakov, Stefan Kolling, Torsten Brezesinski, Pascal Hartmann, Wolfgang G Zeier, and Jürgen Janek. Chemo-mechanical expansion of lithium electrode materials–on the route to mechanically optimized all-solid-state batteries. *Energy & Environmental Science*, 11(8):2142–2158, 2018.

[41] RI Smith, S Hull, MG Tucker, HY Playford, DJ McPhail, SP Waller, and ST Norberg. The upgraded polaris powder diffractometer at the isis neutron source. *Review of scientific instruments*, 90(11):115101, 2019.

[42] O. Arnold, J. C. Bilheux, J. M. Borreguero, A. Buts, S. I. Campbell, L. Chapon, M. Doucet, N. Draper, R. Ferraz Leal, M. A. Gigg, V. E. Lynch, A. Markvardsen, D. J. Mikkelson, R. L. Mikkelson, R. Miller, K. Palmen, P. Parker, G. Passos, T. G. Perring, P. F. Peterson, S. Ren, M. A. Reuter, A. T. Savici, J. W. Taylor, R. J. Taylor, R. Tolchenov, W. Zhou, and J. Zikoysky. Mantid-Data analysis and visualization package for neutron scattering and mu SR experiments. *NUCLEAR INSTRUMENTS & METHODS IN PHYSICS RESEARCH SECTION A-ACCELERATORS SPECTROMETERS DETECTORS AND ASSOCIATED EQUIPMENT*, 764:156–166, November 2014.

[43] Brian H. Toby and Robert B. Von Dreele. *GSAS-II* : the genesis of a modern open-source all purpose crystallography software package. *Journal of Applied Crystallography*, 46(2):544–549, April 2013.

7

[44] Georg Kresse and Jürgen Hafner. Ab initio molecular dynamics for liquid metals. *Physical review B*, 47(1):558, 1993.

[45] Georg Kresse and Jürgen Furthmüller. Efficiency of ab-initio total energy calculations for metals and semi-conductors using a plane-wave basis set. *Computational materials science*, 6(1):15–50, 1996.

[46] Georg Kresse and Jürgen Furthmüller. Efficient iterative schemes for ab initio total-energy calculations using a plane-wave basis set. *Physical review B*, 54(16):11169, 1996.

[47] John P Perdew, Kieron Burke, and Matthias Ernzerhof. Generalized gradient approximation made simple. *Physical review letters*, 77(18):3865, 1996.

[48] G Kresse and J Hafner. Norm-conserving and ultrasoft pseudopotentials for first-row and transition elements. *Journal of Physics: Condensed Matter*, 6(40):8245, 1994.

[49] Georg Kresse and Daniel Joubert. From ultrasoft pseudopotentials to the projector augmented-wave method. *Physical review b*, 59(3):1758, 1999.

[50] Shyue Ping Ong, William Davidson Richards, Anubhav Jain, Geoffroy Hautier, Michael Kocher, Shreyas Cholia, Dan Gunter, Vincent L Chevrier, Kristin A Persson, and Gerbrand Ceder. Python materials genomics (pymatgen): A robust, open-source python library for materials analysis. *Computational Materials Science*, 68:314–319, 2013.

[51] S. Parnell. Battery material candidates sample 1. *Computational Materials Science*, 2020.

7

Curriculum Vitæ

Eveline van der Maas

1993/02/27	Date of birth in Biel, Switzerland
Nationality	Swiss, dutch

University education

2012/09 - 2016/02	**Bachelor of science - University of Bern, Switzerland**
	Faculty of Science
	Program: Geography (major) and Physics (minor)
	Bachelor thesis: The screen bias on a subdaily scale: Analysis of parallel measured temperature series. Grade 6/6
2016/08 - 2018/07	**Master of Science - Delft university of technology**
	Faculty of Electrical Engineering, Mathematics and Computer Science
	Program: Sustainable energy technology
	Master thesis: The interface between Li-metal and the Argyrodite Li6PS5Cl. Grade 9/10
2019/01 - 2023/05	**PhD - Delft university of Technology**
	Faculty of applied science
	Institute: Radiation, science and technology
	PhD thesis: Halide solid electrolytes. From structure to properties

Summer schools and courses
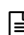
2019/07	**Electrochemistry Summerschool** – A two week school organized by the university of Southampton, about a variety of electrochemical techniques.
2019/08	**JCNS Neutron school** – A 2 week school organized by the Forschungszentrum Jülich and RWTH Achen about measurement techniques at Neutron facilities.
2020/04	**HERCULES** - the Higher European Research Course for Users of Large Experimental Systems. A 5 weeks course on the campus of the ESRF and ILL to learn about instruments and possibilities available at free electron laser facilities, synchrotrons and neutron sources.

List of Publications

1. Niek de klerk, *Eveline van der Maas*, Marnix Wagemaker: Analysis of Diffusion in Solid-State Electrolytes through MD Simulations, Improvement of the Li-Ion Conductivity in β-Li$_3$PS$_4$ as an Example. ACS Appl. Energy Mater. 2018, 1, 7, 3230-3242. http://dx.doi.org/10.1021/acsaem.8b00457

2. Tammo K Schwietert†, Violetta A Arszelewska†, Chao Wang†, Chuang Yu, Alexandros Vasileiadis, Niek JJ de Klerk, Jart Hageman, Thomas Hupfer, Ingo Kerkamm, Yaolin Xu, *Eveline van der Maas*, Erik M Kelder, Swapna Ganapathy, Marnix Wagemaker: Clarifying the relationship between redox activity and electrochemical stability in solid electrolytes. Nat. Mat. 2020, 19, 428-435. https://doi.org/10.1038/s41563-019-0576-0

3. Ming Liu, Chao Wang, Chenglong Zhao, *Eveline van der Maas*, Kui Lin, Violetta A Arszelewska, Baohua Li, Swapna Ganapathy, Marnix Wagemaker: Quantification of the Li-ion diffusion over an interface coating in all-solid-state batteries via NMR measurements. Nature communications 2021, 12, 5943. https://doi.org/10.1038/s41467-021-26190-2

📄 4. Jianwen Liang †,*Eveline van der Maas*†, Jing Luo†, Xiaona Li, Ning Chen, Keegan R. Adair, Weihan Li, Junjie Li, Yongfeng Hu, Jue Liu et al.: A Series of Ternary Metal Chloride Superionic Conductors for High-Performance All-Solid-State Lithium Batteries. Adv. Energy Mater., 2022, 12, 2103921. https://doi.org/10.1002/aenm.202270085

📄 5. *Eveline van der Maas*†, Wenxuan Zhao †, Zhu Cheng, Theodosios Famprikis, Michel Thijs, Steven R. Parnell, Swapna Ganapathy*, Marnix Wagemaker*. Investigation of Structure, Ionic Conductivity, and Electrochemical Stability of Halogen Substitution in Solid-State Ion Conductor Li$_3$YBr$_x$Cl$_6$$_-$$_x$. J. Phys. Chem. C, 2023, 127, 1, 125-132. https://doi.org/10.1021/acs.jpcc.2c07910

📄 6. *Eveline van der Maas*, Theodosios Famprikis, Saskia Pieters, Jonas P. Dijkstra, Zhaolong Li, Steven R. Parnell, Ron Smith, Ernst R. H. van Eck*, Swapna Ganapathy*, Marnix Wagemaker*: Re-investigating the structure-property relationship of the solid electrolyte Li $_3$$_-$$_xIn_1$$_-$$_xZr_xCl_6$ and the impact of In-Zr(IV) substitution. J. Mater. Chem. A, 2023, 11, 4559. https://doi.org/10.1039/d2ta08433c

7. *Eveline van der Maas*, Theodosios Famprikis[1], Deng Zeyu, Wenzuan Zhao[1], Jan Stroes[1], Ernst van Eck[2], Marnix Wagemaker[1], Swapna Ganapathy[1]: Study of diffusion on short time-scales using spin-lattice relaxation times measured at multiple Larmor frequencies: A practical guide to spectral density fitting. *Work in progress*

📄 Included in this thesis.

8

Appendix

8.1 Appendix to chapter 4

Table 8.1: Temperatures of the maximum T_{max}, Larmor frequencies ω_0 L and τ_c (T_{max})* ω_0 for ⁶Li and ⁷ as simulated for a 300, 500 and 850 MHz spectrometer

	6Li	7Li	
ω_0 on 850 MHz [rad/s]	7,40E+08	2,08E+09	
T_{max} on 850 MHz [K]	340	396	
ω_0 * τ_c at T=T_{max} on 850 MHz	0,993	1,004	
ω_0 on 500MHz [rad/s]	4,62E+08	1,22E+09	
T_{max} on 500 MHz [K]	319	365	
ω_0 * τ_c at T=T_{max} on 500 MHz spectrometer	0,998	0,996	
ω_0 on 300MHz [rad/s]	2,78E+08	7,33E+08	
T_{max} on 300 MHz [K]	299	339	
ω_0 * τ_c at T=T_{max} on 300 MHz spectrometer	0,991	0,998	

Table 8.2: Error analysis of Li_6PS_5Cl, 2BPP: Comparison between the median and maximum likelihood estimates and the error margin of the parameter extracted from the posterior probability distributions calculated using the MCMC-sampler.

Parameter	MLE	Median	Uncertainty	Relative error
$K_{D,1}$	2.77E+09	2.67E+09	4.61E+08	17%
$\tau_{0,1}$	9.82E-13	1.95E-12	1.71E-12	87%
$E_{A,1}$	0.16	0.14	0.02	15%
$K_{D,1}$	1.12E+10	1.05E+10	4.70E+08	4%
$\tau_{0,2}$	5.10E-13	1.54E-13	3.70E-14	24%
$E_{A,1}$	0.21	0.25	0.01	3%

Table 8.3: Estimations of the parameter values from the results of the MCMC method for Li_6PS_5Br fit using 2 BPP-type jump processes. Listed are the Maximum likelihood estimate (MLE) or the Median, estimated standard error and relative error (RE) for both the maximum likelihood and Median estimates.

Parameter	MLE	Median	Uncertainty	Relative error	
$K_{D,1}$	$1.11 \cdot 10^{10}$	$1.11 \cdot 10^{10}$	$1.19 \cdot 10^{8}$	1	%
$\tau_{0,1}$	$1.39 \cdot 10^{-12}$	$1.37 \cdot 10^{-12}$	$2.16 \cdot 10^{-13}$	16	%
$E_{A,1}$	0.143	0.144	0.003	2	%
$K_{D,2}$	$1.11 \cdot 10^{10}$	$1.11 \cdot 10^{10}$	$1.19 \cdot 10^{8}$	1	%
$\tau_{0,2}$	$5.10 \cdot 10^{-13}$	$5.73 \cdot 10^{-13}$	$6.00 \cdot 10^{-14}$	12	%
$E_{A,2}$	0.210	0.200	0.003	1	%

Table 8.4: $Li_3YCl_3Br_3$: Estimations of the parameter values from the results of the MCMC method for the **unweighed optimization**. Listed are the Maximum likelihood estimate (MLE) or the Median, estimated standard error and relative error (RE) for both the maximum likelihood and Median estimates.

Parameter	MLE	Median	Uncertainty	RE median %	RE MLE %
$\tau_{0,1}$	5.38E-13	4.54E-13	2.31E-13	50.9%	42.9%
$\tau_{0,2}$	9.83E-13	1.371E-12	5.69E-13	41.5%	57.9%
$\tau_{0,3}$	6.6E-13	1.067E-12	2.86E-13	26.8%	43.3%
$E_{A,1}$	0.1618	0.1638	0.0094	5.7%	5.8%
$E_{A,2}$	0.2433	0.2305	0.0159	6.9%	6.5%
$E_{A,3}$	0.2049	0.1911	0.0078	4.1%	3.8%
$K_{D,6Li,1}$	6.50E+07	6.09E+07	6.18E+06	10.1%	9.5%
$K_{D,6Li,2}$	8.55E+07	8.61E+07	6.25E+06	7.3%	7.3%
$K_{D,6Li,3}$	7.11E+07	6.96E+07	1.05E+07	15.1%	14.7%
$K_{D,7Li,1}$	5.96E+08	5.28E+08	5.11E+07	9.7%	8.6%
$K_{D,7Li,2}$	6.34E+08	5.62E+08	6.81E+07	12.1%	10.7%
$K_{D,7Li,3}$	1.59E+09	1.62E+09	6.67E+07	4.1%	4.2%

Figure 8.1: Posterior probability distributions of the parameter and scatter plots of the relationship parameter as received from the MCMC sampler to investigate the parameter space for the model consisting of two BPP-type jump processes. Calculated using 1000 walkers, 50'000 steps and 5000 burn points, without constraints for lnsigma.
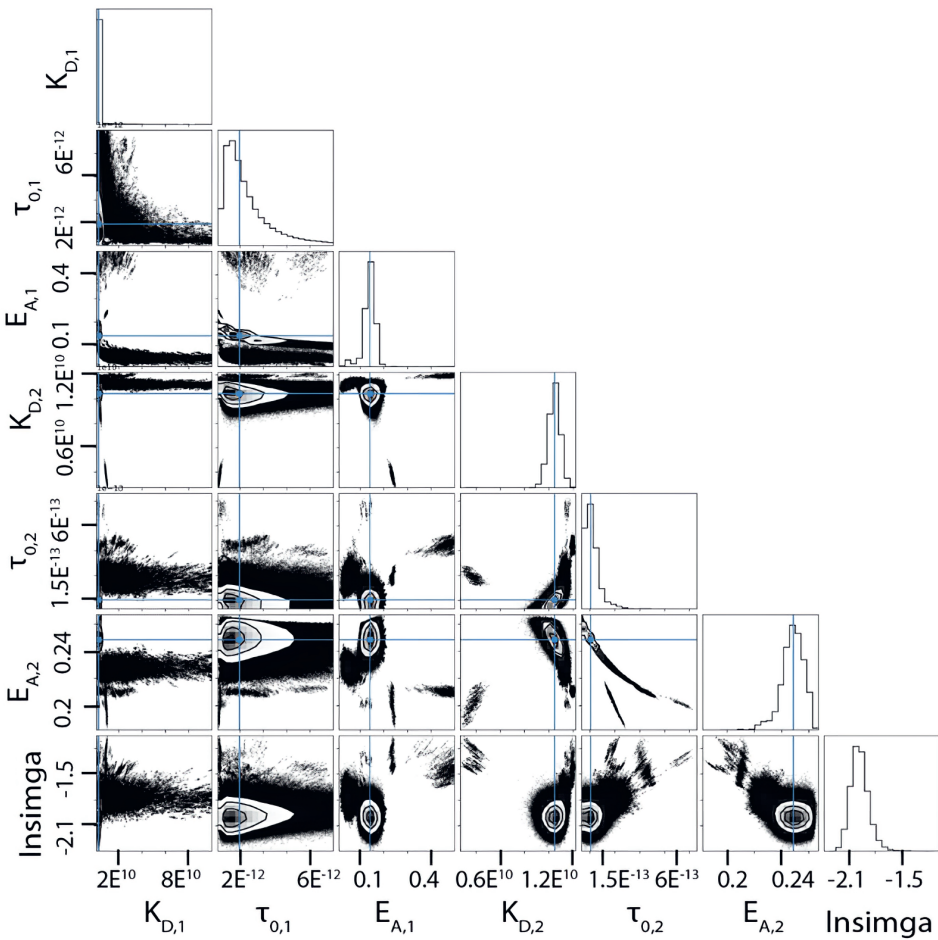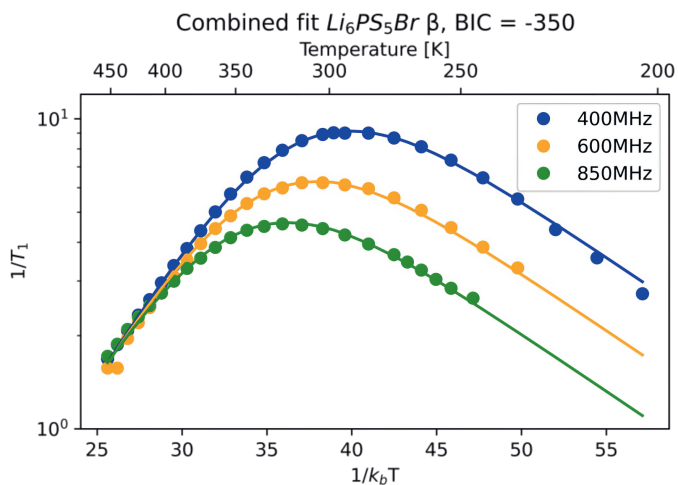
Figure 8.2

Figure 8.3
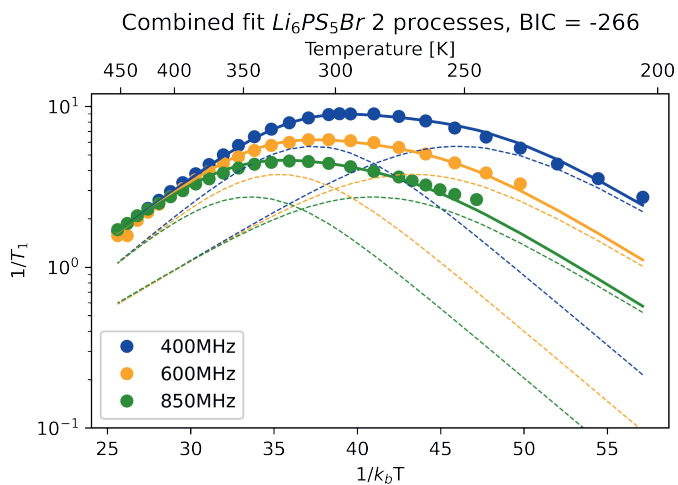
Figure 8.4: Relaxation rates $1/T_1$ of ^{7}Li (top) and ^{6}Li (bottom) of Li$_3$YCl$_3$Br$_3$ fit using a model containing of three independent BPP-type jump processes. E$_a$ [eV] of the individual processes are indicated in the plot. The residuals of the two dataset were not weighed.
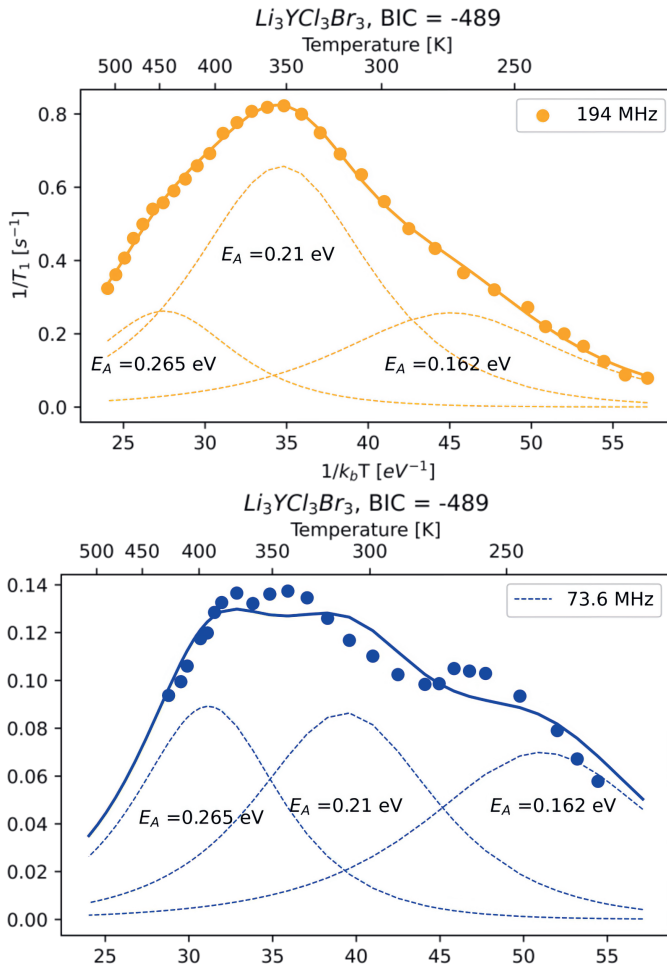
Figure 8.5: Relaxation rates $1/T_1$ of ^{7}Li (top) and ^{6}Li (bottom) of Li$_3$YCl$_3$Br$_3$ fit using a model containing of three independent BPP-type jump processes. E$_a$ [eV] of the individual processes are indicated in the plot. The residuals of the two dataset were weighed differently by an additional factor 4 for the dataset measured at 73.6 MHz.
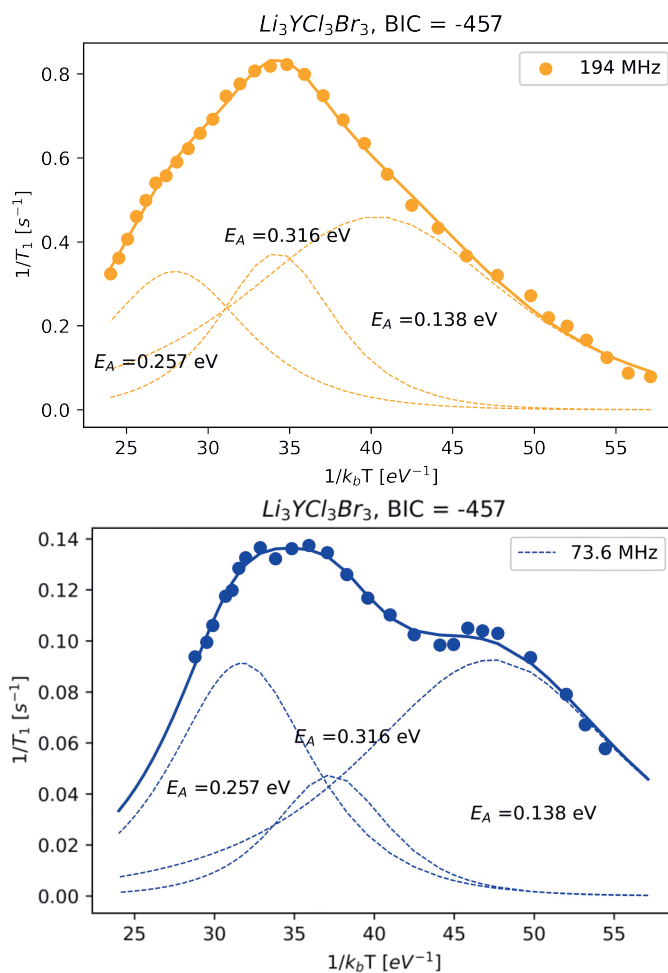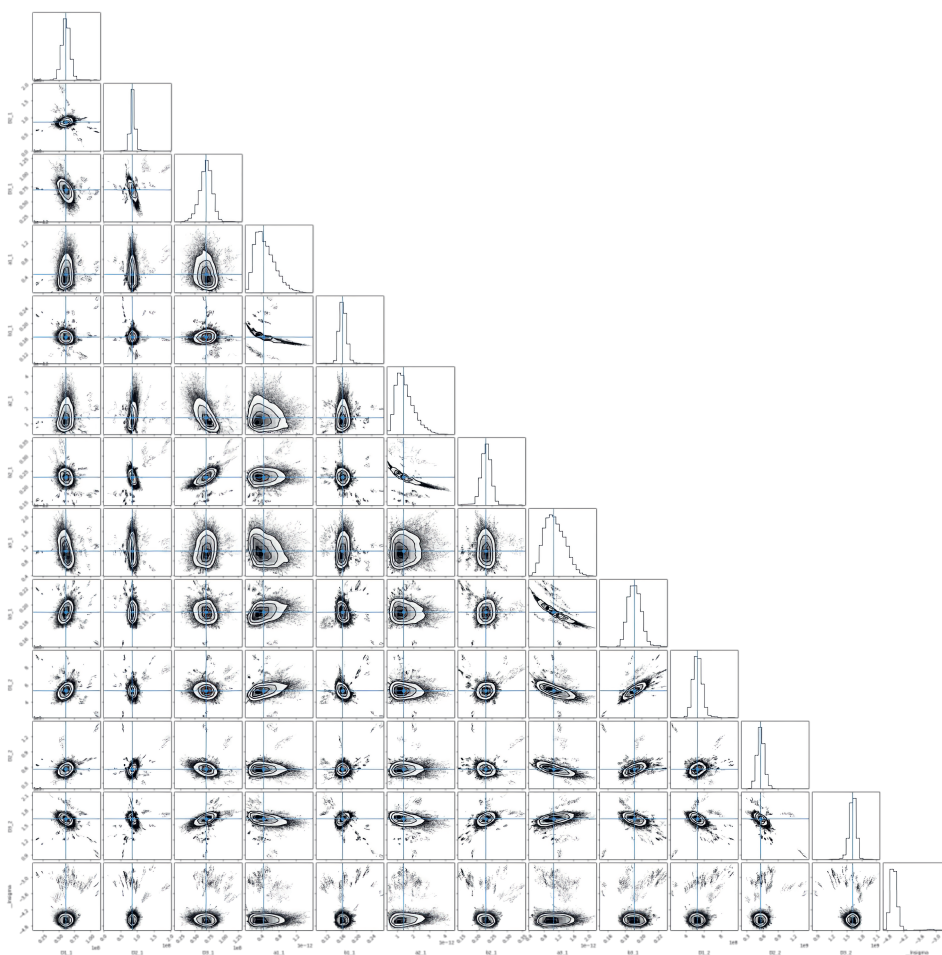
Figure 8.6: Corner plot of Li$_3$YCl$_3$Br$_3$ for the unweighed minimization. The axis can not be shown due to limited space. The plot will be available on github after publication of the paper.
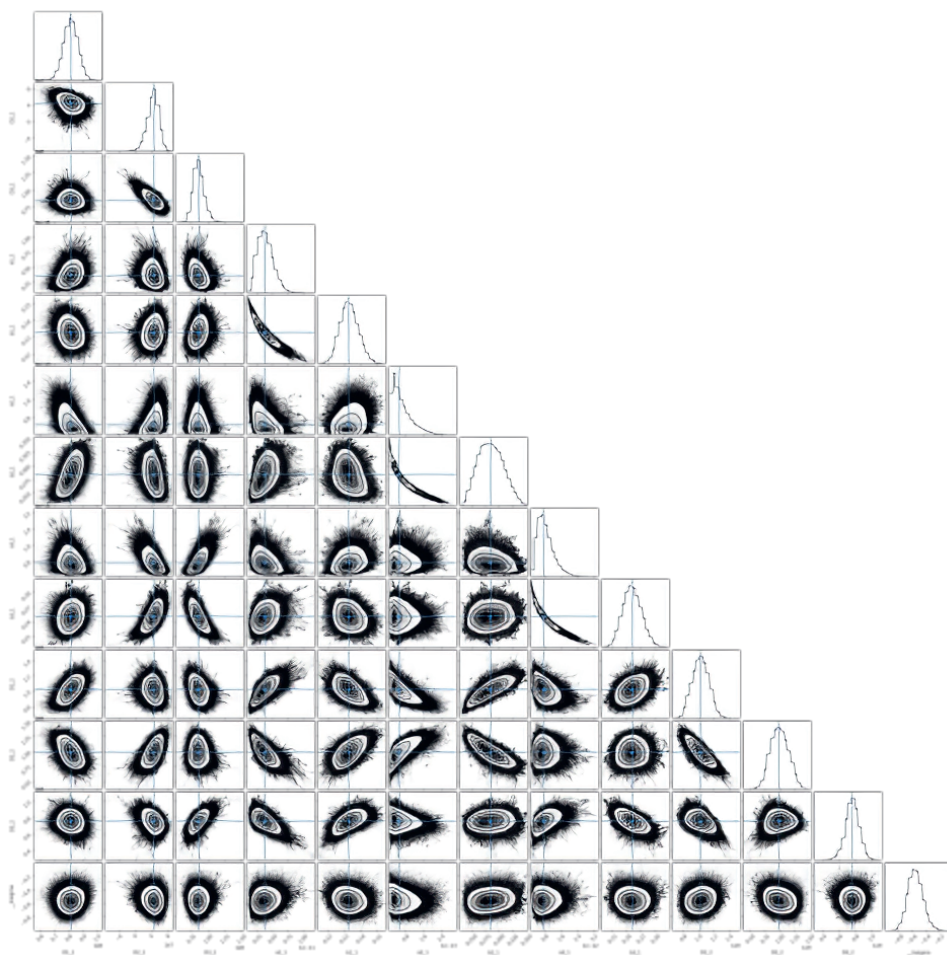
Figure 8.7: Corner plot of Li₃YCl₃Br₃ for the weighed minimization. The axis can not be shown due to limited space. The plot will be available on github after publication of the paper.

Table 8.5: Li$_3$YCl$_3$Br$_3$:Estimations of the parameter values from the results of the MCMC method for the **weighed optimization**. Listed are the Maximum likelihood estimate (MLE) or the Median, estimated standard error and relative error (RE) for both the maximum likelihood and Median estimates.

Parameter	MLE	Median	Uncertainty	RE median%	RE MLE %
$\tau_{0,1}$	1.91E-12	3.70E-12	1.29E-12	35.0 %	67.9%
$\tau_{0,2}$	1.70E-13	4.80E-14	4.10E-14	85.4 %	24.1%
$\tau_{0,3}$	9.49E-13	7.51E-13	3.74E-13	49.8 %	39.4%
$E_{A,1}$	0.1416	0.1327	0.0056	4.2 %	3.9%
$E_{A,2}$	0.2448	0.2839	0.0236	8,3 %	9.6%
$E_{A,3}$	0.2426	0.2503	0.0197	7.9 %	8.1%
$K_{D,6Li,1}$	7.45E+07	8.13E+07	5.01E+06	6.2 %	6.7%
$K_{D,6Li,2}$	5.29E+07	4.41E+07	1.39E+07	31.4 %	26.2%
$K_{D,6Li,3}$	8.83E+07	8.50E+07	7.93E+06	9.3 %	9.0%
$K_{D,7Li,1}$	8.09E+08	1.02E+09	1.10E+08	10.8 %	13.6%
$K_{D,7Li,2}$	1.28E+09	9.84E+08	1.52E+08	15.5 %	11.9%
$K_{D,7Li,3}$	7.71E+08	7.59E+08	8.08E+07	10.6 %	10.5%

Table 8.6: Diffusivities and ionic conductivities σ at 300K for the weighed an unweighed solution, calculated from the fits of the activation energy E_a and pre-exponential factor τ_0. Upper and lower bounds are the bounds given if the parameter E_a and τ_0 are within one standard error (as obtained by raising χ^2 with reduced χ^2_{red}).

unweighed solution		weighed solution	
The diffusivities are			
4.19E-11	$m^{-2}s^{-1}$	1.52E-11	$m^{-2}s^{-1}$
5.76E-12	$m^{-2}s^{-1}$	2.96E-12	$m^{-2}s^{-1}$
8.39E-13	$m^{-2}s^{-1}$	7.71E-13	$m^{-2}s^{-1}$
The conductivities are			
31.4115	$mScm^{-1}$	17.2725	$mScm^{-1}$
4.3135	$mScm^{-1}$	2.5638	$mScm^{-1}$
0.6283	$mScm^{-1}$	0.6474	$mScm^{-1}$
upper limit diffusivity			
3.59E-10	$m^{-2}s^{-1}$	2.93E-11	$m^{-2}s^{-1}$
2.08E-11	$m^{-2}s^{-1}$	4.50E-11	$m^{-2}s^{-1}$
2.58E-12	$m^{-2}s^{-1}$	2.36E-12	$m^{-2}s^{-1}$
uuper limit conductivity			
268.8994	$mScm^{-1}$	37.1336	$mScm^{-1}$
15.5984	$mScm^{-1}$	18.9610	$mScm^{-1}$
1.9292	$mScm^{-1}$	1.7683	$mScm^{-1}$
lower limit diffusivity			
1.33E-11	$m^{-2}s^{-1}$	8.95E-12	$m^{-2}s^{-1}$
2.17E-12	$m^{-2}s^{-1}$	6.32E-13	$m^{-2}s^{-1}$
3.26E-13	$m^{-2}s^{-1}$	3.05E-13	$m^{-2}s^{-1}$
upper limit diffusivity			
9.9793	$mScm^{-1}$	9.4169	$mScm^{-1}$
1.6223	$mScm^{-1}$	0.7105	$mScm^{-1}$
0.2444	$mScm^{-1}$	0.2786	$mScm^{-1}$

8.2 Appendix to chapter 5

Figure 8.8: Lattice parameters (left) and unit cell angle and volume (right) of the Rietveld refinement of the neutron and the x-ray data. The error bars of the volume are smaller than the dots.
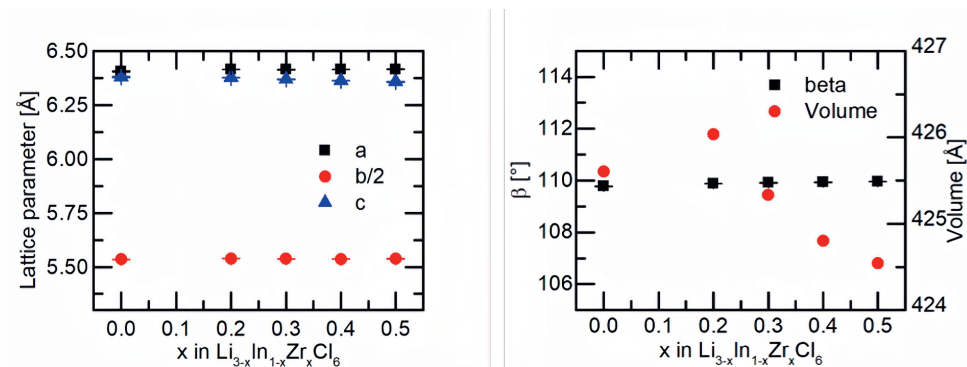
Figure 8.9: Simultaneous Rietveld fit to the neutron diffraction data (top, bank 5) and x-ray diffraction data (bottom) of $Li_{3-x}In_{1-x}Zr_xCl_6$ with x=0.
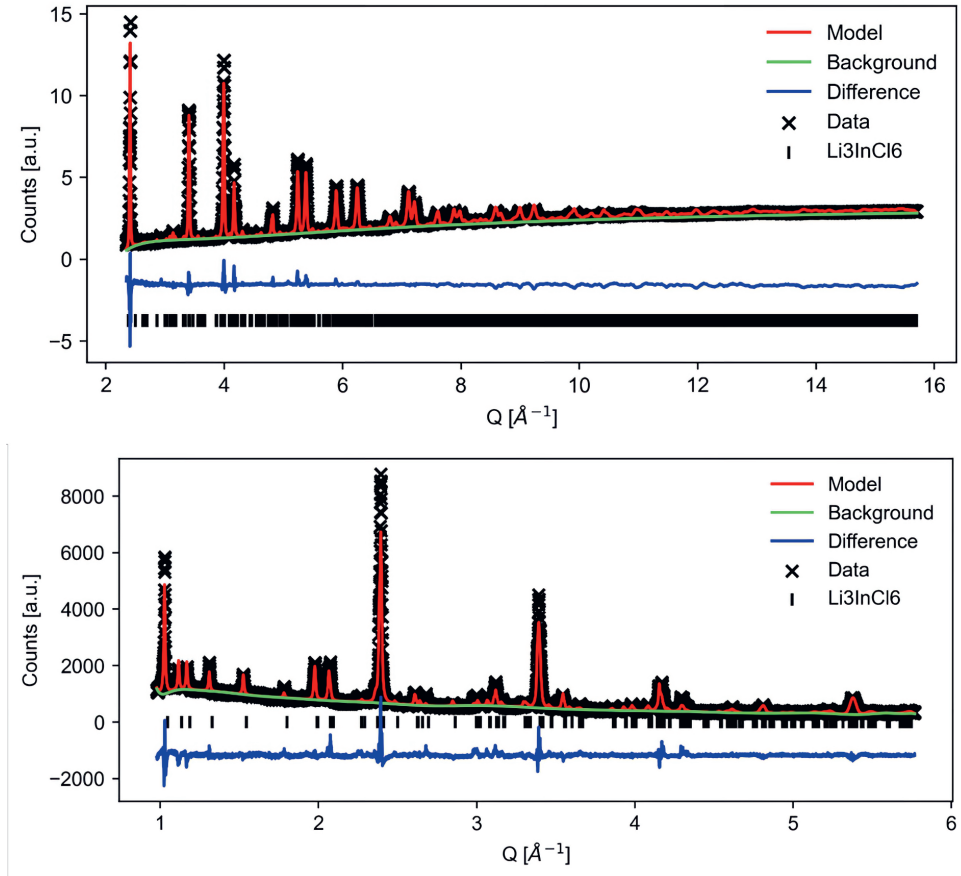

Table 8.7: Errors of the Ac-impedance measurements at room temperature. R is the resistance, h the height of the pellet, A the surface area of the pellet, sigma the ionic conductivity. Errors are calculated based on gaussian error propagation.

x	R [Ω]	dR [Ω]	h [cm]	dh [cm]	A [cm²]	σ [S/cm]	dσ/σ [%]	dσ [S/cm]
0.5	71.9	0.143	0.1	0.005	0.785	1.77E-3	5.004%	8.86 E-5
0.4	64.8	0.184	0.1	0.005	0.785	1.96E-3	5.008 %	9.84E-5
0.3	62.88	0.078	0.1	0.005	0.785	2.02E-3	5.002 %	1.01E-4
0.2	74.29	0.056	0.1	0.005	0.785	1.71E-3	5.001 %	8.57 E-5
0.1	75.1	0.074	0.1	0.005	0.785	1.7E-3	5.001 %	8.48 E-5
0	83.72	0.178	0.1	0.005	0.785	1.52E-3	5.005 %	7.61 E-5

Figure 8.10: Simultaneous Rietveld fit to the neutron diffraction data (top, bank 5) and x-ray diffraction data (bottom) of $Li_{3-x}In_{1-x}Zr_xCl_6$ with x=0.2.
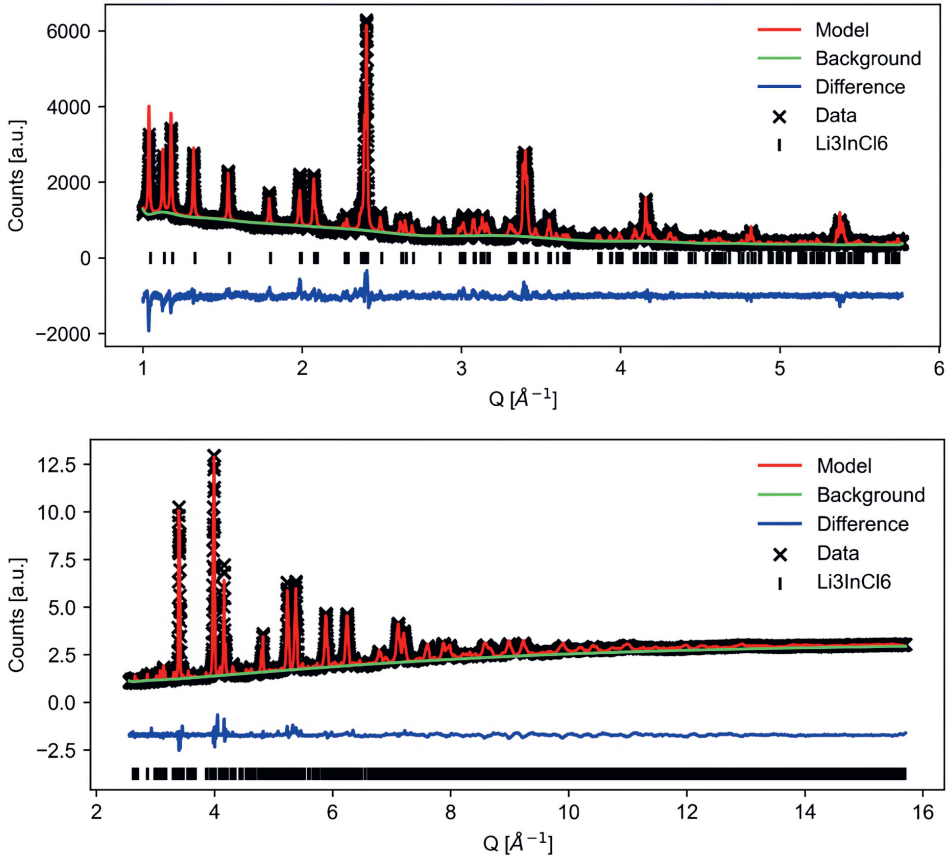
Table 8.8

x	Δ_{Ea} [%]	EA [eV]	dEA [eV]
0.5	3.32	0.2827	0.0094
0.4	2.39	0.2896	0.0069
0.3	3.83	0.277	0.0106
0.2	2.67	0.2975	0.008
0.1	2.2	0.3381	0.0074
0.0	6.36	0.3064	0.0195

Figure 8.11: Simultaneous Rietveld fit to the neutron diffraction data (top, bank 5) and x-ray diffraction data (bottom) of $Li_{3-x}In_{1-x}Zr_xCl_6$ with x=0.3.
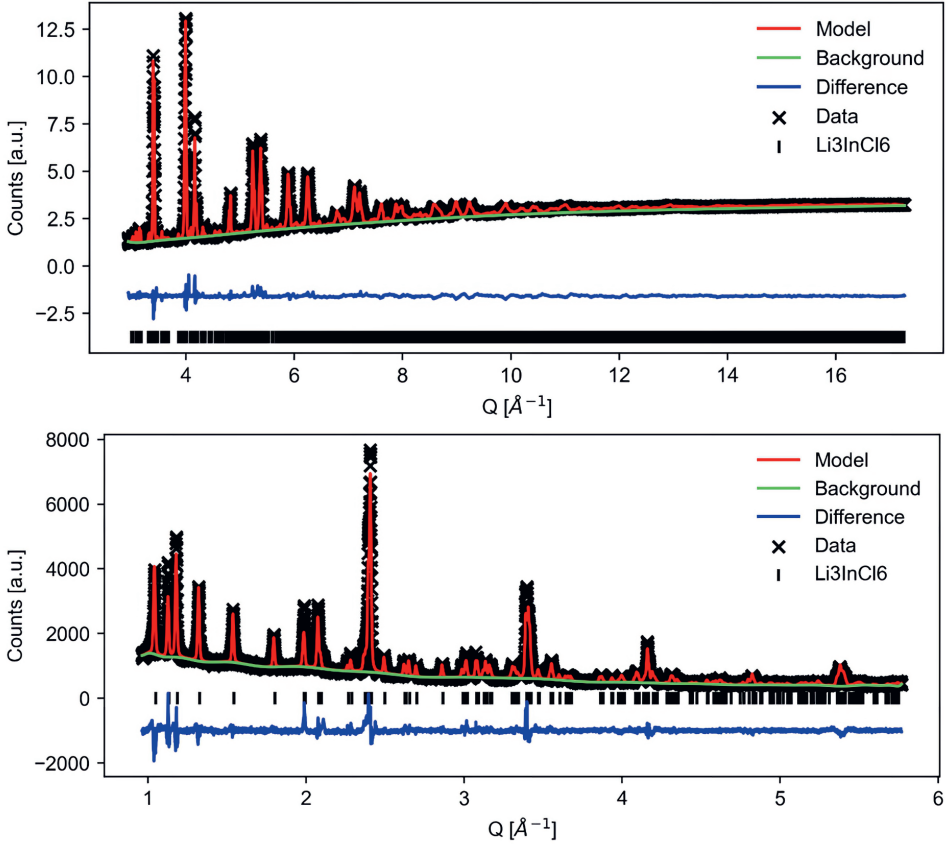

Table 8.9

x	τ_0 [s]	E_a [eV]	β	E_a slope [eV]	Reference
0	$1.5 \cdot 10^{-11}$	0.189	1	0.106	This work
0	$1.5 \cdot 10^{-11}$	0.131	1	0.0212	This work
0.3	3.3±1.7E-13	0.3±0.02	0.29±0.04	0.142	This work
0.5	6.6±2.5E-13	0.28±0.02	0.26±0.02	0.12	This work
0	n.a.	0.291	0.22	n.a.	Helm et al.
0.1	n.a.	0.203	0.44	n.a.	Helm et al.
0.2	n.a.	0.143	0.63	n.a.	Helm et al.
0.3	n.a.	0.117	0.65	n.a.	Helm et al.
0.4	n.a.	0.116	0.66	n.a.	Helm et al.
0.5	n.a.	0.136	0.57	n.a.	Helm et al.

Figure 8.12: Simultaneous Rietveld fit to the neutron diffraction data (top, bank 5) and x-ray diffraction data (bottom) of $Li_{3-x}In_{1-x}Zr_xCl_6$ with x=0.4.
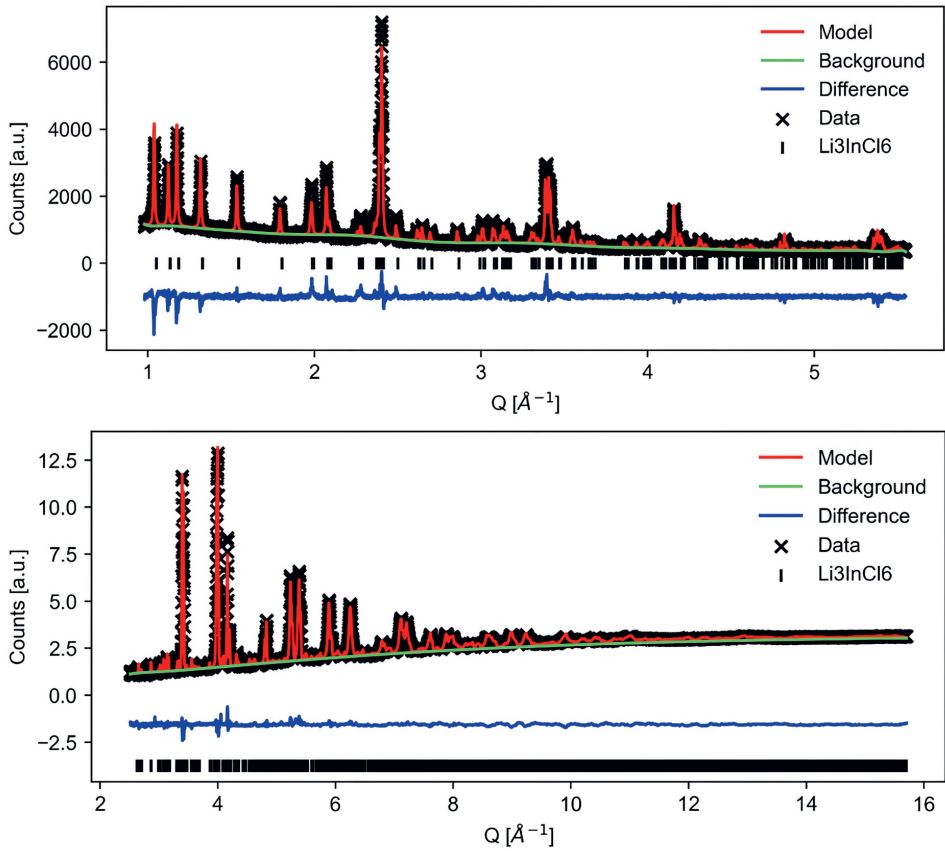
Table 8.10: Comparison of values obtained from spectral density fits of spin-lattice relaxation measurements of $Li_{2.7}In_{0.7}Zr_{0.3}Cl_6$ measured on a 300MHz and 400MHz spectrometer, with data from this thesis, data from Helm et al. as well as the values reported in Helm et al.

Spectrometer	τ_0 [s]	E_a [eV]	β	$C(\tau_0, E_a)$	$C(\tau_0, \beta)$	$C(E_a, \beta)$	Ref.
300MHz	1.46±0.2E-11	0.146±0.005	1	−0.933	-	-	this work
300MHz	1.18±0.8E-12	0.257±0.003	0.365	−0.997	0.962	−0.978	this work
400MHz	1.49±0.1E-11	0.140±0.003	1	−0.991	-	-	this work
400MHz	9.12±0.2E-13	0.256±0.001	0.427	−0.998	0.971	−0.984	this work
300Mhz	1.00±0.2E-10	0.082±0.0004	1	−0.98	-	-	Data from Helm et al.
300Mhz	1.46±1E-11	0.160±0.004	0.437	−0.996	0.978	−0.991	Data from Helm et al.
300Mhz	-	0.117	0.65	-	-	-	Fit from Helm et al.

Figure 8.13: Simultaneous Rietveld fit to the neutron diffraction data (top, bank 5) and x-ray diffraction data (bottom) of $Li_{3-x}In_{1-x}Zr_xCl_6$ with x=0.5.
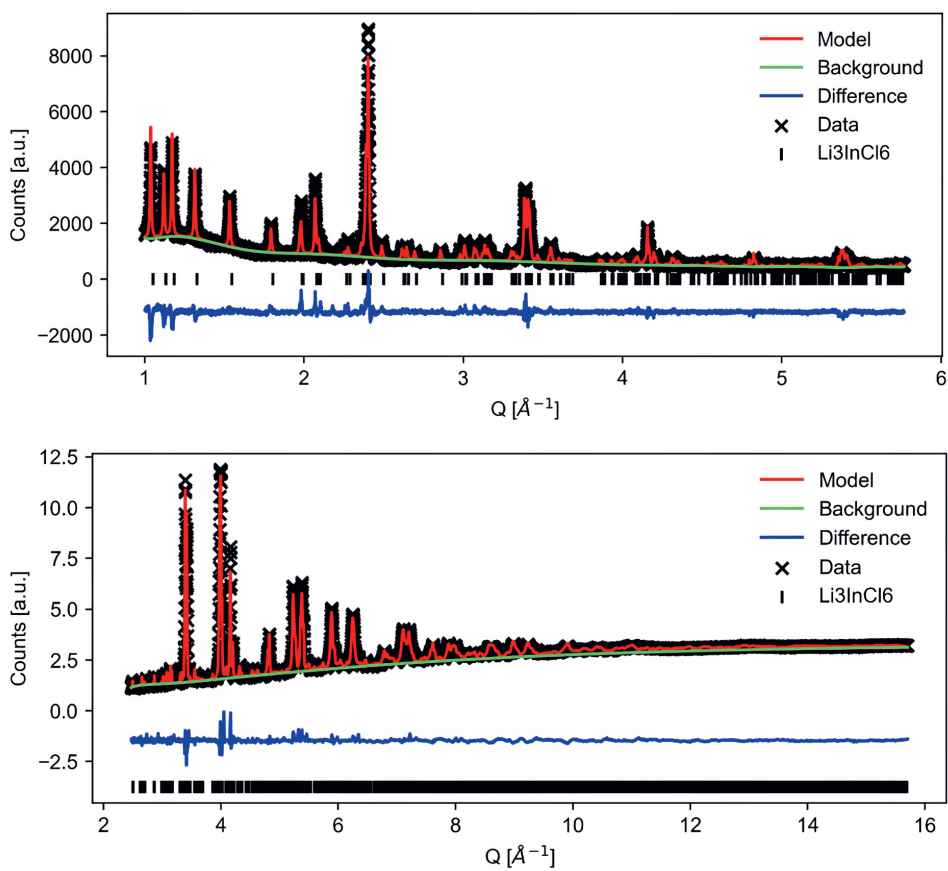
Figure 8.14: Confirmation of the validity of the chosen equivalent circuits to fit the AC-impedance spectra by the Kramers-Krönig analysis. The examples chosen here are from the material $Li_{3-x}In_{1-x}Zr_xCl_6$ with x=0.5 at 50 (high temperature L-R-CPE), 30 (medium temperature L-(R)(P)-CPE) and low temperature (L-(R)(CPE)-(CPE) at -9.4 ℃.
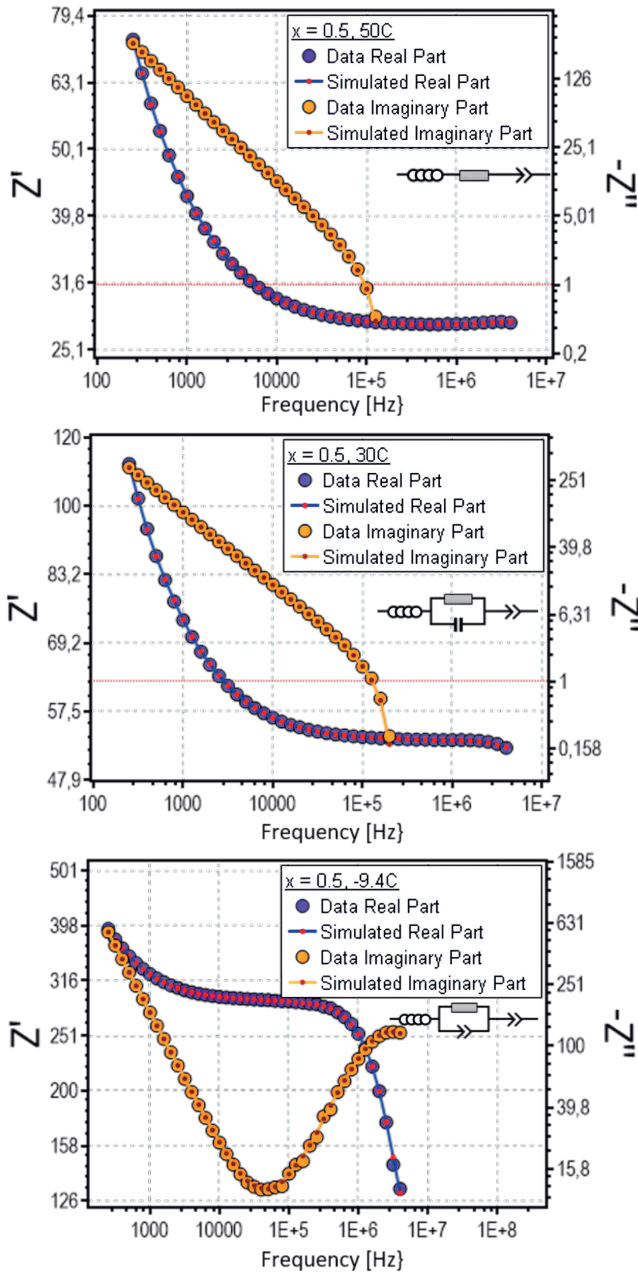
Figure 8.15: Arrhenius Relationship extracted from the AC-impedance measurements of the materials $Li_{3-x}In_{1-x}Zr_xCl_6$ for x=0-0.5.
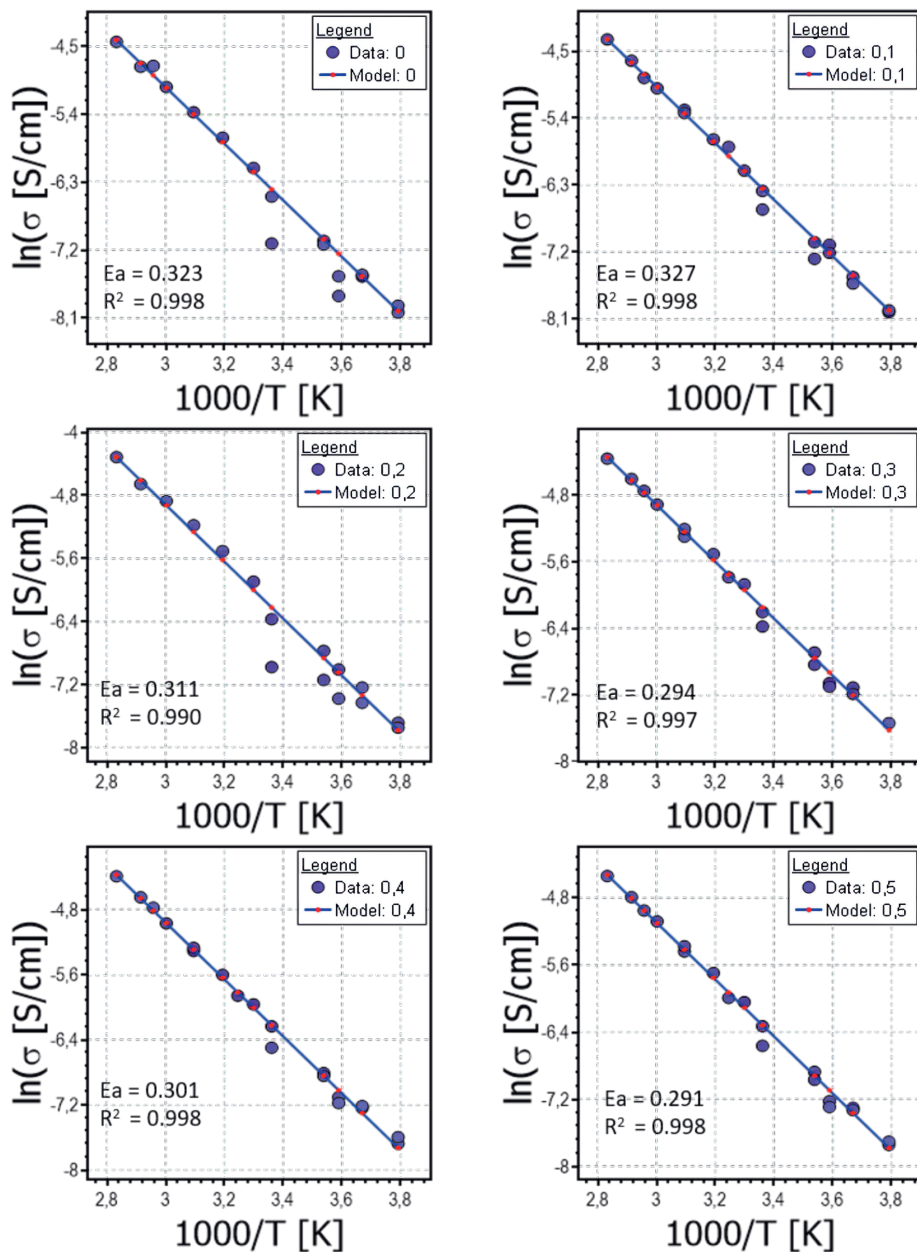
Figure 8.16: Relaxation rates of Li in Li_3InCl_6 measured at three different larmor frequencies plotted on logarithmic scale. 116MHz corresponds to ^{7}Li measured on a 300MHz, 155MHz to ^{7}Li on a 400MHz and 44MHz to ^{6}Li on a 300 MHz spectrometer. The contribution of the individual jump processes to the relaxation rate are shown in red and black (same processes in all plots) and illustrate which process the datasets are sensitive to.
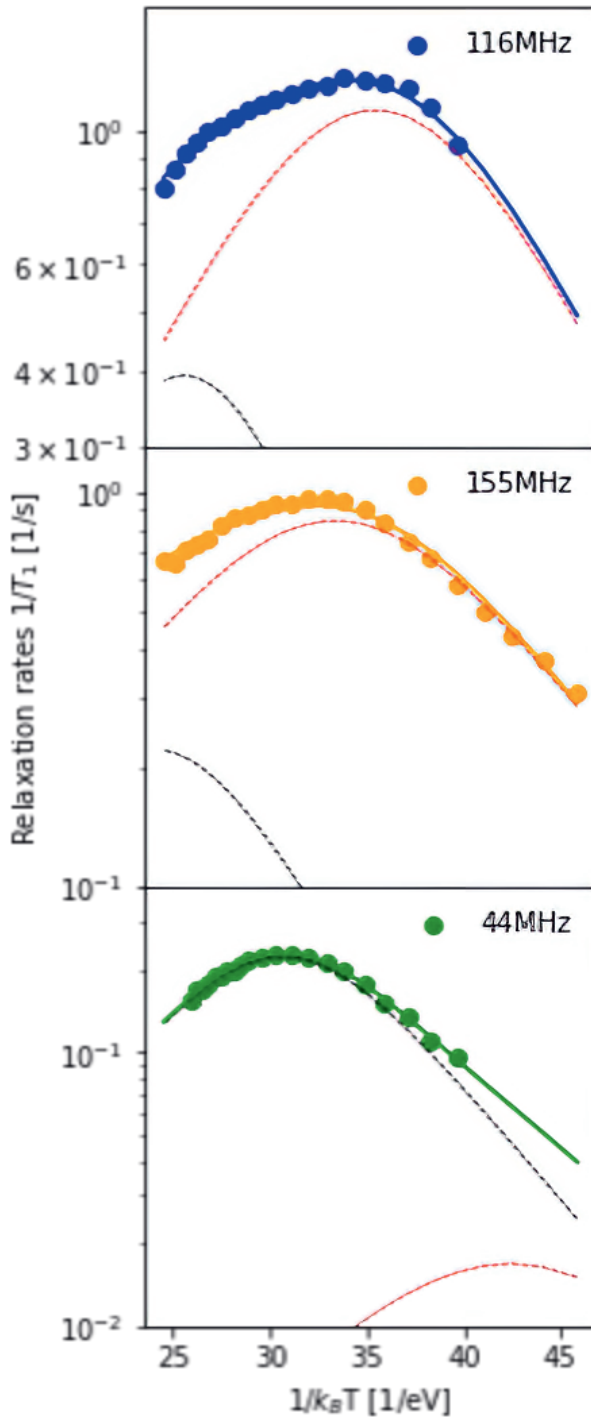
Figure 8.17: The relaxation data of $Li_{3-x}In_{1-x}Zr_xCl_6$ at x=0 and fits of the different models (1-4) as described in the main text (BPP model with one jump process only). The fits are visualized with the T1 in the y-axis, as the differences in the models can be seen more clearly. The plot shows that both empirically modified datasets fit the data well, with a small preference for the modified 2D model (4) as indicated by the smaller BIC.
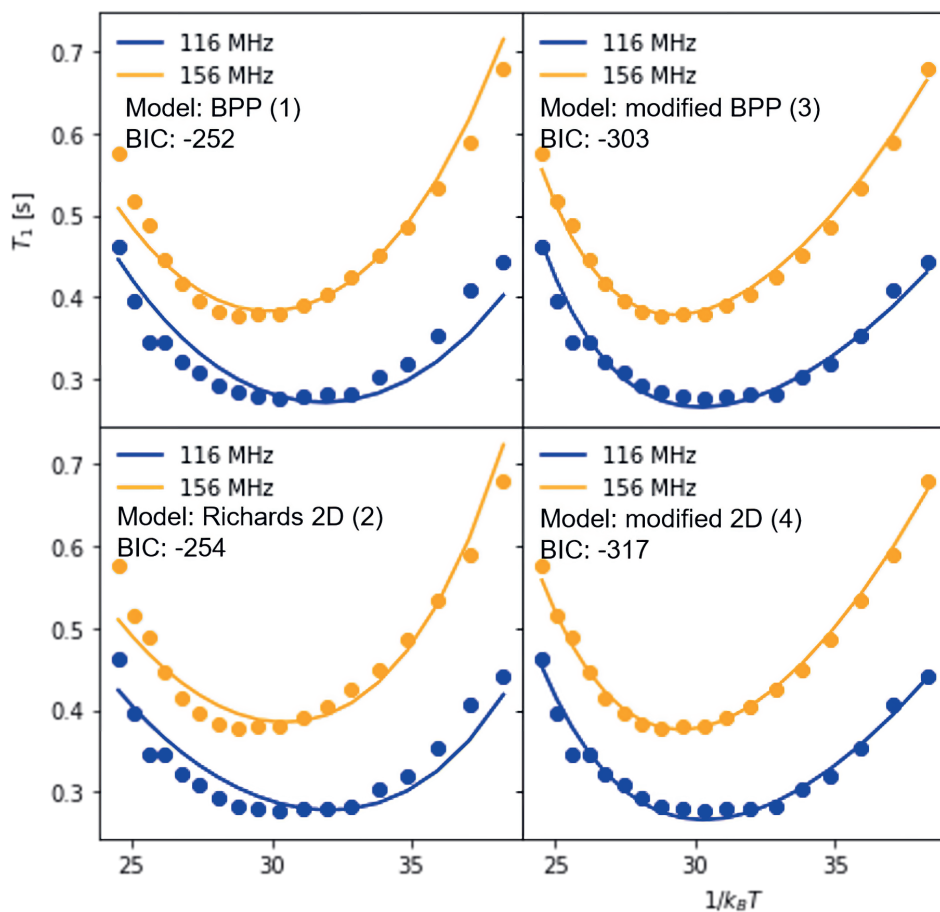
Figure 8.18: The relaxation data of $Li_{3-x}In_{1-x}Zr_xCl_6$ x=0.3 and fits of the different models (1-4) as described in the main text. The fits are visualized with the T1 in the y-axis, as the differences in the models can be seen more clearly. The plot shows that both empirically modified datasets fit the data well, with a small preference for the modified 2D model (4) as indicated by the smaller BIC.
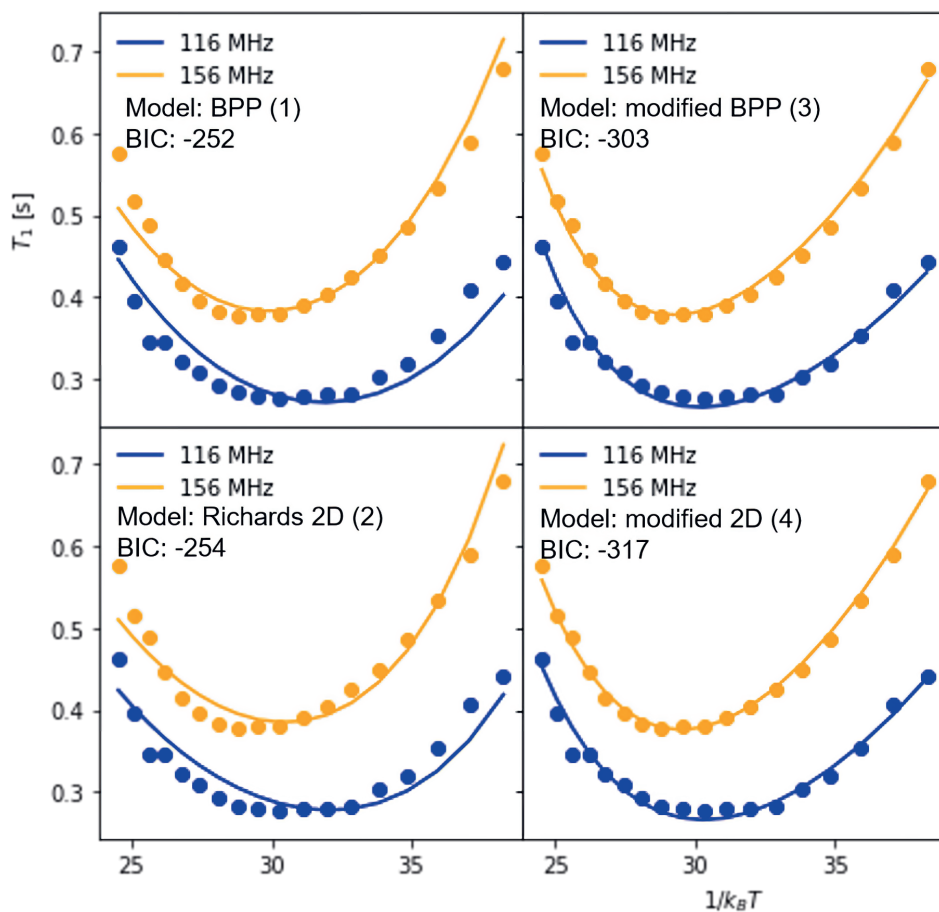
Figure 8.19: The relaxation data of $Li_{3-x}In_{1-x}Zr_xCl_6$ x=0.5 and fits of the different models (1-4) as described in the main text. The fits are visualized with the T1 in the y-axis, as the differences in the models can be seen more clearly. The plot shows that both empirically modified datasets fit the data well, with a small preference for the modified 2D model (4) as indicated by the smaller BIC.
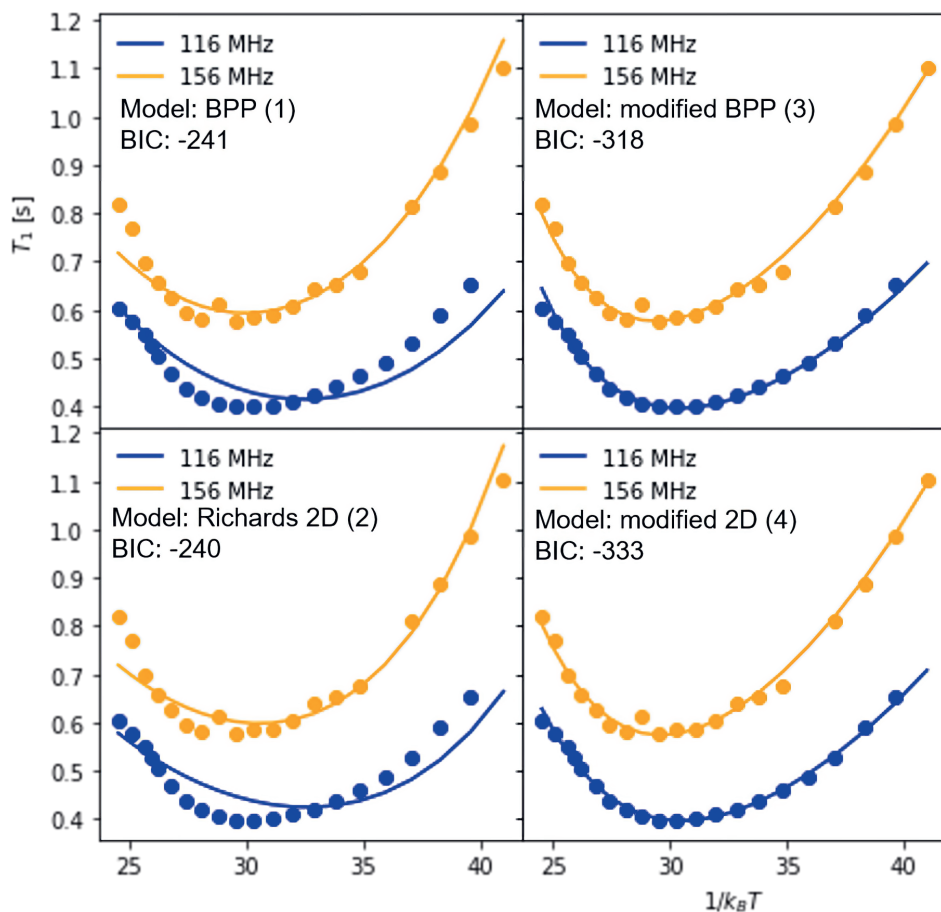
Figure 8.20: Comparison of the data for Li$_{3-x}$In$_{1-x}$Zr$_x$Cl$_6$ (x=0.3). The data from Helm et al.1 represents approximate values obtained using plot digitize

Comparison of individual fits of the BPP and modified BPP model to x=0.3
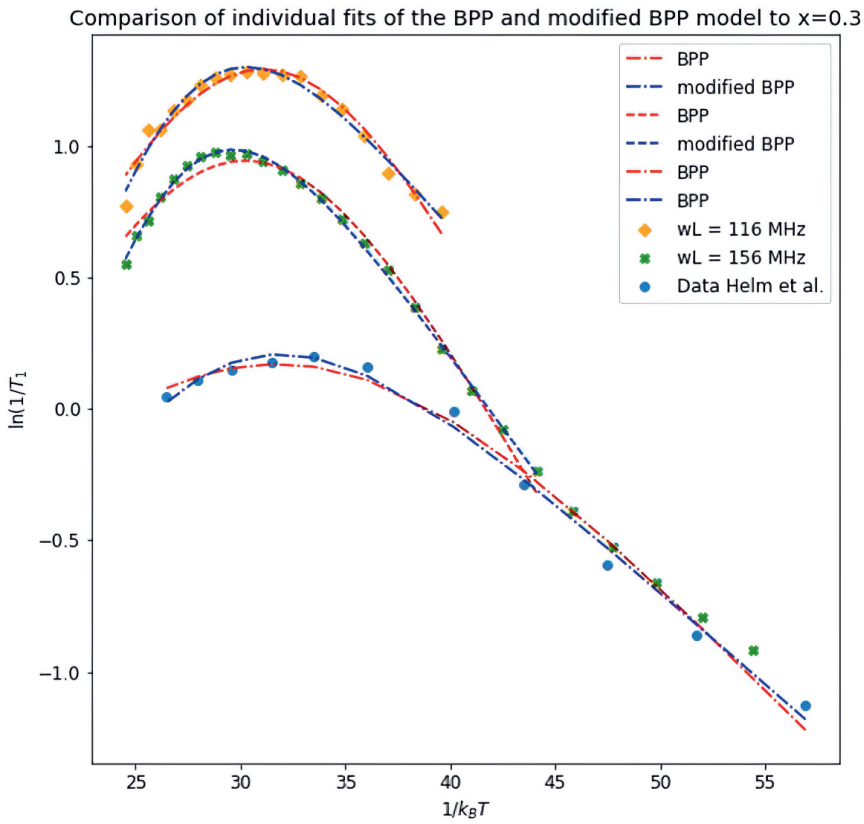
Figure 8.21: Left: Variable temperature ^{7}Li static NMR spectra of Li$_3$InCl$_6$ at 9.4T (156 MHz) at T = 233 K (top) and T = 493K (bottom). Already at 233K the line is motionally narrowed but at 493K the residual broadening is so small that sharp features emerge. Right: The high temperature spectrum at 493K can only be approximated by taking into account a residual quadrupolar coupling of about 6kHz as well as CSA with a span of 3 ppm and a skew of -0.76.
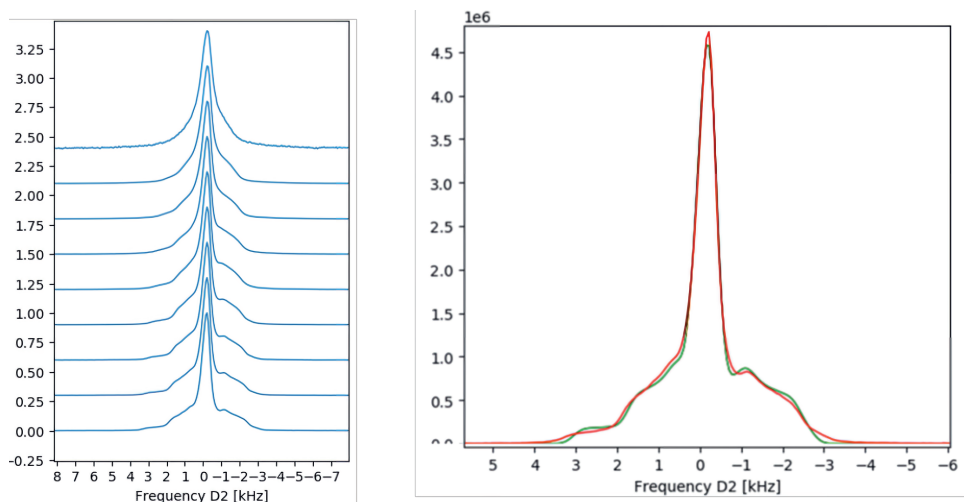
Figure 8.22: ^{7}Li static NMR spectra of Li$_{3-x}$In$_{1-x}$Zr$_x$Cl$_6$, at 9.4T (156 MHz) at T = 493K. The central transition is motionally narrowed in all three samples. The shape of the satellites can only be approximated by a combination of quadrupolar coupling as well as chemical shift anisotropy, see Figure S14. The shape is most pronounced in Li$_3$InCl$_6$, and slightly flattens for the doped samples. The residual chemical shift anisotropy that resolves at the satellites indicates that the motion of the Li-ions across the different sites does not average out completely.
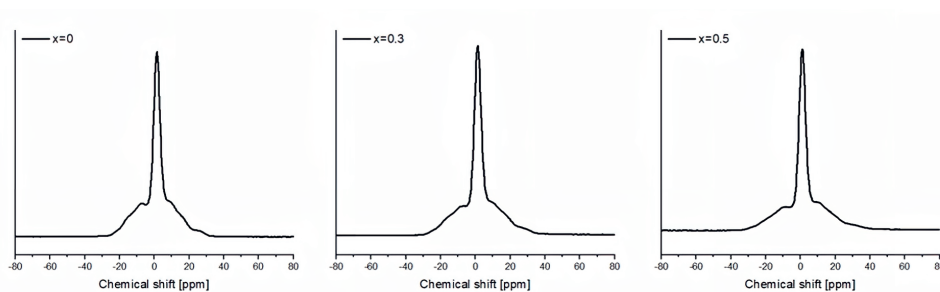
Table 8.11

Ionic conductivity Impedance [S/m]	1.52 E-1	
Charge carrier per unit cell	6	
Unit cell volume [Å]	425.6	
Unit cell volume [m³]	4.26E-28	
charge carrier concentration [#/m³]	1.41E+28	
electric charge e² [C²]	2.5669E-38	
kB [J/K]	1.38E-23	
DAC	1.72E-12	
Jump process	1	2
E_a	0.131	0.189
τ_0 [s]	2.44E-12	2.19E-13

8.3 Appendix to chapter 6

Supplementary text 1

The difference between the diffraction patterns of the ball milled plus annealed samples and the co-melted samples (Figure 8.24 can arise from multiple factors: 1) the formation of a phase with higher symmetry; 2) preferred orientation of powders in the sample holder, 3) anisotropic crystallite size; 4) stacking faults. Considering the good fits of the refinement based on the neutron diffraction data (Figure 8.27-8.31), the formation of a higher symmetry phase is unlikely. To understand how the microstructures of these materials are influenced by the synthetic procedure, scanning electron microscope (SEM) images were taken to probe the morphology of the samples above (Figure 8.26)). It can be observed that the $Li_3YBr_3Cl_3$ ball milled for 8h (BM-LYBC) shows a microstructure in which small spheres with a dimension of around 1 µm agglomerate. During the crystallization occurring during the annealing step at 400 ℃, the microspheres are sintered, thereby the particle size increases to the order of 10 µm. On the other hand, increasingly laminar microstructures are shown in SEM images of $Li_3YBr_3Cl_3$ samples prepared by ball milling followed by annealing at 500 ℃(AN500-LYBC) and only high temperature melting at 650 ℃(HT-LYBC). The thin-flake morphology observed here may suggest an anisotropic growth of the crystal, which could be an indicator for preferred orientation. However, considering recent contributions in literature, it is likely that stacking faults are the reason for the observed mismatch in peak intensities at low angles in the X-ray diffraction data. All these aspects show distinctively in the diffraction pattern, preferential orientation will change relative intensities depending on the degree of the averaging across the different orientations. Anisotropic size will preferentially broaden certain peaks, and stacking faults will lead to a more triangular peak shape. From the diffraction patterns in Figure 8.25, it is difficult to draw conclusions.

Figure 8.23: Unit cell volume per formula unit as a function of composition
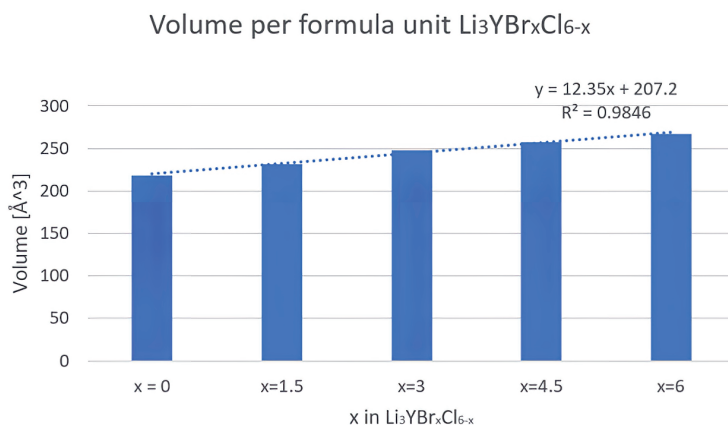

Volume per formula unit $Li_3YBr_xCl_{6-x}$

$y = 12.35x + 207.2$
$R^2 = 0.9846$

Volume [$Å^3$] (y-axis)

x in $Li_3YBr_xCl_{6-x}$ (x-axis)

Figure 8.24: (a) XRD patterns of ball milled (BM) of $Li_3YBr_3Cl_3$ samples as a function of ball milling duration (4-24h). The highlighted peaks (grey) reflect the formation of the ZrO2 phase that grows with increasing ball milling time, due to degradation/shedding from the ball milling balls. The materials prepared show broadened peaks, as is characteristic for ball milled-samples, and some peaks at low angles ($2\theta < 2\theta$ °) (b) Evolution of room temperature ionic conductivity of $Li_3YBr_3Cl_3$ (BM-LYBC) over the ball milling time is shown. The highest ionic conductivity was achieved after 8h of ball milling.
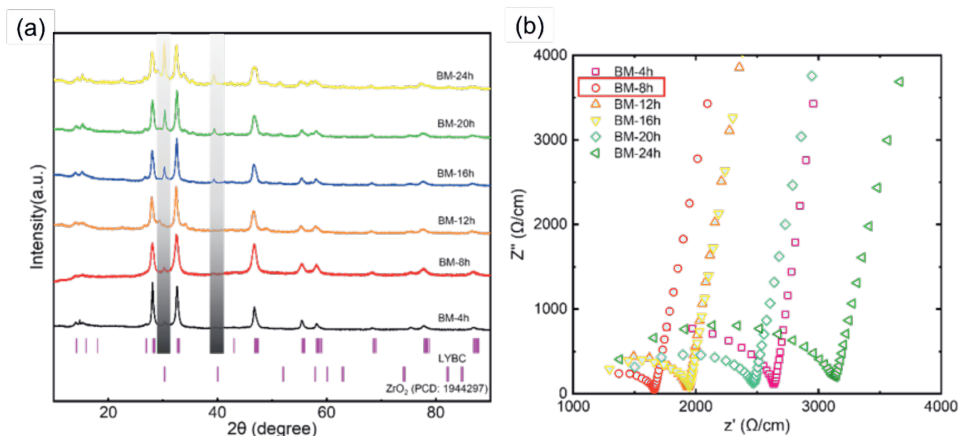
Figure 8.25: XRD patterns of $Li_3YBr_3Cl_3$ (LYBC) samples synthesized by different methods (HT – melted at 650, AN-T annealed at temperature T in ℃ following the ball milling step, BM – mechanochemical synthesis by ball milling for 8h). The diffraction pattern of the LYBC with high crystallinity reported by Liu et al1. is also shown for comparison. Ball milling and annealing at 400-500℃ both show some bragg peaks at $2\theta < 20°$, which disappear for the HT sample (b) Comparison of Nyquist plots of the LYBC samples at room temperature. The highest ionic conductivity was achieved by comelting the precursors at 650℃ (HT).
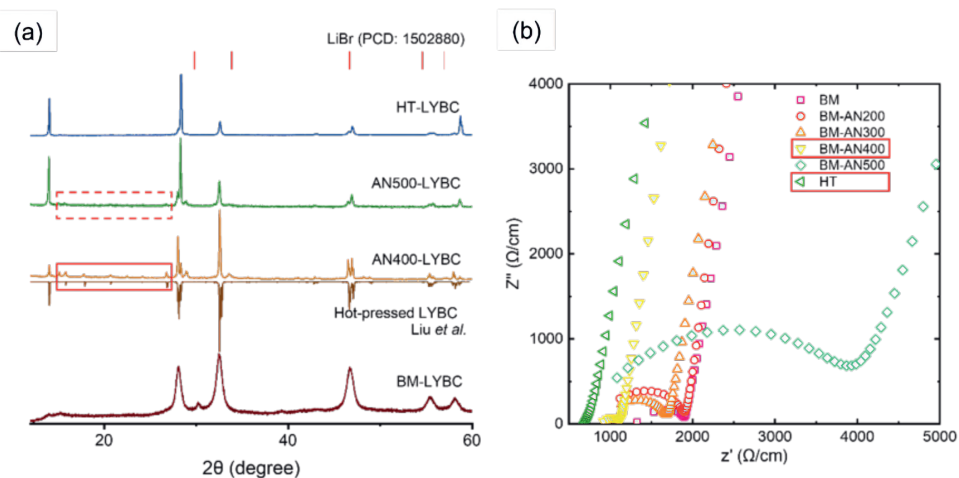
Figure 8.26: Scanning electron microscope (SEM) images of (a) BM-LYBC (b) AN400-LYBC (c) AN500-LYBC and (d) HT-LYBC. For abbreviations see SI Text 1.
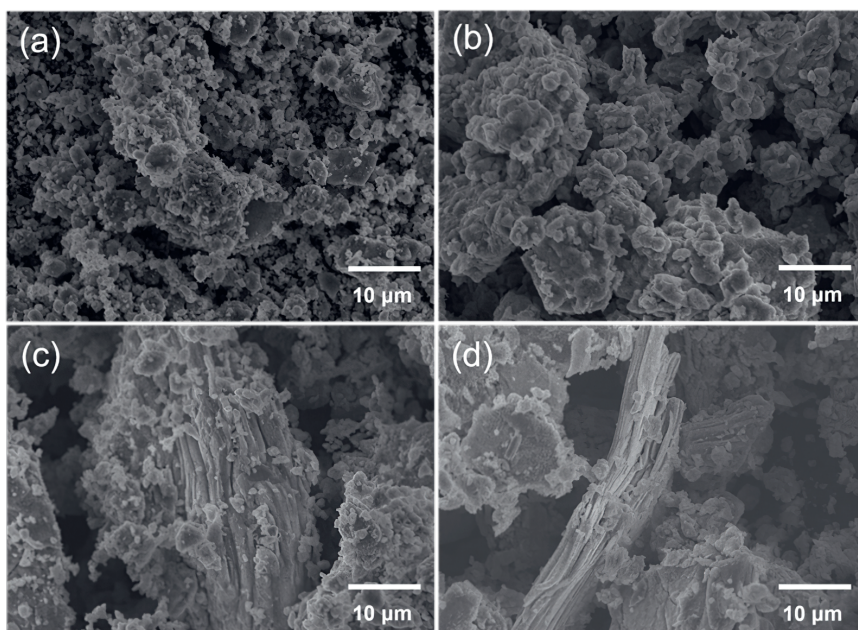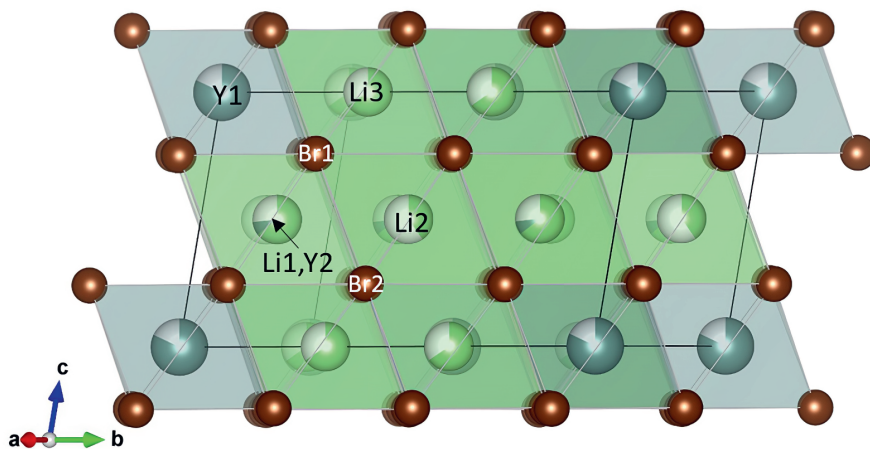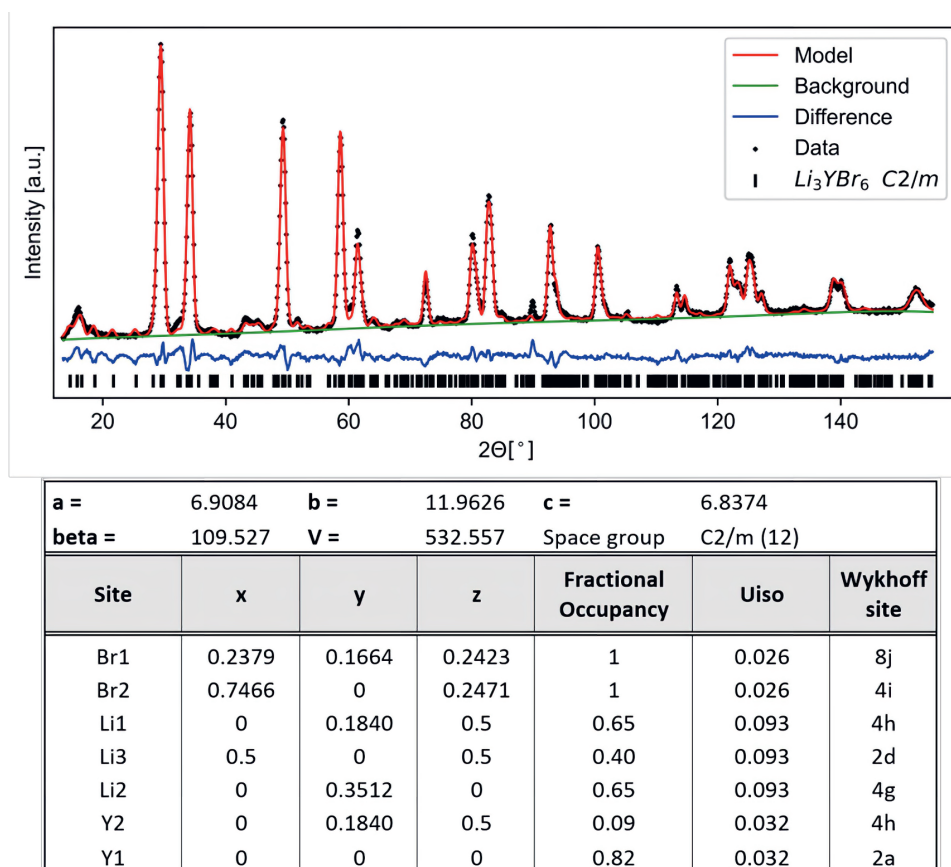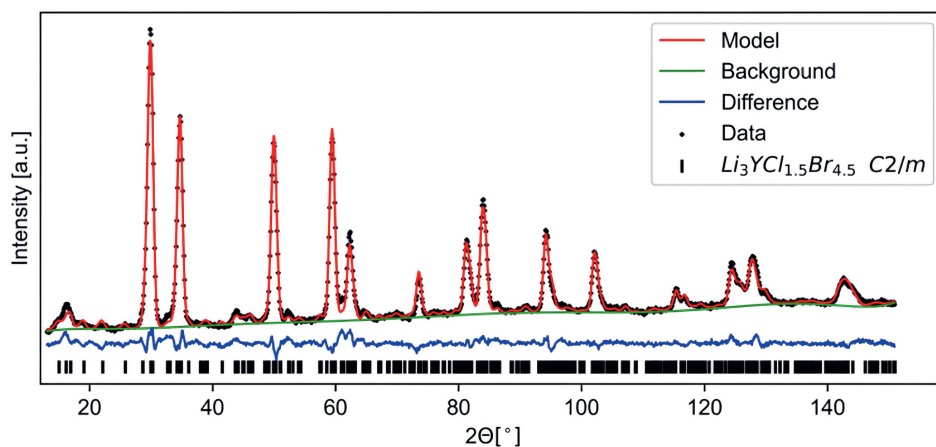
Figure 8.27: Neutron diffraction pattern, structure solution and visualisation of the structure solution for Li_3YBr_6

a =	6.9084	b =	11.9626	c =	6.8374
beta =	109.527	V =	532.557	Space group	C2/m (12)

Site	x	y	z	Fractional Occupancy	Uiso	Wykhoff site
Br1	0.2379	0.1664	0.2423	1	0.026	8j
Br2	0.7466	0	0.2471	1	0.026	4i
Li1	0	0.1840	0.5	0.65	0.093	4h
Li3	0.5	0	0.5	0.40	0.093	2d
Li2	0	0.3512	0	0.65	0.093	4g
Y2	0	0.1840	0.5	0.09	0.032	4h
Y1	0	0	0	0.82	0.032	2a

Figure 8.28: Neutron diffraction pattern, structure solution and visualisation of the structure solution for Li$_3$YCl$_{1.5}$Br$_{4.5}$

Site	x	y	z	Fractional Occupancy	Uiso	Wykhoff site
Br1	0.2464	0.1662	0.2438	0.75	0.031	8j
Br2	0.7492	0	0.2409	0.75	0.031	4i
Cl1	0.2464	0.1662	0.2438	0.25	0.031	8j
Cl2	0.7492	0.0000	0.2409	0.25	0.031	4i
Li1	0	0.1840	0.5	0.60	0.035	4h
Li3	0.5	0	0.5	0.48	0.035	2d
Li2	0	0.3512	0	0.67	0.035	4g
Y2	0	0.1840	0.5	0.12	0.012	4h
Y1	0	0	0	0.77	0.012	2a

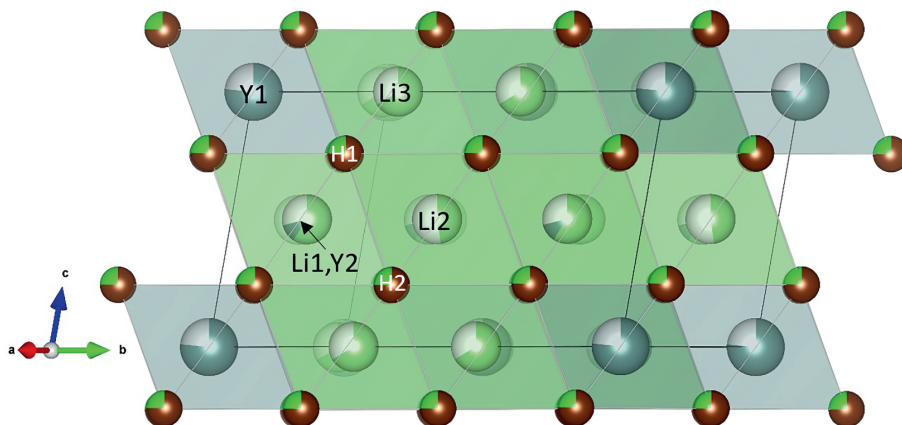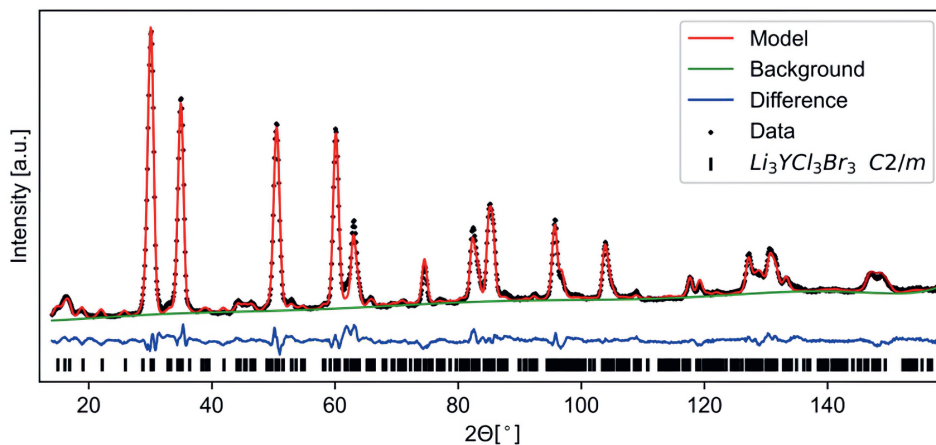a = 6.8455, b = 11.8600, c = 6.7752, beta = 109.442, V = 518.695, Space group C2/m (12)

Figure 8.29: Neutron diffraction pattern, structure solution and visualisation of the structure solution for $Li_3YCl_3Br_3$

a =		6.7436	b =		11.6891		6.6687		
beta =		109.508	V =		495.490	Space group		C2/m (12)	

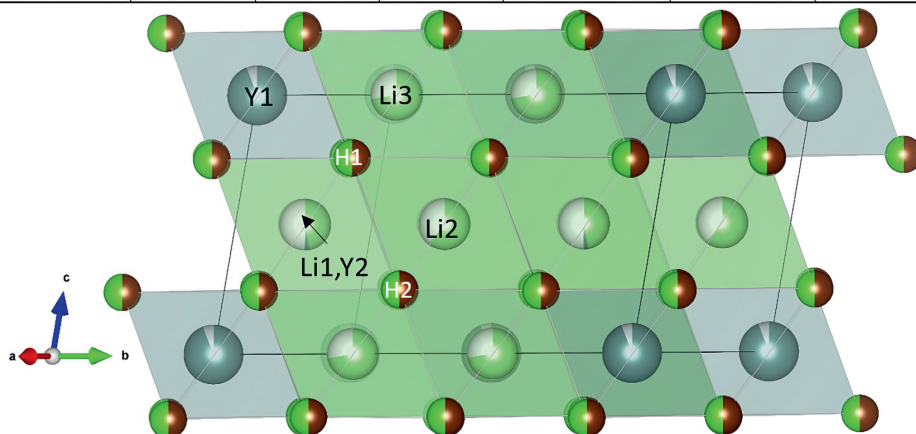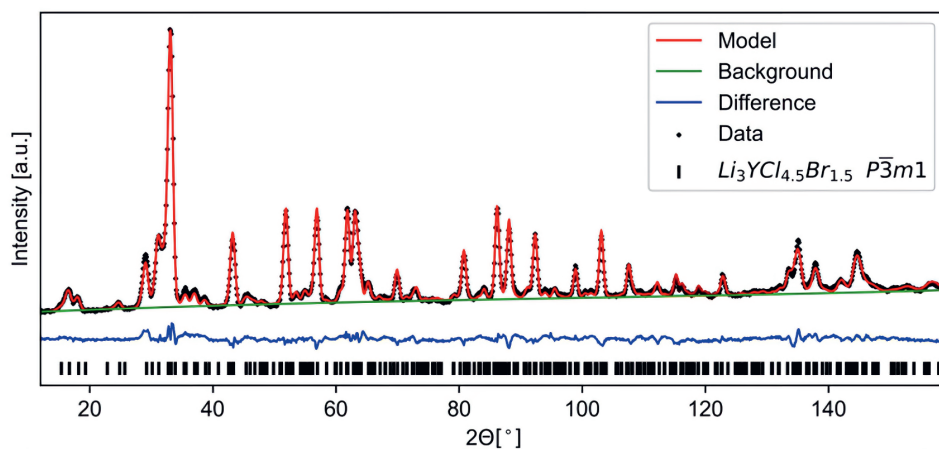| Site	x	y	z	Fractional Occupancy	Uiso	Wykhoff site
Br1	0.2426	0.1636	0.2420	0.50	0.031	8j
Br2	0.7495	0	0.2499	0.50	0.031	4i
Cl1	0.2426	0.1636	0.2420	0.50	0.031	8j
Cl2	0.7495	0	0.2499	0.50	0.031	4i
Li1	0	0.1670	0.5	0.47	0.109	4h
Li3	0.5	0	0.5	0.61	0.109	2d
Li2	0	0.3330	0	0.72	0.109	4g
Y2	0	0.1670	0.5	0.03	0.031	4h
Y1	0	0	0	0.94	0.031	2a

Figure 8.30: Neutron diffraction pattern, structure solution and visualisation of the structure solution for $Li_3YCl_{4.5}Br_{1.5}$

a =	11.3923	b =	11.3929	c =	6.1708		
V =	693.575			Space group	P-3m1 (164)		

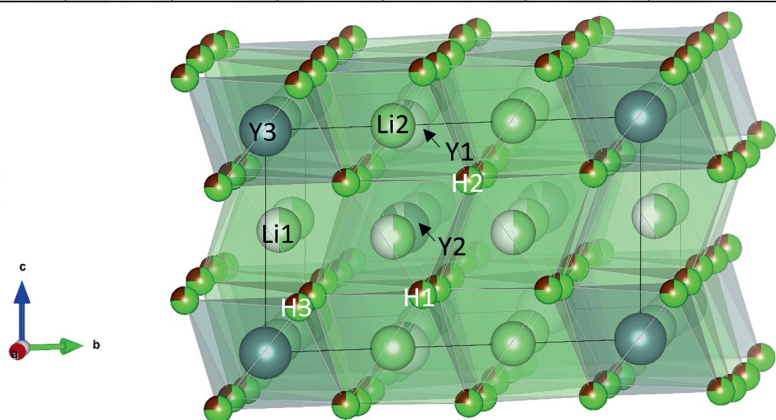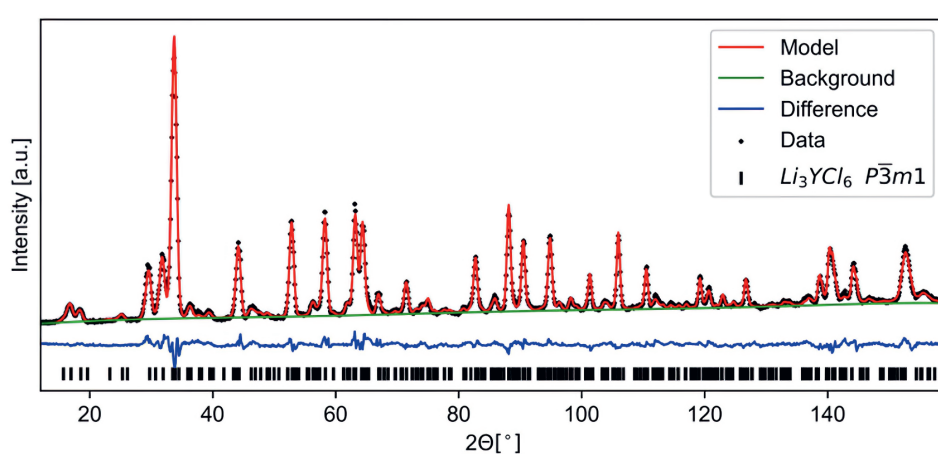| Site	x	y	z	Fractional Occupancy	Uiso	Wykhoff site
Cl1	0.2215	0.7785	0.2676	0.75	0.025	6i
Cl2	0.5546	0.4454	0.2441	0.75	0.025	6i
Cl3	0.8865	0.1135	0.2319	0.75	0.025	6i
Br1	0.2215	0.7785	0.2676	0.25	0.165	6i
Br2	0.5546	0.4454	0.2441	0.25	0.165	6i
Br3	0.8865	0.1135	0.2319	0.25	0.040	6i
Li1	0.3397	0	0.5	0.5	0.040	6h
Li2	0.3397	0	0	1	0.040	6g
Y1	0.3333	0.6667	0.0506	0.07	0.025	2d
Y2	0.3333	0.6667	0.5100	0.93	0.025	2d
Y3	0	0	0	1	0.025	1a

Figure 8.31: Neutron diffraction pattern, structure solution and visualisation of the structure solution for Li_3YCl_6

a =	11.1821	b =	11.1821	c =		6.0278	
V =	653.911			Space group		P-3m1 (164)	

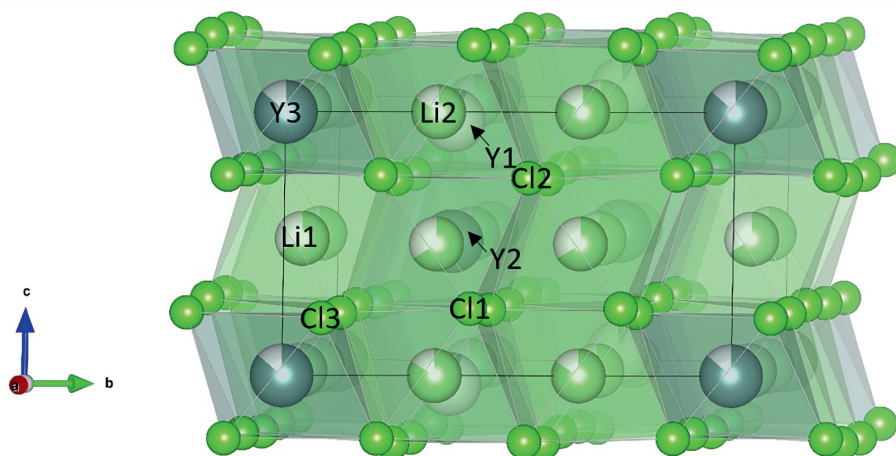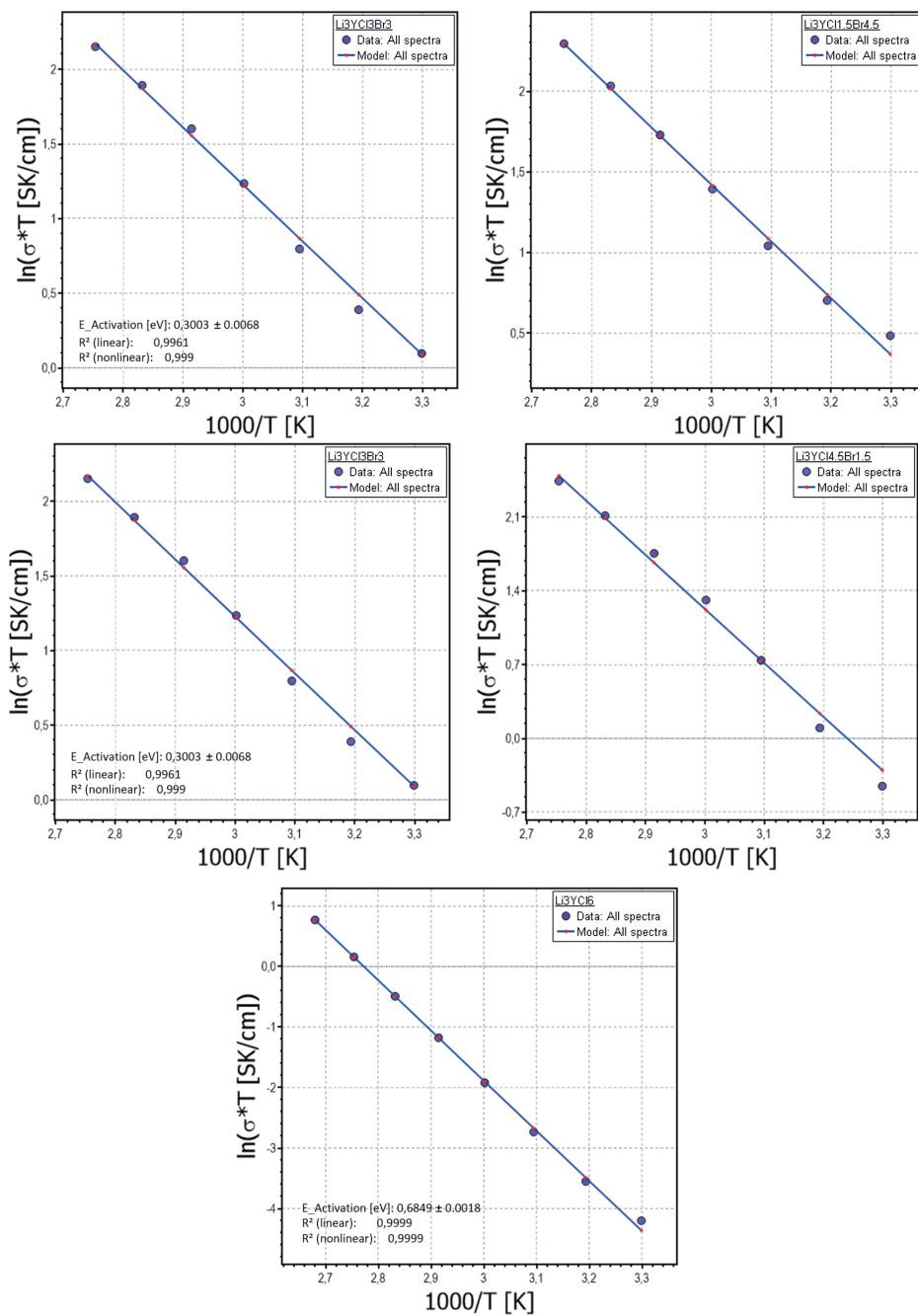| Site	x	y	z	Fractional Occupancy	Uiso	Wykhoff site
Cl1	0.2215	0.7785	0.2676	1	0.022	6i
Cl2	0.5546	0.4454	0.2441	1	0.022	6i
Cl3	0.8865	0.1135	0.2319	1	0.022	6i
Li1	0.3397	0	0.5	0.66	0.075	6h
Li2	0.3397	0	0	0.84	0.075	6g
Y1	0.3333	0.6667	0.0506	0.07	0.020	2d
Y2	0.3333	0.6667	0.5100	1.00	0.020	2d
Y3	0	0	0	0.86	0.020	1a

Figure 8.32: Arrhenius relationships of $Li_3YBr_xCl_{6-x}$

Figure 8.33: First cycle data (left) and long term cycling performance (right) of full cells using NCM811 – Halide SE – Sulphide Argyrodite – Li-In. Top: reference cathode performance in liquid electrolyte. Middle: Li3YCl4.5Br1.5 as halide solid electrolyte. Bottom: Li3YCl1.5Br4.5 as halide solid electrolyte. The batteries were cycled at C/10. The authors note that long-term cycling of these electrolytes also depend on the halide-sulphide solid electrolyte interface, as well as on mechanical properties and the reached capacities.
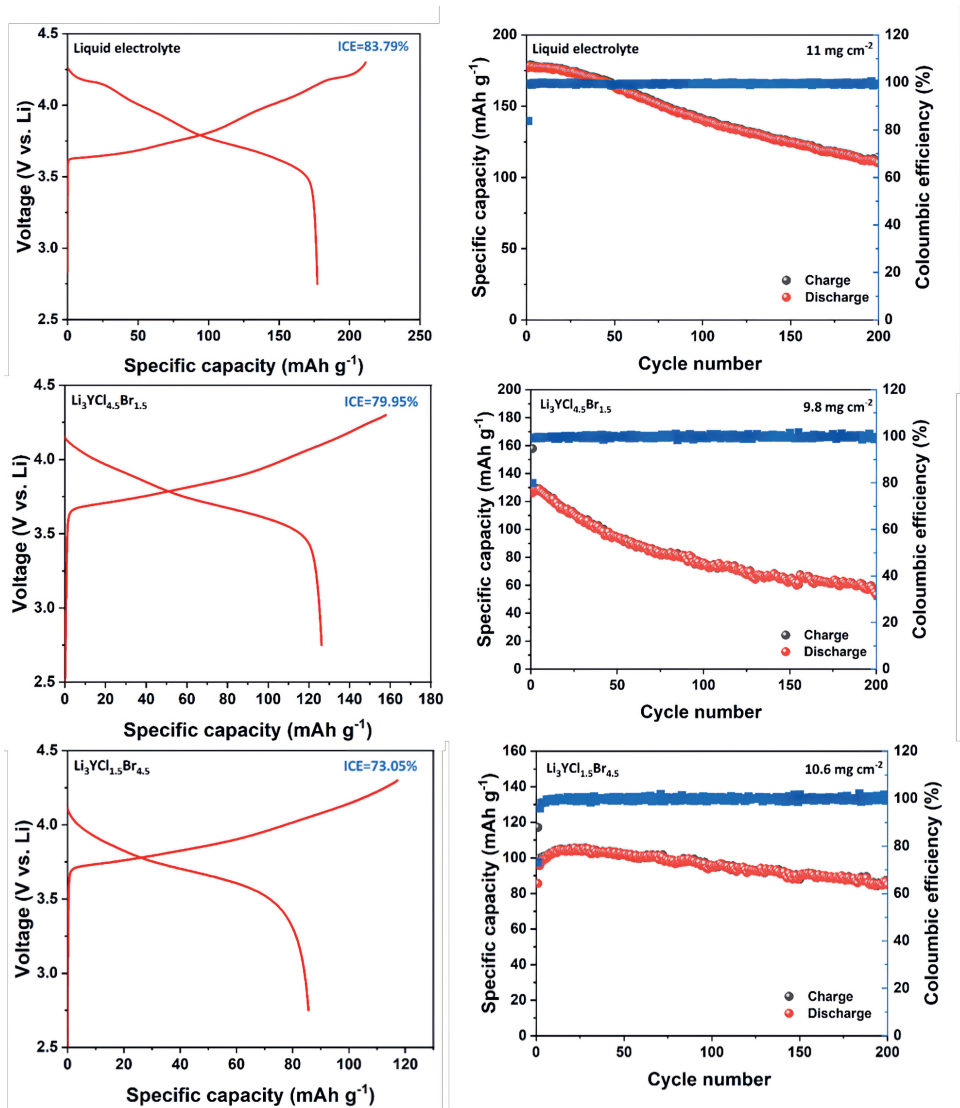
8.4 Appendix to chapter 7

Figure 8.34: Lineshapes of ^{7}Li (ω_0 = 116 MHz) for the $P\bar{3}m1$ (a) and $Pnma$ (b) phases of Li-Y-Cl solid electrolytes at various temperatures. The change in the shape of the satellites is a sign for a change in the electric field gradient around the lithium, as can happen during a phase transition.
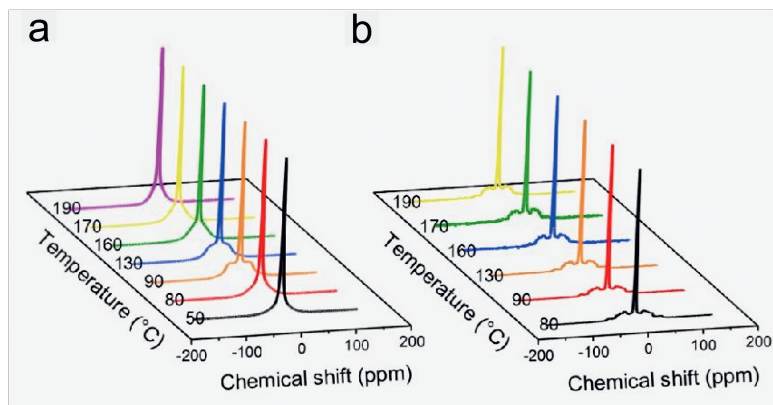
Table 8.12: Jumps between Wyckhoff sites counted from the MD simulations for both the Pnma and the P-3m1 phase of Li3HoCl6 under different temperatures.

Phase	Jump combinations	400	500	600	700	800
	8d1 to 8d1	5	26	83	148	278
	8d1 to 8d2	77	173	246	327	449
	8d2 to 8d1	79	175	246	327	449
Pnma	8d2 to 8d2	2	16	49	75	131
	Total jumps	163	390	624	877	1307
	Jumps between mixed sites [%]	95.7	89.2	78.8	74.6	68.7
	Jumps between same sites [%]	4.3	10.8	21.2	25.4	31.3
	6g to 6g	58	92	159	261	518
	6g to 6h	95	108	220	350	554
	6h to 6g	90	110	218	349	554
P-3m1	6h to 6h	161	245	252	596	926
	Total jumps	404	555	849	1556	2552
	Jumps between mixed sites [%]	45.8	39.3	51.6	44.9	43.4
	Jumps between same sites [%]	54.2	60.7	48.4	55.1	56.6